

**Synthesis, microstructure and
mechanical behaviour of
CuZr-based
bulk metallic glass composites**



Haiyun Wang

A thesis submitted for the degree of
Doctor of Philosophy
July 2018

**Department of Materials Science and Engineering
The University of Sheffield**

Abstract

Bulk metallic glasses (BMGs) have attracted lots of attention owing to their unique physical, chemical and mechanical properties. However, BMGs are still far from practical application due to their catastrophic failure under loading. Substantial efforts have been made to improve their plasticity.

CuZr-based bulk metallic glass composites (BMGMCs) have stood out by introducing transformation induced (TRIP) plasticity to the amorphous matrix. So far most developed BMGMCs are available only with limited dimensions (less than 4 mm in diameter). Furthermore, size and distribution of the second phase in the amorphous matrix are readily influenced by the manufacturing conditions and the purity of the raw materials. Zirconium in high purity is favoured, otherwise, unexpected brittle crystalline phase will precipitate, thereby reducing deformability. Casting temperature will determine the melt status in the mould and the resultant microstructure. High melting temperature and short melting duration in the casting process are preferred, ensuring homogeneous melting and hindering the absorption of the residual oxygen from the atmosphere.

Minor Sn alloying addition (≤ 1 at%) can effectively improve the glass forming ability (GFA) of the ternary metallic system $\text{Cu}_{48}\text{Zr}_{48}\text{Al}_4$, and thereby modifying the microstructures and corresponding mechanical performance. BMGMCs with 0.25 at% Sn addition can reach up to 7 mm in diameter. The B2-CuZr crystalline spheres ranged in size from 10 μm to 40 μm with a volume fraction of $\sim 10\%$ in the glassy matrix in the specimens with a size of 4 – 7 mm without sacrificing compressive strength and plasticity. BMGMCs with 0.75 at% Sn addition could be made up to 8 mm in diameter. The size and volume fraction of B2-CuZr crystalline spheres increased with the increase in specimen dimension. The corresponding compressive mechanical property and work hardening capability were improved.

Minor Ni alloying addition (≤ 1 at%) to the ternary metallic system $\text{Cu}_{48}\text{Zr}_{48}\text{Al}_4$ can effectively adjust the morphology and distribution of *in-situ* formed CuZr crystalline spheres in the glassy matrix and thus improve the deformation performance. Ni addition results in the formation of spear-like martensitic phase dispersed in the B2-CuZr crystalline phase, which may act as nucleation sites for martensitic transformation

upon deformation. With the deformation proceeding, martensitic transformation zone gradually extended from the interface to the inside of crystalline phase (mainly B2). Interaction between untransformed crystalline phase and amorphous matrix, between transformed crystalline phase and amorphous matrix, between untransformed and transformed crystalline phase contributed to the improved plasticity and work-hardening ability.

Phase separation phenomenon was observed in the $\text{Cu}_{47.5}\text{Zr}_{48}\text{Al}_4\text{Co}_{0.5}$ bulk metallic glasses. It is different from the literature, however, AFM and TEM results provided straightforward evidence for the occurrence of the phase separation.

Acknowledgements

First of all, I would like to express my deepest and sincerest gratitude to my first supervisor, Professor W. Mark Rainforth, for his encouragement, support, guidance and patience throughout my PhD study, especially during the last two years. Although he is busy with teaching, research and meetings, he always helps me with electron microscopes. His remarkable knowledge of electron microscopy and his tutorials on electron microscopy have been a great benefit for my study. Secondly, I would like to especially thank my second supervisor, Professor Iain Todd. His enthusiasm and heuristic guidance could always inspire me and impel me to do things in a different manner.

I would like to thank Dr. Philip Mahoney, Dr. Jacob Corteen and Dr. Zhao Yuan Leong in particular; their suggestions and help with Arc Melter maintenance have contributed to carrying on my research in the darkest days.

I would like to express my gratitude to Dr. Le Ma. She always encouraged me and gave the most support for my research ideas. It is impossible to prepare TEM samples with twin-jet electropolishing without her. I also would like to thank Dr. Peng Gong and Dr. Joanne Sharp for their suggestions on twin-jet electropolishing process and TEM operation, respectively. Their help got me through the stumbling blocks to the microstructure study. In addition, I would like to thank Dr. Xin Pan for his company in the laboratory for lots of late night in the darkest of days. It is impossible to do so many fabrication batches within limited time without him.

I would also like to thank the technical staff of the Materials Science department, Sorby Centre and EEE workshop for their training and assistance. I am also very thankful to Dr. Andrew Williams who gave me useful suggestions of sample preparation for microstructure investigation during my initial research project. In addition, I am grateful to Dr. Muhaed Alali for the training on digital image correlation (DIC) strain measurement in tensile testing. Many thanks to Dr. Dikai Guan, who was

always ready to give me assistance and suggestions, especially on EBSD trails. Thank you to all my colleagues and friends for their help and happiness during these years.

Finally I would like to express my utmost gratitude to my family for their unconditional love and support. I am so proud to have them in my life.

List of Symbols

BMG	Bulk metallic glass
BMGMCs	Bulk metallic glass composites
MG	Metallic glass
T_g	Glass transition temperature
T_x	Onset crystallization temperature
ΔT_x	Supercooled liquid region
T_p	Peak crystallization temperature
T_i	The initial temperature of the melt in the casting mould
T_c	The casting temperature
ΔT	Undercooling or supercooling
T_m	The melting temperature
T_K	Kauzmann temperature
R_c	Critical cooling rate
U	The growth rate
I	The nucleation rate
d	The mean crystal size
β	The heating rate
E_g	The activation energy for glass transition
E_x	The activation energy for the onset crystallization
E_p	The energy for peak crystallization

R	The gas constant, 8.314 J/mol
H	Microhardness in nanoindentation
E_r	Reduced Yong's Modulus
STZ	Shear transformation zone
GFA	Glass forming ability
ΔG	The driving force for crystallization
ΔG^*	The activation energy barrier of nucleation
ΔH_f	The enthalpy change from the melt to the crystal
ΔS_f	The entropy change from the melt to the crystal
η	The viscosity
k_B	Boltzmann's constant
ΔC_p	The specific heat difference of the undercooled liquid and glass
SRO	Short range order
MRO	Medium range order
ν	Poisson's ratio
PEL	Potential energy landscape theory
MT	Martensitic transformation
M_s	Martensitic transformation temperature
A_s	Austenitic transformation temperature
TRIP	Transformation induced plasticity

Contents

Abstract.....	I
Acknowledgements.....	III
List of Symbols.....	V
Contents.....	VII
Chapter 1 Introduction.....	1
1.1 Background.....	1
1.2 Thesis layout.....	2
Chapter 2 Literature Review.....	4
2.1. Development of metallic glass and metallic glass composites.....	4
2.2. Metallic glass formation.....	6
2.2.1 Thermodynamics of metallic glass formation.....	8
2.2.2 Kinetics of metallic glass formation.....	8
2.2.3 Correlation of thermodynamics and kinetics of metallic glass formation...	10
2.2.4 Configurations of metallic glass.....	13
2.3. Deformation mechanisms of bulk metallic glass.....	17
2.3.1 Free volume model.....	18
2.3.2 Shear transformation zone theory.....	19
2.3.3 Potential energy landscape theory.....	21
2.3.4 Cooperative shearing model.....	24
2.4. Mechanical properties of bulk metallic glasses.....	26
2.5. Bulk metallic glass matrix composites (BMGMCs).....	30
2.5.1 Nano-scale heterogeneities reinforced BMGMCs.....	31

2.5.2 In-situ dendrite reinforced BMGMCs	32
2.5.3 CuZr-based BMGMCs	35
2.6. References	47
Chapter 3 Experimental Techniques	63
3.1. Bulk metallic glasses/composites preparation and processing.....	63
3.1.1 Melt spinning	63
3.1.2 Argon arc melting.....	64
3.1.3 Argon suction casting	65
3.2. Structure characterisation.....	66
3.2.1 X-ray diffraction (XRD).....	66
3.2.2 Scanning electron microscopy (SEM).....	68
3.2.3 Transmission electron microscopy (TEM)	69
3.3. Thermal analysis	70
3.3.1 Differential scanning calorimetry (DSC)	70
3.4. Mechanical Testing	71
3.4.1 Compression testing and its compliance correction	71
3.4.2 Nanoindentation	73
3.4.3 Elastic modulus measurement	73
3.5. Reference.....	75
Chapter 4 Developments of Large-sized CuZr-based Bulk Metallic Glass Composites with Improved Mechanical Properties by Tailoring Microstructure	76
4.1 Introduction	76
4.2 Experimental	76

4.3 Results and Discussion.....	78
4.3.1 Composition – raw materials purity – microstructure relationship	78
4.3.2 Composition – manufacturing condition – microstructure relationship	82
4.3.3 Composition – cooling rate – microstructure relationship	91
4.3.4 Crystallization kinetics of 0.25 at% and 0.75 at% Sn-doped CuZr-based BMGMCs	102
4.3.5 Mechanical properties.....	106
4.4 Conclusions	115
4.5 References	117
Chapter 5 Formation of CuZr-based Bulk Metallic Glass Composites with improved mechanical properties by optimizing microstructure.....	124
5.1 Introduction	124
5.2 Experimental	124
5.3 Results	125
5.3.1 Microstructure evolution with Ni addition	125
5.3.2 Mechanical properties.....	130
5.3.3 Microstructure of the as-cast 0.75 at% Ni-doped CuZr BMGMCs.....	132
5.4 Discussion	134
5.4.1 Effect of Ni on the GFA	134
5.4.2 Deformation mechanisms	135
5.5 Conclusion.....	142
5.6 References	144
Chapter 6 Phase Separation in $\text{Cu}_{47.5}\text{Zr}_{48}\text{Al}_4\text{Co}_{0.5}$ Bulk Metallic Glass	149

6.1 Introduction	149
6.2 Experimental	151
6.3 Results	152
6.3.1 Structural characterization of the as-spun and as-cast samples	152
6.3.2 Mechanical properties.....	158
6.4 Discussion	160
6.4.1 Structural phase separation	160
6.4.2 Relationship between phase separation and mechanical property.....	164
6.5 Conclusions	166
6.6 References	167
Chapter 7 Alloying Addition Effects	170
7.1 Discussion	170
7.2 References	173
Chapter 8 Summary and Conclusions.....	174
Chapter 9 Suggestions and Future work	178
Appendix.....	180

Chapter 1 Introduction

1.1 Background

Bulk metallic glasses (BMGs) have attracted extensive attention because of their excellent properties, such as high strength, large elastic limit (up to 2%), high hardness and excellent corrosion resistance. However, BMGs are still far from practical application due to their catastrophic failure under tension. So far substantial efforts have been made to improve their plasticity, including *in-situ* induced soft crystalline phase in an amorphous matrix composite structure, *ex-situ* induced crystalline phase in a glass-forming matrix composite structure and liquid phase separated composite structure. The *in-situ* formed two phase metallic glass composites mainly refers to dendrite reinforced and shape memory phase reinforced bulk metallic glass composites. However, the dendrite reinforced BMGMCs do exhibit some drawbacks, such as the necessity to introduce the toxic element Be into the system, the observation of early necking and strain softening under tension.

In comparison, shape memory phase reinforced BMGMCs can overcome this shortcoming by introducing phase transformation-induced (TRIP) concept to the glassy matrix media. However, most developed shape memory BMGMCs are limited in the attainable dimensions (typically less than 4 mm in diameter). Furthermore, the microstructures are sensitive to the manufacturing conditions. Practical engineering application for TRIP-reinforced BMGMCs is still a fairy tale at present. Therefore, the development of large-scale shape memory BMGMCs with improved mechanical performance is desperately required.

The aim of this project is to optimize microstructures, including the size and distribution of crystals in the glassy matrix, thereby improving the mechanical properties of the CuZr-based bulk metallic glass composites. It has been achieved by minor alloying additions. Ni and Sn were selected as minor additions to the CuZr-based

system. Both Ni and Sn have large negative heat of mixing with Zr and small positive heat of mixing with Cu, therefore, it may result in the preference of heterogeneous nucleation and microstructure optimization of the composites. In the project, large-scaled shape memory BMGMCs with improved mechanical properties were developed by minor addition of Sn. The manufacturing conditions, which may affect the microstructures of the resultant BMGMCs, were investigated in detail. The reinforcing mechanism and corresponding deformation mechanism were explored as well. The distribution of crystalline phase in the amorphous matrix was manipulated and thereby improving mechanical properties by adding minor Ni. In addition, phase separated microstructure and the resulting compressive deformation behaviour was studied in $\text{Cu}_{47.5}\text{Zr}_{48}\text{Al}_4\text{Co}_{0.5}$ BMG.

1.2 Thesis layout

This thesis consists of 8 chapters. The main information will be briefly introduced as follows:

Chapter 2 presents the basic theory and definition related in this project and reviews the research progress on development of BMGMCs, mechanism studies and strategies for the distribution and morphology of reinforced crystalline phase in the past a few years. The challenges in the future are mentioned as well.

Chapter 3 introduces the main experimental techniques in the project. It includes specimen preparation, microstructure characterization and mechanical testing.

Chapter 4 studies the influence of the purity of the raw materials (Zr), manufacturing condition (*i.e.* melting current and melting time) and casting mould configuration on the size and distribution of crystalline phase in the glassy matrix and resultant mechanical performance. A systematic microstructure – cooling rate – deformation behaviour relationship for the alloy with the composition of $\text{Cu}_{47.75}\text{Zr}_{48}\text{Al}_4\text{Sn}_{0.25}$ and $\text{Cu}_{47.25}\text{Zr}_{48}\text{Al}_4\text{Sn}_{0.75}$ has been presented.

Chapter 5 investigated the Ni alloying addition effect on the microstructure and deformation performance.

Chapter 6 demonstrates the phase separation phenomenon in $\text{Cu}_{47.5}\text{Zr}_{48}\text{Al}_4\text{Co}_{0.5}$ BMG.

Chapter 7 and Chapter 8 summarize the main conclusions and propose some suggestions for the future work.

Chapter 2 Literature Review

2.1. Development of metallic glass and metallic glass composites

Metallic glasses (MGs) are a class of solid metallic alloys that lack translational or orientational long-range periodic order in atomic structure, which is different from their crystalline counterparts [1, 2], as outlined in Figure 2.1. Bulk metallic glasses (BMGs) represent MGs with characteristic size in excess of 1 mm [3-5].

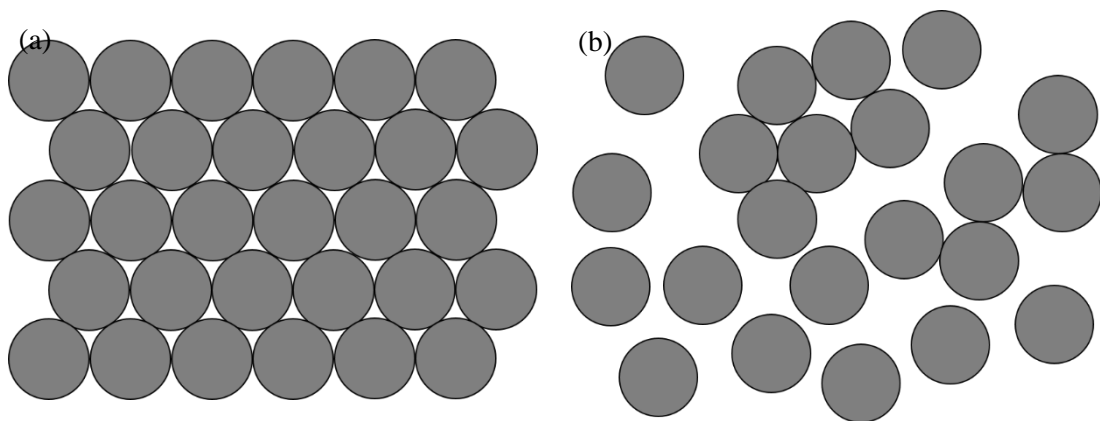


Figure 2.1. A schematic of crystalline and amorphous atomic structures: (a) Crystalline atomic arrangement; (b) Amorphous atomic arrangement.

The first MG, with an eutectic composition of $\text{Au}_{75}\text{Si}_{25}$, was discovered and reported by Klement *et al.* in 1960 [6]. It was produced by splat quenching metallic liquids at very high cooling rates of the order of $10^5 - 10^6$ K/s. As such, the nucleation and growth of crystalline phase was dramatically suppressed, and the configuration of the melt was ‘frozen’ to the ambient temperature. As a result, MGs possess favourable material properties, including high yield strength, high elasticity, high corrosion resistance and high flexibility [5, 7, 8].

Since then, substantial effort has been made to explore potential compositions of MGs coupling with rapid solidification techniques, among which the invention of melt spinning

method has speeded up the research progress [9, 10]. However, the formation of MGs was limited to the forms of thin ribbons, wires and powders with dimensions from 20 μm to 100 μm during the period from 1960s to 1970s. The momentum was gained in 1974 when Chen and Turnbull [11, 12] synthesized ternary Pd-Cu-Si alloys with 1 mm diameter using simple suction casting method at relatively lower cooling rates in the range of the order of 10^3 K/s. This is the formation of the first BMGs. Later, BMGs with sizes up to centimetres of melt compositions of Pd-Ni-P and Pt-Ni-P were extensively studied, which were produced through boron oxide fluxing quenching at very low critical cooling rates of 10 K/s [13, 14]. Unfortunately, the use of noble metals restricted their practical applications even though they were with greater volumes.

An important breakthrough in BMG development was made with the discovery of multicomponent alloy systems by Inoue and collaborators [2, 15-18]. These new BMGs exhibit excellent glass forming ability (GFA), similar to those of the Pt- and Pd-based BMGs. Building on Inoue's findings, Peker and Johnson [2, 19, 20] developed a family of multicomponent Zr-based BMGs in 1990s. The BMG with a composition of $\text{Zr}_{41.2}\text{Ti}_{13.8}\text{Cu}_{12.5}\text{Ni}_{10.0}\text{Be}_{22.5}$, known as Vitreloy 1, was the first commercial BMG. Large samples in the form of rods up to 14 mm in diameter could be produced by casting in silica containers. To date, it is still the one of the best glass formers. Inspired by these successes, significant progress has been achieved in Fe-, Ni-, Ti- and Cu-based BMGs with excellent GFA [8, 21]. The advent of the BMGs with large sizes allows for the conventional characterization of the mechanical, physical and chemical properties systematically, and raises the hope for possible applications as structural materials. Ever since the discovery of the first BMG, researchers were working on the improvement of GFA and the development of BMGs with large volumes through crystallization suppression during solidification. As a consequence, BMGs up to 80 mm in diameter have been found [22, 23].

So far, BMGs with different dimensions and compositions have been substantially explored via microalloying or developing different manufacturing methods [24-30]. The fabrication methods mainly include the rapid solidification (including gas atomization, melt

spinning, suction casting, *etc.*) and solid-state amorphization (such as mechanical alloying and mechanical milling). In recent years, novel processes [31, 32], such as additive layer manufacturing and vapour deposition, have attracted much attention to avoid the geometry limitations.

The synthesis of large scale BMGs has triggered the research interest in understanding the underlying mechanisms of their brittleness and how to improve it [4, 33]. The heterogeneous structure with crystalline phases reinforced in a BMG matrix has been introduced to stabilize glassy phase against catastrophic failure and to enhance global plasticity [34-36]. However, most rules to design new BMGs or BMG composites are empirical, which are not universally applicable. Therefore, to understand the underlying mechanism of the formation of BMGs or BMG composites, the principles for quantitative and effective composition design of BMGs and its composites are required.

2.2. Metallic glass formation

MGs are disordered metallic materials that lack long-range periodicity at the atomic scale. In other words, their atomic configuration can be regarded as the ‘frozen’ structure of a liquid during rapid solidification on the laboratory timescale [6, 37-39]. The process of rapid quenching a melt is a competition between the undercooled liquid and the crystalline phase, during which the rate of volume or enthalpy change of the liquid decreases abruptly and continuously to a value comparable to that of a crystalline solid, resulting in a strong viscosity increase. Therefore, there is no opportunity for the atoms in the undercooled liquid to diffuse, rearrange and form crystalline phase with long-range periodicity, as illustrated in Figure 2.2. Glass forming ability (GFA) is used to describe the capability of the MG melt to suppress crystallization in preference to the formation of glassy phase upon solidification. As such, the competition between the liquid phase and the crystalline phase will determine the formation of MGs [40]. Assuming steady-state nucleation, the nucleation rate is determined by the interaction of thermodynamics and kinetics of the melt as shown:

$$I = N_v^0 \vartheta D \exp\left(-\frac{\Delta G^*}{kT}\right) \quad (\text{Equation 2.1.})$$

where N_v^0 is the monatomic number per volume; ϑ is the frequency rate; k is the Boltzmann's constant; D is the effective diffusion coefficient; T is the absolute temperature; ΔG^* is the activation energy barrier of nucleation.

ΔG^* is also given as $\Delta G^* = 16\pi\sigma^3/\Delta G^2$, where σ is the interfacial energy between the melt and crystalline phase, and ΔG is the driving force for crystallization. Consequently, it is essential to take thermodynamics (the crystallization driven force), dynamics (the diffusivity or viscosity) and structural fluctuation (the configuration) into consideration to understand metallic glass formation.

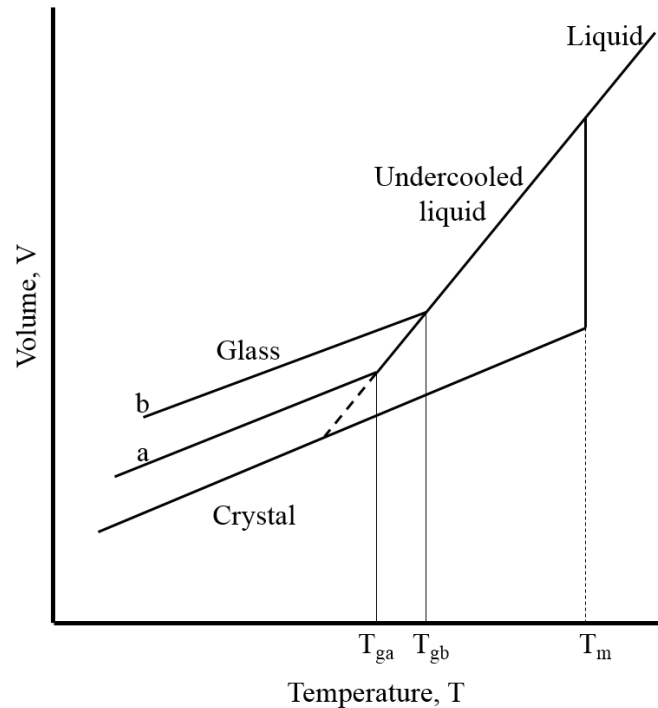


Figure 2.2. Volume change as a function of temperature for a crystal and a glassy material, where: T_m is the liquid temperature; T_{ga} is the glass transition temperature at a slow cooling rate; T_{gb} is the glass transition temperature at a fast cooling rate. (Redrawn from ref.[39])

2.2.1 Thermodynamics of metallic glass formation

From thermodynamic considerations, the glassy phase will be retained if its Gibbs free energy is relatively lower than that of the competitive crystalline phase. In other words, the driving force for crystallization is naturally as low as possible in the supercooled liquid melt during the process of bulk metallic glass formation [41, 42], as expressed in Equation 2.2 and 2.3:

$$\Delta G = G_{glass} - G_{crystal} \quad (\text{Equation 2.2})$$

$$\Delta G = \Delta H_f - T\Delta S_f \quad (\text{Equation 2.3})$$

where ΔG is the driving force for crystallization; G_{glass} is the Gibbs free energy of the glassy phase (liquid melt); $G_{crystal}$ is the Gibbs free energy of the crystalline phase; ΔH_f is the change of enthalpy from the melt to the crystal; ΔS_f is the change of entropy from the melt to the crystal; T is the liquid temperature.

The smaller the value of ΔG is, the smaller the driving force of crystallization, and therefore the lower the nucleation rate, and the better the GFA is. There are two approaches to decrease the crystallization driving force ΔG on the basis of the above thermodynamic equations. One is to reduce the melt enthalpy (ΔH_f) by lowering the chemical potential between constituents in the undercooled melt; the other is to increase the melt entropy (ΔS_f) [17]. It is expected that the introduction of a large number of components to the alloy system results in the enlargement of ΔS_f . In addition, the increase in ΔS_f will cause the increase in the degree of dense random atomic packing in the melt, which is in favour of a decrease of ΔH_f and an increase of the interfacial energy between solid and liquid phase. This is consistent with the concept of the ‘confusion principle’ [43] and Inoue’s first empirical rule [21].

2.2.2 Kinetics of metallic glass formation

In consideration of the solidification process, the liquid will experience a transition to the glassy state, assuming that the crystallization could be controlled or avoided. The liquid will

be ‘retained’ to the ambient temperature if the cooling rate is extremely large. Thus, the glass formation is a kinetic process in nature.

From standpoint of kinetics, viscosity (η) of the liquid is an important parameter to determine the GFA of an alloy [44]. Viscosity is related to the mobility of the atoms in the melt upon cooling. As such, the increase in viscosity will result in the decrease in atomic diffusivity no matter metallic or non-metallic. In this respect, viscosity is sensitive to temperature, especially close to glass transition temperature (T_g). The behaviour of viscosity with the temperature approaching T_g can be quantitatively characterized by the concept of fragility (m) [38, 45-47]. It is defined as Equation 2.4:

$$m = \left[\frac{d\eta(T_g/T)}{d(T_g/T)} \right]_{T=T_g} \quad (\text{Equation 2.4})$$

The melt with low fragility value belongs to ‘strong’ system, while that with high value belongs to ‘fragile’ system. The value of fragility is typically located between at least 16 for the ‘strong’ liquid and 200 for the ‘fragile’ liquid.

For ideal liquids (*e.g.* silica), the temperature dependence of viscosity can be described by the Arrhenius functionality, mathematically expressed as Equation 2.5 [39, 45, 48]:

$$\eta = \eta_o \exp(E/k_B T) \quad (\text{Equation 2.5})$$

where E is activation energy for viscous flow, which is temperature independent; η_o is a pre-exponential constant accounting for the high-temperature viscosity and is assumed temperature independent; k_B is Boltzmann’s constant.

However, most metallic alloy liquids and water exhibit non-Arrhenius behaviour, which can be well represented with the Vogel-Fulcher-Tammann (VFT) equation [39, 45, 49]:

$$\eta = \eta_o \exp[DT_o/(T - T_o)] \quad (\text{Equation 2.6})$$

where η is the viscosity; η_o is the viscosity at the infinite temperature; T_o is the Vogel-Fulcher temperature, where the barrier with respect to flow would go to infinity; D is the measure of the kinetic fragility of the liquid and is temperature independent.

Figure 2.3 shows a fragility plot originally proposed by Angell [45], comparing the viscosity of a variety of glass forming liquids as a function of the temperature normalization against the T_g . According to the Equation 2.5, $\log(\eta)$ and $\log(1/T)$ will exhibit a linear relationship for the ideal Arrhenius behaviour [39]. However, there is a viscosity deviation from the linear extrapolation of the high temperature trend with the decrease of the temperature, showing a non-Arrhenius behaviour as illustrated in Figure 2.3. The fit with the Equation 2.6 was good. Silica is a strong liquid, whereas o-terphenyl is fragile liquid. The strong liquid (with low fragility) behaviour exhibits high viscosity, sluggish kinetics and thus the retarded nucleation and the inhibited growth of crystalline clusters in the undercooled melt. As such, it results in a large GFA and the high thermostability of supercooled liquid [44, 50-52].

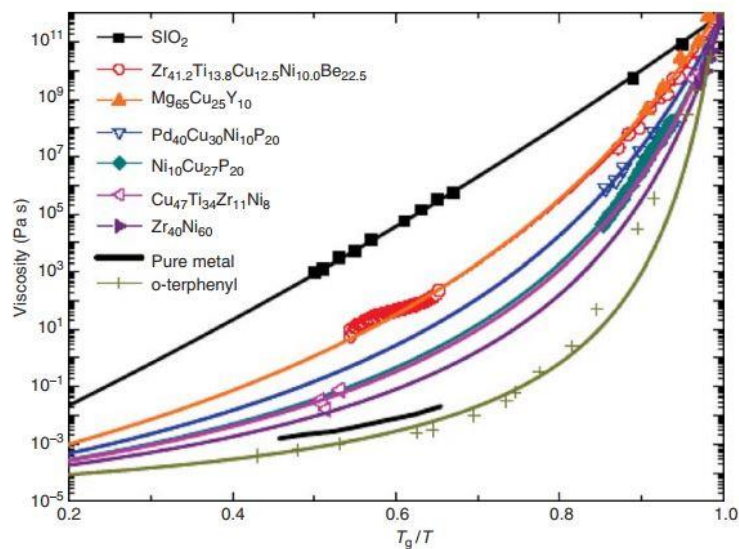


Figure 2.3. An Angell plot with a comparison of the viscosities of different glass forming melts. (Taken from ref. [53])

2.2.3 Correlation of thermodynamics and kinetics of metallic glass formation

The correlation of thermodynamics and kinetics of metallic glass formation can be expressed by Equation 2.7 according to Adam and Gibbs's [54] molecule kinetic theory:

$$\eta \text{ or } t = A \exp\left(\frac{B}{TS_c(T)}\right) \quad (\text{Equation 2.7})$$

where η and t refer to the viscosity and relaxation time, respectively. A and B are temperature-independent constants. $S_c(T)$ is the temperature-dependent configurational entropy of the liquid. It measures the number of available inherent structural states in the MG melt system [39, 44], which determines the minimum possible cluster size and energy barrier for the relaxation. It is the reflection of the structural order in the melt, and thus suggests the fundamental structural origin of the thermodynamic and dynamic properties.

As depicted in Equation 2.7, the increase in viscosity (or relaxation time) of the melt with the temperature approaching T_g arises from the reduction in the number of the configurations that the melt can sample [54].

Hypothetically, there is a non-zero temperature where the liquid entropy is equal to the crystal entropy. It is defined as the Kauzmann temperature, T_K [39], where the ideal glassy state with the lowest energy will be attained. In theory, the entropy of a perfect crystal at absolute zero exactly equals zero. With continuous cooling, the liquid entropy will become negative. Nevertheless, the entropy is a non-negative quantity inherently. This is known as the entropy crisis [55].

In essence, the entropy crisis results from the fact that configurational entropy of the melt is higher than that of the crystal, attributed to the higher atomic degrees of freedom in the liquid [39]. The configurational entropy $S_c(T)$ can be determined by experimentally measuring the excess specific heat ΔC_p as the Equation 2.8:

$$\left(\frac{\partial S_c}{\partial T}\right)_p = \frac{\Delta C_p}{T} \quad (\text{Equation 2.8})$$

where ΔC_p is the difference of the specific heat capacity of the undercooled liquid and the ‘frozen’ glass at a given pressure. Therefore, the melt possesses higher heat capacity in comparison with its counterpart ‘frozen’ ideal glass. As such, the melt entropy will be consumed and vanishes at T_K during the supercooling of the melt [39]. However, glass transition occurs at the temperature above T_K , which prevents the further reduction in the configurational entropy of the system. As a result, the viscosity of the system deviates from the

normal behaviour, which determines the configuration of the as-formed glass [39].

The crystallization rate of the undercooled melt depends on competition of the increasing Gibbs free energy driving force (thermodynamics) and the increasing viscosity (dynamics) upon cooling, resulting in the creation of the typical time – temperature – transformation (TTT) diagram to further understand glass formation, as schematically shown in Figure 2.4. In this diagram, a nose-like shape curve separates the crystalline and amorphous phase and a straight line with arrow indicates the critical cooling rate (R_c) for the glass formation. For the good glass formers, the position of the nose-shaped curve will be moved to the right side with a longer time scale and a decreased R_c .

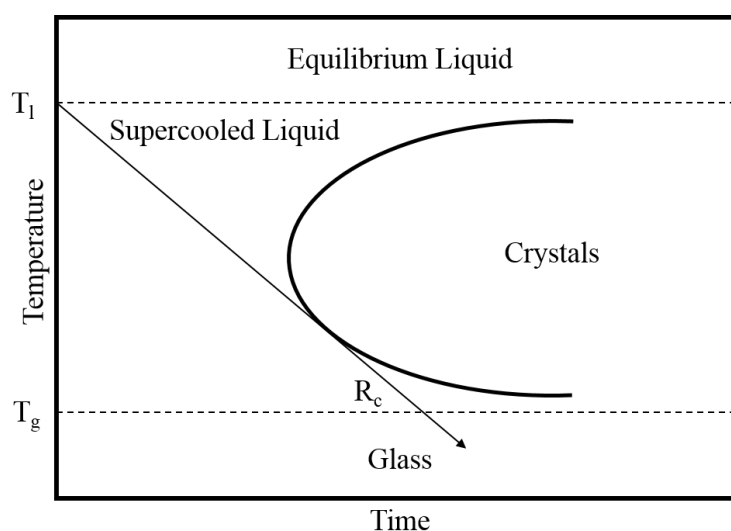


Figure 2.4. A schematic of a typical TTT diagram of glass formation. The slope R_c represents the critical cooling rate for glass formation.

Most of the BMGs with good GFA are produced by rapid quenching from a superheated melt via arc-melting and suction casting in a water cooled copper mould. Thus BMGs are the product of non-equilibrium solidification in nature and the cooling rate will determine relaxation and viscosity of the melt upon supercooling [38]. From this perspective, the structures and the properties of BMGs will be sensitive to the processing history. As such, processing parameters should be well controlled and preparation method and its process should

be taken into account when comparing two MGs, even with the same composition.

2.2.4 Configurations of metallic glass

The atomic and electronic structures are believed to be the fundamental factors to deeply understand the formation and the physical properties of MGs/BMGs/BMGMCs [7, 56-59]. According to the classical crystal nucleation theory, the nucleation rate strongly relies on the atomic diffusivity and the viscosity of the undercooled melt for the metallic alloy. In this viewpoint, the liquid with high viscosity and density is expected to be a more stable state, and therefore a better glass former. Local icosahedral order has been suggested to be the basic structure unit in the supercooled liquids and amorphous alloys on the account of the highly close-packed configuration, the lack of periodicity and the difficulty of growth [60]. It is suggested that the atomic size ratio of 0.902 between the solute atom and the solvent atom is essential to form close packed icosahedra-like short range order in the glassy structure [56] and the atomic size ratio of constituent elements was regarded as a key factor to affect GFA, especially for binary alloy system comprising of transition elements [61]. As Inoue has reported that the composition of the best glassy former is normally located in a very narrow composition range [21]. A slight change in the composition of a MG will result in a significant change of its property. Therefore, an understanding of the local atomic structure of a good glassy former will be a feasible solution to the reliable and quantitative design of BMGs with high GFA and excellent properties. Some structural models for MGs will be summarised as follows.

Bernal's dense random-packing model is the most accepted structural model, in which the metallic glass is treated as the frozen metallic melt [62-64]. In Bernal's original idea, the atoms, assumed as the hard spheres with identical/near identical sizes, are randomly and densely packed without the crystalline arrangement introduction. It is known as dense random packing of hard spheres (DRPHS). In the model, Bernal has proposed that five types of free spaces with different atomic packing arrangements are supposed to be the basic structural units, such that the atoms will be packed as densely as possible, as illustrated in Figure 2.5. According to Bernal's model, five clusters with moderate distortion are mixed contained in the glassy

structure (in Figure 2.5) to produce a dense and efficient amorphous structure. It can be satisfactorily adapted to monatomic metallic alloys, in which constituent elements have comparable atomic sizes. However, it fails to give insight of short range order (SRO) and medium range order (MRO) in the multicomponent amorphous alloy system.

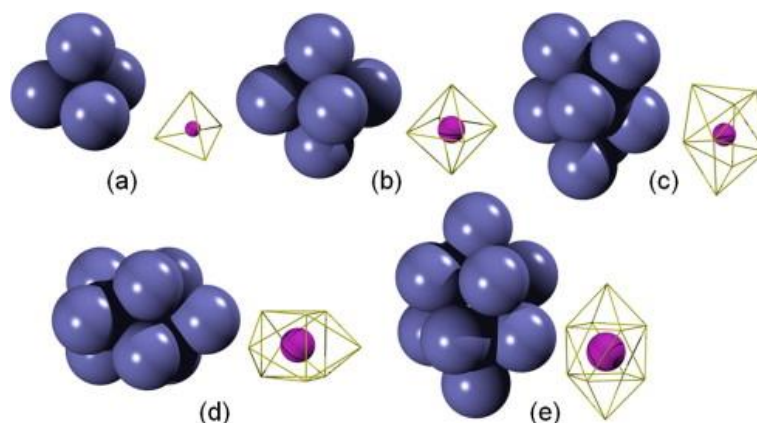


Figure 2.5. A schematic of Bernal's holes: (a) tetrahedron; (b) octahedron; (c) tetragonal dodecahedron; (d) trigonal prism capped with three half octahedra; (e) Archimedean antiprism capped with two half octahedral. (Taken from ref. [38])

In light of the Bernal's DRPHS model, Gaskell [65, 66] has proposed a stereochemical model, in which the SRO in the amorphous structure is very similar to that in the counterpart crystalline structure with an alike composition. The differences arise in the MRO – the stereochemical unit packing is in order in crystals, while that is in random in glasses. This model was applied to explain the structure of the transition metal-metalloid amorphous structure. Take the glassy structure containing Ni – P for example, it was suggested that the configurational unit of a tricapped trigonal prism (Ni_3P) was present both in the MG and in its corresponding crystal, as shown in Figure 2.6. It agreed well with the diffraction experimental results, which further proved that SROs in MGs are alike in corresponding crystalline materials. However, Gaskell's model could not be applied to metal-metal based MGs.

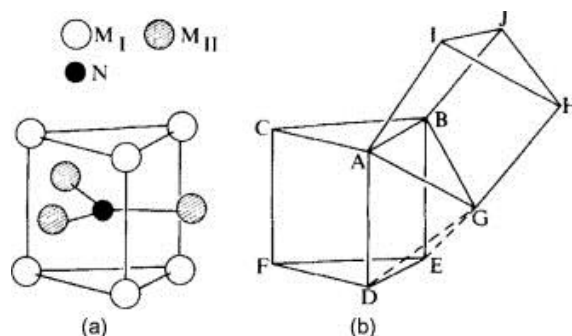


Figure 2.6. A schematic of Gaskell's stereochemical model for transition metal – metalloid MGs: (a) N is the metalloid atom, MI and MII are the transition metal atoms. (b) Connection of the basic unit. (Taken from ref. [66])

It is impossible to extend the local densely packed atomic structure to the macroscopic scale by the repetition of the SROs or MROs in the MGs with the same way in the crystalline materials. Miracle [67-69] has presented an atomic structure model of metallic glasses, which is known as efficient cluster packing model (ECP). In his model, the efficiently packed solute-centered atomic cluster is retained as the local structure unit and is ideally modelled as spheres. An extended structure will be obtained by efficiently packing these spheres into the face-centered cubic (FCC) or the hexagonal close-packed (HCP) three-dimensional structure frame. In such a manner, a densely close-packing structure will be achieved and its amorphous nature will be maintained, as schematically illustrated in Figure 2.7. Miracle's model has described the accommodation of MRO in the glassy structure. However, the MRO cannot extend beyond 1 nm due to the internal strains and packing frustrations. As such, the disordered nature of the MGs can be preserved.

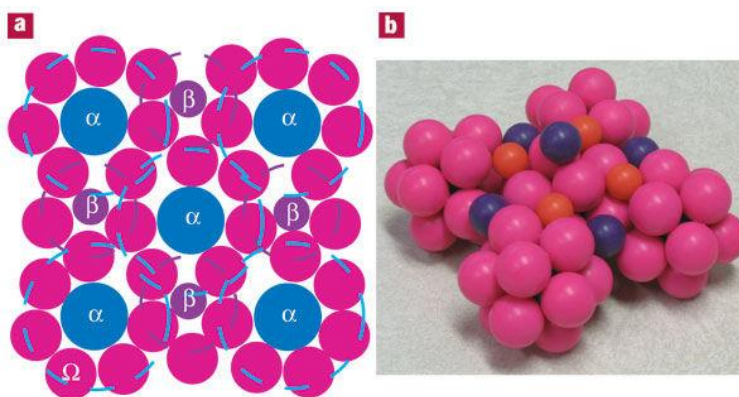


Figure 2.7. A schematic of Miracle's efficient cluster packing model in which an extendable efficiently close packed structure is achieved by packing sphere-like clusters into the FCC or HCP configuration frame: (a) a 2D representation of a densely close packed structure; (b) a 3D cluster model.

On the basis of experimental results and computational simulations, Sheng and his co-workers [70] have proposed a cluster packing scheme to resolve the atomic-level structure of MGs. They analysed a range of typical binary MG systems, in which different chemistry and atomic size ratios are involved. They clarified the different types of SRO and the nature of the MRO based on the systematic analysis. In this model, the SRO clusters were treated as rigid balls and the MRO clusters were regarded as icosahedral packings of these rigid balls. It suggested that the icosahedral fivefold cluster packing, other than FCC or HCP cluster packing, is more favourable in SRO cluster network in MGs, as schematically represented in Figure 2.8. The bonding between SRO clusters may strongly depend on the composition. The dense packed structure without the periodic symmetry may extend to approximately 2 nm in MGs.

The dense close-packed SRO or MRO clusters proposed above were targeted to provide a reasonable explanation of atomic glassy structure and a deep understanding of the glass formation and corresponding mechanical behaviours.

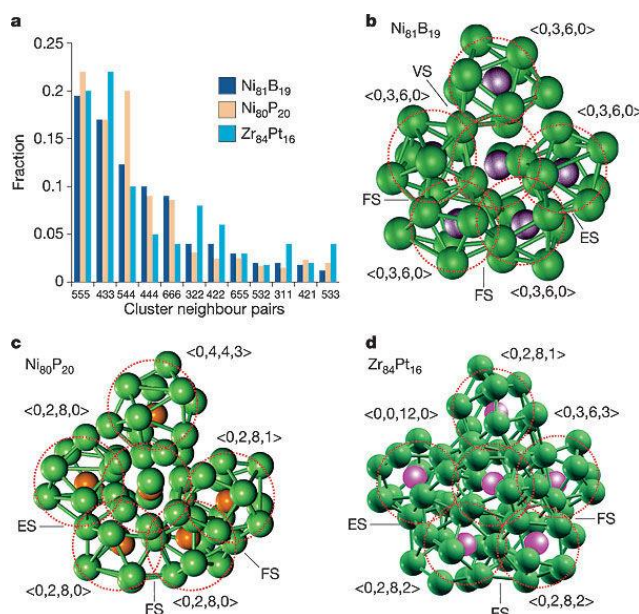


Figure 2.8. Schematics of the packing of the solute-centred quasi-equivalent clusters, showing their MRO. (Taken from ref. [70])

The disordered atomic structure of MGs can be extensively examined through various experimental techniques, including X-ray/neutron diffraction, X-ray absorption fine structure (XRAFS), Nuclear magnetic resonance (NMR), Positron annihilation spectroscopy (PAS), Fluctuation electron microscopy and Transmission electron microscopy (TEM) [70-79]. Different methods have their own pros and cons, such that they could not give an identical atomic configuration, especially for the multicomponent MG system.

2.3. Deformation mechanisms of bulk metallic glass

The primary feature for a metallic structure is the atomic bonding, so that the strain can be accommodated through changes within the atomic scale at low energy [4]. However, the atomic bonding will be broken and reformed without significant concern in a covalent solid or in an ionic solid. For MGs, the local atomic arrangement requires high energy due to the lack of atomic long range order structure.

During deformation of MGs, a general agreement has been achieved that the local atomic rearrangement is required to accommodate the shear strain [37, 38, 56]. The volume or size of

the rearranged local area strongly relies on the metallic glass systems [38]. A fundamental understanding of the relationship between structure and deformation behaviour of MGs is still in demand in spite of the development of MGs in recent years. Therefore, several different theories of deformation mechanism in MGs structure will be addressed as the following sections.

2.3.1 Free volume model

Based upon the theories of Cohen and Turnbull [80] and applied to glass deformation by Spaepen [81], free volume model describes a diffusion controlled atomic jump in an ideal liquid of hard spheres. It allows atoms within the metallic glass matrix to move through gaps between atoms to the regions with high free volume. The localised plastic deformation is regarded as a series of discrete atomic jump in the glass [4] as depicted schematically in Figure 2.9.

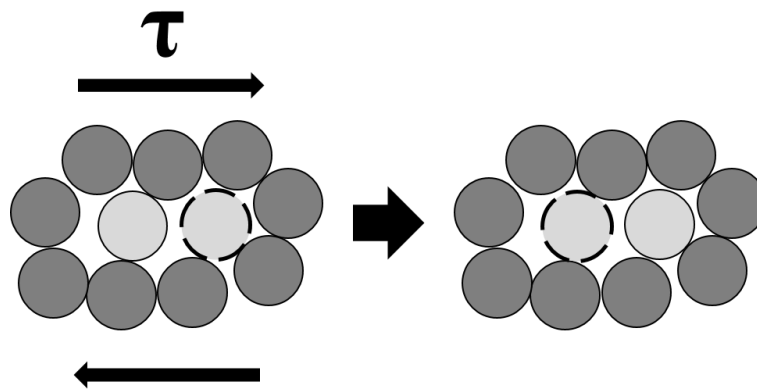


Figure 2.9. A 2D schematic illustration of atomic deformation mechanism – free volume model (Adapted from ref.[4]).

The free volume refers to the empty space among atoms and is assumed to be distributed statistically in the metallic glass system [80, 82, 83]. The weak mechanical coupling, between the free volume region and the surrounding, results in the proneness to inelastic relaxation by local atomic rearrangement without significant change in the surroundings [4, 56, 81, 84, 85].

As a result, these sites can act as the preferred regions, where the destabilization in amorphous structure will be initiated by applied stress.

Deformation-induced strain softening upon mechanical loading is a distinct feature for a metallic glass, as pointed out by Gilman and Saepen [56, 81, 86]. In a crystal, displacement upon loading results in a configuration with the same density. However, in the glassy structure, it leads to the creation of free volume due to the lack of periodic structure and translational symmetry. It is a dynamic process with creation and annihilation of free volume [4, 56, 81, 84]. At low applied stress, the free volume maintains constant because of the equal rate of creation and annihilation of free volume. As applied stress increases, creation rate becomes larger than annihilation rate. Consequently, softening occurs with increasing free volume.

The free volume model provides a simple and clear explanation for the local strain softening of metallic glass [87-89]. It is the most popular theory to describe the plastic flow of metallic glass and has been widely used to analyse and explain mechanical properties qualitatively. However, there still exist some limitations in the free volume model. First of all, it is based on the hard sphere model. Only the movement of a single atom is considered in this model, but a single atomic jump does not accommodate shear strain [4]. Moreover, the creation of free volume regions results in the initiation of plastic deformation, not the deformation process itself. It fails to depict how the constituent atoms move and rearrange within shear bands during deformation process.

2.3.2 Shear transformation zone theory

On the basis of two dimensional atomic-analogue bubble raft simulation, Argon and Kuo [90] originally proposed the “shear transformation zone” (STZ) model to explain plastic deformation of amorphous metals. It essentially showed that a local cluster of close packed atoms rearrange and reorganise spontaneously and cooperatively to accommodate a shear displacement under an applied stress, as shown in Figure 2.10. Upon the application of a shear stress, the STZ essentially involves a small cluster of atoms that undergoes an inelastic shear distortion from one relatively low energy configuration to another with low energy through an

intermediate activated state with higher energy and larger volume [84, 91]. As the applied shear stress increases, more STZs will be activated, resulting in the formation of shear bands.

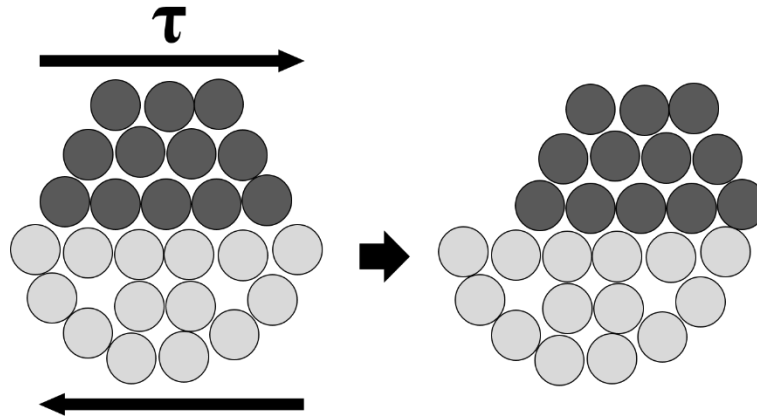


Figure 2.10. A 2D schematic illustration of atomic deformation mechanism – shear transformation zones (STZs) (Adapted from ref. [4])

A STZ is not a structural defect in metallic glasses, which is different from a lattice dislocation in a crystal [4]. Rather, the STZ is a change from one strain state to the next. As Argon [85] suggested that a STZ corresponds to a thin disc area containing the shear transformation direction after a change in the local region, which is typically around 5 – 10 atoms in diameter.

Argon [4, 85] proposed the first quantitative model to further describe STZ behaviour, in which the STZ was treated as an Eshelby-type inclusion problem [92]. In this approach, the STZ operates in the elastic confinement of surrounding glassy matrix, leading to the stress and strain redistribution around the STZs. The free energy for STZ activation in terms of the elastic constants of the metallic glass is given as [85, 92]:

$$\Delta F_o = \left[\frac{7-5\nu}{30(1-\nu)} + \frac{2(1+\nu)}{9(1-\nu)} \beta^2 + \frac{1}{2\gamma_o} \cdot \frac{\tau_o}{\mu(T)} \right] \cdot \mu(T) \cdot \gamma_o^2 \cdot \Omega_o \quad (\text{Equation 2.9})$$

where ν is Poisson's ratio, τ_o is the athermal shear stress at which the STZ transforms, and $\mu(T)$ is the temperature-dependent shear modulus. The second term in the brackets refers to the strain energy for a dilatation related to STZ action, in which β is the ratio of the dilatation to the shear

strain. γ_0 is the characteristic strain of an STZ, which varies with compositions and structures, usually in the order of ~ 0.1 . Ω_0 generally consists of a few up to perhaps ~ 100 atoms as observed by simulations and indirect experiment measurement. The energy of an STZ is estimated to be on the order of $1 - 5$ eV, or $\sim 20 - 120$ kT_g , with k and T_g the Boltzmann constant and glass transition temperature, respectively. This suggests the STZ is the fundamental unit for the deformation of all metallic glass, although its structure, size and energy scales may vary from one to the other.

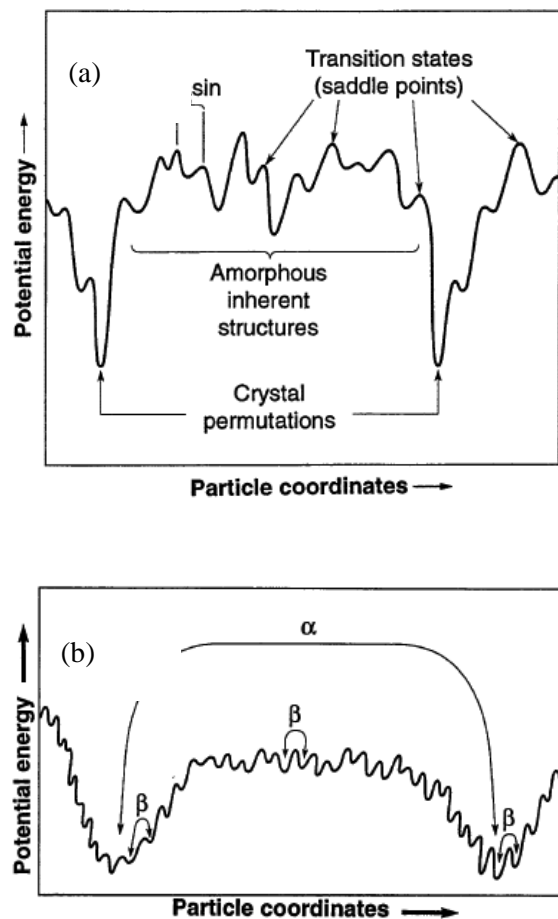
Based on Argon's [85] and Spaepen's [81] analog models, a dynamic theory associated with the STZ operation has been developed in which the STZ is treated as a flow defect and free volume is the measure of the structural disorder and density of the STZ [1, 4, 38, 84, 93-97]. Thus, the deformation behaviour of metallic glass can be described by the motion for the number density of the STZ. The theory is summarized as follows: (1) The transformation of the STZ is irreversible along the same shear direction due to the saturation of the system. (2) The creation and annihilation rate of the STZ is proportional to that of irreversible plastic deformation as the creation rate of the newly formed STZ is as high as that of transformation of the pre-existing STZ. (3) The attempt frequency of the transition is related to the noise in the system, being driven by the strain rate. (4) The applied stress has a significant influence on the transition rates between jammed and flowing.

2.3.3 Potential energy landscape theory

The potential energy landscape (PEL) theory was first proposed by Goldstein [49] and applied by Stillinger [98] to explain flow behaviour in glasses and viscous liquids. It describes all the potential energies of a multi particle system and outlines the relationship between potential energy and particle coordinates, as schematically represented in Figure 2.11.a. The sharpest, deepest valley in PEL, corresponding to the lowest energy state in the system, indicates a stable phase with well-defined atomic coordinate, i.e. crystalline states. The relatively deeper, yet diffuse valleys, defined as 'mega basins', indicate metastable states with a range of potential atomic coordinates. These basins, known as 'inherent states (IS)', refer to

short to medium range order in the BMG structure. A glassy structure with a configuration close to that of the crystal, with relatively lower energy, can be defined as ‘ideal glass’. Transitions or ‘saddle points’ are represented by the peaks between all the basins within the structure. These define the energy barriers, which have to be surmounted in order to change atomic configurations from one type to another.

Figure 2.11. A schematic of the potential energy landscape (PEL) theory: (a) A cross profile of a potential energy hypersurface in the multidimensional configuration space for a multi particle system; (b) Two-scale potential energy topography characteristic, *i.e.* two relaxation processes, in the configuration space. (Taken from ref. [98])



The PEL illustrates atomic relaxation behaviour in the BMG. There are two kinds of relaxation events, α relaxation and β relaxation [98-101], as shown in Figure 2.11.b. β relaxation defines minor configurational changes associated with relatively small energy

barriers. It is attributed to the transition and activation of STZs, which are reversible and thus anelastic. α relaxation deals with a hopping event from one basin to the next, signifying a significant change in the metallic glassy structure, which is irreversible. It is connected with plastic deformation of the glassy system. Linked with two relaxation processes are different time scales on which these fundamental deformation processes occur. β relaxation happens relatively faster than α relaxation.

The glass transition occurs in company with a slowing down of the relaxation process [39]. It exhibits how α and β relaxation respond to the temperature change in Figure 2.12. The α relaxation dominates at high temperature ($T > T_g$), slows down as the temperature decreases, and then vanishes in the proximity of the glass transition temperature (T_g). The β relaxation commences being active as the temperature decreases and becomes dominant when it approaches T_g .

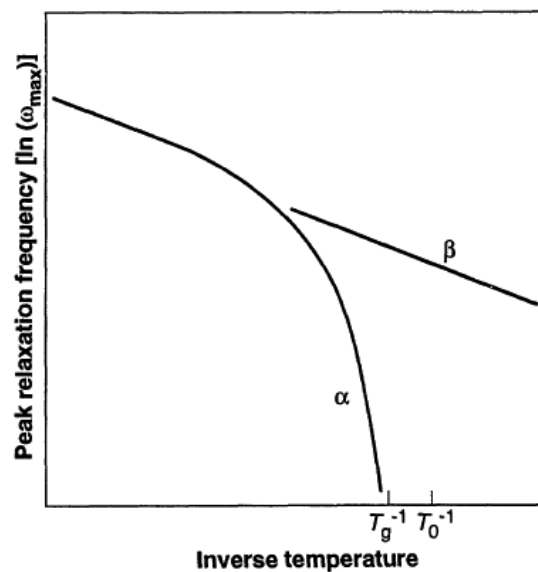


Figure 2.12. A schematic of temperature dependence of relaxation events (α and β relaxation) in a glass forming liquid. Both relaxation processes contribute to the relaxation behaviour at high temperatures ($T > T_g$). When T_g is approached, the α reaction slows down significantly, whereas the β relaxation becomes dominant. (Taken from ref.[98])

The PEL acts as a useful tool to identify the underlying flow mechanism of the amorphous metals. The influence of elastic energy on the PEL is deliberated to further elucidate mechanical behaviour of the metallic glass [102-104]. As indicated in Figure 2.13, the external shear stress can reduce, and even eliminate the energy barrier between two basins corresponding to two relaxation events on the basis of simulations [105-107]. One configuration is energetically favoured than the other one. As a consequence, the atomic arrangement will be changed to a more stable state under the applied loading. It has been experimentally shown that STZ corresponds well with the classic thermodynamic theories on the basis of the PEL [108].

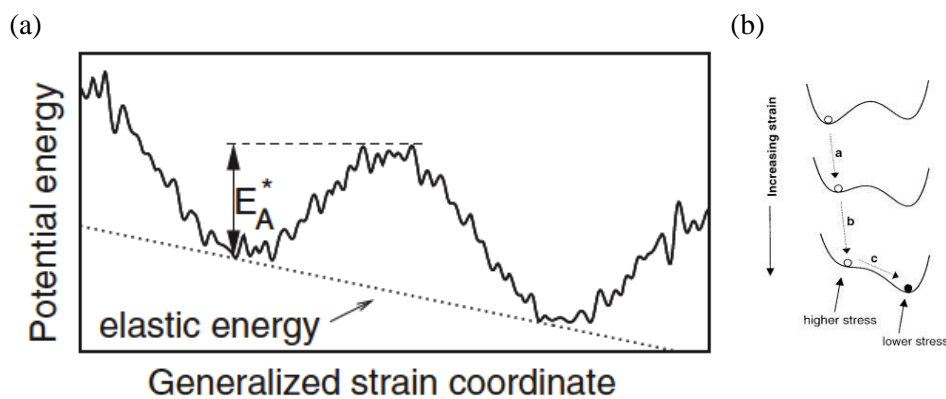


Figure 2.13. A schematic illustration of influence of shearing on the potential energy landscape: (a) A schematic of the potential energy landscape of an individual STZ under applied shear stress (Taken from ref. [105]). The slope of elastic energy represents the shear stress level on STZ. Applied shear stress tilts PEL. (b) A schematic representation of a mechanical instability (Taken from ref. [107]).

2.3.4 Cooperative shearing model

On the basis of the concept of inherent states (IS) and PEL [39, 98, 107, 109, 110] and inspired by Frenkel's work for shear strength determination of the defect free crystal [111], Johnson and Samwer [108, 112] have proposed a cooperative shearing model (CSM) of STZs. It was developed to elucidate a temperature dependence of plastic yielding in the form of $T^{2/3}$,

and to interpret plasticity behaviour of metallic glasses at room temperature effectively. This model builds a relationship between the structure of metallic glasses and their energetics, and thus provides an interpretation of their deformation in combination of STZs.

A quantitative description is given as Equation 2.10 [108], which successfully describes the Newtonian behaviour, non-Newtonian behaviour and strain localization.

$$\alpha\eta\dot{\gamma}^2 \delta W / \delta \varepsilon = \frac{(W - W_e)(W/W_o)^q}{\eta/G_o} \quad (\text{Equation 2.10})$$

where $\dot{\gamma}$ is the strain rate; $\delta W / \delta \varepsilon = (\partial W / \partial T) / (\partial \varepsilon / \partial T)$, the thermodynamic parameter, denotes changes in W with respect to changes in ε (W is the activation barrier for shear flow and ε is the flow induced shift in the specific configurational potential energy of shear zones); η/G (η is the viscosity and G is the shear modulus) is the Maxwell relaxation time; α is a model parameter incorporating two unknown proportionality constants: the conversion efficiency of dissipated energy into potential energy, and a factor quantifying the deviation of the system's relaxation rate from Maxwellian.

Following CSM, energetic considerations and molecular dynamics simulations, Pan and his co-workers [113] have developed an experimental method to quantitatively characterise the STZs of metallic glasses. The experimental measurements are in good agreement with theoretical estimations, suggesting that STZs contain tens to hundreds of atoms and are 1.3 – 1.9 nm in diameter approximately. The size of STZs exhibits a coincidence with the predicted size of solute-centered clusters of 1 – 1.5 nm [58, 114], which may imply a potential intrinsic correlation between STZs and the medium range orders (MROs) [115].

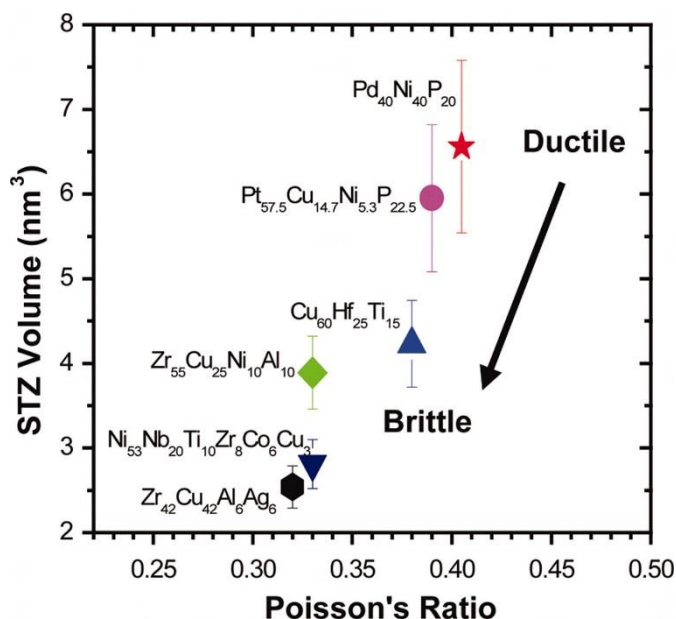


Figure 2.14. Correlation of ductility, STZ volume and Poisson's ratio. (Taken from ref. [113])

As shown in Figure 2.14, the calculated STZ volumes of plastic flow of metallic glasses increase with Poisson's ratio and ductility, indicating a large STZ promotes the formation of multiply shear bands during deformation and thereby improves plasticity. In addition, STZs with large size may serve as the nucleation seeds of nanocrystallization within shear bands during deformation, mitigating strain softening and leading to large plasticity [116]. Therefore, the calculation of the volume of STZs is a useful tool to understand the mechanical properties of BMGs in atomic scale.

2.4. Mechanical properties of bulk metallic glasses

MGs are promising engineering materials in possession of excellent mechanical, physical and chemical properties due to their atomic disordered nature and thereby dislocation free structure [1, 9, 117, 118]. In general, the MGs will elastically deformed in the early stage, then plastically deformed with negligible plastic strain and finally fractured in a catastrophic manner upon applied loading [1, 4, 33, 119, 120]. In comparison with other engineering materials, MGs usually exhibit a higher strength with elastic strain of 2% [5, 120, 121], as demonstrated in

Figure 2.15.

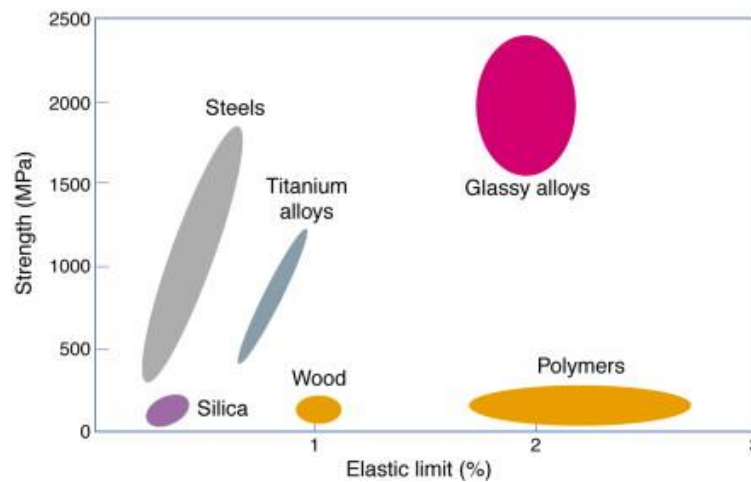


Figure 2.15. A schematic of the comparison of the strength and elastic limit of metallic glasses with other engineering materials. (Taken from ref. [5])

As the dimension of the MG decreases to submicro- or nano-scale, the corresponding mechanical behaviour, including the yielding strength and strain, fracture strength and strain, display an ascending trend as shown in Figure 2.16 [122, 123]. With the dimension reduction to nano-scale, the strength and corresponding elastic strain limit rises to twice as high as strength and nearly three times as large as elastic strain of the micro-scaled BMGs, which agrees well with the ideal elastic limit of the MG. A collection of mechanical behaviour data for thousands of metals, alloys, metallic composites and MGs was quantitatively summarised and compared by Ashby and Greer [124] with three various plots. These data include Young's modulus, yield strength and elastic strain limit. They concluded that MGs have larger elastic strain, can store more elastic energy per unit volume (*i.e.* higher resilience), lower damping and higher toughness in some cases in comparison with other conventional engineering materials.

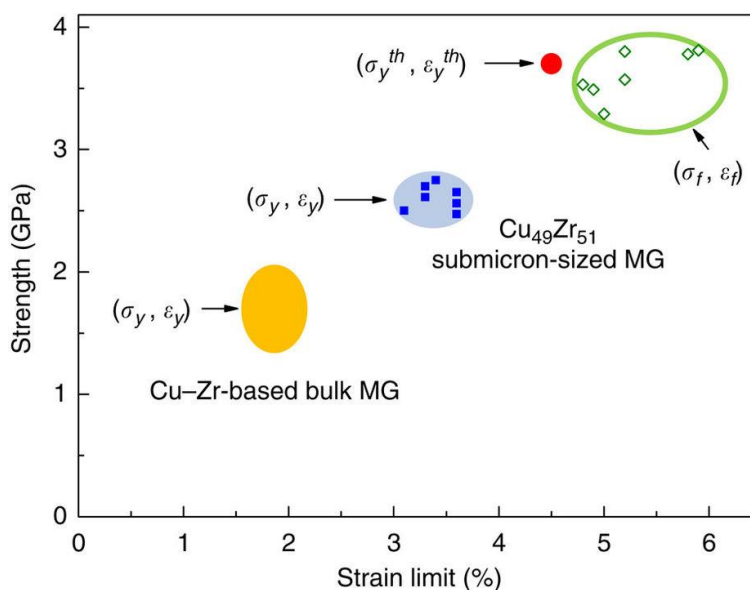


Figure 2.16. A diagram with the illustration of strength and elastic strain limit on different size scale in CuZr-base MGs. (Taken from ref. [122])

It has been reported that the elastic moduli of the BMGs have correlations with the glass transition temperature, melting temperature, mechanical properties, GFA, and even liquid fragility by summarising and comparing the relevant experimental data from various BMG families [46]. It revealed a clear linear relationship between Young's modulus E and fracture tensile strength σ for BMGs $E/\sigma = 50$ and between compression shear stress τ_Y and shear modulus G at yielding $\tau_Y = \gamma_C G$ ($\gamma_C = 0.0268$) based on different elements with representative compositions. The correlations could assist in a further understanding of the glass formation, the nature of the glass and the effect on physical properties. Elastic modulus could be regarded as the strain response of the material upon an applied stress, *i.e.* strain resistance [125, 126]. As such, it can reflect the intrinsic stiffness of the atomic bonding to a certain extent. Dong *et al.* [125, 127] found that the elastic moduli of the MGs were almost identical to that of their solvents by a comparison of the related measurements of various MGs (Figure 2.17). It indicated that the MGs elastic moduli were dominated by their base element metals. The elastic deformation occurred preferentially at the solvent-rich junctions.

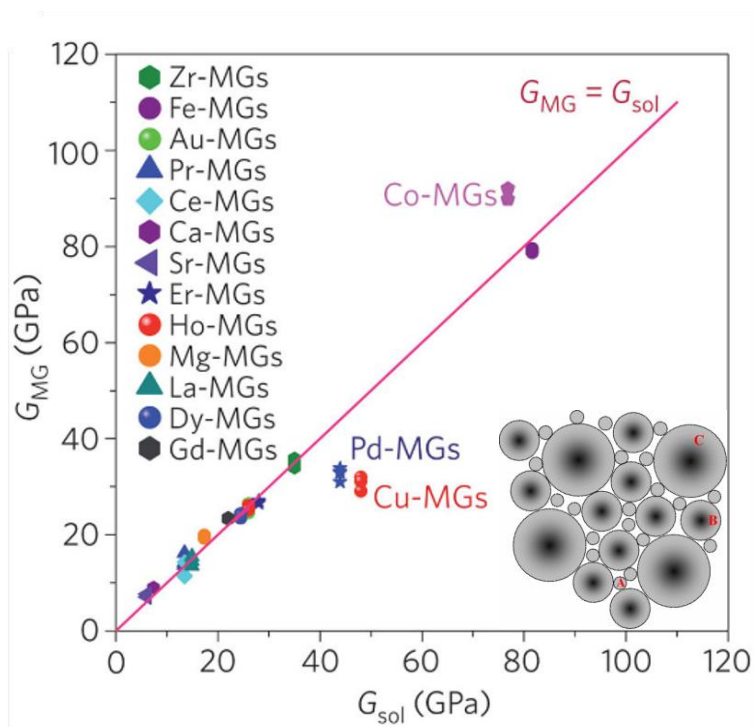


Figure 2.17. A plot of a comparison between elastic moduli of MGs and their solvent metals with an inset of a schematic illustration of solvent-rich cluster junctions in an amorphous structure. (Adapted from ref. [125, 127])

The mechanical behaviour during plastic deformation will be determined by both extrinsic and intrinsic factors [1, 4, 33, 128, 129]. The extrinsic factors include the testing conditions (*i.e.* strain rate, testing temperature and machine stiffness and *etc.*) and the aspect ratio of the specimen. The MGs will experience a brittle-to-ductile transition if the testing temperature [130] or testing strain rate [131] has been changed. The formation of multiple shear bands is preferred with the increase in the machine stiffness, which will further affect the MGs deformation behaviour [132]. The plasticity of the MGs increases gradually as the aspect ratio of the sample decreases from 2 to 0.5 [133]. The intrinsic factor mainly refers to the configurational features of the amorphous phase, such as the size scale and the nature of the heterogeneous precipitations [1, 4]. The introduction of the structural heterogeneities to the glassy system will affect the formation and the propagation of shear bands, further changing the mechanical stability of the samples upon loading [128, 129].

2.5. Bulk metallic glass matrix composites (BMGMCs)

Even though most of BMGs possess very high strength, they usually show negligible plasticity and catastrophic failure through localized shear bands, particularly in tension. Once a shear band is activated in the metallic glass structure upon loading, it will propagate rapidly due to the lack of microstructural features as barriers, resulting a disastrous failure [1, 4]. Therefore, extensive effort has been made to improve the plasticity of BMGs. The approaches for plasticity improvement of BMGs include composition modification [134, 135], prior plastic deformation [136-139], surface treatment [137, 140], nanolamination [141, 142] and the introduction of the second phase to the amorphous system [143-147]. The second phase, introduced into MG, plays an important role in the improvement of mechanical properties of bulk metallic glass matrix composites (BMGMCs). In general, the second phase will be more ductile or softer in comparison with the base alloy in the form of the crystalline phase or glassy phase. The induced phase will act as the obstacle against the propagation of the shear bands, dissipate the strain energy during deformation and thus further multiply the formation of shear bands [148].

BMGMCs can be prepared by the ex-situ and in-situ processing routes according to the evolution of the second phase formation (Figure 2.18) [119, 149]. Formation of ex-situ BMGMCs is a two-step process by adding a foreign phase in the form of fibers, wires, spheres, *etc.* to the glassy matrix through a second processing (such as casting and powder metallurgy) or by partial devitrification of MGs via thermal treatment or severe plastic distortion. While the formation of in-situ BMGMCs is a single-step process by direct cooling the melt into two different phases via the way of chemical separation of the supercooled liquid. For ex-situ BMGMCs, there are two disadvantages: weak interfacial bonding and ease of precipitation of brittle intermetallics. In comparison, in-situ BMGMCs exhibit a strong interfacial bonding between the reinforced phase and the amorphous phase, allowing an effective load transfer during deformation. Three types of *in-situ* BMGMCs will be introduced as follows.

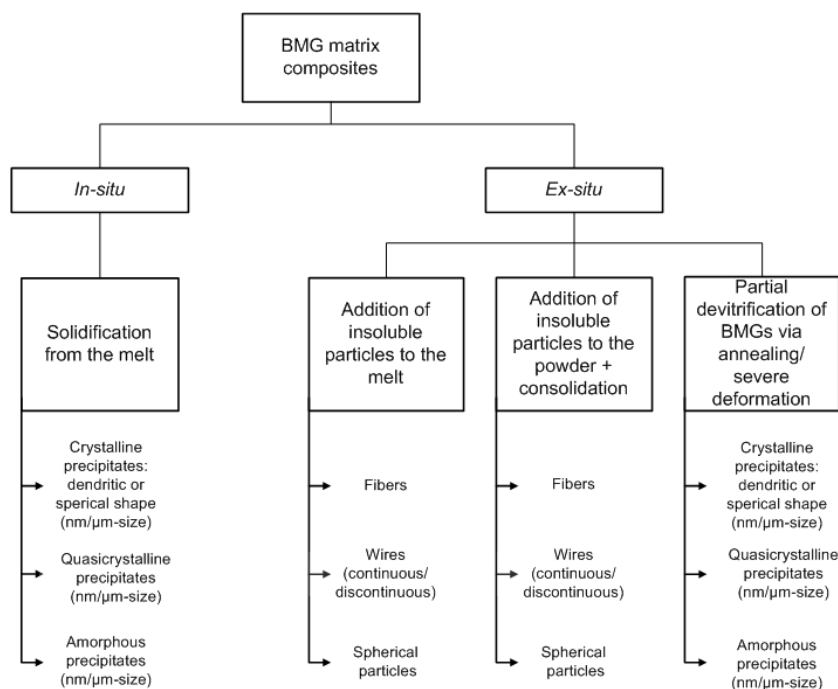


Figure 2.18. A schematic illustration of the different processing routes for BMGMCs. (Taken from ref. [149])

2.5.1 Nano-scale heterogeneities reinforced BMGMCs

Plasticity enhancement can be achieved through inducing nano-scale heterogeneities into the amorphous matrix, such that extensive shear bands will be initiated, multiplied, interacted and branched during deformation [150]. Reasonable control of the casting process will introduce different microstructural heterogeneities into the glassy system, including nanocrystallization, free volume and short- or medium- ranged clusters, phase separation [145, 151-155].

It was reported that BMGs with composition of $Zr_{53}Ti_5Ni_{10}Cu_{20}Al_{12}$ and $Zr_{60}Cu_{20}Pd_{10}Al_{10}$ exhibited significant plastic strains [151, 156]. It was attributed to the nanocrystalline precipitates with size around 2 nm in the glassy matrix according to the high resolution transmission electron microscopy (HRTEM) observation. It was suggested that the stress concentration in the vicinity of the nanocrystals resulted in the shear band multiplication, thus, the increase in ductility.

It was found that the BMG $\text{Cu}_{45}\text{Zr}_{46}\text{Al}_7\text{Ti}_2$ showed a plasticity up to 32.5% on deformation, which resulted from the creation of large amount of randomly distributed free volume in the glass [154]. The existence of free volume could lead to the extensive shear band formation, branching, interaction, and self-healing of minor cracks.

The short- or medium-range order cluster is a common configurational feature for BMGs [38], although BMGs exhibit different mechanical behaviour, ductile or brittle. Some researchers [155] have found the degree of icosahedra short range order cluster increases with increasing Nb alloying and BMGs will possess excellent plasticity with appreciate range of degree of short range order clusters by the investigation in Zr-Cu-Ni-Al-Nb_x (x=0 – 10 at%) BMGs. The icosahedra short range order could mediate the local distribution of free volumes and prompt the deformation-induced crystallization upon deformation, which was regarded as the underlying mechanism of the extraordinary plasticity.

2.5.2 In-situ dendrite reinforced BMGMCs

In-situ BMGMCs can be produced by precipitation or chemical separation during solidification to form a second phase in the amorphous matrix. The reinforced phase can be crystalline state or can be glassy state the same amorphous nature as the matrix. In the case of crystalline phase reinforced composites, the original glass composition is modified taking the composition of the primary crystallized phase as reference. Upon cooling the primary crystalline phase precipitates from the supercooled liquid first, then the remaining liquid with a composition close to a glass former will solidify as amorphous matrix. The crystal reinforcement can be in the form of dendrites, spheres and quasicrystal in nano-scale or micro-scale [119, 149]. The glassy phase reinforced BMG can be formed through liquid phase separation during solidification [119, 149, 157]. The alloy composition and the cooling rate will control the morphology, the characteristic size, the distribution and the volume fraction of the second phase. The amorphous structure correlated with the chemical inhomogeneity on the micron scale will contribute to the plasticity improvement, the soft phases surrounding the hard phases, resulting in the extensive shear band formation, interaction and multiplication.

Hays and Kim developed the first toughened *in-situ* BMGMCs with a composition close to Vit1 in 1999 [35, 158], in which a β -phase dendrite was formed in an amorphous matrix. Its microstructure is as shown in Figure 2.19. The BMGMCs was fabricated with the concept of chemical decomposition in Zr-Ti-Cu-Ni-Be, considering that Cu, Ni and Be have little or no solubility in the body centered cubic (BCC) phase of Zr-Ti. By partially replacing Cu, Ni and Be with Zr and Ti, a thermodynamic equilibrium will be established between BCC dendritic inclusions and the eutectic liquid. Upon quenching, the eutectic liquid will freeze to a glassy matrix with homogeneous distribution of crystalline dendrites. This is the first BMGMCs with both the high tensile strength and significant necking in tension ($\sim 3\%$) [36].

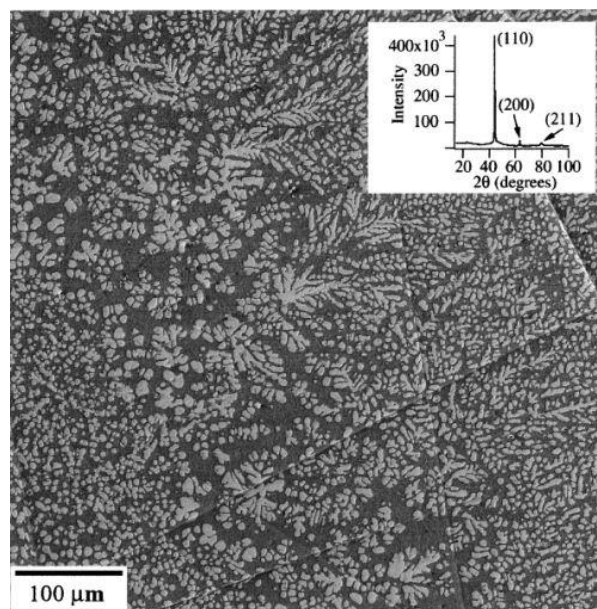


Figure 2.19. SEM backscattered electron image of in situ dendritic BMGMCs. (Taken from ref. [35])

Many BMGMCs, with compositions near Vit1, have been developed in a variety of systems since then, however, little improvement in mechanical properties such as strength and plasticity has been achieved [159-161]. It could be caused by the unique chemistry of Be-bearing composites, the size of the dendrites and the toughness of the amorphous matrix [158]. Progress has been made with the proposal of a series of guidelines for creation of toughened BMGMCs [162]. (1) The formation of BMGMCs requires a highly processable MG former

with sluggish crystallization. (2) A thermodynamic equilibrium between primary crystalline phase and the remained melt is required to avoid heterogeneous nucleation in the matrix. (3) The shear modulus (G) of the crystalline phase should be lower than that of the glassy phase, such that cracks will be diverted or inhibited by the soft crystals rather than direct propagation. (4) The microstructural length scale should match the characteristic length scale to impede shear band extension, suppress shear band opening and avoid crack development. (5) The interfacial fracture toughness should be high enough to prevent the crack growth along it. However, most dendritic BMGMCs display strain softening in tension even though with reasonable plasticity [34].

A work hardening Ti-based dendritic BMGMC has been discovered with introducing Ta into the metallic system [163] (Figure 2.20). The composite with a composition of $\text{Ti}_{48}\text{Zr}_{27}\text{Ni}_6\text{Be}_{14}\text{Ta}_5$ exhibited large plasticity with significant strain hardening in tension, which is attributed to the deformation-induced martensitic transformation of the crystalline dendrites. The concept of TRIP (transformation-induced plasticity) was applied to dendritic BMGMC system, which suggests a new guideline for the design of BMGMCs with high performance.

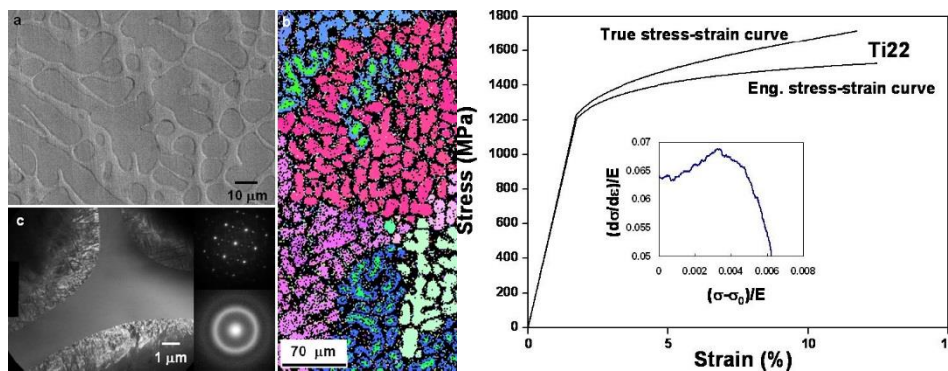


Figure 2.20. Microstructure of the Ti-based BMG composite (Right) and room temperature tensile ductility of $\text{Ti}_{48}\text{Zr}_{27}\text{Ni}_6\text{Be}_{14}\text{Ta}_5$ BMGMC (Left). (Adapted from ref. [163])

2.5.3 CuZr-based BMGMCs

Significant improvement of mechanical properties (mainly in tension) has been achieved in ductile dendritic solid solution reinforced BMGMCs, which is almost exclusively confined to Ti-Zr-Be-based BMGMCs. They do exhibit some drawbacks, such as macroscopic strain softening and obvious early on-set necking, further limiting their application as structural materials [164]. Advancement in BMGMCs has been obtained with the application of the concept of transformation induced plasticity.

Basic concepts

The ductility and toughness can be significantly enhanced by a diffusionless phase transformation during deformation in some crystalline materials, known as TRIP effect (transformation induced plasticity) [129, 165-167] and TWIP effect (twinning induced plasticity) [168, 169]. The dominant strain softening in glassy matrix may be overcompensated if the TRIP/TWIP effect could be utilized in composition design of in situ BMGMCs and its fabrication. So far the most extensively investigated TRIP/TWIP-mediated BMGMCs are CuZr-based glassy alloys. The equiatomic intermetallic shape memory alloy $\text{Cu}_{50}\text{Zr}_{50}$ exhibits the same shape memory effect as NiTi (Nitinol) [164]. It has two different metastable structures, *i.e.* high temperature stable phase B2 with a cubic primitive structure (Pm-3m) and low temperature stable phase B19' with a monoclinic structure (P2₁/m and Cm) [166, 170], as schematically illustrated in Figure 2.21. There are two CuZr B19' martensitic structures, P2₁/m for the 'normal' martensitic structure and Cm for the superstructure.

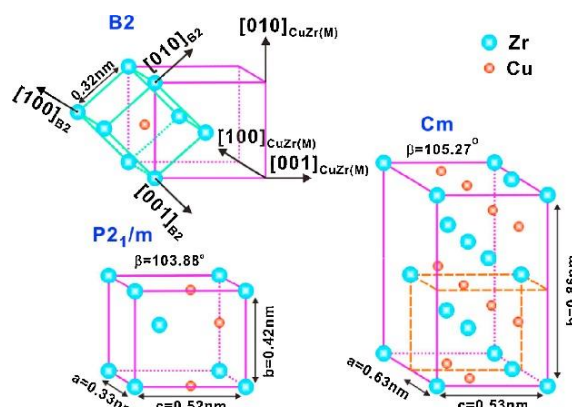


Figure 2.21. A schematic of crystalline structures of B2 and B19'. (Taken from ref.[171])

The origin and the breakthrough

According to the binary Cu-Zr phase diagram, B2 phase is stable above 988 K and will decompose into two equilibrium phases $\text{Cu}_{10}\text{Zr}_7$ and CuZr_2 when temperature decreases below it [172]. The B2 CuZr will transform to martensite B19' upon deformation or cooling. This is its shape memory effect. The eutectoid decomposition and martensitic transformation could be avoided by rapid quenching, such that B2 phase could be preserved in room temperature [170]. It was originally demonstrated for a two-phase shape memory metallic glass composites in $\text{Cu}_{47.5}\text{Zr}_{47.5}\text{Al}_5$ by proper adjustment of composition and cooling rate to induce 'austenite' B2 phase and suppress martensite formation in glassy matrix [173]. Replacement of Cu or Zr with alloying elements may change its martensitic transformation behaviour [167, 174, 175]. Taken these into consideration, mechanical behaviour of CuZr-based BMGMCs could be improved by composition modification on the basis of $\text{Cu}_{50}\text{Zr}_{50}$. A breakthrough was achieved by the creation of a shape memory metallic glass composite in Cu-Zr-Al-Co [165]. A pronounced work hardening has been achieved both in compression and tension. In addition, tensile ductility has increased up to 7% (Figure 2.22a), which is a significant progress in comparison with other CuZr-based BMGMCs with negligible plasticity in tension. As shown in Figure 2.22b, a typical CuZr-based BMGMC microstructure comprises homogeneous distributed spherical CuZr B2 phase and amorphous phase matrix. By comparing the XRD patterns before

and after tension (Figure 2.22c), it suggests that crystalline phases underwent a phase transformation from B2 to B19' during deformation. The change in morphology of crystalline phase (Figure 2.22d, e) before and after deformation and the nanometer-scaled martensite (Figure 2.22f) in the fractured sample further provide evidence of the occurrence of the martensitic transformation. Therefore, the stress-induced martensitic transformation in the BMGMCs will be the controlling mechanism for the enhanced strain hardening and tensile plasticity.

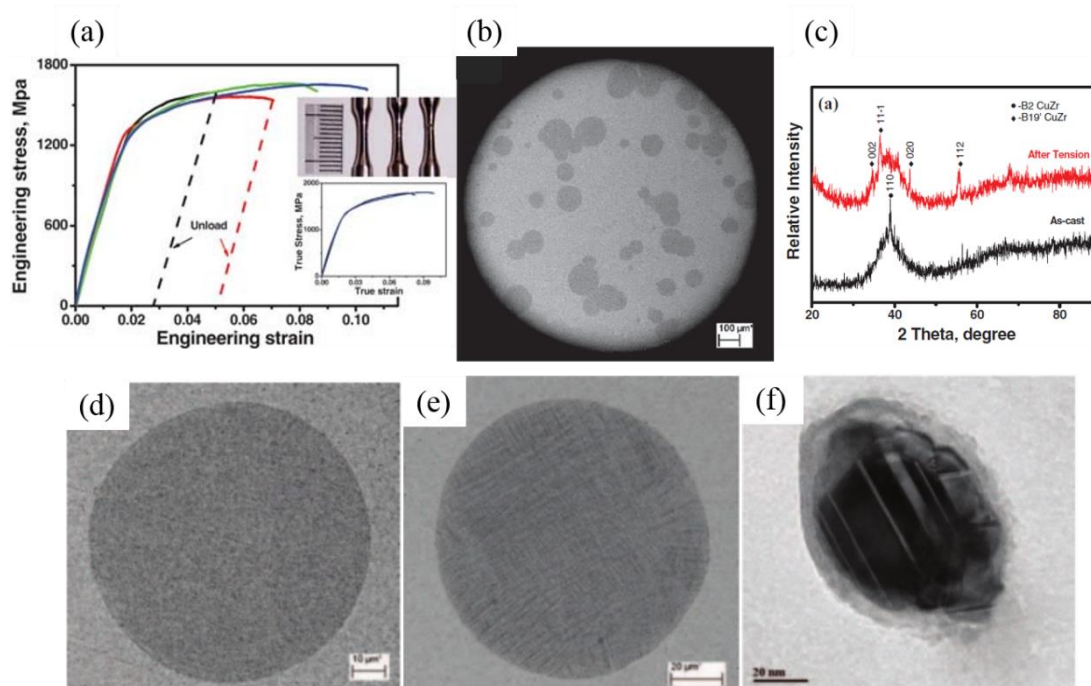


Figure 2.22. An experimental result summary of CuZrAlCo BMGMCs: (a) Engineering tensile stress-strain curve; (b) a typical SEM image showing the cross-section microstructure; (c) XRD pattern before and after tensile testing; (d) a morphology of B2 phase before tension; (e) a morphology of crystalline phase after tension; (f) TEM image of the small crystalline phase after tension. (Adapted from ref. [165])

General deformation mechanism and reinforcement distribution effect

The microstructure evolution and mechanical property dependence on alloy composition and cooling rate in the system of $(\text{Cu}_{0.5}\text{Zr}_{0.5})_{100-x}\text{Al}_x$ ($x=1-10$ at%) has been systematically

investigated [167]. It was reported that characteristics of the BMGMCs, *i.e.* the morphology, distribution, volume fraction of the reinforced crystalline phase, will determine their mechanical behaviour. As such, plastic performance of BMGMCs can be properly controlled through composition adjustment and fabrication conditions. The shear bands deflect and multiply at the interface between the reinforced crystalline phase and glassy matrix (Figure 2.23a, b). It was suggested that the spherical crystals act as strong block barriers for rapid propagation of shear bands, and thus effectively enhance the plasticity. It is known as the blocking effect, mainly contributing to plasticity improvement. Das and his co-workers [176] conjectured that martensitic phase transformation from B2 CuZr to B19' CuZr could release the stress concentration around them and impede free volume accumulation. Therefore, the rapid propagation of shear bands could be hindered, further stress is required to move shear bands and thus restrain early necking and work softening. Hence B2 phase transformation results in strain hardening and early necking suppression. In addition, finite element analysis (Figure 2.23c) elucidates that homogeneous distribution of B2 CuZr phase will result in uniform strain field in the matrix during deformation, and thus improve ductility.

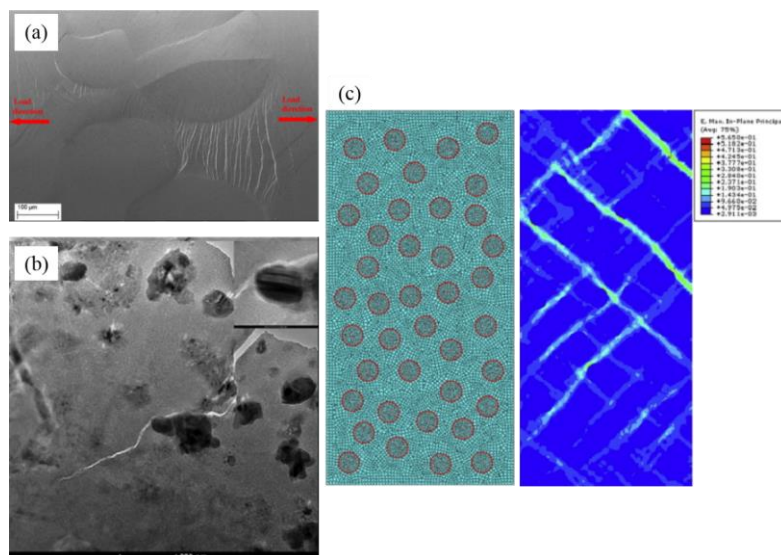


Figure 2.23. (a) SEM image of the lateral fractured surface; (b) a TEM image showing crack propagation in $\text{Cu}_{48}\text{Zr}_{48}\text{Al}_4$ BMGMC after tensile fracture; (c) a FEA model of strain field upon tension illustrating the reinforcement distribution effect on plasticity. (Adapted from ref. [167])

Alloying addition effect on mechanical performance

Deformation twinning, as a dominant carrier of plasticity, is an important mode for strain energy relaxation in nanocrystalline metal and alloys. Mechanical properties could be improved by tailoring the capability of deformation twinning in metallic nanocrystals [177-180]. Wu *et al.* [168, 175] attempted to enhance the propensity of deformation twinning in the reinforced B2 crystals in the CuZr-based BMGMCs by tailoring the stacking fault energy (SFE) of the primary slip system with minor alloying addition, and thereby improve mechanical performance of the BMGMCs. The stacking fault energy, referring to the energy per cost unit area incurred by displacing two parts in a crystal through a shift vector across a certain plane, governs the twinning event [181]. They calculated SFE in the system with alloying element substitution for Cu by *ab initio* calculations and revealed that alloying additions will dramatically affect SFE (Figure 2.24a). According to the literature [182], SFE is particularly related to the charge density change during the formation of the stacking fault. *Ab initio* calculation results clearly show that the alloying elements, which increase the electron charge density redistribution, will increase the SFE as well (Figure 2.24b). In general, a lower SFE may promote the initiation of deformation twinning, and further activate martensitic transformation [183]. Therefore, they prepared some CuZr-based BMGMCs with different alloying additions. The mechanical performances demonstrated that alloying elements, which could reduce SFE, could effectively improve plasticity. The differences in the morphology of B2 nanocrystals (Figure 2.24c, d) between BMGMCs without and with alloying doping further revealed that twinning embryos with the B19' martensitic lattice will be easy to nucleate in the rapid quenched BMGMCs with additions that could reduce SFE. Furthermore, they also found that both the electronegativity and the atomic radius difference between the parent element and the alloying element is closely associated with the SFE of the B2 structure with alloying addition, as illustrated in Figure 2.24e. The smaller the difference of electronegativity and radius between the doping element and the doped element is, the smaller the SFE of the resultant B2 structure is. Therefore, the deformation twinning and martensitic transformation could be tailored by altering the SFE through minor alloying addition, and thereby further improving mechanical properties.

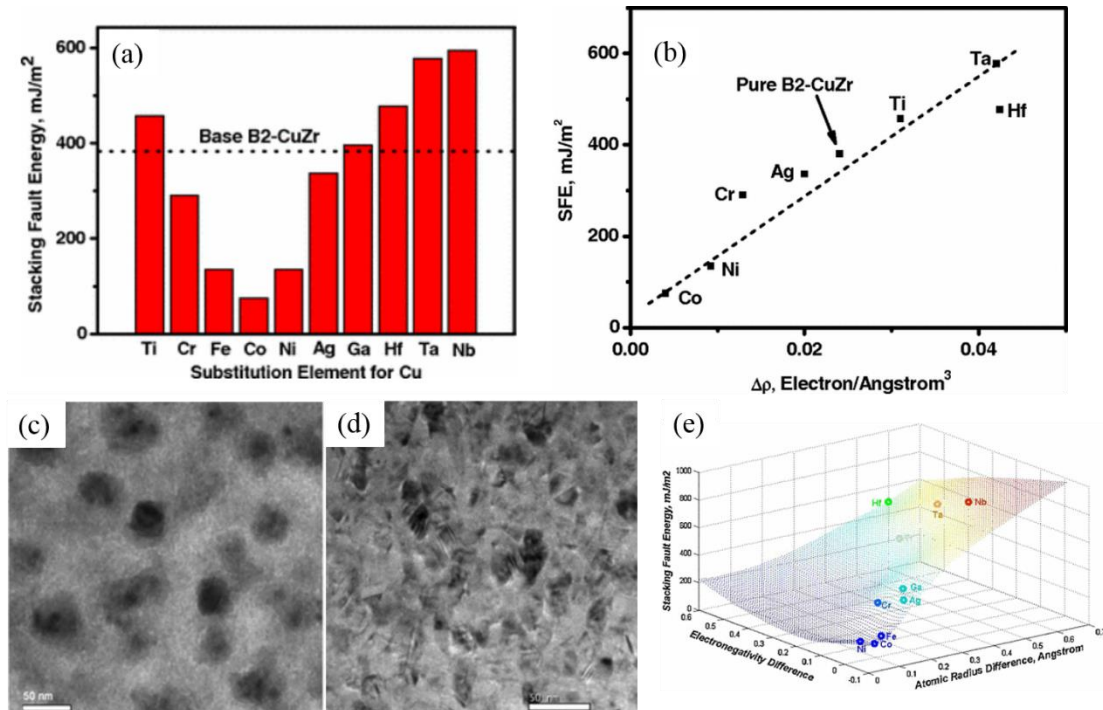


Figure 2.24. Effect of alloying additions on SFE in the system: (a) SFE of the CuZr B2 phase with different alloying additions; (b) The SFE values of the B2 phase with alloying doping as a function of the electronic density change redistribution on the slip system; (c) HRTEM image of the B2 nanocrystals without alloying; (d) HRTEM image of the B2 nanocrystals with alloying; (e) Dependence of the SFE of the doped B2 phase on the electronegativity and radius difference. (Adapted from ref. [168])

Distribution and morphology manipulation of B2 CuZr phase in amorphous matrix

It has been verified that the homogeneous distribution of the CuZr B2 phase will result in the uniform strain field during deformation, and thereby is beneficial for mechanical performance of BMGMCs [167, 173, 174]. However, the size and distribution of micro-scale crystals are usually heterogeneous due to the large temperature gradient and varying cooling rates across the sample as well as the ‘Soret effect’ in the casting process [149, 167, 173, 174, 184-187]. It has been reported that CuZr B2 crystals tend to form a patch-like structure as its volume fraction increases, which will deteriorate the mechanical properties of the BMGMCs [167, 174]. Therefore, it is essential to control the nucleation and growth of B2 crystalline phase to manipulate microstructure and thus plasticity.

Liu *et al.* [188] have successfully homogenized the size and distribution of CuZr B2 crystals in the CuZr-based BMGMCs by adding Ta alloying to the system. They found the microstructure is featureless with 0.5 at% Ta addition and B2 phase particles is homogeneously dispersed in the amorphous matrix with 0.9 at% Ta addition, as shown in Figure 2.25. Therefore, it was speculated that the promoted nucleation in the BMGMCs with 0.9 at% Ta alloying could be induced by the superabundant Ta element over its solute limit (0.5 at%) in the glassy matrix. Considering the negligible solubility of Ta in the base elements (*i.e.* Cu, Zr and Al) at room temperature [189], positive heat of mixing between Ta and main elements (*i.e.* Cu and Zr) [190] and high melting temperature of Ta ($\sim 3027^\circ\text{C}$) [189], the superabundant Ta addition tends to precipitate from the amorphous matrix in the form of pure Ta or Ta-rich cluster in subnanometer scale. Owing to the same BCC crystalline structure of Ta crystal and CuZr B2 phase with similar lattice parameters ($a = 3.3058\text{\AA}$ for Ta and 3.2562\AA for B2 CuZr), the precipitates may serve as potent nuclei for the nucleation, thereby benefiting uniform nucleation. The crystal growth may be restricted due to the sluggish growth kinetics.

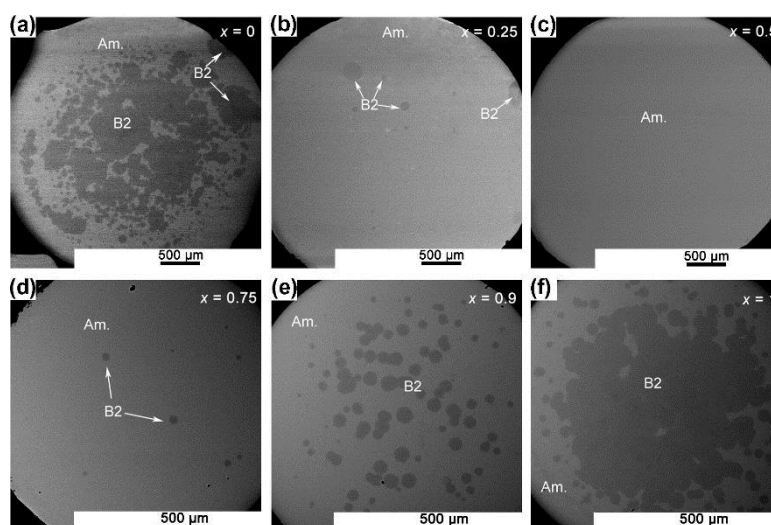


Figure 2.25. Backscattered SEM images showing the distribution evolution of the B2 crystalline particles in the amorphous matrix with different Ta alloying addition content from 0 at% to 0.9 at%. (Taken from ref. [188])

Liu's work has provided a strategy in optimizing the microstructure of the BMGMCs.

However, the size of the specimens is limited to 3 mm in diameter. Song and her co-workers' study [191] has made significant progress for the CuZr-based BMGMCs with large dimension up to 8 mm in diameter and enhanced tensile properties (i.e. prominent work hardening capability and ductility $\sim 7\%$). In their work, the GFA of the CuZr-based BMGMCs was enhanced with a fully amorphous structure up to 4mm and a single B2 CuZr dispersed composite structure up to 7 mm. The TRIP-reinforced BMGMCs with uniformly distributed transformable crystals has been achieved with addition of 0.75 at% Sn to the system. The basic design concept is illustrated in Figure 2.26. In their study, Zr_5Sn_3 , as potent nucleants for heterogeneous nucleation, precipitated at the very early stage during solidification (corresponding to the step in Figure 2.26b). As the cooling proceeds, B2 CuZr phase nucleates copiously at preferential sites (corresponding to the step in Figure 2.26c). This is because of the large negative heat of mixing between Zr and Sn [190], high melting temperature (1988 °C) [189] and low planar disregistry between Zr_5Sn_3 and B2 CuZr . Upon further cooling, B2 CuZr phase grows slightly and the residual melt freezes into a glassy matrix (corresponding to the step in Figure 2.26d). The mechanism underlying is coincident with that of Liu's work. They are on the basis of inoculation operation, which is widely used in the grain refinement in the crystalline alloys.

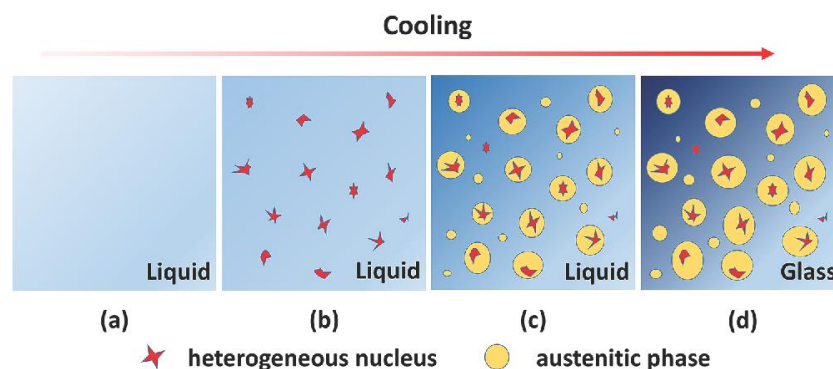


Figure 2.26. A schematic of the concept for developing large-scaled BMGMCs with a homogeneous distributed B2 CuZr phase and good mechanical properties: (a) undercooled glass forming melt; (b) nucleants formation; (c) copious nucleation of the B2 CuZr phase; (d) glass formation of the residual metallic melt. (Taken from ref. [191])

The microstructural percolation phenomenon

As introduced in previous sections, the mechanical performance of BMGMCs strongly depends on their microstructure [128, 188, 192]. Therefore, it is invariably essential to elucidate the correlations between microstructures and corresponding mechanical properties for microstructure design and tuning to achieve desirable mechanical properties. Recently, Liu *et al.* [193] have investigated the tensile properties of a series of Cu_{47.5}Zr_{47.5}Al₅ BMGMCs with different microstructures and correlated them systematically. The crystalline phase volume fraction in the study ranged from 0% to 100%. The percolation phenomenon is experimentally observed by matching the characteristic microstructural length scales of crystal particle size and interparticle spacing. The variation of tensile ductility (e_T) with crystalline volume fraction (V_c) is presented in Figure 2.27, showing a unimodal-hump shaped relationship. The maximum e_T could be reached when the V_c varies from 40% to 60%, beyond which e_T decreases steeply on both sides of the plateau. It corresponds to a microstructural transition, where the microstructure of the BMGMCs is the most effective in impeding shear bands propagation. This transition is termed as percolation, and transition point as percolation threshold. The relationship between e_T and V_c can be quantitatively expressed as:

$$e_T \propto (V_c^p - V_c)^{-\beta} \quad (\text{Equation 2.11})$$

where V_c^p is the critical crystalline volume fraction (*i.e.*, the percolation threshold) to form microstructural percolation, and β is a power exponent [194]. The calculation is consistent with the experimental results with V_c^p and β quantified as 55% and 2, respectively. The percolation theory is successfully applied to the CuZr-based BMGMCs. The composites with V_c less than V_c^p is glass dominated. As such, B2 CuZr crystals dispersed in the continuous glassy matrix and σ_{UTS} will be determined by the shear fracture of the matrix. The composites with V_c higher than V_c^p is crystal dominated. As such, the crystalline could be regarded as the matrix and the fracture behaviour will be controlled by the intergranular and transgranular fracture of the polycrystals.

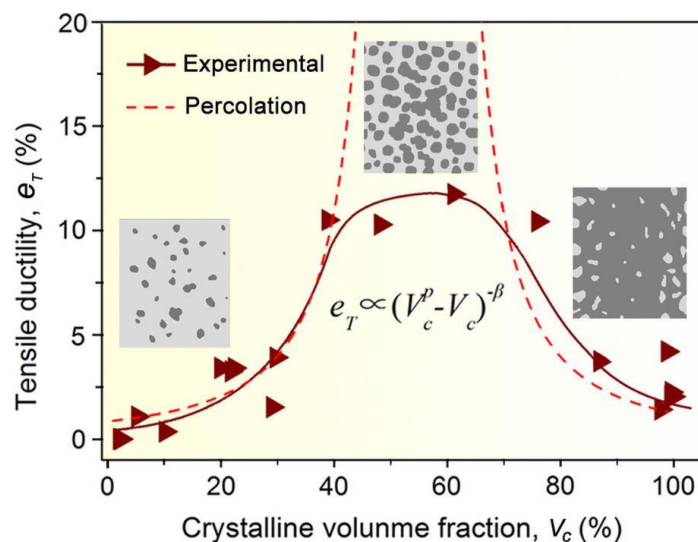


Figure 2.27. Dependence of tensile plasticity on crystalline volume fraction. The tensile plasticity can be quantitatively described with the percolation theory as denoted by the dashed curves and the corresponding composite microstructures are illustrated in the insets. (Taken from ref. [193])

Microscopic transformation-mediated deformation mechanism

Large plasticity and work hardening capability could be achieved in BMGMCs through introducing TRIP concept into BMGs. However, the deformation mechanism underlying is far from being well understood. Wu and his co-workers [195] have studied the deformation behaviour of CuZr-based BMGMCs with different B2 CuZr phase crystalline volume (75% and 25%) with an *in situ* neutron diffraction technique. Two yielding phenomena were revealed by the evolution of lattice strains in B2 CuZr phase and microscopic strains in the amorphous phase, providing microscopic evidence for the proposed triple-yielding mechanism. The phase transformation behaviour in BMGMCs could be characterized by load transfer and cooperative deformation among the B2 crystals, the newly formed B19' crystals and the amorphous phase. At the first yielding the martensitic transformation (MT) commences. As the stress increases to the second yielding, the MT proceeds and loading is transferred from the transforming B2 CuZr phase to untransformed B2 and amorphous phase. When the stress increases beyond the second yielding, the transformation continues and a great amount of B19' phase has been formed. At the same time, the amorphous phase starts to yield and thus shear bands initiate at

the interface. At this stage, untransformed B2 phase and transformed B19' phase will sustain load transferred from yielding glassy phase and transforming B2 phase. It is suggested that the rigid B2 and B19' crystalline phase will act as barriers to hinder the shear bands propagation in the glass until fracture, where the strain accommodation ability of the glassy phase will be exhausted.

The threshold lattice strain for MT is similar in T1 ($V_c = 75\%$) and T2 ($V_c = 25\%$), but the threshold stress for MT is different (Figure 2.28a). Thus, the TRIP-reinforced BMGMCs are strain controlled from this aspect. T2 with a lower B2 CuZr crystalline volume fraction requires a higher threshold stress to reach the same threshold strain (Figure 2.28a), resulting from the larger confinement effect from the surrounding amorphous matrix. Thus, it leads to a higher yield strength. In TRIP steels, strain-induced phase transformation was due to the numerous martensitic nucleation sites resulting from plastic strain [196]. However, in the TRIP-reinforced BMGMCs, strain-induced MT happened even before plastic deformation without identified highly-potent nucleation sites. Further molecular dynamic (MD) simulation (Figure 2.28b) indicated that the interface may contribute to the initiation of MT as potential nucleation sites due to the lattice mismatch and elastic mismatch between B2 and the glassy phase. When the MT is activated, it will gradually move to the inside of B2 CuZr phase as deformation proceeds. Therefore, the interface between B2 and amorphous phase plays an important role in MT not only as nucleation sites for MT but also as load transfer media during deformation.

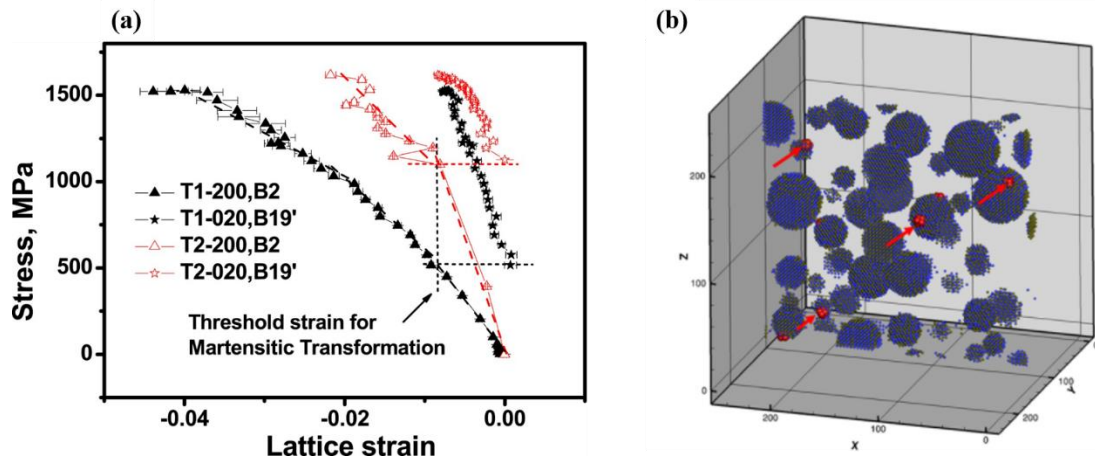


Figure 2.28. (a) Plots of applied stress vs. microscopic strains of the $\{100\}$ B2 and $\{020\}$ B19' crystals in T1 ($V_c=75\%$) and T2 ($V_c=25\%$); (b) MD simulation for slices 5nm thick for screening of atoms with 13.88° deviation from 90° in the crystalline phases (atoms in red) at the strain that the martensitic transformation started to take place in BMGMCs with 25% crystalline phase. (Adapted from ref. [195])

2.6. References

- [1] M.M. Trexler, N.N. Thadhani, Mechanical properties of bulk metallic glasses, *Progress in Materials Science* 55(8) (2010) 759-839.
- [2] W.L. Johnson, Bulk glass-forming metallic alloys: Science and technology, *MRS bulletin* 24(10) (1999) 42-56.
- [3] J. Schroers, Processing of Bulk Metallic Glass, *Advanced Materials* 22(14) (2010) 1566-1597.
- [4] C.A. Schuh, T.C. Hufnagel, U. Ramamurty, Overview No.144 - Mechanical behavior of amorphous alloys, *Acta Materialia* 55(12) (2007) 4067-4109.
- [5] M. Telford, The case for bulk metallic glass, *Materials Today* 7(3) (2004) 36-43.
- [6] W. Klement Jun, R.H. Willens, P.O.L. Duwez, Non-crystalline Structure in Solidified Gold-Silicon Alloys, *Nature* 187 (1960) 869.
- [7] M. Chen, A brief overview of bulk metallic glasses, *Npg Asia Materials* 3 (2011) 82.
- [8] J.C. Qiao, J.M. Pelletier, Dynamic Mechanical Relaxation in Bulk Metallic Glasses: A Review, *Journal of Materials Science & Technology* 30(6) (2014) 523-545.
- [9] A. Inoue, A. Takeuchi, Recent development and application products of bulk glassy alloys, *Acta Materialia* 59(6) (2011) 2243-2267.
- [10] H. Liebermann, C. Graham, Production of amorphous alloy ribbons and effects of apparatus parameters on ribbon dimensions, *IEEE Transactions on Magnetics* 12(6) (1976) 921-923.
- [11] H.S. Chen, Thermodynamic considerations on the formation and stability of metallic glasses, *Acta Metallurgica* 22(12) (1974) 1505-1511.
- [12] H.S. Chen, The glass transition temperature in glassy alloys: Effects of atomic sizes and the heats of mixing, *Acta Metallurgica* 22(7) (1974) 897-900.
- [13] A. Drehman, A. Greer, D. Turnbull, Bulk formation of a metallic glass: Pd₄₀Ni₄₀P₂₀, *Applied Physics Letters* 41(8) (1982) 716-717.
- [14] H.W. Kui, A.L. Greer, D. Turnbull, Formation of bulk metallic glass by fluxing, *Applied Physics Letters* 45(6) (1984) 615-616.

- [15] A. Inoue, T. Zhang, N. Nishiyama, K. Ohba, T. Masumoto, Preparation of 16 mm Diameter Rod of Amorphous Zr₆₅Al_{7.5}Ni₁₀Cu_{17.5} Alloy, *Materials Transactions, JIM* 34(12) (1993) 1234-1237.
- [16] A. Inoue, T. Zhang, T. Masumoto, Zr-Al-Ni Amorphous Alloys with High Glass Transition Temperature and Significant Supercooled Liquid Region, *Materials Transactions, JIM* 31(3) (1990) 177-183.
- [17] A. Inoue, High Strength Bulk Amorphous Alloys with Low Critical Cooling Rates (<I>Overview</I>), *Materials Transactions, JIM* 36(7) (1995) 866-875.
- [18] A. Inoue, T. Nakamura, N. Nishiyama, T. Masumoto, Mg-Cu-Y Bulk Amorphous Alloys with High Tensile Strength Produced by a High-Pressure Die Casting Method, *Materials Transactions, JIM* 33(10) (1992) 937-945.
- [19] X. Lin, W. Johnson, Formation of Ti-Zr-Cu-Ni bulk metallic glasses, *Journal of applied physics* 78(11) (1995) 6514-6519.
- [20] A. Peker, W.L. Johnson, A highly processable metallic glass: Zr_{41.2}Ti_{13.8}Cu_{12.5}Ni_{10.0}Be_{22.5}, *Applied Physics Letters* 63(17) (1993) 2342-2344.
- [21] A. Inoue, Stabilization of metallic supercooled liquid and bulk amorphous alloys, *Acta materialia* 48(1) (2000) 279-306.
- [22] N. Nishiyama, A. Inoue, Flux Treated Pd-Cu-Ni-P Amorphous Alloy Having Low Critical Cooling Rate, *Materials Transactions, JIM* 38(5) (1997) 464-472.
- [23] N. Nishiyama, K. Takenaka, H. Miura, N. Saidoh, Y. Zeng, A. Inoue, The world's biggest glassy alloy ever made, *Intermetallics* 30 (2012) 19-24.
- [24] W.H. Wang, Roles of minor additions in formation and properties of bulk metallic glasses, *Progress in Materials Science* 52(4) (2007) 540-596.
- [25] Z.P. Lu, C.T. Liu, Role of minor alloying additions in formation of bulk metallic glasses: A Review, *Journal of Materials Science* 39(12) (2004) 3965-3974.
- [26] C.T. Liu, Z.P. Lu, Effect of minor alloying additions on glass formation in bulk metallic glasses, *Intermetallics* 13(3-4) (2005) 415-418.
- [27] R. Benedictus, K. Han, C. Træholt, A. Böttger, E.J. Mittemeijer, Solid state amorphization in Ni-Ti systems: the effect of structure on the kinetics of interface and grain-boundary amorphization, *Acta Materialia* 46(15) (1998) 5491-5508.

- [28] M.D. Demetriou, J.P. Schramm, C. Veazey, W.L. Johnson, J.C. Hanan, N.B. Phelps, High porosity metallic glass foam: A powder metallurgy route, *Applied Physics Letters* 91(16) (2007) 161903.
- [29] C. Suryanarayana, Mechanical alloying and milling, *Progress in Materials Science* 46(1) (2001) 1-184.
- [30] B.X. Liu, W.S. Lai, Q. Zhang, Irradiation induced amorphization in metallic multilayers and calculation of glass-forming ability from atomistic potential in the binary metal systems, *Materials Science and Engineering: R: Reports* 29(1) (2000) 1-48.
- [31] S. Pauly, L. Löber, R. Petters, M. Stoica, S. Scudino, U. Kühn, J. Eckert, Processing metallic glasses by selective laser melting, *Materials Today* 16(1) (2013) 37-41.
- [32] G. Parisi, F. Sciortino, Flying to the bottom, *Nature Materials* 12 (2013) 94.
- [33] T.C. Hufnagel, C.A. Schuh, M.L. Falk, Deformation of metallic glasses: Recent developments in theory, simulations, and experiments, *Acta Materialia* 109 (2016) 375-393.
- [34] D.C. Hofmann, J.-Y. Suh, A. Wiest, G. Duan, M.-L. Lind, M.D. Demetriou, W.L. Johnson, Designing metallic glass matrix composites with high toughness and tensile ductility, *Nature* 451(7182) (2008) 1085-1089.
- [35] C.C. Hays, C.P. Kim, W.L. Johnson, Microstructure Controlled Shear Band Pattern Formation and Enhanced Plasticity of Bulk Metallic Glasses Containing *in situ* Formed Ductile Phase Dendrite Dispersions, *Physical Review Letters* 84(13) (2000) 2901-2904.
- [36] F. Szuecs, C.P. Kim, W.L. Johnson, Mechanical properties of Zr_{56.2}Ti_{13.8}Nb_{5.0}Cu_{6.9}Ni_{5.6}Be_{12.5} ductile phase reinforced bulk metallic glass composite, *Acta Materialia* 49(9) (2001) 1507-1513.
- [37] Y.Q. Cheng, E. Ma, H.W. Sheng, Atomic level structure in multicomponent bulk metallic glass, *Phys Rev Lett* 102(24) (2009) 245501.
- [38] Y.Q. Cheng, E. Ma, Atomic-level structure and structure–property relationship in metallic glasses, *Progress in Materials Science* 56(4) (2011) 379-473.
- [39] P.G. Debenedetti, F.H. Stillinger, Supercooled liquids and the glass transition, *Nature* 410 (2001) 259.
- [40] W.H. Wang, C. Dong, C.H. Shek, Bulk metallic glasses, *Materials Science and Engineering: R: Reports* 44(2–3) (2004) 45-89.

- [41] D.A. Porter, K.E. Easterling, M. Sherif, Phase Transformations in Metals and Alloys, (Revised Reprint), CRC press 2009.
- [42] C. Suryanarayana, A. Inoue, Bulk metallic glasses, CRC press 2010.
- [43] A.L. Greer, Confusion by design, Nature 366 (1993) 303.
- [44] R. Busch, J. Schroers, W.H. Wang, Thermodynamics and Kinetics of Bulk Metallic Glass, MRS Bulletin 32(08) (2011) 620-623.
- [45] C.A. Angell, Formation of glasses from liquids and biopolymers, Science 267(5206) (1995) 1924-1935.
- [46] W.H. Wang, Correlations between elastic moduli and properties in bulk metallic glasses, Journal of Applied Physics 99(9) (2006) 093506.
- [47] C.A. Angell, Spectroscopy simulation and scattering, and the medium range order problem in glass, Journal of Non-Crystalline Solids 73(1) (1985) 1-17.
- [48] X.F. Bian, B.A. Sun, L.N. Hu, Y.B. Jia, Fragility of superheated melts and glass-forming ability in Al-based alloys, Physics Letters A 335(1) (2005) 61-67.
- [49] M. Goldstein, Viscous Liquids and the Glass Transition: A Potential Energy Barrier Picture, The Journal of Chemical Physics 51(9) (1969) 3728-3739.
- [50] R. Busch, The thermophysical properties of bulk metallic glass-forming liquids, JOM 52(7) (2000) 39-42.
- [51] L. Shadovspeaker, R. Busch, On the fragility of Nb-Ni-based and Zr-based bulk metallic glasses, Applied Physics Letters 85(13) (2004) 2508-2510.
- [52] S. Mukherjee, J. Schroers, W.L. Johnson, W.K. Rhim, Influence of Kinetic and Thermodynamic Factors on the Glass-Forming Ability of Zirconium-Based Bulk Amorphous Alloys, Physical Review Letters 94(24) (2005) 245501.
- [53] R. Busch, W. Liu, W.L. Johnson, Thermodynamics and kinetics of the Mg₆₅Cu₂₅Y₁₀ bulk metallic glass forming liquid, Journal of Applied Physics 83(8) (1998) 4134-4141.
- [54] G. Adam, J.H. Gibbs, On the Temperature Dependence of Cooperative Relaxation Properties in Glass-Forming Liquids, The Journal of Chemical Physics 43(1) (1965) 139-146.
- [55] P.G. Wolynes, Entropy Crises in Glasses and Random Heteropolymers, Journal of Research of the National Institute of Standards and Technology 102(2) (1997) 187-194.

- [56] M. Chen, Mechanical Behavior of Metallic Glasses: Microscopic Understanding of Strength and Ductility, *Annual Review of Materials Research* 38(1) (2008) 445-469.
- [57] U. Mizutani, Electronic structure of metallic glasses, *Progress in Materials Science* 28(2) (1983) 97-228.
- [58] H.W. Sheng, W.K. Luo, F.M. Alamgir, J.M. Bai, E. Ma, Atomic packing and short-to-medium-range order in metallic glasses, *Nature* 439(7075) (2006) 419-25.
- [59] A.L. Greer, E. Ma, Bulk Metallic Glasses: At the Cutting Edge of Metals Research, *MRS Bulletin* 32(8) (2011) 611-619.
- [60] F.C. Frank, Supercooling of liquids, *Proceedings of the Royal Society of London. Series A. Mathematical and Physical Sciences* 215(1120) (1952) 43.
- [61] T. Egami, Y. Waseda, Atomic size effect on the formability of metallic glasses, *Journal of Non-Crystalline Solids* 64(1) (1984) 113-134.
- [62] J.D. Bernal, Geometry of the Structure of Monatomic Liquids, *Nature* 185 (1960) 68.
- [63] J.D. Bernal, The structure of liquids, *Scientific American* 203(2) (1960) 124-137.
- [64] J.D. Bernal, The Bakerian Lecture, 1962 The structure of liquids, *Proceedings of the Royal Society of London. Series A. Mathematical and Physical Sciences* 280(1382) (1964) 299.
- [65] P.H. Gaskell, A new structural model for transition metal-metalloid glasses, *Nature* 276 (1978) 484.
- [66] P.H. Gaskell, A new structural model for amorphous transition metal silicides, borides, phosphides and carbides, *Journal of Non-Crystalline Solids* 32(1) (1979) 207-224.
- [67] D.B. Miracle, A structural model for metallic glasses, *Nature Materials* 3 (2004) 697.
- [68] D.B. Miracle, The efficient cluster packing model – An atomic structural model for metallic glasses, *Acta Materialia* 54(16) (2006) 4317-4336.
- [69] D.B. Miracle, W.S. Sanders, O.N. Senkov, The influence of efficient atomic packing on the constitution of metallic glasses, *Philosophical Magazine* 83(20) (2003) 2409-2428.
- [70] H.W. Sheng, W.K. Luo, F.M. Alamgir, J.M. Bai, E. Ma, Atomic packing and short-to-medium-range order in metallic glasses, *Nature* 439 (2006) 419.
- [71] X.k. Xi, L.l. Li, B. Zhang, W.h. Wang, Y. Wu, Correlation of Atomic Cluster Symmetry and Glass-Forming Ability of Metallic Glass, *Physical Review Letters* 99(9) (2007) 095501.

- [72] T. Fujita, K. Konno, W. Zhang, V. Kumar, M. Matsuura, A. Inoue, T. Sakurai, M.W. Chen, Atomic-Scale Heterogeneity of a Multicomponent Bulk Metallic Glass with Excellent Glass Forming Ability, *Physical Review Letters* 103(7) (2009) 075502.
- [73] E. Rutherford, The scattering of α and β particles by matter and the structure of the atom, *The London, Edinburgh, and Dublin Philosophical Magazine and Journal of Science* 21(125) (1911) 669-688.
- [74] D. Ma, A.D. Stoica, X.L. Wang, Power-law scaling and fractal nature of medium-range order in metallic glasses, *Nat Mater* 8(1) (2009) 30-4.
- [75] D.B. Miracle, T. Egami, K.M. Flores, K.F. Kelton, Structural Aspects of Metallic Glasses, *MRS Bulletin* 32(8) (2011) 629-634.
- [76] F. Jiang, Y. Zhao, L. Zhang, S. Pan, Y. Zhou, L. He, J. Sun, Dependence of Ductility on Free Volume in a Cu-Zr-Based Metallic Glass, *Advanced Engineering Materials* 11(3) (2009) 177-181.
- [77] X. Gu, K.J. Livi, T.C. Hufnagel, Structure of shear bands in zirconium-based metallic glasses observed by transmission electron microscopy, *MRS Online Proceedings Library Archive* 754 (2002).
- [78] P. Donovan, W. Stobbs, The structure of shear bands in metallic glasses, *Acta Metallurgica* 29(8) (1981) 1419-1436.
- [79] A. Rodriguez, Principles of magnetic resonance imaging, *Revista mexicana de fisica* 50(3) (2004) 272-286.
- [80] M.H. Cohen, D. Turnbull, Molecular Transport in Liquids and Glasses, *The Journal of Chemical Physics* 31(5) (1959) 1164-1169.
- [81] F. Spaepen, A microscopic mechanism for steady state inhomogeneous flow in metallic glasses, *Acta metallurgica* 25(4) (1977) 407-415.
- [82] P.S. Steif, F. Spaepen, J.W. Hutchinson, Strain Localization in Amorphous Metals, *Acta Metallurgica* 30(2) (1982) 447-455.
- [83] V.A. Khonik, The kinetics of irreversible structural relaxation and homogeneous plastic flow of metallic glasses, *Phys Status Solidi A* 177(1) (2000) 173-189.
- [84] J. Langer, Shear-transformation-zone theory of deformation in metallic glasses, *Scripta Materialia* 54(3) (2006) 375-379.

- [85] A.S. Argon, Plastic deformation in metallic glasses, *Acta Metallurgica* 27(1) (1979) 47-58.
- [86] J.J. Gilman, Mechanical behavior of metallic glasses, *Journal of Applied Physics* 46(4) (1975) 1625-1633.
- [87] K.M. Flores, E. Sherer, A. Bharathula, H. Chen, Y.C. Jean, Sub-nanometer open volume regions in a bulk metallic glass investigated by positron annihilation, *Acta Materialia* 55(10) (2007) 3403-3411.
- [88] P. de Hey, J. Sietsma, A. van den Beukel, Structural disordering in amorphous Pd₄₀Ni₄₀P₂₀ induced by high temperature deformation, *Acta Materialia* 46(16) (1998) 5873-5882.
- [89] J. Li, F. Spaepen, T.C. Hufnagel, Nanometre-scale defects in shear bands in a metallic glass, *Philosophical Magazine A* 82(13) (2002) 2623-2630.
- [90] A.S. Argon, H.Y. Kuo, Plastic flow in a disordered bubble raft (an analog of a metallic glass), *Materials Science and Engineering* 39(1) (1979) 101-109.
- [91] M.L. Falk, J.S. Langer, Dynamics of viscoplastic deformation in amorphous solids, *Physical Review E* 57(6) (1998) 7192-7205.
- [92] J.D. Eshelby, The determination of the elastic field of an ellipsoidal inclusion, and related problems, *Proceedings of the Royal Society of London A: Mathematical, Physical and Engineering Sciences*, The Royal Society, 1957, pp. 376-396.
- [93] M.L. Falk, J.S. Langer, L. Pechenik, Thermal effects in the shear-transformation-zone theory of amorphous plasticity: Comparisons to metallic glass data, *Physical Review E* 70(1) (2004) 011507.
- [94] J.S. Langer, Dynamics of shear-transformation zones in amorphous plasticity: Formulation in terms of an effective disorder temperature, *Physical Review E* 70(4) (2004) 041502.
- [95] J.S. Langer, Microstructural shear localization in plastic deformation of amorphous solids, *Physical Review E* 64(1) (2001) 011504.
- [96] C.A. Schuh, A.C. Lund, Atomistic basis for the plastic yield criterion of metallic glass, *Nat Mater* 2(7) (2003) 449-52.
- [97] A.C. Lund, C.A. Schuh, Yield surface of a simulated metallic glass, *Acta Materialia* 51(18) (2003) 5399-5411.

- [98] F.H. Stillinger, A topographic view of supercooled liquids and glass formation, *Science* (1995) 1935-1939.
- [99] C.A. Angell, Formation of glasses from liquids and biopolymers, *Science* 267(5206) (1995) 1924.
- [100] J.S. Harmon, M.D. Demetriou, W.L. Johnson, K. Samwer, Anelastic to Plastic Transition in Metallic Glass-Forming Liquids, *Physical Review Letters* 99(13) (2007) 135502.
- [101] S. Sastry, The relationship between fragility, configurational entropy and the potential energy landscape of glass-forming liquids, *Nature* 409 (2001) 164.
- [102] F.H. Stillinger, P.G. Debenedetti, Energy landscape diversity and supercooled liquid properties, *The Journal of Chemical Physics* 116(8) (2002) 3353-3361.
- [103] W.L. Johnson, M.D. Demetriou, J.S. Harmon, M.L. Lind, K. Samwer, Rheology and Ultrasonic Properties of Metallic Glass-Forming Liquids: A Potential Energy Landscape Perspective, *MRS Bulletin* 32(08) (2007) 644-650.
- [104] F. Sciortino, Potential energy landscape description of supercooled liquids and glasses, *Journal of Statistical Mechanics: Theory and Experiment* 2005(05) (2005) P05015.
- [105] S.G. Mayr, Activation energy of shear transformation zones: a key for understanding rheology of glasses and liquids, *Phys Rev Lett* 97(19) (2006) 195501.
- [106] G. Gagnon, J. Patton, D.J. Lacks, Energy landscape view of fracture and avalanches in disordered materials, *Physical Review E* 64(5) (2001) 051508.
- [107] D.L. Malandro, D.J. Lacks, Relationships of shear-induced changes in the potential energy landscape to the mechanical properties of ductile glasses, *The Journal of Chemical Physics* 110(9) (1999) 4593-4601.
- [108] M.D. Demetriou, J.S. Harmon, M. Tao, G. Duan, K. Samwer, W.L. Johnson, Cooperative Shear Model for the Rheology of Glass-Forming Metallic Liquids, *Physical Review Letters* 97(6) (2006) 065502.
- [109] J.P.K. Doye, D.J. Wales, Saddle points and dynamics of Lennard-Jones clusters, solids, and supercooled liquids, *The Journal of Chemical Physics* 116(9) (2002) 3777-3788.
- [110] D.J. Wales, A Microscopic Basis for the Global Appearance of Energy Landscapes, *Science* 293(5537) (2001) 2067.

- [111] J. Frenkel, The theory of the elastic limit and the solidity of crystal bodies, *Z Phys* 37 (1926) 572-609.
- [112] W.L. Johnson, K. Samwer, A Universal Criterion for Plastic Yielding of Metallic Glasses with a $(T/T_g)^{2/3}$ Temperature Dependence, *Physical Review Letters* 95(19) (2005) 195501.
- [113] D. Pan, A. Inoue, T. Sakurai, M.W. Chen, Experimental characterization of shear transformation zones for plastic flow of bulk metallic glasses, *Proceedings of the National Academy of Sciences* 105(39) (2008) 14769-14772.
- [114] D.B. Miracle, A structural model for metallic glasses, *Nat Mater* 3(10) (2004) 697-702.
- [115] Y. Zhang, A.L. Greer, Thickness of shear bands in metallic glasses, *Applied Physics Letters* 89(7) (2006) 071907.
- [116] M. Chen, A. Inoue, W. Zhang, T. Sakurai, Extraordinary Plasticity of Ductile Bulk Metallic Glasses, *Physical Review Letters* 96(24) (2006) 245502.
- [117] M. Carmo, R.C. Sekol, S. Ding, G. Kumar, J. Schroers, A.D. Taylor, Bulk Metallic Glass Nanowire Architecture for Electrochemical Applications, *ACS Nano* 5(4) (2011) 2979-2983.
- [118] W.H. Wang, The elastic properties, elastic models and elastic perspectives of metallic glasses, *Progress in Materials Science* 57(3) (2012) 487-656.
- [119] J. Eckert, J. Das, S. Pauly, C. Duhamel, Mechanical properties of bulk metallic glasses and composites, *Journal of Materials Research* 22(02) (2007) 285-301.
- [120] B.A. Sun, W.H. Wang, The fracture of bulk metallic glasses, *Progress in Materials Science* 74(0) (2015) 211-307.
- [121] A.L. Greer, Metallic glasses, *Science* 267(5206) (1995) 1947-53.
- [122] L. Tian, Y.-Q. Cheng, Z.-W. Shan, J. Li, C.-C. Wang, X.-D. Han, J. Sun, E. Ma, Approaching the ideal elastic limit of metallic glasses, *Nature Communications* 3 (2012) 609.
- [123] Y.Q. Cheng, E. Ma, Intrinsic shear strength of metallic glass, *Acta Materialia* 59(4) (2011) 1800-1807.
- [124] M.F. Ashby, A.L. Greer, Metallic glasses as structural materials, *Scripta Materialia* 54(3) (2006) 321-326.
- [125] W.H. Wang, Family traits, *Nature Materials* 11 (2012) 275.

- [126] G.N. Greaves, A.L. Greer, R.S. Lakes, T. Rouxel, Poisson's ratio and modern materials, *Nat Mater* 10(11) (2011) 823-37.
- [127] D. Ma, A.D. Stoica, X.L. Wang, Z.P. Lu, B. Clausen, D.W. Brown, Elastic Moduli Inheritance and the Weakest Link in Bulk Metallic Glasses, *Physical Review Letters* 108(8) (2012) 085501.
- [128] K. Song, S. Pauly, B. Sun, J. Tan, M. Stoica, U. Kühn, J. Eckert, Correlation between the microstructures and the deformation mechanisms of CuZr-based bulk metallic glass composites, *AIP Adv* 3 (2013) 012116.
- [129] S. Pauly, S. Gorantla, G. Wang, U. Kuhn, J. Eckert, Transformation-mediated ductility in CuZr-based bulk metallic glasses, *Nat Mater* 9(6) (2010) 473-7.
- [130] D. Klaumunzer, R. Maass, F.H. Dalla Torre, J.F. Löffler, Temperature-dependent shear band dynamics in a Zr-based bulk metallic glass, *Applied Physics Letters* 96(6) (2010) 061901.
- [131] J.H. Chen, M.Q. Jiang, Y. Chen, L.H. Dai, Strain rate dependent shear banding behavior of a Zr-based bulk metallic glass composite, *Mat Sci Eng a-Struct* 576 (2013) 134-139.
- [132] Z. Han, W.F. Wu, Y. Li, Y.J. Wei, H.J. Gao, An instability index of shear band for plasticity in metallic glasses, *Acta Materialia* 57(5) (2009) 1367-1372.
- [133] F.F. Wu, Z.F. Zhang, S.X. Mao, Compressive properties of bulk metallic glass with small aspect ratio, *Journal of Materials Research* 22(02) (2011) 501-507.
- [134] J. Das, M.B. Tang, K.B. Kim, R. Theissmann, F. Baier, W.H. Wang, J. Eckert, "Work-Hardenable" Ductile Bulk Metallic Glass, *Physical Review Letters* 94(20) (2005) 205501.
- [135] J. He, I. Kaban, N. Mattern, K.K. Song, B.A. Sun, J.Z. Zhao, D.H. Kim, J. Eckert, A.L. Greer, Local microstructure evolution at shear bands in metallic glasses with nanoscale phase separation, *Scientific Reports* 6 (2016) 25832.
- [136] M.H. Lee, K.S. Lee, J. Das, J. Thomas, U. Kühn, J. Eckert, Improved plasticity of bulk metallic glasses upon cold rolling, *Scripta Materialia* 62(9) (2010) 678-681.
- [137] Y. Zhang, W.H. Wang, A.L. Greer, Making metallic glasses plastic by control of residual stress, *Nat Mater* 5(11) (2006) 857-860.
- [138] K.K. Song, S. Pauly, Y. Zhang, S. Scudino, P. Gargarella, K.B. Surreddi, U. Kühn, J. Eckert, Significant tensile ductility induced by cold rolling in Cu_{47.5}Zr_{47.5}Al₅ bulk metallic glass, *Intermetallics* 19(10) (2011) 1394-1398.

- [139] O. Haruyama, K. Kisara, A. Yamashita, K. Kogure, Y. Yokoyama, K. Sugiyama, Characterization of free volume in cold-rolled Zr₅₅Cu₃₀Ni₅Al₁₀ bulk metallic glasses, *Acta Materialia* 61(9) (2013) 3224-3232.
- [140] Q. Wang, Y. Yang, H. Jiang, C. Liu, H. Ruan, J. Lu, Superior tensile ductility in bulk metallic glass with gradient amorphous structure, *Scientific reports* 4 (2014) 4757.
- [141] A. Donohue, F. Spaepen, R.G. Hoagland, A. Misra, Suppression of the shear band instability during plastic flow of nanometer-scale confined metallic glasses, *Applied Physics Letters* 91(24) (2007) 241905.
- [142] T.G. Nieh, J. Wadsworth, Bypassing shear band nucleation and ductilization of an amorphous–crystalline nanolaminate in tension, *Intermetallics* 16(9) (2008) 1156-1159.
- [143] W. Zhang, Q. Zhang, A. Inoue, Synthesis and Mechanical Properties of New Cu-Zr-based Glassy Alloys with high Glass-Forming Ability, *Advanced Engineering Materials* 10(11) (2008) 1034-1038.
- [144] N. Zheng, R.T. Qu, S. Pauly, M. Calin, T. Gemming, Z.F. Zhang, J. Eckert, Design of ductile bulk metallic glasses by adding "soft" atoms, *Applied Physics Letters* 100(14) (2012) 141901.
- [145] X.H. Du, J.C. Huang, K.C. Hsieh, Y.H. Lai, H.M. Chen, J.S.C. Jang, P.K. Liaw, Two-glassy-phase bulk metallic glass with remarkable plasticity, *Applied Physics Letters* 91(13) (2007) 131901.
- [146] P. Gargarella, S. Pauly, M. Samadi Khoshkhou, U. Kühn, J. Eckert, Phase formation and mechanical properties of Ti–Cu–Ni–Zr bulk metallic glass composites, *Acta Materialia* 65(0) (2014) 259-269.
- [147] S.S. Chen, H.R. Zhang, I. Todd, Phase-separation-enhanced plasticity in a Cu_{47.2}Zr_{46.5}Al_{5.5}Nb_{0.8} bulk metallic glass, *Scripta Materialia* 72–73(0) (2014) 47-50.
- [148] M. Ferry, K.J. Laws, C. White, D.M. Miskovic, K.F. Shamlaye, W. Xu, O. Biletska, Recent developments in ductile bulk metallic glass composites, *MRS Communications* 3(1) (2013) 1-12.
- [149] J. Eckert, J. Das, S. Pauly, C. Duhamel, Processing Routes, Microstructure and Mechanical Properties of Metallic Glasses and their Composites, *Advanced Engineering Materials* 9(6) (2007) 443-453.

- [150] J. Schroers, W.L. Johnson, Ductile bulk metallic glass, *Physical Review Letters* 93(25) (2004) 255506.
- [151] C. Fan, A. Inoue, Ductility of bulk nanocrystalline composites and metallic glasses at room temperature, *Applied Physics Letters* 77(1) (2000) 46-48.
- [152] Y.C. Kim, J.H. Na, J.M. Park, D.H. Kim, J.K. Lee, W.T. Kim, Role of nanometer-scale quasicrystals in improving the mechanical behavior of Ti-based bulk metallic glasses, *Applied Physics Letters* 83(15) (2003) 3093-3095.
- [153] Z.W. Zhu, S.J. Zheng, H.F. Zhang, B.Z. Ding, Z.Q. Hu, P.K. Liaw, Y.D. Wang, Y. Ren, Plasticity of bulk metallic glasses improved by controlling the solidification condition, *Journal of Materials Research* 23(4) (2011) 941-948.
- [154] L.Y. Chen, Z.D. Fu, G.Q. Zhang, X.P. Hao, Q.K. Jiang, X.D. Wang, Q.P. Cao, H. Franz, Y.G. Liu, H.S. Xie, S.L. Zhang, B.Y. Wang, Y.W. Zeng, J.Z. Jiang, New class of plastic bulk metallic glass, *Phys Rev Lett* 100(7) (2008) 075501.
- [155] Z.W. Zhu, L. Gu, G.Q. Xie, W. Zhang, A. Inoue, H.F. Zhang, Z.Q. Hu, Relation between icosahedral short-range ordering and plastic deformation in Zr–Nb–Cu–Ni–Al bulk metallic glasses, *Acta Materialia* 59(7) (2011) 2814-2822.
- [156] C. Fan, C. Li, A. Inoue, V. Haas, Deformation behavior of Zr-based bulk nanocrystalline amorphous alloys, *Physical Review B* 61(6) (2000) R3761-R3763.
- [157] D.H. Kim, W.T. Kim, E.S. Park, N. Mattern, J. Eckert, Phase separation in metallic glasses, *Progress in Materials Science* 58(8) (2013) 1103-1172.
- [158] D.C. Hofmann, Bulk metallic glasses and their composites: a brief history of diverging fields, *Journal of Materials* 2013 (2013).
- [159] Z. Zhu, H. Zhang, Z. Hu, W. Zhang, A. Inoue, Ta-particulate reinforced Zr-based bulk metallic glass matrix composite with tensile plasticity, *Scripta Materialia* 62(5) (2010) 278-281.
- [160] C. Fan, R.T. Ott, T.C. Hufnagel, Metallic glass matrix composite with precipitated ductile reinforcement, *Applied Physics Letters* 81(6) (2002) 1020-1022.
- [161] U. Kühn, J. Eckert, N. Mattern, L. Schultz, ZrNbCuNiAl bulk metallic glass matrix composites containing dendritic bcc phase precipitates, *Applied Physics Letters* 80(14) (2002) 2478-2480.

- [162] D.C. Hofmann, W.L. Johnson, Improving Ductility in Nanostructured Materials and Metallic Glasses: “Three Laws”, Materials Science Forum, Trans Tech Publ, 2010, pp. 657-663.
- [163] C.P. Kim, Y.S. Oh, S. Lee, N.J. Kim, Realization of high tensile ductility in a bulk metallic glass composite by the utilization of deformation-induced martensitic transformation, Scripta Materialia 65(4) (2011) 304-307.
- [164] D.C. Hofmann, Shape memory bulk metallic glass composites, Science 329(5997) (2010) 1294-1295.
- [165] Y. Wu, Y. Xiao, G. Chen, C.T. Liu, Z. Lu, Bulk Metallic Glass Composites with Transformation-Mediated Work-Hardening and Ductility, Advanced Materials 22(25) (2010) 2770-2773.
- [166] S. Pauly, J. Das, J. Bednarcik, N. Mattern, K.B. Kim, D.H. Kim, J. Eckert, Deformation-induced martensitic transformation in Cu–Zr–(Al,Ti) bulk metallic glass composites, Scripta Materialia 60(6) (2009) 431-434.
- [167] Y. Wu, H. Wang, H.H. Wu, Z.Y. Zhang, X.D. Hui, G.L. Chen, D. Ma, X.L. Wang, Z.P. Lu, Formation of Cu–Zr–Al bulk metallic glass composites with improved tensile properties, Acta Materialia 59(8) (2011) 2928-2936.
- [168] Y. Wu, D. Zhou, W. Song, H. Wang, Z. Zhang, D. Ma, X. Wang, Z. Lu, Ductilizing bulk metallic glass composite by tailoring stacking fault energy, Physical review letters 109(24) (2012) 245506.
- [169] D.C. Lagoudas, Shape memory alloys: modeling and engineering applications, Springer Science & Business Media 2008.
- [170] J.W. Seo, D. Schryvers, TEM investigation of the microstructure and defects of CuZr martensite. Part I: Morphology and twin systems, Acta Materialia 46(4) (1998) 1165-1175.
- [171] S. Yang, D. Li, X.S. Wang, J.W. Guo, S.F. Zhang, L. He, Mechanical behavior and wear performance of a Ti-based bulk metallic glass composite containing dendritic and intermetallic phases, Materials Science and Engineering: A.
- [172] D. Arias, J.P. Abriata, Cu-Zr (Copper-Zirconium), Journal of Phase Equilibria 11(5) (1990) 452-459.

- [173] S. Pauly, G. Liu, G. Wang, J. Das, K. Kim, U. Kuhn, D. Kim, J. Eckert, Modeling deformation behavior of Cu–Zr–Al bulk metallic glass matrix composites, *Applied Physics Letters* 95(10) (2009) 101906-101906-3.
- [174] S. Pauly, G. Liu, G. Wang, U. Kühn, N. Mattern, J. Eckert, Microstructural heterogeneities governing the deformation of Cu 47.5 Zr 47.5 Al 5 bulk metallic glass composites, *Acta Materialia* 57(18) (2009) 5445-5453.
- [175] D.Q. Zhou, Y. Wu, H. Wang, X.D. Hui, X.J. Liu, Z.P. Lu, Alloying effects on mechanical properties of the Cu–Zr–Al bulk metallic glass composites, *Computational Materials Science* 79 (2013) 187-192.
- [176] J. Das, K. Kim, W. Xu, B. Wei, Z. Zhang, W. Wang, S. Yi, J. Eckert, Ductile metallic glasses in supercooled martensitic alloys, *Materials transactions* 47(10) (2006) 2606-2609.
- [177] K. Lu, L. Lu, S. Suresh, Strengthening Materials by Engineering Coherent Internal Boundaries at the Nanoscale, *Science* 324(5925) (2009) 349.
- [178] X.L. Wu, Y.T. Zhu, Y.G. Wei, Q. Wei, Strong Strain Hardening in Nanocrystalline Nickel, *Physical Review Letters* 103(20) (2009) 205504.
- [179] Y.H. Zhao, Y.T. Zhu, X.Z. Liao, Z. Horita, T.G. Langdon, Tailoring stacking fault energy for high ductility and high strength in ultrafine grained Cu and its alloy, *Applied Physics Letters* 89(12) (2006) 121906.
- [180] E. Ma, Y.M. Wang, Q.H. Lu, M.L. Sui, L. Lu, K. Lu, Strain hardening and large tensile elongation in ultrahigh-strength nano-twinned copper, *Applied Physics Letters* 85(21) (2004) 4932-4934.
- [181] N. Hatcher, O.Y. Kontsevoi, A.J. Freeman, Role of elastic and shear stabilities in the martensitic transformation path of NiTi, *Physical Review B* 80(14) (2009) 144203.
- [182] Y. Qi, R.K. Mishra, Ab initio study of the effect of solute atoms on the stacking fault energy in aluminum, *Physical Review B* 75(22) (2007) 224105.
- [183] S. Pauly, G. Liu, S. Gorantla, G. Wang, U. Kühn, D.H. Kim, J. Eckert, Criteria for tensile plasticity in Cu–Zr–Al bulk metallic glasses, *Acta Materialia* 58(14) (2010) 4883-4890.
- [184] Y.F. Sun, B.C. Wei, Y.R. Wang, W.H. Li, T.L. Cheung, C.H. Shek, Plasticity-improved Zr–Cu–Al bulk metallic glass matrix composites containing martensite phase, *Applied Physics Letters* 87(5) (2005) 051905.

- [185] S. Pauly, J. Das, C. Duhamel, J. Eckert, Martensite Formation in a Ductile Cu_{47.5}Zr_{47.5}Al₅ Bulk Metallic Glass Composite, *Advanced Engineering Materials* 9(6) (2007) 487-491.
- [186] Y. Liu, C.T. Liu, E.P. George, X.Z. Wang, Thermal diffusion and compositional inhomogeneity in cast Zr₅₀Cu₅₀ bulk metallic glass, *Applied Physics Letters* 89(5) (2006) 051919.
- [187] Y. Liu, C.T. Liu, E.P. George, X.Z. Wang, The Soret effect in bulk metallic glasses, *Intermetallics* 15(4) (2007) 557-563.
- [188] Z. Liu, R. Li, G. Liu, W. Su, H. Wang, Y. Li, M. Shi, X. Luo, G. Wu, T. Zhang, Microstructural tailoring and improvement of mechanical properties in CuZr-based bulk metallic glass composites, *Acta Materialia* 60(6–7) (2012) 3128-3139.
- [189] H. Okamoto, L. Kacprzak, P. Subramanian, Binary alloy phase diagrams, ASM international 1996.
- [190] A. Takeuchi, A. Inoue, Classification of bulk metallic glasses by atomic size difference, heat of mixing and period of constituent elements and its application to characterization of the main alloying element, *Materials Transactions* 46(12) (2005) 2817-2829.
- [191] W. Song, Y. Wu, H. Wang, X. Liu, H. Chen, Z. Guo, Z. Lu, Microstructural Control via Copious Nucleation Manipulated by In Situ Formed Nucleants: Large-Sized and Ductile Metallic Glass Composites, *Advanced Materials* 28(37) (2016) 8156-8161.
- [192] R.L. Narayan, P.S. Singh, D.C. Hofmann, N. Hutchinson, K.M. Flores, U. Ramamurty, On the microstructure–tensile property correlations in bulk metallic glass matrix composites with crystalline dendrites, *Acta Materialia* 60(13) (2012) 5089-5100.
- [193] Z. Liu, G. Liu, R. Qu, Z. Zhang, S. Wu, T. Zhang, Microstructural percolation assisted breakthrough of trade-off between strength and ductility in CuZr-based metallic glass composites, *Scientific reports* 4 (2014).
- [194] C.-W. Nan, Physics of inhomogeneous inorganic materials, *Progress in Materials Science* 37(1) (1993) 1-116.
- [195] Y. Wu, D. Ma, Q.K. Li, A.D. Stoica, W.L. Song, H. Wang, X.J. Liu, G.M. Stoica, G.Y. Wang, K. An, X.L. Wang, M. Li, Z.P. Lu, Transformation-induced plasticity in bulk metallic glass composites evidenced by in-situ neutron diffraction, *Acta Materialia* 124 (2017) 478-488.

[196] G. Song, Z. Sun, L. Li, X. Xu, M. Rawlings, C.H. Liebscher, B. Clausen, J. Poplawsky, D.N. Leonard, S. Huang, Z. Teng, C.T. Liu, M.D. Asta, Y. Gao, D.C. Dunand, G. Ghosh, M. Chen, M.E. Fine, P.K. Liaw, Ferritic Alloys with Extreme Creep Resistance via Coherent Hierarchical Precipitates, *Scientific Reports* 5 (2015) 16327.

Chapter 3 Experimental Techniques

3.1. Bulk metallic glasses/composites preparation and processing

3.1.1 Melt spinning

Melt spinning is a widely utilised technique to produce metallic glass ribbon samples. This technique involves a melt jet formation by ejecting molten alloy onto a water-chilled rapidly rotating copper wheel surface through a hole, as illustrated in Figure 3.1. Several pieces of raw material were loaded into a quartz crucible with a 0.5-1 mm diameter hole ground in the nozzle at the end. The chamber was evacuated to a pressure of 6.0×10^{-5} Torr through two-step rotary and diffusion pump, and then backfilled with 3/5 atmosphere of argon. Heating of the alloy was via induction heating. Once melting was achieved, the melt was ejected through the nozzle onto the copper wheel rotating at 45 m/s under an overpressure of nearly 40 kPa. This setup results in the formation of ribbons with a thickness of 35 μm and width of 3 – 4 mm.

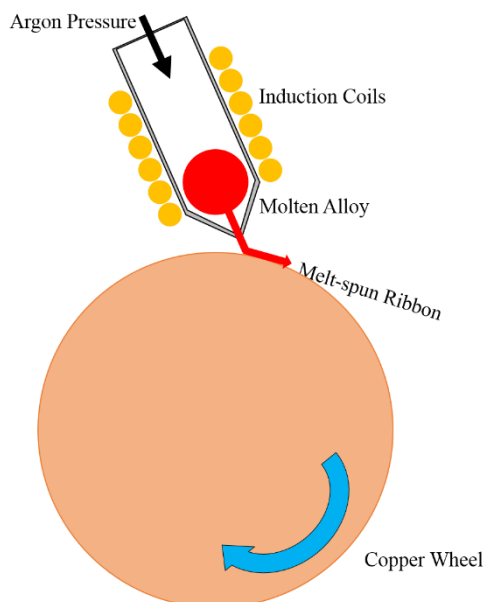


Figure 3.1. A schematic of a melt spinner equipment.

3.1.2 Argon arc melting

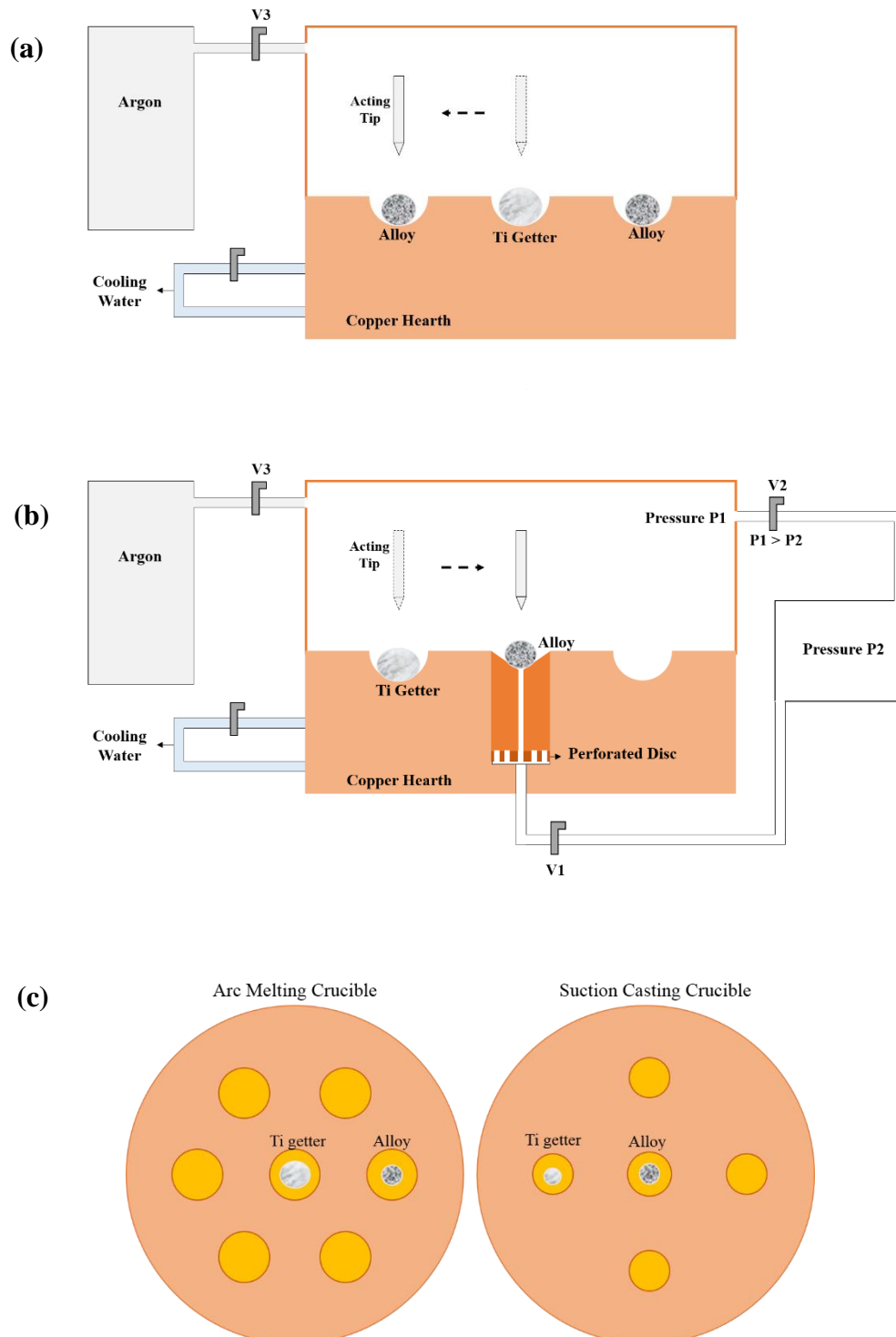


Figure 3.2. A schematic illustration of (a) Arc melting; (b) Suction casting equipment; (c) the layout of the crucible for melting and casting.

Bulk metallic glass/composite (BMG/BMGCs) ingots were prepared by arc melting constituent elements with a high purity of $\geq 99.8\%$. The elemental alloys were carefully cleaned with 800, 1200 and 2500 grit grinding paper, and then washed in an acetone and isopropanol bath to remove oxidation and dirt on the surface prior to weighing. The required masses of each element were calculated in atomic fraction (at %) calculation and weighed out with a Precisa XB120A precision electronic balance to an accuracy of 0.0001g. The weighed element pieces were ultrasonically cleaned in an isopropanol bath at room temperature for 3 minutes, and then were placed onto the outer crucibles of copper melting hearth of the MAM1 Edmund Bühler Arc melter. A CP titanium getter was placed in the center crucible, as illustrated in Figure 3.2. The arc melter chamber was evacuated to 0.1 Torr, and then backfilled with purified argon to 0.3 bar. The operation was repeated for a further 3 times. After the last evacuation a vacuum of 3×10^{-5} Torr was achieved. Once the optimum vacuum was achieved, the chamber was backfilled with purified argon to the working pressure of 0.7 bar. Cooling water was applied to the copper hearth during melting. The Ti getter was melted to minimise residual oxygen content in the chamber, and then followed by melting each BMG/BMGCs alloy for 15 seconds. The element mixture was remelted at least four times to optimize mixing and achieve chemical homogeneity with ingot button flipped between each melt step. The Ti getter was melted prior to each alloy melting stage. After melting, the master alloy ingots were weighed to ensure mass loss during preparation of less than 0.1%.

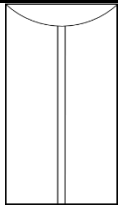
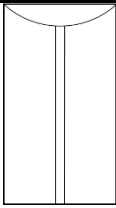
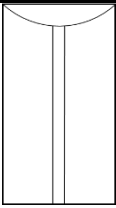
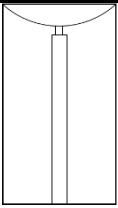
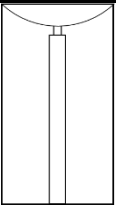
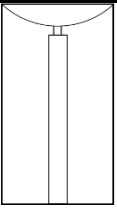
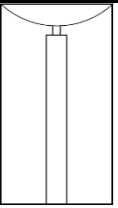
3.1.3 Argon suction casting

For casting, the individual master alloy ingot was placed on the top of the appropriate copper casting mould and a Ti getter was placed on the crucible. The evacuation procedure was the same as for arc melting except for the casting pressure, which was appropriate for the size of the specific copper mould upon final evacuation step. The casting pressure is denoted as pressure P2 (shown in Figure 3.2). The corresponding casting conditions are listed in Table 3.1.

Once the vacuum was achieved, the cooling water was switched on and left for at least 2 minutes before quenching. The chamber was then backfilled with argon to 0.7 bar (indicated as pressure P1 in Figure 3.2) and the Ti-getter was melted to remove the remaining oxygen. The alloy ingot was melted for several seconds to obtain a homogeneous melt, and then the valve V1 was opened to allow suction casting the master alloy into the water-chilled copper mould, as illustrated in Figure 3.2.

Table 3.1. Typical mixture weight, melting current and casting pressures applied for casting BMG/BMGMCs melts into the different water-cooled copper moulds with different configurations.

Note: The reading for the full melting current power is 10.

Mould schematic							
Mould diameter [mm]	2	3	4	5	6	7	8
Mixture weight [g]	2	3	4	5	7.5	10.5	13.5
Melting current	4	4	5	6	6	7	8
Casting pressure [Torr]	5.5×10^{-1}	5.5×10^{-1}	5.5×10^0	5.5×10^{-1}	4.0×10^{-1}	3.0×10^{-1}	2.5×10^{-1}

3.2. Structure characterisation

3.2.1 X-ray diffraction (XRD)

X-ray diffraction (XRD) analysis was carried out for the phase identification of the prepared specimens. Several thin slices (~ 2 mm thick) were taken from the middle of the as-cast rod with different diameter to ensure large scanning area for reliable results. Figure 3.3 illustrates the position of the as-cast rod the tested slices were taken from, their layout on the sample holders and the examined side with respect to the as-cast rod. The number of thin slices

for XRD investigation corresponding to the specimens with different sizes is outlined in Table 3.2. Each slice was ground with P1200 and P2500 grit grinding papers and ultrasonic cleaned in isopropanol bath before mounted onto the plastic specimen holders with the same surface level using Apiezon Compound Q putty.

Table 3.2. Number of slices taken from the rod with different diameter for X-ray diffraction analysis.

Rod Diameter [mm]	2	3	4	5	6	7	8
Number of Slices	6	3	1	1	1	1	1

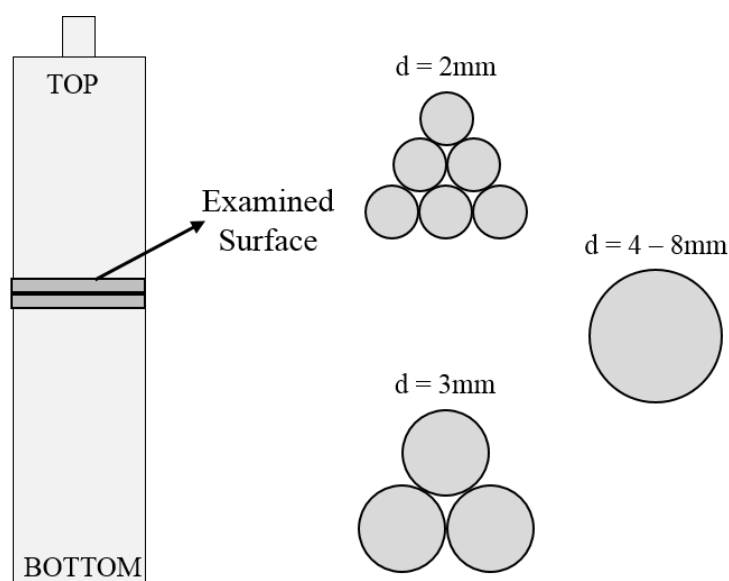


Figure 3.3. A schematic illustration of the thin XRD specimen position with respect to the as-cast rod and the layout for XRD examination.

XRD was performed with a Siemens D5000 CuK α X-ray diffractometer over 30° to 90° with a scanning speed of $1^\circ/\text{min}$ and a step size of 0.02° . The operating voltage and current of the instrument was 40kV and 30mA, respectively. The crystalline phases can be identified with

the software Sieve+, which is based on the PDF-4+ database of the International Center for Diffraction Data (ICDD) [1].

3.2.2 Scanning electron microscopy (SEM)

Scanning electron microscopy (SEM) was utilized for further microstructure observation. One 5mm high section was taken from the middle part of the as-cast rod and was cold mounted with Buehler EpoxiCure™2 epoxy resin and hardener, as shown in Figure 3.4. Grinding and polishing was carried out carefully with Buehler Automet 250 to expose a mirror finished cross section from P2500 grip paper down to 1 μm diamond suspension and then 0.04 μm colloidal silica (silco) suspension. Final cleaning was done in the isopropanol bath with ultrasonic apparatus before SEM observation. Fracture topography of the samples after compression testing was also investigated by SEM to provide more information about fracture modes and cause of fracture.

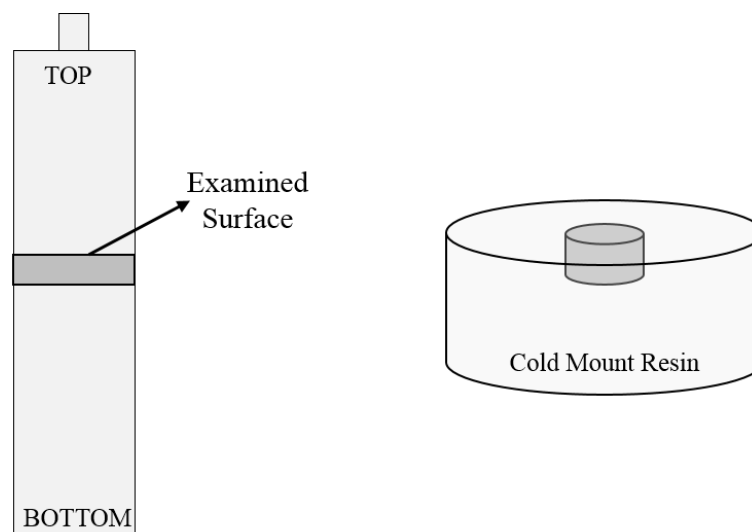


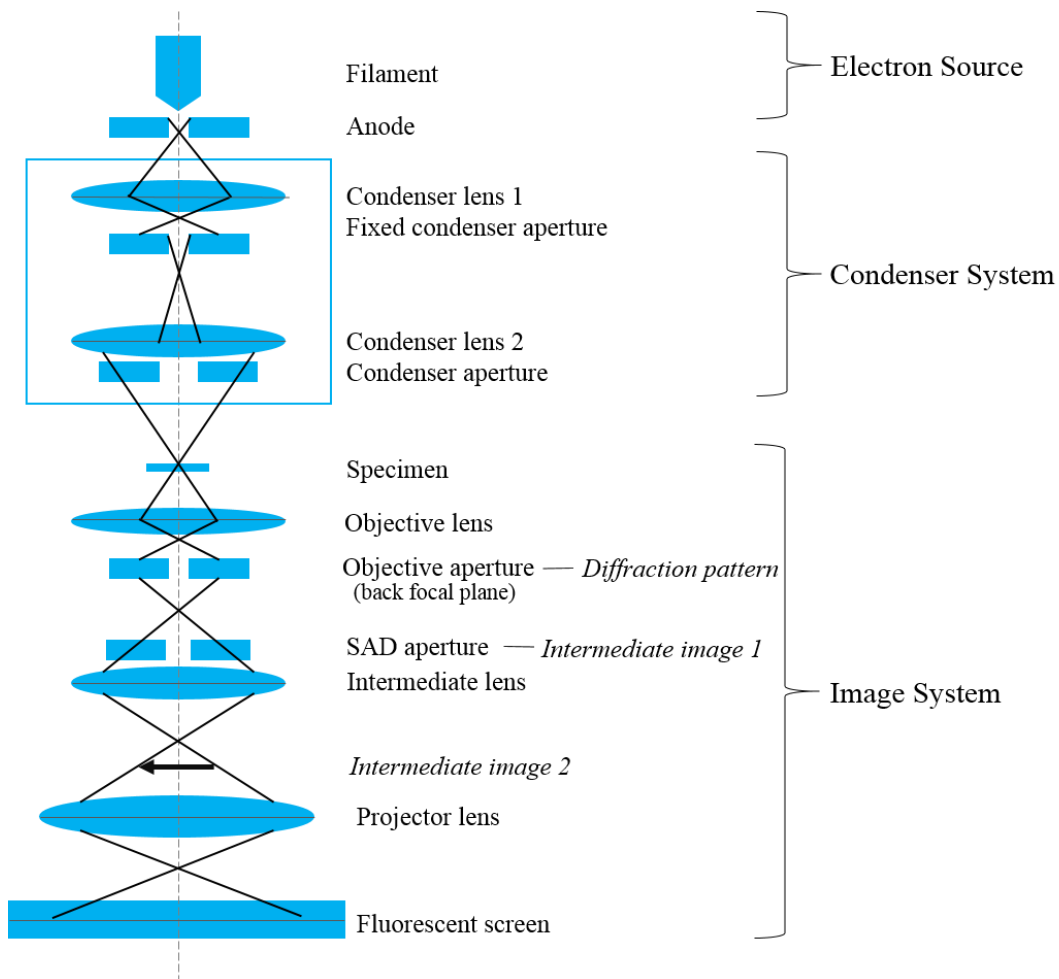
Figure 3.4. A schematic illustration of the position of SEM specimen with respect to the as-cast rod and the cold mounted SEM sample.

A FEI Inspect F50 FEG-SEM equipped with Energy-dispersive X-ray (EDS) detector was utilized for both imaging and EDS analysis of the as-cast rods, and a FEI Inspect F FEG-SEM was for the fracture characterization. An acceleration voltage of 5 kV and a spot size of 5 with a scanning speed of 50 ms were usually used for microstructural observation and a voltage of 15 kV for EDS analysis.

3.2.3 Transmission electron microscopy (TEM)

Transmission electron microscopy (TEM) was undertaken to further analyse amorphous phase, precipitated crystal phase and the interface of as-cast and as-deformed BMGMCs in this study.

Figure 3.4. A schematic of basic TEM equipment components.



TEM samples were prepared by two methods, *i.e.*, electropolishing and ion milling, in which the later one was undertaken with liquid nitrogen to hinder the crystallization. The bulk samples were taken from the middle part of the rod for as-cast BMGMCs, and from the area near primary shear plane for as-compressed BMGMC. The slices were mechanically ground and polished to 70 μm for electropolishing, and further down to 20 μm for ion milling. Twin-jet electropolishing was conducted in the solution of 10% Nital ($\text{HNO}_3:\text{CH}_3\text{OH}=1:9$) with a direct voltage of 14 V at a temperature around 233 K. TEM thin foil samples with high quality can be obtained by careful control of operation parameters.

As schematically shown in Figure 3.4, the TEM mainly consists three parts: the electron source, the condenser system and the imaging system [2]. An electron beam is produced and accelerated under a high accelerating voltage in the gun, and then is focused into a small illumination disc reaching the ultrathin foil specimen after passing through condenser lens [3, 4]. Then the concentrated electron beam passes through the thin foil and interacts with it. A magnified image will be formed after electron beam moves down through objective lens and will be further magnified by subsequent projective lens. The final image or diffraction pattern is observed on the fluorescent screen or CCD [4].

The detailed TEM microstructure observation was conducted with four microscopes. A Philips EM 420 operated at 120 kV and A FEI Tecnai T20 operated at 200 kV were both used for microstructure observation and phase identification. A JEOL 2010F operated at 200 kV was used for nano-scaled microstructure observation, HRTEM and EDS. Aberration-corrected FEG JEOL Z3100R05 operated at 300 kV was used for HRTEM and scanning transmission electron microscopy (STEM).

3.3. Thermal analysis

3.3.1 Differential scanning calorimetry (DSC)

Thermal stability of the amorphous phases (glass transition temperature, T_g and crystallization temperature, T_x) of the as-cast rod was evaluated with Differential Scanning Calorimetry (DSC) (PerkinElmer Diamond DSC). DSC was conducted at the rate of 20 K/min heating from 353 K to 873 K and then cooling from 873 K to 353 K under a continuous flow of purified argon gas. The test samples were taken from the middle part of the ingots and the as-cast rods, and then manually ground to obtain flat surfaces. Approximately 10 mg of sample was weighed, ultrasonic cleaned in the isopropanol bath and then placed in an aluminium pan. An empty aluminium pan was needed as a reference. Parallel testing under the same condition was carried out with two empty aluminium pans, which was subtracted from each measurement as a baseline.

3.4. Mechanical Testing

3.4.1 Compression testing and its compliance correction

3.4.1.1 Compression testing

Uniaxial compression testing and tensile testing are widely chosen to evaluate mechanical properties of materials, such as Young's modulus, yield strength and plastic strain. Considering the sample size (30 mm length) and limits to the equipment, uniaxial compression testing was utilised to measure its mechanical properties.

The test cylinders with diameter of 3 mm and height of 4.5 mm or 6 mm (aspect ratio = 1.5 or 2) [5] were sectioned from the middle part of the as-cast rods using a Struers Minitom with an aluminium oxide blade with rotation speed of 330 rpm. Figure 3.5 schematically depicts how the test specimens machined and where they were from. Before testing, the ends of the cylinders were carefully ground and polished with custom-designed holders to ensure its parallelism and to reduce friction between the testing surface and platen.

The specimens were placed between two boron nitride platens. A thin layer of grease was applied in the interface to further avoid significant friction. The uniaxial compression testing was performed with Zwick/Roell testing machine at a strain rate of $1 \times 10^{-4} \text{ s}^{-1}$. At least three samples were tested for each as-cast cylinder with a specific composition and diameter to ensure its reproducibility. A parallel compliance testing was conducted under the same condition as the testing specimen for each measurement. The necessity and its method will be given in Section 3.4.1.2.

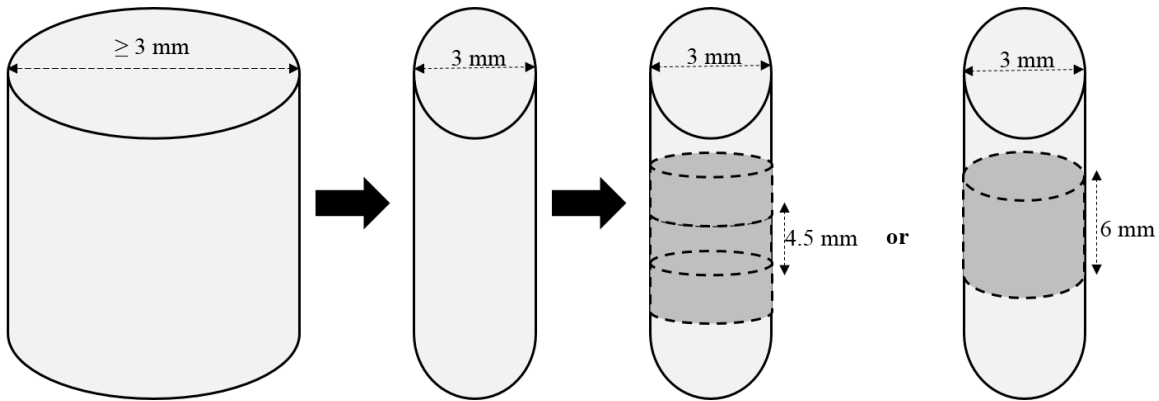


Figure 3.5. Schematic of compression testing sample position: Ni/Co alloyed BMG alloy ($d=3\text{mm}$) with aspect ratio=2; Sn alloyed BMG alloy ($d \geq 3\text{ mm}$) with aspect ratio=1.5.

3.4.1.2 Compression testing compliance correction

It is essential to correct the compression testing result to obtain an accurate and consistent experimental data in this project. There exists two main disadvantages in the testing. Firstly friction between the specimen and compression platens exists even though the interface has been lubricated. It is also difficult to trace the real deformation without an extensometer.

Three accurate methods to characterise machine compliance in simple compression testing have been reported [6]. They are Direct Technique, Elastic Deformation of Known Material and Finite Plastic Strains. The techniques are based on the assumption that the recorded displacement is the sum of the displacement of the sample and the loading system under the same load, as expressed in Equation 3.1:

$$\delta_R = \delta_S + \delta_C \quad (\text{Equation 3.1})$$

where: δ_R – The recorded displacement,

δ_S – The deformation of the specimen,

δ_C – The displacement of the loading system.

Method I “Direct Method” was adopted in the study. The deformation of the loading system was directly measured without any specimens between compression platens. Afterwards the testing specimen was placed between the compression tools and the same procedure was repeated under the same condition. This was the recorded load-displacement data. The actual load-deformation relationship was acquired by subtracting displacement of loading system from the recorded, as illustrated in the Figure 3.6.

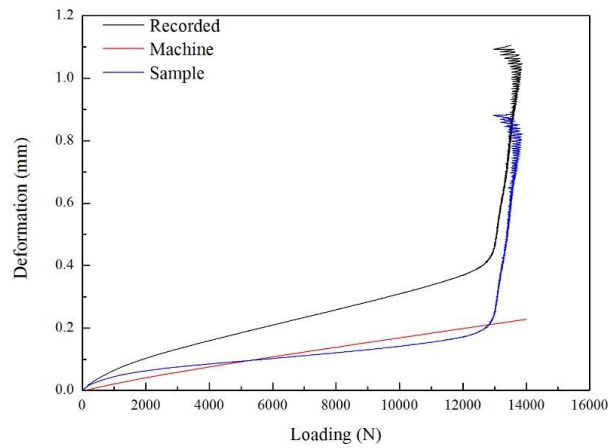


Figure 3.6. Illustration of characterisation of machine compliance based on the “Direct Technique”.

3.4.2 Nanoindentation

The hardness (H) and reduced elastic modulus (E_r) of the specimens were obtained by nanoindentation. Nanoindentation was carried out on a Hysitron TI Premier Nano-mechanical testing instrument and also a TriboScope system mounted on a DI AFM with a Nanoscope III controller. The difference in mechanical properties between amorphous matrix phase and CuZr B2 crystalline phase was investigated. At least five different areas were probed for each phase. Indentation was performed in the center of the large region for each phase to minimize the influence of the surrounding phases.

3.4.3 Elastic modulus measurement

Elastic constants of the as-cast bulk BMG and BMGMC, such as shear modulus (G), bulk modulus (B), Young’s modulus (E) and Poisson ratio (ν), were determined with ultrasound velocity instrument (EPOCH 600, OLYMPUS) [7].

Before measurement, the specimen density was measured with distilled water as standard based on the Archimedeian principle using a balance (New Classic MF MS104S/01) with accuracy of ± 0.0001 g.

$$\rho_s = \frac{\rho_w}{1 - m_w/m_a} \quad (\text{Equation 3.2})$$

where: ρ_s – Density of specimen,
 ρ_w – Density of water,
 m_w – Specimen weight in water,
 m_a – Specimen weight in air.

Then the elastic moduli were derived from the sound velocities and known specimen density by applying following equations [8]:

$$v = \frac{1}{2} \frac{v_l^2 - 2v_s^2}{v_l^2 - v_s^2} \quad (\text{Equation 3.3})$$

$$G = \rho v_s^2 \quad (\text{Equation 3.4})$$

$$E = 2G(1 + v) \quad (\text{Equation 3.5})$$

$$B = \rho \left(v_l^2 - \frac{4}{3} v_s^2 \right) \quad (\text{Equation 3.6})$$

3.5. Reference

- [1] *ICDD database*. Available: www.icdd.com.
- [2] J. Rodenburg. *Tutorials in Transmission Electron Microscopy*. Available: <http://www.rodenburg.org/index.html>
- [3] P. J. Goodhew, J. Humphreys, and R. Beanland, *Electron microscopy and analysis*: CRC Press, 2000.
- [4] D. Williams and C. Carter, *Transmission electron microscopy: a textbook for materials science*: Springer, 2009.
- [5] A. International, "ASTM E9-09, Standard Test Methods of Compression Testing of Metallic Materials at Room Temperature," ed. West Conshohocken, PA, 2009.
- [6] S. R. Kalidindi, A. Abusafieh, and E. El-Danaf, "Accurate characterization of machine compliance for simple compression testing," *Experimental Mechanics*, vol. 37, pp. 210-215, 1997/06/01 1997.
- [7] S. Pauly, "Phase formation and mechanical properties of metastable Cu-Zr-based alloys," Doctor, Technische Universität Dresden, 2010.
- [8] S. Kim, H. Ledbetter, and Y. Y. Li, "Elastic constants of four Fe-Cr-Ni-Mn alloys," *Journal of materials science*, vol. 29, pp. 5462-5466, 1994.

Chapter 4 Developments of Large-sized CuZr-based Bulk Metallic Glass Composites with Improved Mechanical Properties by Tailoring Microstructure

4.1 Introduction

Bulk metallic glasses (BMGs) have attracted lots of attention because of their excellent properties, such as high strength, large elastic limit (up to 2%), high strength and hardness and excellent corrosion resistance [1-3]. Nevertheless, strain softening behaviour and room-temperature brittleness have limited their real structural applications [4-6]. To overcome this shortcoming many strategies have been proposed and shape memory phase reinforced bulk metallic glass composites (BMGMCs) have proved to be an effective solution [7-9]. However, most shape memory phase reinforced bulk metallic glass composites (BMGMCs) are limited to the attainable dimensions (less than 4 mm in diameter). In addition, the microstructures are sensitive to the manufacturing conditions. Thus, practical engineering applications for TRIP-reinforced BMGMCs is still a fairy tale at present. Therefore, the development of large-scaled shape memory BMGMCs with improved mechanical performance is required.

In this chapter, CuZr-based metallic glass composites with large dimensions and improved mechanical properties were developed. A thorough investigation of the microstructure dependence on composition and cooling rate in the $\text{Cu}_{48-x}\text{Zr}_{48}\text{Al}_4\text{Sn}_x$ ($x=0.25, 0.5, 0.75, 1, 1.25, 1.5$ at%) system was carried out. In addition, the influence of manufacturing condition and raw material purity on the microstructure evolution was studied systematically. The main purposes were to develop large-sized CuZr-based BMGMCs with optimized microstructure and appreciable deformation behaviour and to understand the homogenization mechanism and the underlying deformation mechanisms.

4.2 Experimental

Master alloys with nominal composition of $\text{Cu}_{48-x}\text{Zr}_{48}\text{Al}_4\text{Sn}_x$ ($x=0.25, 0.5, 0.75, 1, 1.25, 1.5$ at%) were fabricated by arc melting constituting elements with high purity ($\geq 99\%$) in a Ti-gettered argon atmosphere. Each ingot was melted at least four times to ensure compositional

homogeneity. Mass loss for each ingot during preparation was negligible (≤ 0.1 wt%). Cylinder samples with diameter of 2 mm up to 8 mm and length of 30 mm were prepared by water-cooled copper mould suction casting. Manufacturing parameters, such as the alloy melt weight, the melting power and remelting times in the melting process, vacuum and casting procedures, were strictly controlled to minimize the instability and uncontrollability in the solidification process.

The glass transformation temperature (T_g) and crystallization temperature (T_x) were measured by Differential Scanning Calorimetry (DSC) in a Perkin Elmer DSC Diamond from 303 K to 863 K with a heating rate of 20 K/min. Phase identification in the as-cast alloys were analysed by X-ray diffraction (XRD) in a Siemens D5000 diffractometer (Cu $K\alpha$ radiation, with changer). Microstructures of as-cast specimens and fracture surface morphology were observed by scanning electron microscopy (FEI Inspect F50/F FEG SEM) with an energy-dispersive spectrometer in backscattered mode and transmission electron microscopy (TEM). TEM observation was carried out on two different microscopes. They are Philips EM 420 operated at 120 kV for microstructure observation, and JEOL 2010F at 200 kV for high resolution TEM (HRTEM). The samples for TEM investigation were mechanically thinned to around 80 μm and then twin-jet electropolished using $\text{HNO}_3:\text{CH}_3\text{OH} = 1:9$ solution at the temperature of 233 K. Volume fraction of the crystalline phases was estimated from the SEM images with the image software ImageJ [10].

Nanoindentation testing was carried out on a well-polished transverse section surface of the as-cast and fractured specimen $\text{Cu}_{48-x}\text{Zr}_{48}\text{Al}_4\text{Sn}_x$ ($x=0.25, 0.5, 0.75$ and 1 at%) in 7 mm diameter at room temperature using Hysitron TI Premier Nano-mechanical testing instrument. The indentation load regime was set for a grid of 2×2 indents spaced 5 μm apart, centred in the middle of the crystalline phase and the glass matrix phase. Uniaxial compression testing was performed on the samples at a strain rate of $1 \times 10^{-4} \text{ s}^{-1}$ at room temperature. The test samples with a diameter of 3 mm and height to diameter ratio of 1.5:1 were machined from the as-cast rods. The ends were carefully ground and polished with custom-designed holder to ensure the parallelism and minimum frictions between testing samples and the equipment platens.

4.3 Results and Discussion

4.3.1 Composition – raw materials purity – microstructure relationship

In this section, the effect of raw material purity on its microstructure and compressive deformation behaviour was evaluated. Zirconium with two different purities and two suppliers was used for alloy preparation. The composition of the zirconium provided by the suppliers are given in Table 4.1. One contained 1400 ppm oxygen, denoted as L-Zr; the other contained 150 ppm oxygen, denoted as H-Zr. Other constituent elements were in the high purity of ~ 99.99 %. All the samples investigated in this section were prepared in the same processing conditions and in the same shape configuration, with diameter of 5 mm and length of 30 mm.

Table 4.1. The compositions of Zirconium with different purity from different suppliers

ppm (max)	Zr (%)	Hf (ppm)	Fe+Cr (ppm)	C (ppm)	H (ppm)	N (ppm)	O (ppm)
Batch 1 (L-Zr)	99.0	7000	800	100	4	40	1400
Batch 2 (H-Zr)	99.9	300	110	50	20	20	150

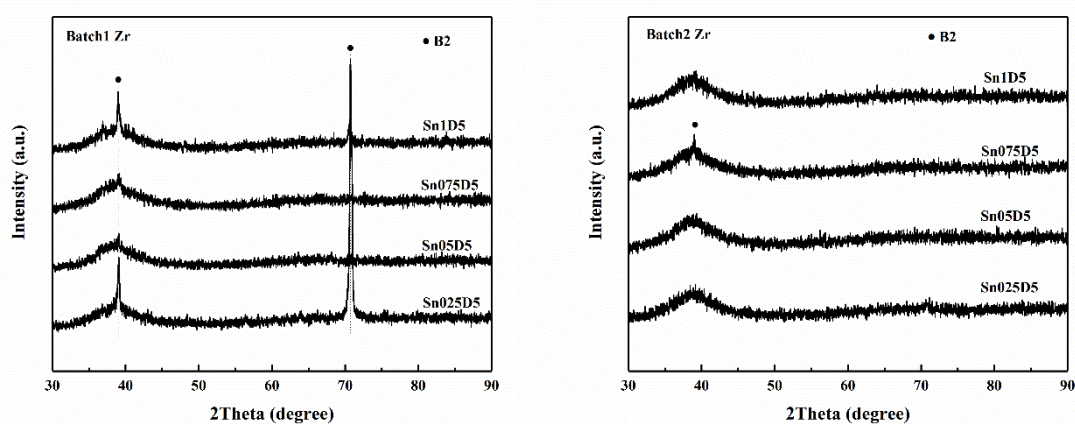


Figure 4.1. XRD pattern of $\text{Cu}_{48-x}\text{Zr}_x\text{Al}_4\text{Sn}_x$ ($x=0.25, 0.5, 0.75, 1$ at%) BMGMCs prepared by L-Zr and H-Zr, respectively.

Figure 4.1 shows the XRD patterns of the as-cast Sn-doped CuZr-based BMGs prepared by different Zr. It exhibits a typical characteristic for BMGMCs consisting of CuZr B2 phase crystal peaks and broad amorphous hump for L-Zr BMGMCs. However, no crystalline phase was detected in the H-Zr BMGs except for 0.75 at% Sn-doped alloys. In comparison, it indicates that high content of oxygen will deteriorate the glass forming ability and lead to the crystals formation in the glassy matrix.

Backscattered cross-sectional SEM images of the Sn-doped alloys prepared with the different Zr feedstock are present in Figure 4.2. For H-Zr CuZr-based alloys, no microstructural features were detected in the 0.25 at% and 0.5 at% Sn-doped BMG (Figure 4.2b, d), indicating the formation of fully amorphous phase. As Sn addition increased to 0.75 at% (Figure 4.2f) and 1 at% (not shown here), spherical CuZr B2 phase precipitates were observed in the glassy matrix. The crystalline phase particles were well separated and uniformly distributed. In contrast, a crystal reinforced glass composite structure was observed in all Sn-doped alloys prepared with L-Zr, as shown in Figure 4.2a, c, e. Therefore, there was a marked difference in microstructure of the samples when comparing the H-Zr to the L-Zr. Crystalline phases in the L-Zr sample were prone to impinging together to form patch-like features. In addition, two crystalline phases were observed in the glassy phase matrix. One is dendrite-like feature (as indicated by white arrows in Figure 4.2) with size range of 2 – 4 μm in black contrast, which was somewhat independent of the Sn addition. It is likely that this was due to the high oxygen content in the Zr, which has been reported before [11]. The other is patch-like feature with dark grey contrast, mainly located in the centre region of the as-cast rods. The size of this phase ranged from 20 μm up to 180 μm . It is important to point out that these microscale crystals exhibiting dark contrast precipitate uniformly in the dark grey crystalline phase and amorphous phase. EDS measurement (Table 4.2) showed that this small black dendritic phase is enriched in Al (~ 10.6 at%) compared with surrounding glassy matrix (~ 3.7 at%) and CuZr crystalline phase (~ 3.7 at%), which resulted in the compositional contrast in backscattered electron mode.

The difference between L-Zr and H-Zr is the high content of oxygen in L-Zr. It has been reported that the solubility of oxygen in Zr is ~ 30 at% at 473 K [12]. Therefore, the oxygen will uniformly dissolve into the alloys and no related oxide will be formed in both L-Zr and H-Zr CuZr-based BMGMCs. Thus, the effect of oxygen in the current alloys is to promote the formation of dendrite in the initial solidification stage.

Compression testing of both series of CuZr-based BMGMCs under the same testing conditions was performed and Figure 4.3 shows the corresponding engineering stress strain curves. For each alloy, the test was repeated at least three times to check the variation from specimen to specimen. The deformation behaviour for the BMGs with different Zr purity was drastically different. All samples from L-Zr fractured catastrophically without an obvious yield point. Nevertheless, the deformation ability of the specimens from H-Zr was improved, with elastic deformation to the yield point around 1600 MPa and then plastically deformed until fractured. It has been reported that the oxygen impurity can cause embrittlement [13, 14]. It was found that oxygen impurities may change the crystallization mode in metallic glass alloys and result in the formation of metastable crystallization products. The thermostability may be lowered correspondingly. The difference in deformation response in the BMGMCs prepared with L-Zr and H-Zr may result from oxygen impurity.

In summary, the purity of the raw materials had a significant influence on the precipitated crystals, microstructure of the BMG/BMGMCs, and thereby the corresponding mechanical behaviour. Oxygen impurities in the Zr may change the crystallization mode of the BMG, leading to the formation of the brittle crystals in the glassy matrix. It may result in the instability to sustain the stress flow and then catastrophic failure.

Table 4.2. SEM-EDS analysis in glass matrix, CuZr B2 phase and black precipitates of the as-cast $\text{Cu}_{47.25}\text{Zr}_{48}\text{Al}_4\text{Sn}_{0.75}$ in the diameter of 5 mm prepared by L-Zr.

	Cu (at%)	Zr (at%)	Al (at%)	Sn (at%)
Black Phase	38.3	50.76	10.64	0.32
Glass Matrix	47.1	48.42	3.78	0.72
B2	46.82	48.66	3.76	0.78

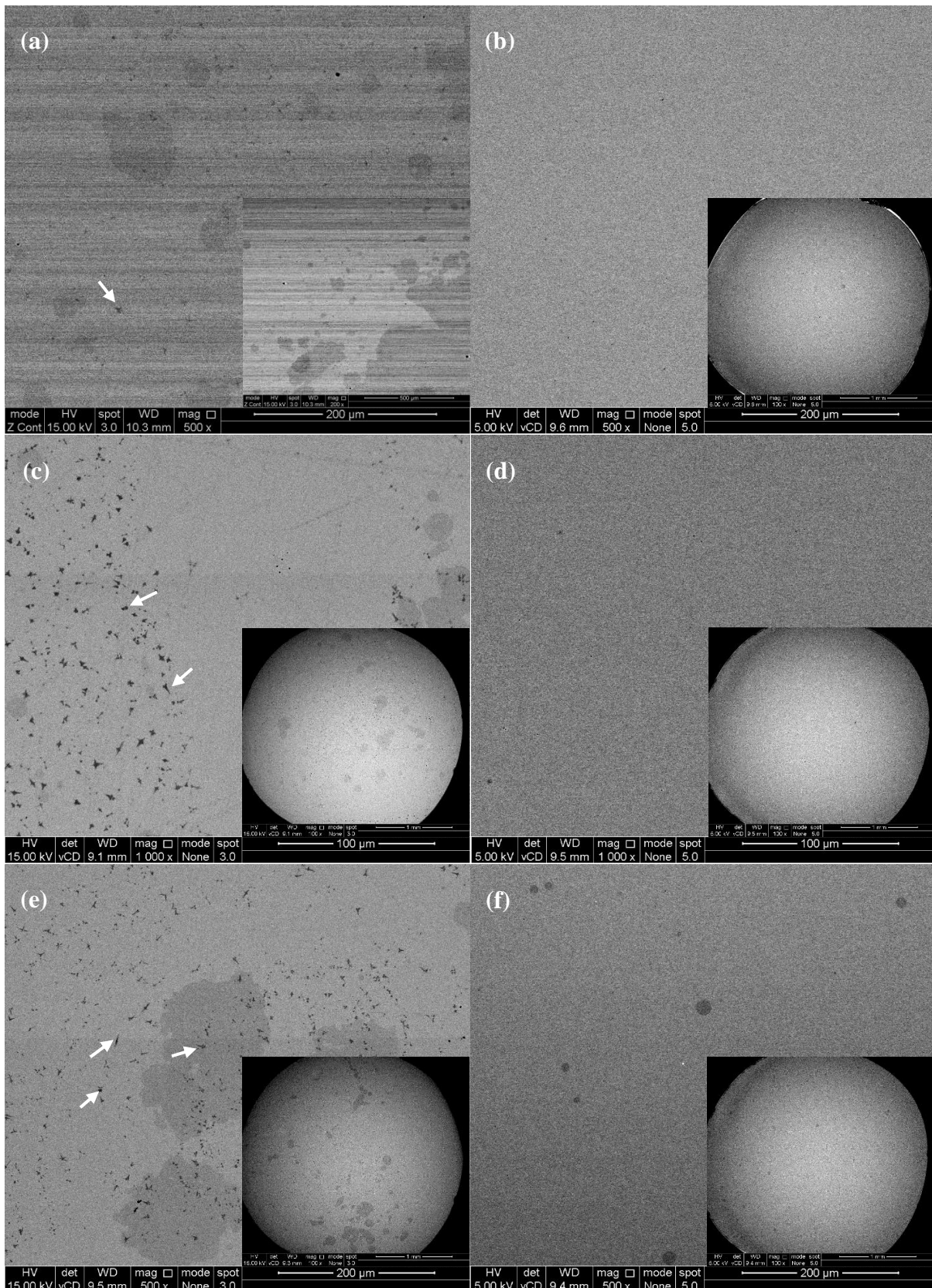
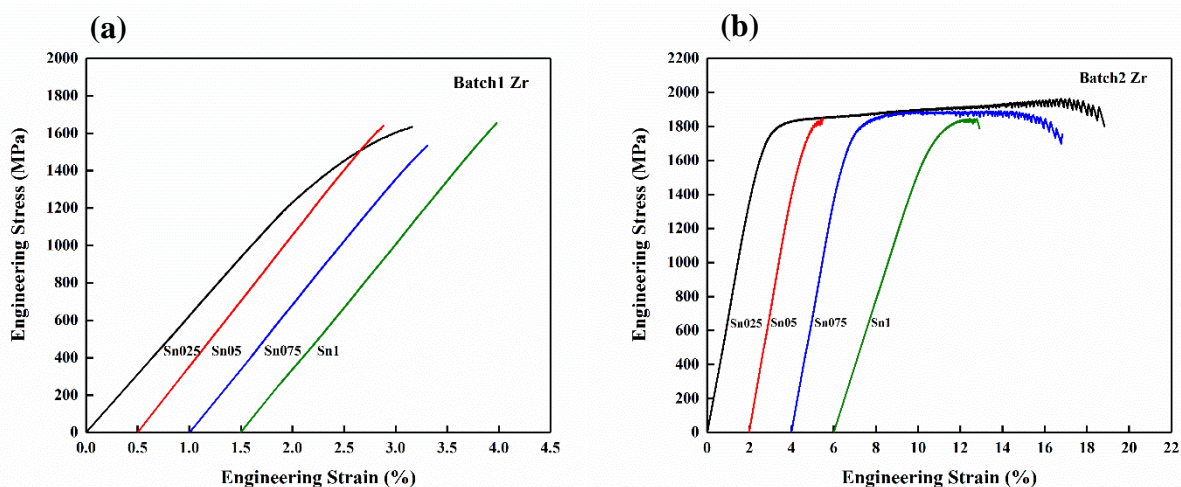


Figure 4.2. Cross-section backscattered SEM images of the as-cast $\text{Cu}_{48-x}\text{Zr}_{48}\text{Al}_4\text{Sn}_x$ ($x=0, 0.5, 0.75$ at%) BMG alloys in diameter of 5 mm prepared with L-Zr and H-Zr, respectively: (a)(b) $x=0$ at%; (c)(d) $x=0.5$ at%; (e)(f) $x=0.75$ at%.

Figure 4.3. Compressive engineering stress strain curves of the as-cast $\text{Cu}_{48-x}\text{Zr}_x\text{Al}_4\text{Sn}_x$ ($x=0.25, 0.5, 0.75$ and 1) BMGMCs in diameter of 5 mm prepared with (a) L-Zr and (b) H-Zr, respectively.

0.5, 0.75 and 1 at%) BMGMCs in diameter of 5 mm prepared with (a) L-Zr and (b) H-Zr, respectively.

4.3.2 Composition – manufacturing condition – microstructure relationship

The size, shape and distribution of the *in-situ* formed CuZr B2 crystalline phase will influence the performance of shape memory phase reinforced BMGMCs [15]. They strongly depend on the composition and manufacturing conditions [15, 16]. In addition, CuZr B2 phase precipitates polymorphously from the melt, which is different from that of beta-dendrites in the Ti-based BMGMCs. Thus the semi-solid process, utilizing the temperature span between the solidification point of the crystalline phase and amorphous matrix, is not applicable to CuZr-based BMGMCs [17]. In this section, manufacturing conditions, including melting current/time and mould configuration, were explored to properly control the formation of the CuZr B2 phase in the amorphous matrix. The CuZr-based BMGMCs with the composition of $\text{Cu}_{47.25}\text{Zr}_{48}\text{Al}_4\text{Sn}_{0.75}$ was selected to investigate the formation and the distribution of the CuZr B2 phase in the amorphous matrix and thereby determine the appropriate fabrication conditions for the CuZr-based BMGMCs with different sizes in the current study.

4.3.2.1 Effect of the melting current/time

The thermostability, crystallization and the mechanical behaviour of the BMG/BMGMCs will be influenced by the melting current and time in the casting process (*i.e.* adjusting the casting temperature) [18-21]. $\text{Cu}_{47.25}\text{Zr}_{48}\text{Al}_4\text{Sn}_{0.75}$ cylinder rods in the diameter of 4, 5, 6 and 7 mm were fabricated by suction casting with different melting current or time. The corresponding casting parameters are listed in Table 4.3.

Table 4.3. The melting current and melting time for $\text{Cu}_{47.25}\text{Zr}_{48}\text{Al}_4\text{Sn}_{0.75}$ BMG/BMGMCs (designated as Sn0.75) in different diameters.

Diameter (mm)	Melting current (% full power)	Melting time (s)	f_{crystal} (vol%)	Designation
4	40 ± 5	5 ± 1	26 ± 2.5	D4C45
	40 ± 5	15 ± 1	2.5 ± 0.4	D4C415
5	40 ± 5	15 ± 1	3.2 ± 1.0	D5C415
	50 ± 5	5 ± 1	4.5 ± 0.7	D5C55
	50 ± 5	10 ± 1	2.5 ± 0.5	D5C510
	70 ± 5	5 ± 1	5.2 ± 0.6	D5C75
6	50 ± 5	5 ± 1	5.6 ± 0.5	D6C55
	50 ± 5	10 ± 1	4.6 ± 0.6	D6C510
	70 ± 5	5 ± 1	8.6 ± 0.5	D6C75
7	70 ± 5	5 ± 1	10.4 ± 1.2	D7C75
	80 ± 5	5 ± 1	12.2 ± 1.5	D7C85

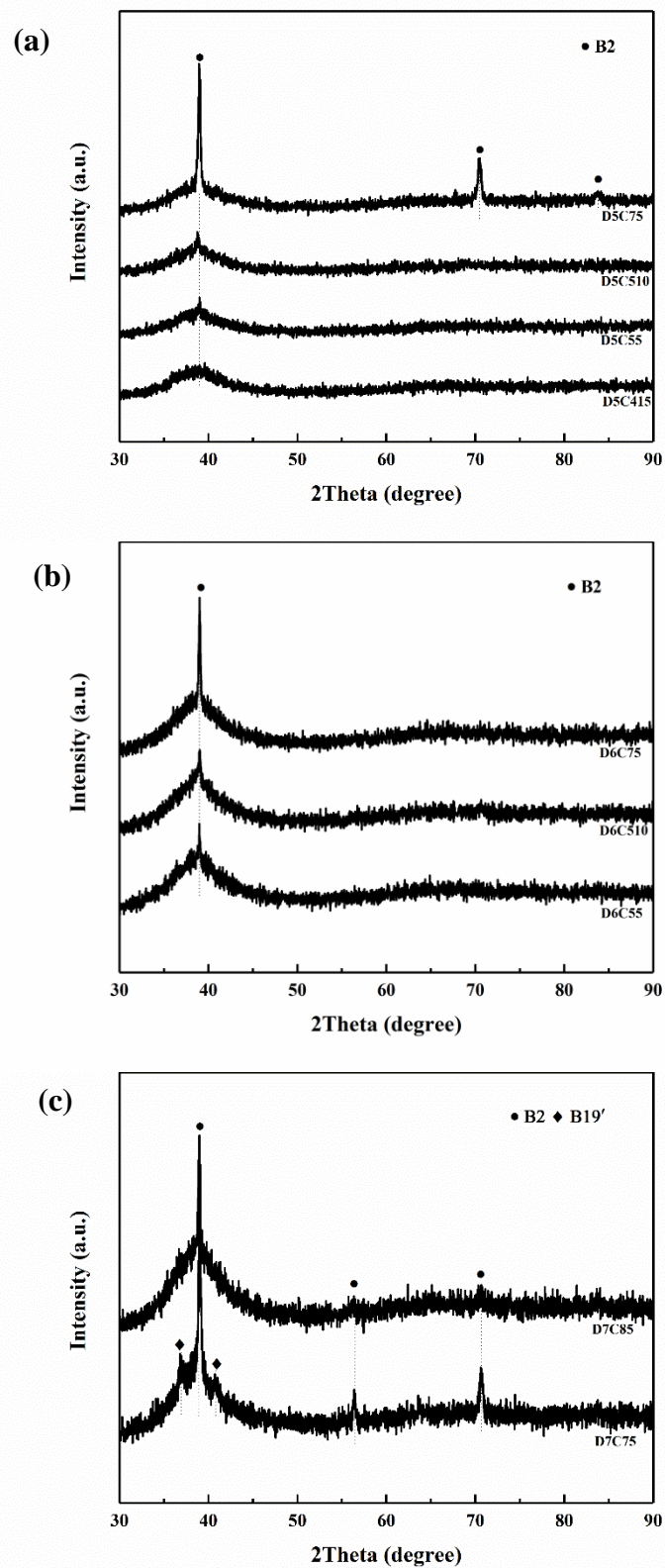


Figure 4.4. XRD patterns of the as-cast $\text{Cu}_{47.25}\text{Zr}_{48}\text{Al}_4\text{Sn}_{0.75}$ BMG/BMGMCs in the diameter of (a) 5 mm, (b) 6 mm and (c) 7 mm prepared with different melting current or melting time.

Figure 4.4 gives the XRD patterns of the as-cast $\text{Cu}_{47.25}\text{Zr}_{48}\text{Al}_4\text{Sn}_{0.75}$ BMG/BMGMCs alloys in different diameters fabricated in different manufacturing conditions. High melting current (or long melting time in the casting process) suggests the high casting temperature of alloy melt. When the ingot was melted with the current around 40% full power for nearly 15 s, the obtained 5 mm rod was fully amorphous (Figure 4.4a). As the melting current / time increases, CuZr B2 crystalline peaks were superimposed on a broad hump, indicating the formation of BMGMCs. Additionally, the intensity of the crystalline peaks enhances with the increases in melting current / time. The same observations were made for the alloys with a cast diameter of 6 mm (Figure 4.4b). For the BMGMCs in size of 7 mm, the change in the melting current has no influence on the composite structure. Other crystalline peaks, identified as martensitic B19', were detected except for CuZr B2 phase crystalline peaks when the applied current was lower (Figure 4.4c).

The backscattered cross-sectioned SEM images showing the morphology and distribution of crystals in the amorphous matrix of the BMGMCs in the size of 5 mm and 6 mm are present in Figure 4.5. The crystalline volume fractions in the as-cast BMGMCs estimated according to the SEM images are given in Table 4.3. It can be seen that the content, size and distribution of the crystalline precipitates in the glassy matrix changes as the casting condition (*i.e.* melting current and time) changes, further confirming the XRD results. As shown in Figure 4.5a, d and f for samples D5C55, D6C55 and D6C75, the CuZr B2 crystals are well separated and homogeneously distributed. When the casting current increased, the spherical crystals were prone to aggregating and forming large particles or patch-like structure near the edge even though the crystalline volume fraction was less than 8 vol% (Figure 4.5b, c, e). Furthermore, as the cooling rate decreased (*i.e.* the casting size increases from 5 mm to 6 mm), the B2 crystal size increased. Therefore, the formation, volume fraction and distribution of the CuZr B2 phase in the amorphous matrix for CuZr-based BMG/BMGMCs are sensitive to the preparation condition and cooling rate.

The same copper mould was utilized to prepare BMG/BMGMCs rods in the same size through different casting parameters. Thus, the cooling ability of the mould itself was identical. In theory, the critical glass forming dimension (or the critical cooling rate, R_c) is inherently determined by the metallic system itself [18]. When the applied cooling rate is less than the critical cooling rate, crystalline phase will precipitate in the amorphous matrix. During fabrication, the solidification process for each casting operation cannot be guaranteed in the same condition. The as-cast microstructure, fully amorphous or composite, largely depends on

the status of liquid melts and the temperature of cooling water *etc.*, among which the former will be mainly determined by the casting temperature and thereby the way of crystallization.

In combination with the XRD patterns and SEM images, it can be seen that there exists a “casting threshold”, below or above which the crystal content, size and distribution will be dramatically different. In a lower energetic state, it may result in crystal aggregation; otherwise, it may prefer the fully amorphous state. As reported, local crystal-like clusters in the melt that act as preferential nucleation sites can contribute to the homogeneous crystal precipitates in the supercooled liquid during solidification [22, 23]. In the current study the cylinder specimen was prepared by suction casting into a water-cooled copper mould. Thus, it is reasonable to assume that the liquid melt was supercooled in the copper mould. During cooling, some local atomic clusters or high temperature compounds will be formed uniformly in the melt. As the cooling proceeds, they will act as nuclei for the reinforcing phase (*i.e.* B2 phase crystals in CuZr-based BMGMCs), resulting in copious homogeneous nucleation of crystals. The precipitates will grow polymorphously on further cooling. Under rapid cooling, the remaining melt will solidify into the glassy matrix. The casting temperature (T_c) will determine the initial temperature of the liquid melt (T_i) in the mould, thereby affecting the microstructure of the as-cast CuZr-based BMG/BMGMCs. The solidification process from different T_c is illustrated in Figure 4.6. Lower T_c leads to the higher undercooling (ΔT), thus promoting crystal nucleation. Therefore, the growing small crystals tend to coalesce with each other, forming large crystalline phase. Nevertheless, higher T_c will decrease ΔT , hindering crystal nucleation. When T_c reaches to the temperature of about $1.4T_m$ (the melting temperature) [18], the metastable local atomic cluster or the high temperature compound in the melt will disappear, thus increasing GFA to some extent. In addition, long-time melting will increase the opportunity for the liquid melt to absorb the oxygen remaining in the atmosphere [18], which may incur unfavourable crystallization and deteriorate materials mechanical performance. Therefore, the microstructural characteristics, including crystallite size and distribution, can be optimized by properly adjusting casting temperature via changing melting current or melting duration. High melting current and short melting duration are preferred. High melting current results in a homogeneous melt and short melting duration could effectively suppress the oxygen absorption from the atmosphere, thereby hindering the formation of the brittle crystalline phases.

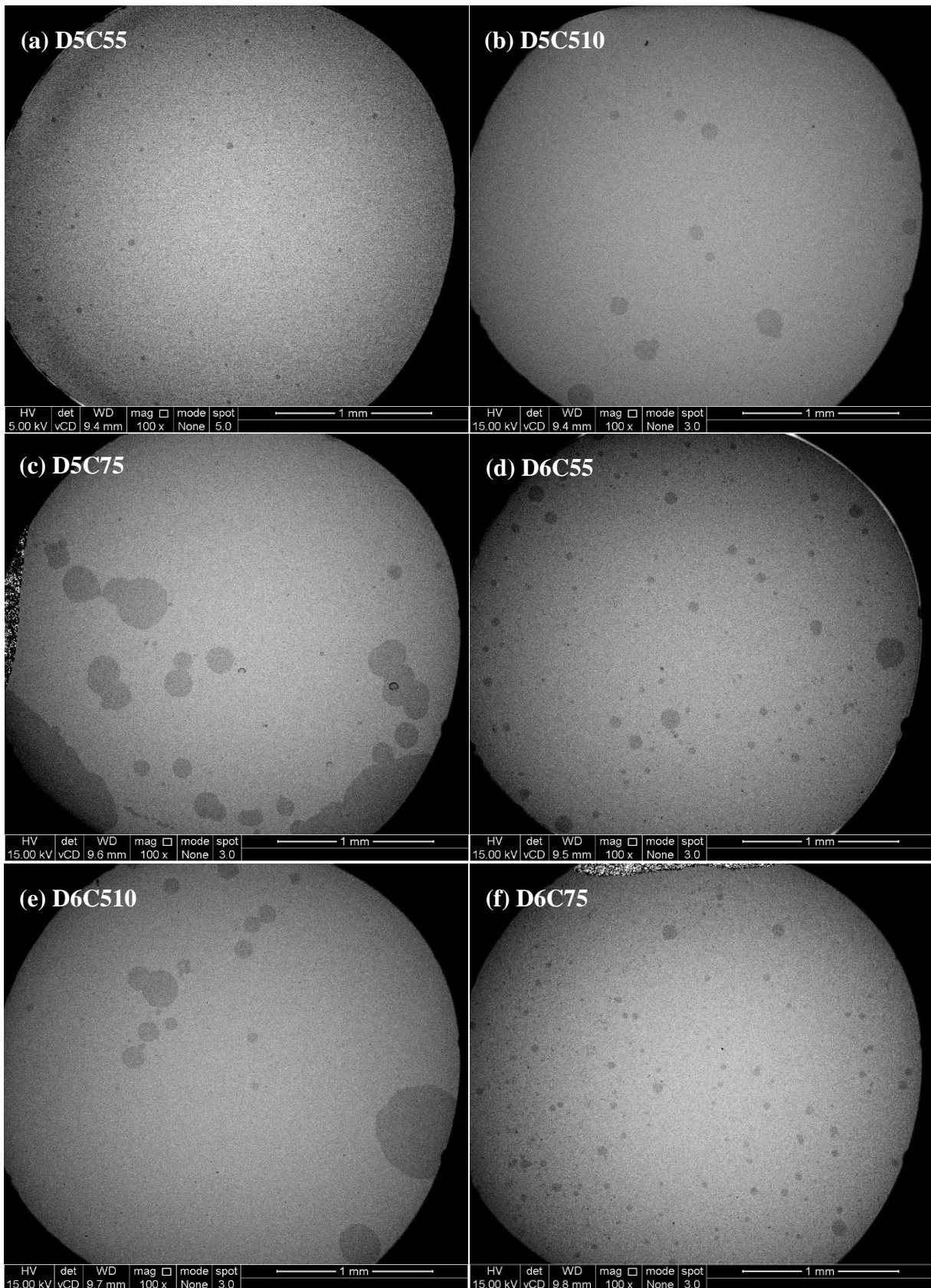


Figure 4.5. Backscattered SEM images showing microstructure evolution of the as-cast $\text{Cu}_{47.25}\text{Zr}_{48}\text{Al}_4\text{Sn}_{0.75}$ in the diameter of 5 mm and 6 mm prepared with different melting currents/times: (a)-(c) $d=5$ mm; (d)-(f) $d=6$ mm.

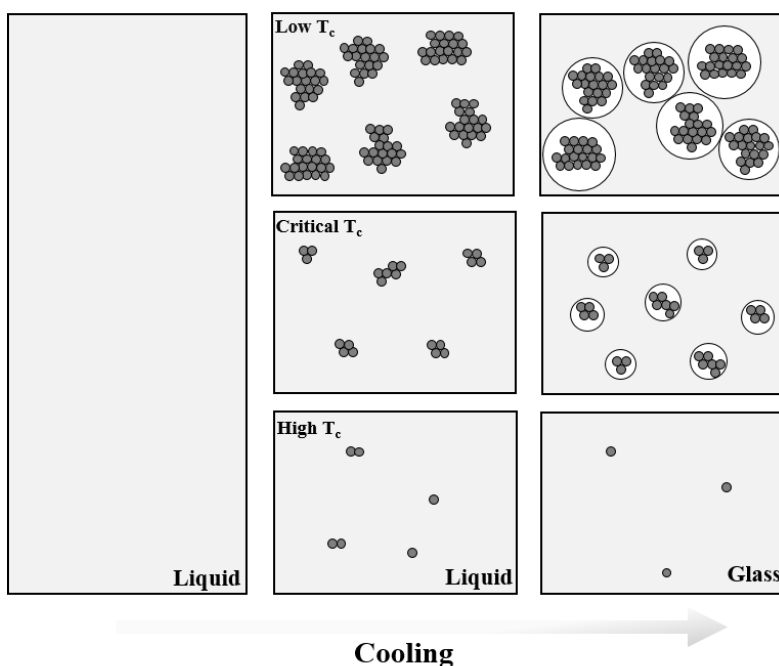


Figure 4.6. Schematic illustration of the solidification process comparison from low casting temperature, critical casting temperature and high casting temperature.

4.3.2.2 Effect of the casting mould configuration

Microstructures and mechanical properties are dependent on composition and manufacturing processing [24, 25]. For large-sized ($d \geq 5$ mm) CuZr-based BMG/BMGMCs fabrication, it is difficult to control the melt status before casting, and thus influencing the solidification process. In order to minimize the uncertainty in the casting process, the configuration of the copper mould was adjusted to provide controllability in the solidification. In this section, the effect of copper mould configuration on the solidification and the formation of the second phase in the as-cast CuZr-based BMGMCs is studied.

Figure 4.7 is a schematic of the design of the copper mould. Figure 4.7a is the conventional mould design with a cylindrical orifice in a fixed diameter, denoted as B. In this case, the melt automatically flowed into the orifice once the ingot started to melt. The casting process was out of control. Figure 4.7b gives the modified mould design with an inlet increased from 3 mm to the specific dimension in two steps, denoted as M. In this case, the melt was sucked into the orifice when the ingot was homogeneously mixed by arc melting. Casting process and the solidification was in control.

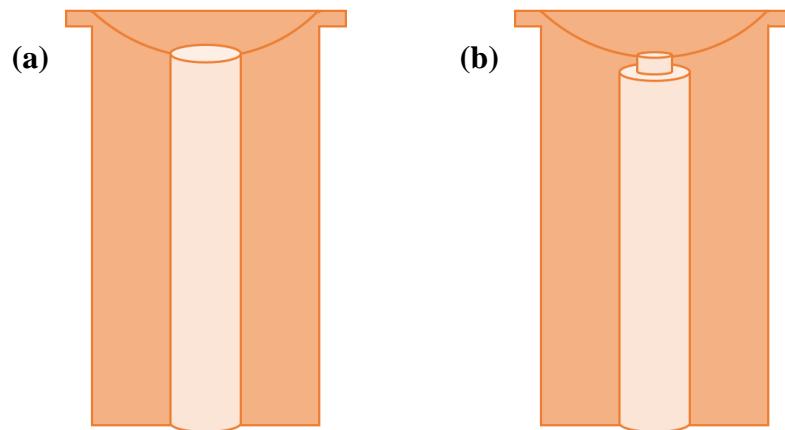


Figure 4.7. Schematic of the casting mould configuration for large-size BMGMCs manufacture ($d \geq 5$ mm): (a) the initial design of the copper mould with an orifice in one specific diameter (Mould B); (b) the modified design of the copper mould with the inlet increased from 3 mm to a specific size (≥ 5 mm) in two step (Mould M).

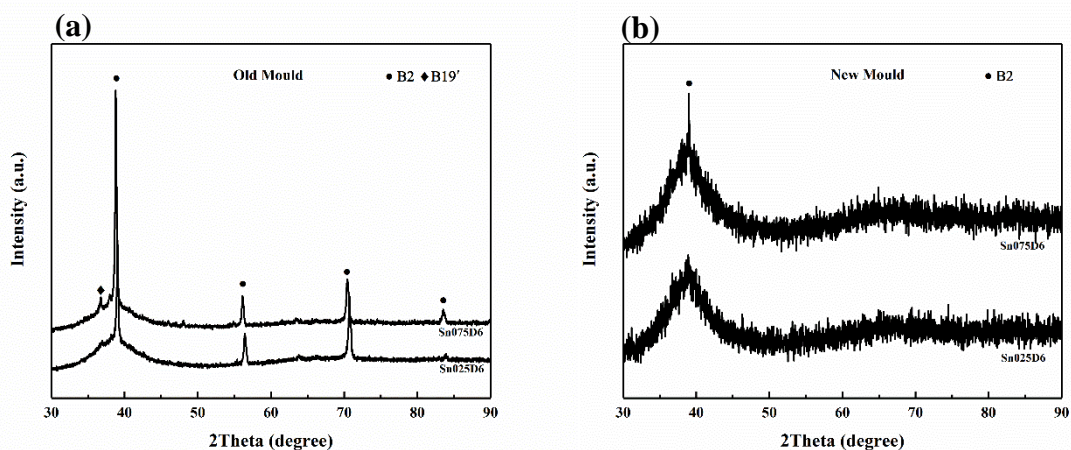


Figure 4.8. XRD patterns of the as-cast 0.25 at% Sn-doped and 0.75 at% Sn-doped CuZr-based BMGMCs ($d=6$ mm) prepared with moulds in different configurations: (a) Mould B; (b) Mould M.

Figure 4.8 gives the XRD patterns for 0.25 at% and 0.75 at% Sn-alloyed CuZr-based BMGMCs with a size of 6 mm prepared with Mould B and Mould M, respectively. Both B2 and B19' phases were detected in the BMGMCs fabricated with Mould B. In comparison, only CuZr B2 phase was identified and its intensity dramatically decreased in the BMGMCs obtained in the modified copper mould. It suggests that effective control of the liquid melt status and casting process could suppress the precipitation of martensitic B19' phase.

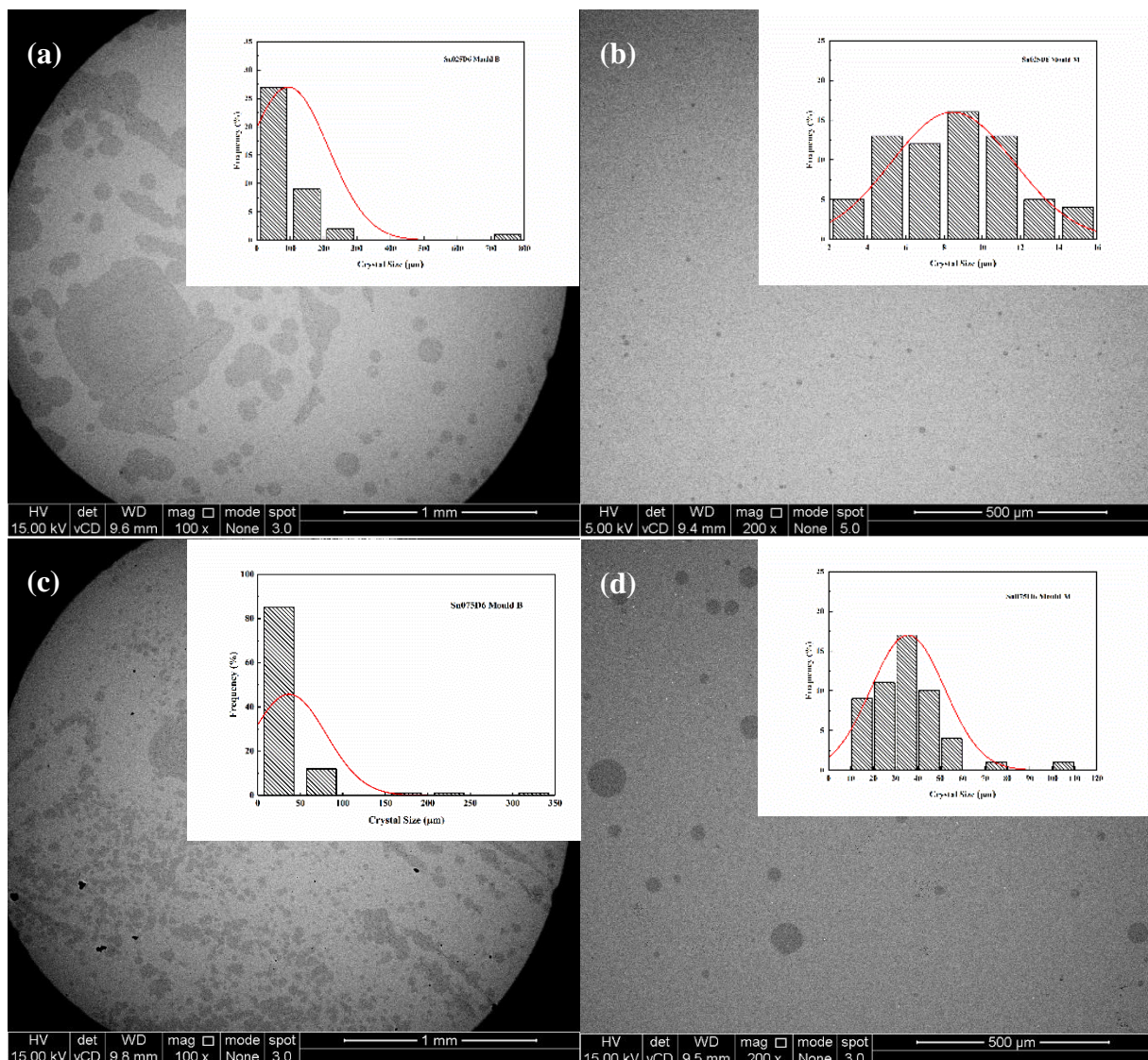


Figure 4.9. Backscattered SEM images of 0.25 at% and 0.75 at% Sn-doped CuZr-based composites in the diameter of 6 mm prepared with Mould B / Mould M: (a) 0.25 at% Sn addition in Mould B; (b) 0.25 at% Sn addition in Mould M; (c) 0.75 at% Sn addition in Mould B; (d) 0.75 at% Sn addition in Mould M; Insets are corresponding crystal size distribution.

Backscattered SEM images (Figure 4.9) present the microstructures of the as-cast 0.25 at% and 0.75 at% Sn-doped CuZr-based BMGMCs prepared with Mould B and Mould M, respectively. The corresponding crystal size distribution in the amorphous matrix is shown in the inset. It is obvious that the crystalline phase tends to coalesce together to form coarse grains in Mould B, in correspondence with the crystal size distribution statistics. In contrast, B2 CuZr crystals are well separated and uniformly distributed in the amorphous matrix for the BMGMCs

obtained in the Mould M. The B2 phase precipitates in 0.25 at% Sn-doped BMGMCs were mainly in the range of 6 – 12 μm and that in 0.75 at% Sn-doped alloys were mainly located in the range of 30 – 50 μm . Hence, the optimum composite microstructure with B2 phase crystals homogeneously distributing in the glassy matrix was obtained by suction casting into Mould M.

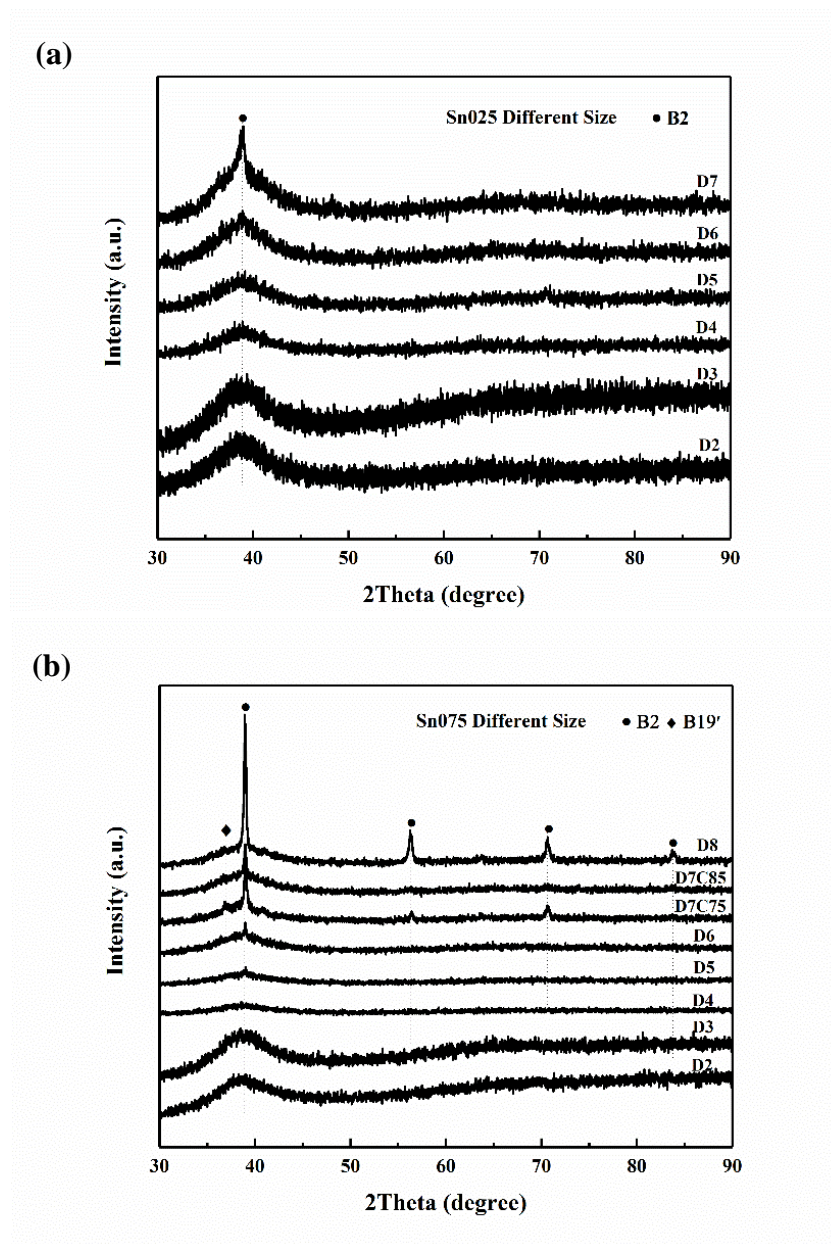
Therefore, it can be concluded that proper modification or design of the copper mould configuration can change the melt status and thus the solidification process upon cooling. Crystallization from the undercooled liquid is highly sensitive to the composition and impurities and thermal history in the melt [15, 18, 26, 27]. Before mould modification, numerous unmelted crystals may exist in the melt, which can promote the nucleation and growth of the CuZr B2 phase during solidification, causing crystal aggregation and impingement [28, 29]. The liquid melt status can be effectively controlled by introducing a short neck to the larger-sized casting mould (Mould M), which would allow adjusting of the melting time, and thus changing the melt temperature. The detrimental effects of oxides and other contaminants could also be mitigated or eliminated by increasing melting time or melt temperature. In comparison with Mould B, the unmelted impurities are expected to be dissolved by elongating melting time in the Mould M. Thus, the heterogeneous nucleation of CuZr B2 crystals could be suppressed to some extent, contributing to the homogenization of the size and distribution of B2 CuZr crystals in the amorphous matrix.

4.3.3 Composition – cooling rate – microstructure relationship

As discussed, the purity of the raw materials, the casting temperature, melting time and casting mould configuration will significantly affect the size and distribution of crystals precipitated in the glass matrix of CuZr-based metallic glass composites. Therefore, the elemental metals in high purity ($\geq 99.9\%$) were from the same fabrication batch and were provided by the same supplier. In addition, manufacturing environment and processing parameters were strictly controlled to the same to guarantee the repeatability. To investigate the microstructural dependence on the minor addition and cooling rate in $\text{Cu}_{48-x}\text{Zr}_{48}\text{Al}_4\text{Sn}_x$ ($x=0.25, 0.5, 0.75, 1, 1.25, 1.5\text{at}\%$), specimens with different Sn contents and casting diameters were prepared and examined. The corresponding manufacturing conditions are given in the Appendix.

4.3.3.1 Microstructural evolution with Sn addition and cooling rate

Figure 4.10. XRD pattern of the as-cast $\text{Cu}_{48-x}\text{Zr}_{48}\text{Al}_4\text{Sn}_x$ BMG/BMGMCs prepared in different



cooling rates: (a) $\text{Cu}_{47.75}\text{Zr}_{48}\text{Al}_4\text{Sn}_{0.25}$; (b) $\text{Cu}_{47.25}\text{Zr}_{48}\text{Al}_4\text{Sn}_{0.75}$.

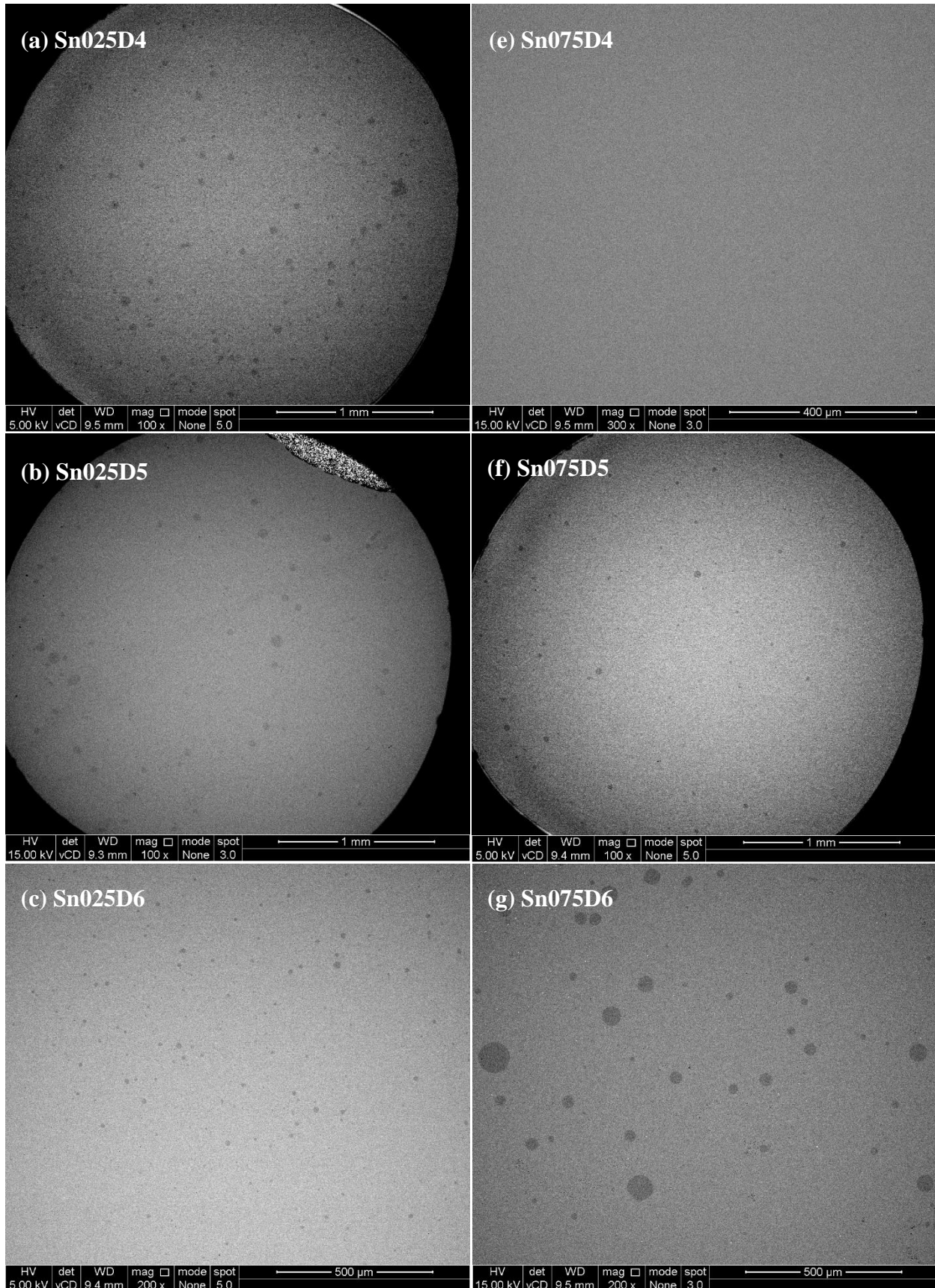
The microstructure changes significantly as Sn addition content and cooling rate changes. When the casting diameter is 3 mm for Sn addition from 0.25 at% to 1.5 at%, the corresponding XRD pattern exhibit a single broadening hump, indicating the fully amorphous nature in the as-cast cylindrical specimens. With the further reduction in cooling rate, *i.e.*, casting diameter >3 mm, the microstructure evolves differently as the Sn addition changes. Figure 4.10 shows the XRD traces of the specimens with composition of $\text{Cu}_{47.75}\text{Zr}_{48}\text{Al}_4\text{Sn}_{0.25}$ and

$\text{Cu}_{47.25}\text{Zr}_{48}\text{Al}_4\text{Sn}_{0.75}$ in various casting sizes. As the rod diameter increases to 4 mm, a sharp small crystalline peak identified as B2 CuZr phase overlapped with the amorphous hump for $\text{Cu}_{47.75}\text{Zr}_{48}\text{Al}_4\text{Sn}_{0.25}$, as shown in Figure 4.10a. The intensity of the B2-CuZr crystalline peak increased with further decrease in the cooling rate. Furthermore, no other crystalline phase was detected in $\text{Cu}_{47.75}\text{Zr}_{48}\text{Al}_4\text{Sn}_{0.25}$ alloys with the diameter up to 7 mm. Therefore, it can be demonstrated that the microstructural evolution of the CuZr-based metallic alloy in the composition of $\text{Cu}_{47.75}\text{Zr}_{48}\text{Al}_4\text{Sn}_{0.25}$ is as follows: fully amorphous \rightarrow B2 CuZr phase + amorphous matrix, as the cooling rate decreases. A similar trend was presented in the alloy with 0.5 at% Sn addition, but with different critical casting size ($d = 4$ mm) (as shown in the Appendix). However, the further increase in casting diameter to 7 mm for the metallic alloy $\text{Cu}_{47.25}\text{Zr}_{48}\text{Al}_4\text{Sn}_{0.75}$, two various trends were observed according to different casting temperatures, as illustrated in Figure 4.10b. The lower casting temperature (denoted as D7C75) leads to the formation of martensitic B19' phase, whereas only B2 CuZr phase was recognized in the samples obtained with higher casting temperature. The composite structure comprising B2 CuZr crystalline phase and the glassy matrix can be achieved even in the samples with size of 8 mm. With the further increase in Sn addition content to 1 at%, microstructural evolution with the cooling rate changes considerably (as shown in Appendix). The cooling rate reduction, *i.e.*, the increase in casting diameter to 6 mm and 7 mm, results in the formation of another two crystalline phases, which were recognized as CuZr B19' phase and Zr_5Sn_3 [30, 31]. Thus, the corresponding microstructure evolved in the following sequence: fully amorphous \rightarrow B2 CuZr phase + amorphous matrix \rightarrow B2 CuZr phase + B19' CuZr phase + Zr_5Sn_3 , as the cooling rate reduced. Nevertheless, with the size limit of the arc melter (MAM1, Edmund Bühler) equipment, microstructure changes with further reduction in cooling rate ($d \geq 8$ mm) could not be studied.

In addition, the morphology evolution of the crystalline phases, including the shape, size and distribution in the glassy matrix, with the Sn addition content and cooling rate was investigated, as demonstrated in Figure 4.11. The backscattered SEM images were taken from the central parts of the as-cast CuZr-based BMG/BMGMCs. The 0.25 at% Sn-doped alloys exhibited a composite structure with spherical B2 CuZr crystals uniformly dispersed in the amorphous matrix when cast into 4 mm cylindrical rods, which is in line with the XRD result. The size of B2 crystals is in the range of 20 – 35 μm with the volume fraction of 8.2 ± 0.6 %. Surprisingly, the spherical B2 crystalline phase still exists in the glassy matrix with no obvious increase in grain size and volume fraction as the casting size is raised up to 7 mm, as displayed

in Figure 4.11a-d. Despite uniform dispersion in the glassy matrix, the B2 crystal size and volume fraction grows as the casting size increases for the alloys with 0.75 at% Sn addition, as shown in Figure 4.11e-h. For the 0.5 at% Sn alloys, CuZr B2 phase appeared heterogeneously in the 5 mm cast rods (as shown in Appendix). The crystalline phase was prone to coalesce into patch-like shapes. The size and volume fraction of patch-like crystals further increases with decrease in the cooling rate. The same trend was observed in the 1 at% Sn-doped alloys. As the casting size increased to 6 mm and 7 mm, numerous small white crystalline phase, identified as Zr_5Sn_3 , were uniformly precipitates in the alloy. It has been reported that Zr_5Sn_3 could act as potent nucleant for the heterogeneous nucleation of CuZr B2 phase and thereby retard the rapid growth of the crystalline phase during solidification [32]. However, it was not the case for 1 at% Sn-doped alloys in the current study. During the fast cooling, a large temperature gradient will be formed, leading to composition variation in the melt, known as the “Soret effect” [33, 34]. The larger specimen size, the slower the cooling rate, the longer the thermal diffusion time, and thus the greater composition difference is in the larger specimens. It may result in the growth combination of crystalline phase.

The microstructural evolution with the Sn addition contents and the casting diameters of the as-cast $Cu_{48-x}Zr_{48}Al_4Sn_x$ ($x=0.25, 0.5, 0.75, 1, 1.25, 1.5$ at%) alloys is schematically summarized in Figure 4.12. It shows that the Sn addition can improve glass forming ability, tailor the phase formation and further facilitate the microstructure, thereby resulting in the formation of the large-sized CuZr-based BMGMCs. From a microstructural perspective, the desired composite structure with homogeneous CuZr-B2 phase distribution in the glassy matrix could be obtained with 0.25 at% and 0.75 at% Sn additions. The underlying homogenization mechanism and detailed microstructure formation for $Cu_{47.75}Zr_{48}Al_4Sn_{0.25}$ and $Cu_{47.25}Zr_{48}Al_4Sn_{0.75}$ alloys will be discussed in following sections.



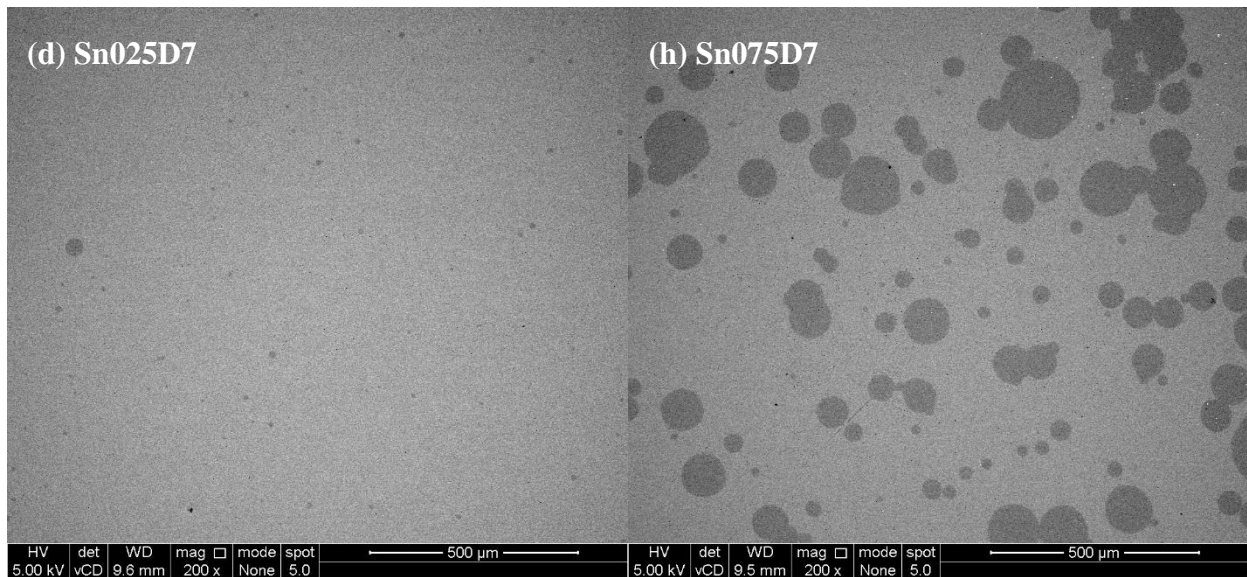


Figure 4.11. Backscattered cross-sectional SEM images of the as-cast $\text{Cu}_{48-x}\text{Zr}_{48}\text{Al}_4\text{Sn}_x$ ($x=0.25, 0.75$ at%) BMG/BMGMCs showing microstructure evolution as cooling rate and composition changes: (a-d) microstructure changes of $\text{Cu}_{47.75}\text{Zr}_{48}\text{Al}_4\text{Sn}_{0.25}$ with different casting diameters; (e-h) microstructure changes of $\text{Cu}_{47.25}\text{Zr}_{48}\text{Al}_4\text{Sn}_{0.75}$ with different casting diameters.

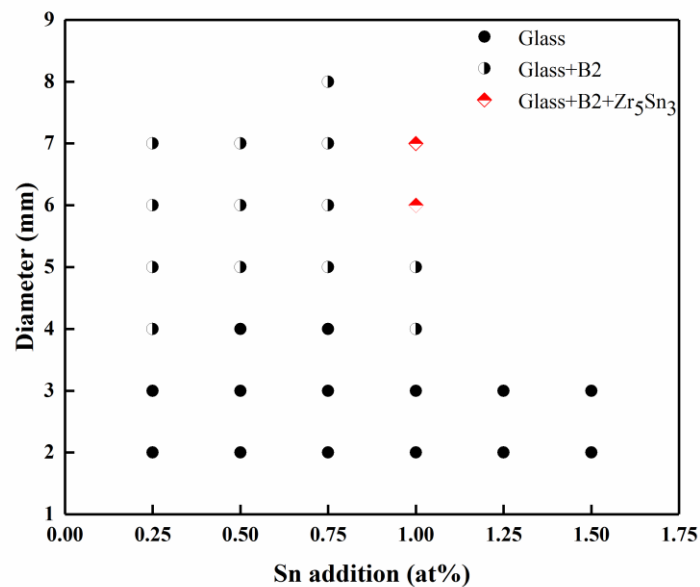


Figure 4.12. Microstructural evolution with Sn addition content and cooling rate in the as-cast $\text{Cu}_{48-x}\text{Zr}_{48}\text{Al}_4\text{Sn}_x$ ($x=0.25, 0.5, 0.75, 1, 1.25, 1.5$ at%) alloys.

4.3.3.2 Microstructure evolution in as-cast $\text{Cu}_{47.75}\text{Zr}_{48}\text{Al}_4\text{Sn}_{0.25}$ BMGMCs

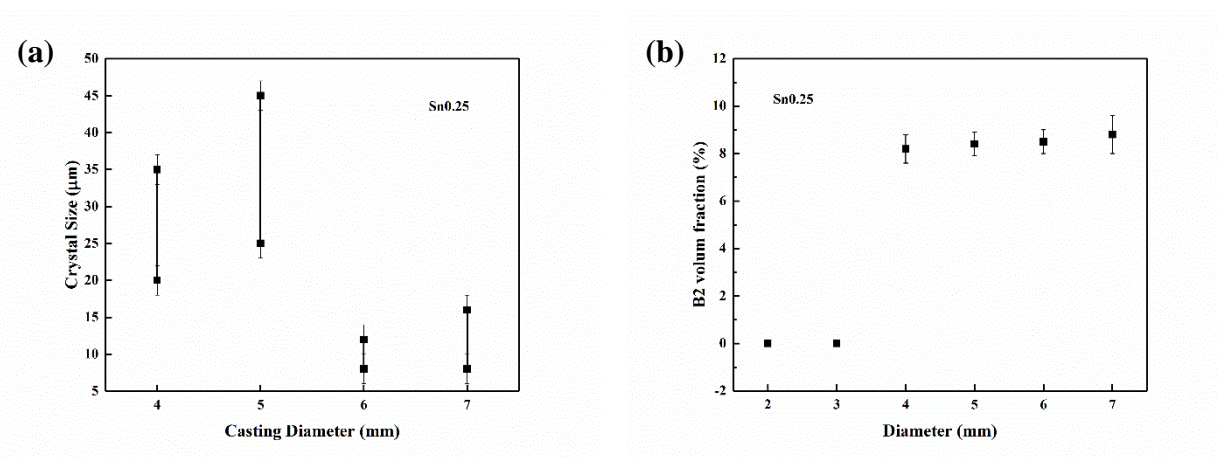


Figure 4.13. (a) The relationship between casting size and crystalline phase volume fraction; (b) Crystal size distribution in glassy matrix in $\text{Cu}_{47.75}\text{Zr}_{48}\text{Al}_4\text{Sn}_{0.25}$ with different sizes.

The increase in the casting rod diameter to 4 mm and above (*i.e.* the reduction in cooling rate) will result in the formation of CuZr crystalline phase reinforced glass matrix composites. As shown in the SEM images, microscale crystals were embedded uniformly in the amorphous matrix. Figure 4.13a shows size distribution of crystal particles in $\text{Cu}_{47.75}\text{Zr}_{48}\text{Al}_4\text{Sn}_{0.25}$ BMGMCs with different sizes. The statistics were obtained from the measurements of 100 particles for each size. The crystal size were mainly in the range of 20 – 40 μm for 4 mm and 5 mm rods, and in the range of 10 – 20 μm for 6 mm and 7 mm rods. The crystal growth was suppressed to some extent. In addition, the crystalline volume fractions are maintained around 9 vol% despite the difference in cooling rates. Thus, there existed more nucleation sites in the larger samples comparing with the smaller ones.

According to the classic solidification theory, nucleation and crystal growth are in a competitive relationship during the process [35, 36]. The driving force for both processes are from the energy, composition and structural fluctuations in the melt. With the increase in casting rod size, the number of the crystal particles increases without obvious growth, indicating less driving force for grain growth in $\text{Cu}_{47.75}\text{Zr}_{48}\text{Al}_4\text{Sn}_{0.25}$ alloys. An equation has been deduced to predict the grain size during solidification [37]:

$$d = \left(\frac{U}{\Gamma}\right)^{\frac{1}{4}} \quad (\text{Equation 4.1})$$

where U is the growth rate, I denotes the nucleation rate and d is the mean crystal size. Therefore, the crystalline grain size will decrease with the increase in nucleation rate at a given crystal growth rate. Furthermore, it has been shown that in any metallic system the maximum in the nucleation rate can be expected to be at lower temperatures than the maximum in the growth rate [36, 38]. Thus, it can be assumed that higher nucleation rate has been reached in larger samples. On the other hand, the heat of mixing between Zr and Sn is largely negative ($Zr-Sn = -43\text{kJ/mol}$), while that between Cu and Sn ($Cu-Sn = +7\text{ kJ/mol}$), between Al and Sn ($Al-Sn = +4\text{ kJ/mol}$) are positive [39]. It will result in the formation of copious Zr-Sn clusters in the supercooled melt with minor Sn addition, acting as nucleation sites for the crystallization.

Figure 4.14. TEM images of (a) glassy matrix and (b) CuZr B2 crystalline phase in the as-cast $Cu_{47.75}Zr_{48}Al_4Sn_{0.25}$ BMGMCs in diameter of 7 mm; insets are corresponding SAED patterns.

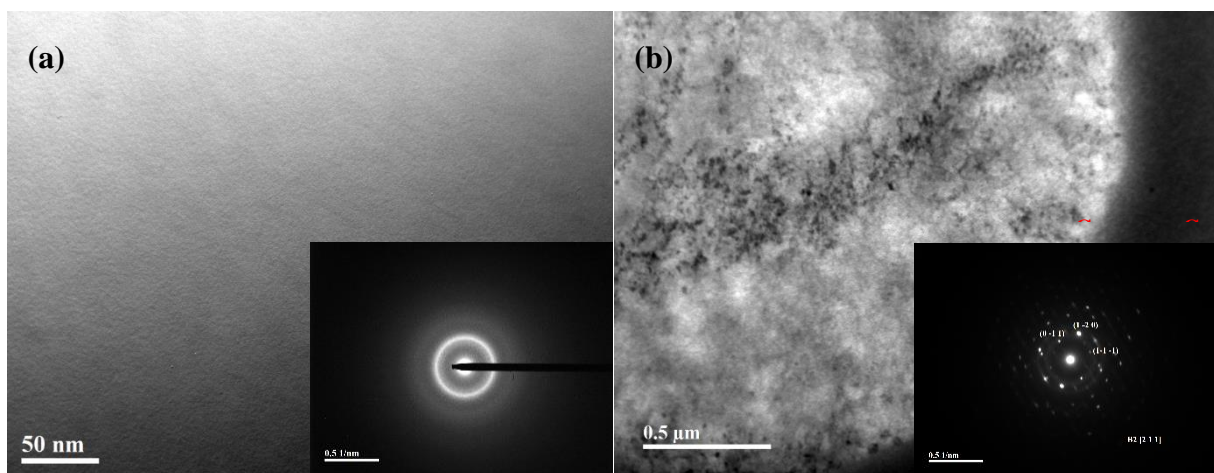
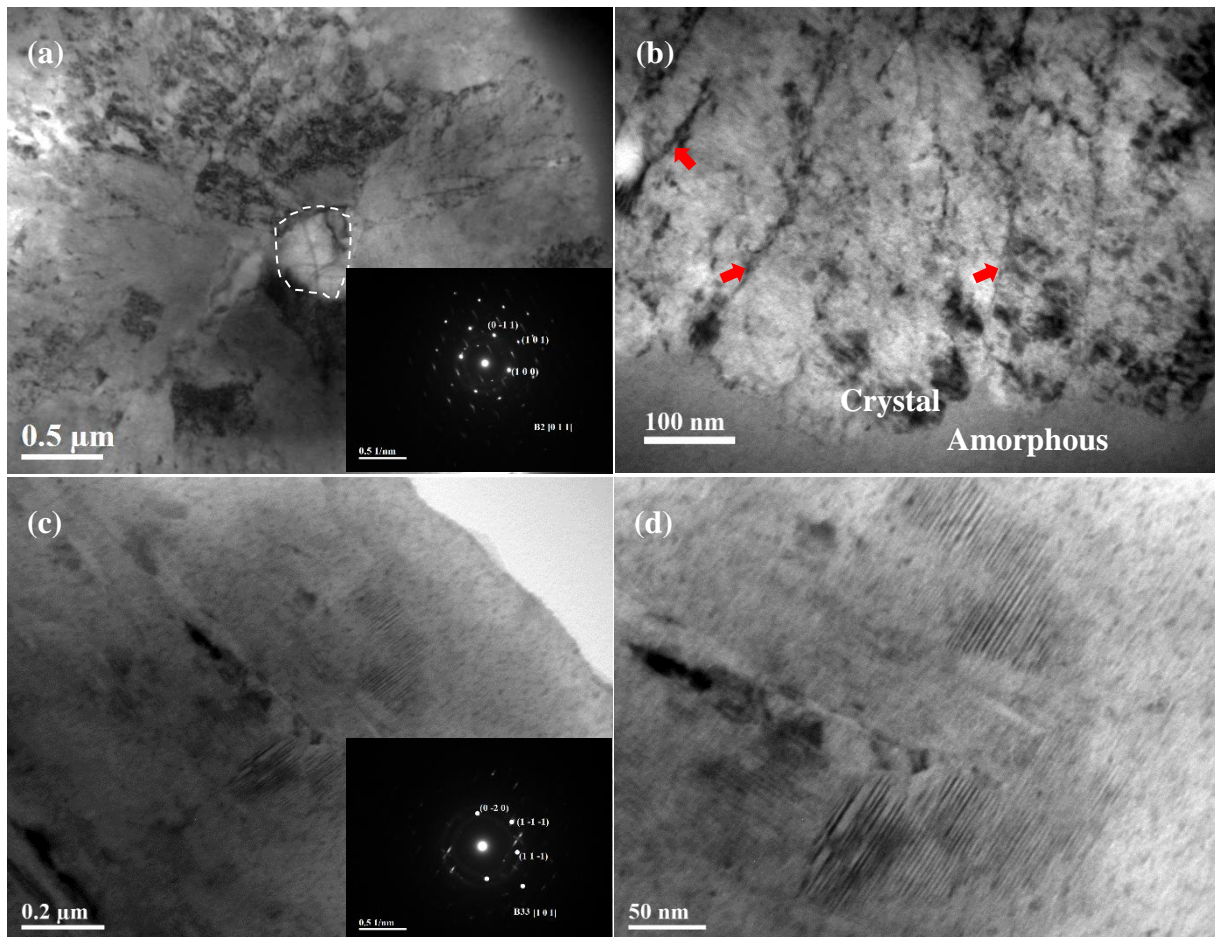


Figure 4.14 shows typical TEM images of the amorphous matrix and CuZr B2 particles in the as-cast $Cu_{47.75}Zr_{48}Al_4Sn_{0.25}$ BMGMCs. No nanoscale crystalline phase was observed in the glassy matrix. It was confirmed by the SAED pattern, a diffuse ring typical of amorphous structure, in the inset of Figure 4.14a. As mentioned before, the size of CuZr crystalline phase in 0.25 at% Sn doped alloys ranges from 10 to 50 μm . The B2 structure of the crystalline phase is identified by the corresponding electron diffraction pattern shown in the inset of Figure 4.14b. Occasionally, B33 phase was observed in vicinity of the interface (not shown here). It may be induced by the thermal stress concentration during rapid solidification.

Therefore, it is speculated that the addition of minor Sn (0.25 at%) causes local compositional fluctuation in the melt, further leading to the formation of the atomic cluster. It is supposed to account for the homogenization of crystal size and its distribution in the amorphous matrix in $Cu_{47.75}Zr_{48}Al_4Sn_{0.25}$ BMGMCs.

4.3.3.3 Microstructure evolution in as-cast $\text{Cu}_{47.25}\text{Zr}_{48}\text{Al}_4\text{Sn}_{0.75}$ BMGMCs during solidification

Figure 4.15. TEM images showing the microstructure of the as-cast $\text{Cu}_{47.25}\text{Zr}_{48}\text{Al}_4\text{Sn}_{0.75}$



BMGMCs in 6 mm diameter: (a) crystalline phase in low magnification; (b) the interface between crystals and glassy matrix; (c) strip-substructure near interface in low magnification; (d) strip-substructure near interface in high magnification: Insets are corresponding SAED patterns.

Figure 4.15 displays the typical bright field TEM images showing the microstructure of an as-cast $\text{Cu}_{47.25}\text{Zr}_{48}\text{Al}_4\text{Sn}_{0.75}$ BMGMCs rod in the diameter of 6 mm. A spherical crystalline grain was embedded in the featureless glassy matrix. The crystalline phase was identified as austenitic B2-CuZr phase, as shown in Figure 4.15a. It presented a structure with a core (denoted by white dashed circle) surrounded by columnar grains (Figure 4.15b), which is similar to a characteristic casting ingot structure. Therefore, the solidification process during

rapid suction casting was suggested as follows. The corresponding schematic illustration of solidification mechanism is as shown in Figure 4.16.

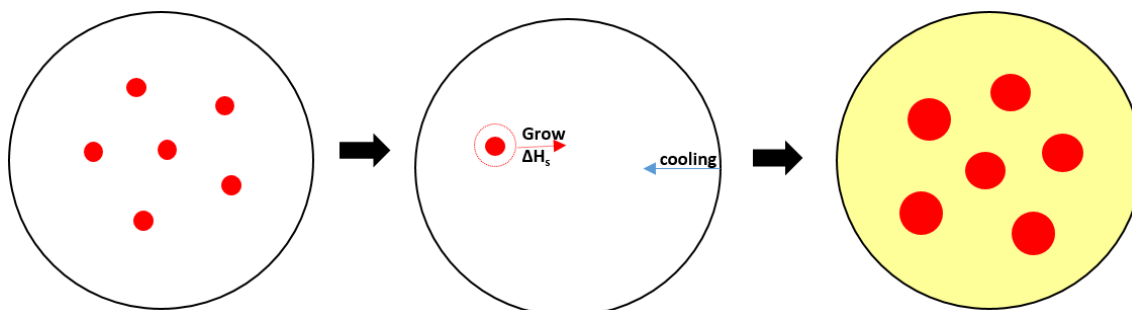


Figure 4.16. The schematic illustration of the solidification mechanism of $\text{Cu}_{47.25}\text{Zr}_{48}\text{Al}_4\text{Sn}_{0.75}$ BMGMCs.

First of all, it should be clarified that no line compound Zr_5Sn_3 was observed in 0.75 at% Sn doped CuZr BMGMCs. It has been reported that the formation of the line compound Zr_5Sn_3 will facilitate the crystallization by acting as potent nucleant for the heterogeneous nucleation of the metallic glass composites with 0.75 at% Sn addition [32], which is not applicable to the current alloys. However, the heat of mixing between Zr and Sn is largely negative with the value of -43 kJ/mol, while that between Sn and Cu is positive with the value of $+7$ kJ/mol [39]. It suggests that Zr has a strong affinity with Sn, thus leading to the formation of copious Zr-Sn based structural ordering clusters in the melt. In addition, no crystals were observed in the regions close to the casting mould surface. As reported local structural clusters may exist in the melt during low temperature casting [40]. Thus, it is reasonable to assume that the melt was in the same undercooling condition in the initial solidification stage, and the Zr-Sn structural ordering clusters were formed and dispersed homogeneously in the melt. These structural orderings will grow into nucleants upon cooling. The heat extraction direction during the growth of the nucleants was radially outwards. Therefore, the temperature around the nucleants is higher than that of the surrounding melt. It indicates the undercooling increases radially from the nucleant core to the surrounding melt, resulting in the radial growth. Furthermore, the cooling direction is opposite to the growth direction, leading to the columnar grain formation. It is known that CuZr B2 phase crystallizes polymorphically from the melt, thus, the constitutional supercooling in front of the interface is negligible. The cooling rate is larger than heat extraction rate during the rapid cooling, leading to the reduction in the supercooling

in front of the interface as the solidification proceeds. Once there is no supercooling, the crystal growth will stop. The remaining liquid will solidify into amorphous phase.

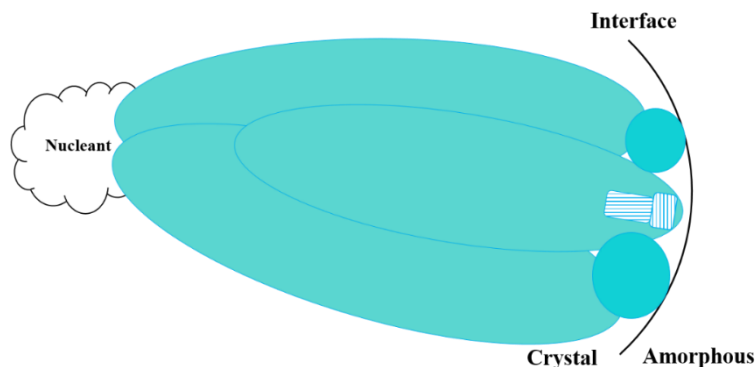
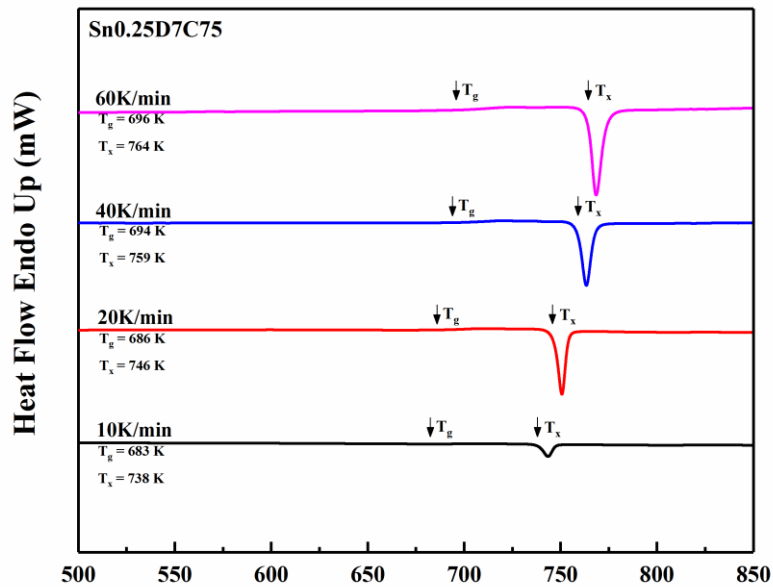


Figure 4.17. The schematic illustration of the substructures in vicinity of interface between crystals and amorphous matrix in $\text{Cu}_{47.25}\text{Zr}_{48}\text{Al}_4\text{Sn}_{0.75}$ BMGMCs.

TEM images have revealed more details of the B2-CuZr particles (Figure 4.15c and d). Some nanoscale strip-like features, close to the interface between crystal and glass matrix, intersect each other. They were confirmed to be B33 martensitic phase by the SAED in the inset of Figure 4.15c. This is the first time that a martensitic structure has been observed in as-cast CuZr-based metallic glass composites. It may be caused by the thermal stress concentration during rapid solidification [41, 42] or by introducing minor Sn alloying addition. On the basis of the structural details in TEM images and suggested solidification process, the crystalline structure is schematically illustrated in Figure 4.17. The crystalline core was surrounded by the columnar grains with nanoscale strip martensitic structure in vicinity of the interface. Wu *et al.* have found that microalloying can tailor the deformation twinning potency by altering the stacking fault energy (SFE), thereby improving the mechanical properties [43, 44]. The nanoscale martensitic structure may act as nucleation sites to promote martensitic transformation, resulting in the improved mechanical properties of the current CuZr-based BMGMCs. Nevertheless, the roles of the existing martensitic structure need further studies and in-depth analysis.

4.3.4 Crystallization kinetics of 0.25 at% and 0.75 at% Sn-doped CuZr-based BMGMCs

(a)



(b)

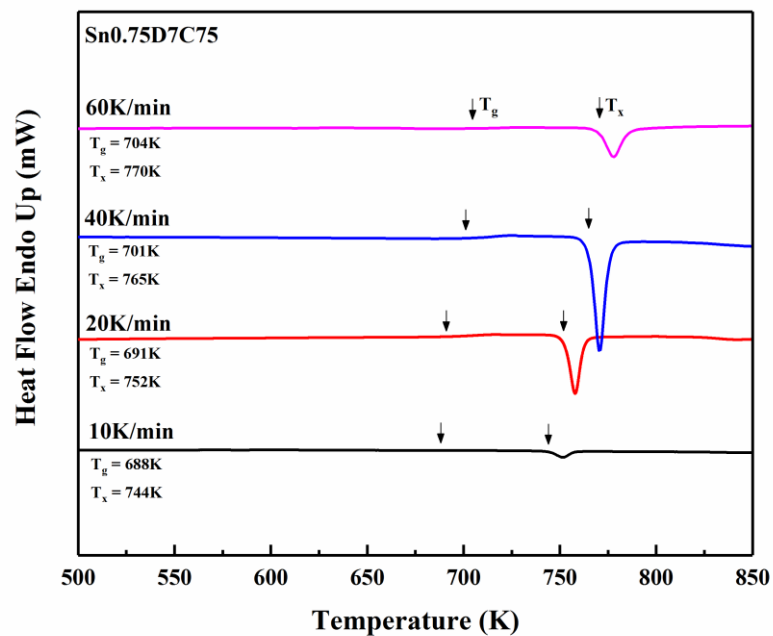


Figure 4.18. Continuous DSC curves of the as-cast CuZr-based BMG alloys in the diameter of 7 mm: (a) Cu_{47.75}Zr₄₈Al₄Sn_{0.25}, (b) Cu_{47.25}Zr₄₈Al₄Sn_{0.75}.

Figure 4.18 shows the non-isothermal DSC curves of the as-cast 7 mm CuZr-based alloys with the composition of $\text{Cu}_{47.75}\text{Zr}_{48}\text{Al}_4\text{Sn}_{0.25}$ and $\text{Cu}_{47.25}\text{Zr}_{48}\text{Al}_4\text{Sn}_{0.75}$ obtained at various heating rates of 10, 20, 40 and 60 K/min. They all exhibit an exothermic event following the glass transition process. Characteristic temperatures, *i.e.* T_g (glass transition temperature), T_x (onset crystallization temperature) and T_p (peak crystallization temperature), tend to shift to higher temperatures with increasing heating rate, indicating the dependence on the heating rate during continuous heating process. As Sn addition increases from 0.25 at% to 0.75 at%, T_g , T_x and T_p increases correspondingly at the same heating rate. However, the supercooled liquid region ΔT_x changes from 60 K for 0.25 at% Sn-doped alloys to 61 K for 0.75 at% Sn-doped alloys, implying that the thermal stability of the supercooled liquid for these two alloys is almost the same.

The activation energy corresponding to the glass transition and crystallization process under continuous heating condition can be evaluated by the Kissinger equation [45, 46]:

$$\ln\left(\frac{\beta}{T^2}\right) = -\frac{E}{RT} + C \quad (\text{Equation 4.2})$$

where β is the heating rate, R is the gas constant (8.314 J/mol), T is the characteristic temperature (T_g , T_x , and T_p) at the certain heating rate, E is the apparent activation energy for the corresponding process. E_g is the activation energy for glass transition, E_x is the activation energy for the onset crystallization and E_p is the energy for peak crystallization.

The Kissinger plots for $\text{Cu}_{47.75}\text{Zr}_{48}\text{Al}_4\text{Sn}_{0.25}$ and $\text{Cu}_{47.25}\text{Zr}_{48}\text{Al}_4\text{Sn}_{0.75}$ alloys for a diameter of 7 mm are shown in Figure 4.19a and b. By the linear fitting method, the corresponding activation energy are calculated to be 479.4 ± 8.0 kJ/mol (E_g), 296.9 ± 2.5 kJ/mol (E_x), 315.9 ± 3.0 kJ/mol (E_p) for $\text{Cu}_{47.75}\text{Zr}_{48}\text{Al}_4\text{Sn}_{0.25}$, and 391.3 ± 7.5 kJ/mol (E_g), 301.7 ± 2.6 kJ/mol (E_x), 306.5 ± 4.0 kJ/mol (E_p) for $\text{Cu}_{47.25}\text{Zr}_{48}\text{Al}_4\text{Sn}_{0.75}$, respectively. Glass transition cooling is the result of the slowdown of the internal relaxation of the supercooled liquid. The viscosity of the melt increases and thereby aggravating crystallization. To some extent, glass formation depends on the competition between the supercooled liquid and the formation of crystals. For both alloys, the value of E_g is the largest, then is E_p , and the last is E_x . It indicates that grain growth process is more difficult than the nucleation process [47, 48] for both alloys. Therefore, it is rationalized that the formation of large-sized cylindrical rods with well separated and uniformly distributed crystals in glassy matrix can be achieved for these two compositions. CuZr BMG alloys with 0.25 at% Sn possess a much higher E_g comparing with that of 0.75 at% Sn-doped alloys, suggesting that more energy is needed to restructure atomic configuration in

the glass transition process. Thus, supercooled liquid for the former alloy is more stable and resistant to crystallization. During crystallization, 0.75 at% Sn alloy exhibits larger E_x , yet less E_p in comparison with the alloys containing 0.25 at% Sn. The onset crystallization temperature corresponds to the nucleation process, and the peak crystallization temperature relates to the growth process. Accordingly, E_x and E_p represents the activation energy for nucleation and growth, respectively [49]. It is known that crystallization includes nucleation and grain growth processes. Consequently, there is a lower energy barrier to overcome to initiate the nucleation process and more energy is required for further growth for 0.25 at% Sn alloys. This is in line with the microstructural evolution with the decreasing cooling rate for $\text{Cu}_{47.75}\text{Zr}_{48}\text{Al}_4\text{Sn}_{0.25}$ alloys, *i.e.*, the precipitation of 10-20 μm CuZr B2 crystals in the as-cast rod from 4 mm to 7 mm. However, the crystalline phase forms in the amorphous matrix when the rod size is up to 5 mm and the crystal size increases as the rod diameter increases for $\text{Cu}_{47.25}\text{Zr}_{48}\text{Al}_4\text{Sn}_{0.75}$ alloys.

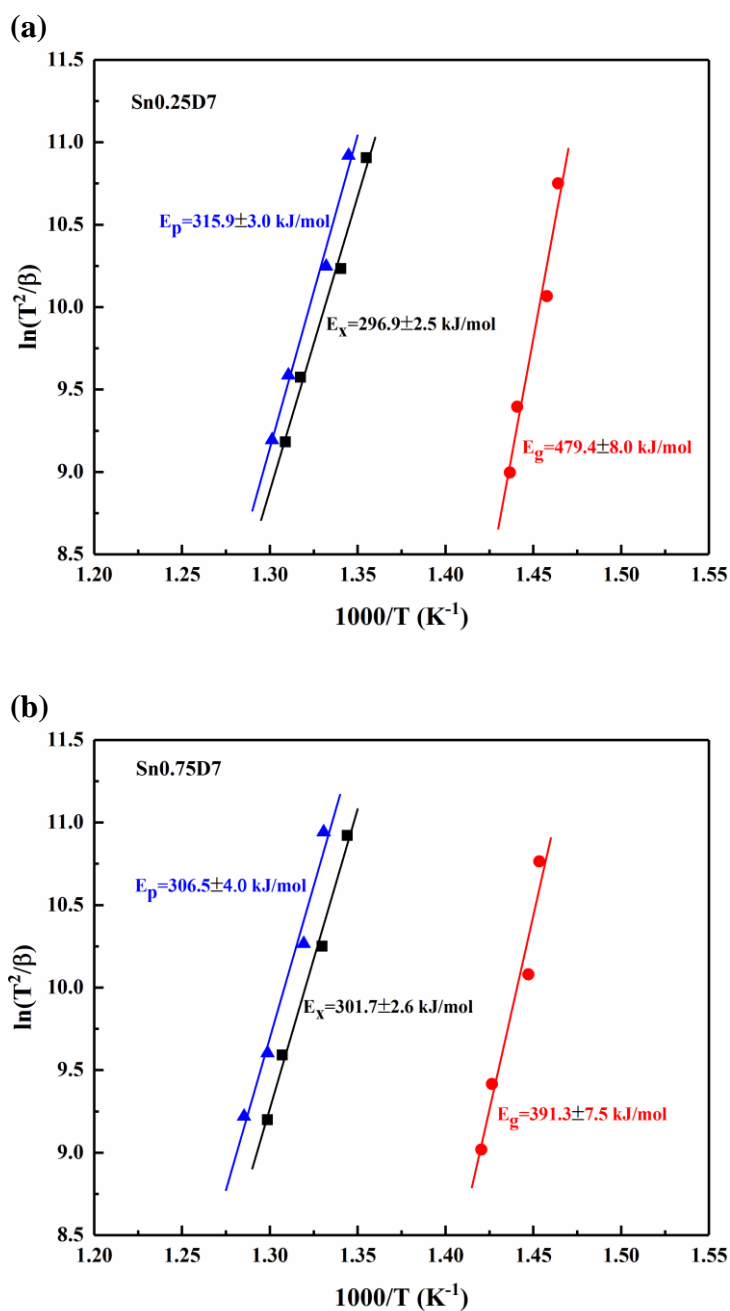


Figure 4.19. Kissinger plots based on the continuous DSC measurements at different heating rates for the as-cast alloys with a diameter of 7 mm: (a) $\text{Cu}_{47.75}\text{Zr}_{48}\text{Al}_4\text{Sn}_{0.25}$ BMGMCs, (b) $\text{Cu}_{47.25}\text{Zr}_{48}\text{Al}_4\text{Sn}_{0.75}$ BMGMCs.

4.3.5 Mechanical properties

4.3.5.1 Compression properties

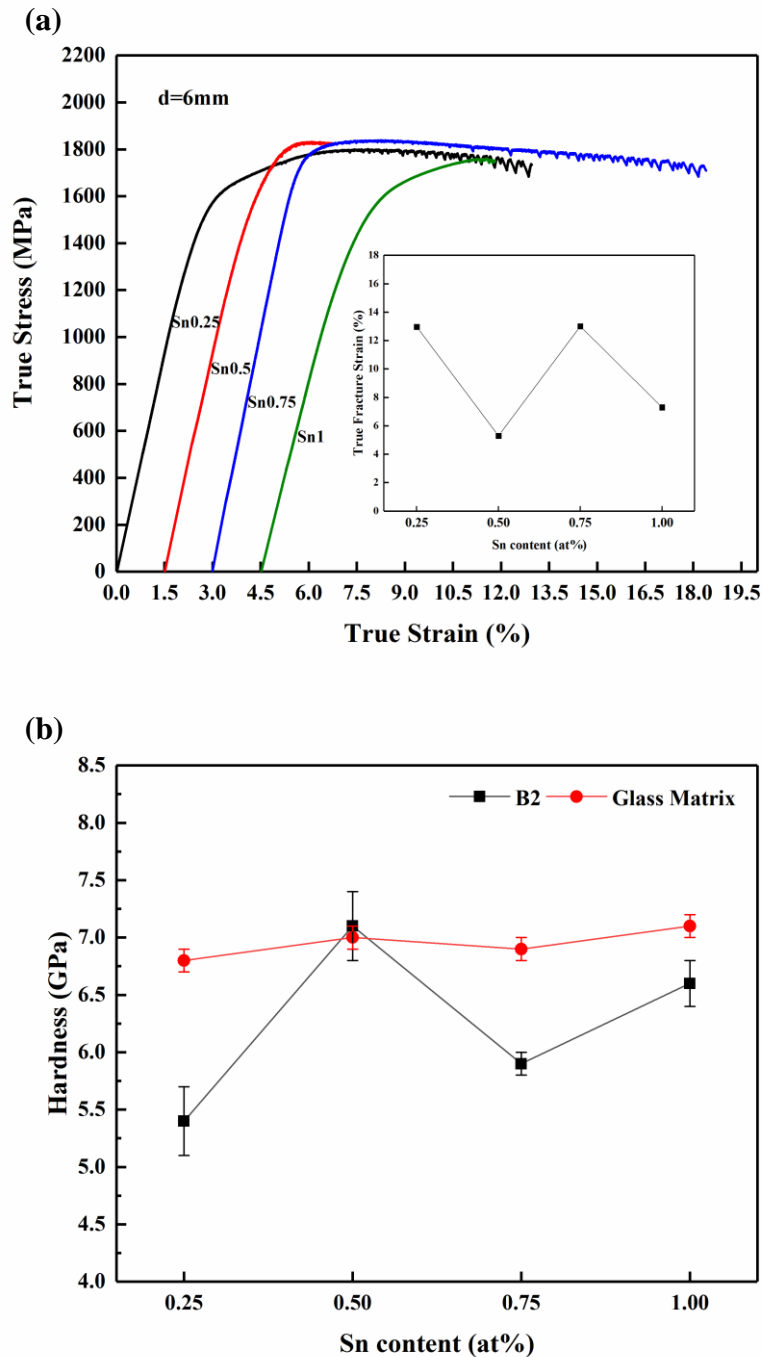


Figure 4.20. (a) True compressive stress strain curves for the 6 mm rod specimens with different Sn contents, the inset is relationship between Sn contents and true fracture strain; (b) The relationship between the microhardness of the crystalline phase/glass matrix and Sn content.

The compression properties of the current Sn-doped CuZr-based BMGMCs with different casting diameters were systematically investigated in detail. The relationship between plasticity and composition will be given as follows. As an example, Figure 4.20a shows the compressive true stress strain curves of CuZr-based BMG composites doped with various Sn contents with a diameter of 6 mm. They plastically deformed in a different manner, which strongly depended on their microstructures. The 0.25 at% Sn samples exhibit excellent work-hardening ability and plasticity. After yielding at 1413 ± 30 MPa, the specimen showed work-hardening up to a maximum compressive strength of 1800 ± 30 MPa, and then gradually reduced with further increase in strain until final fracture at the strength of 1734 ± 30 MPa. The total plastic strain was $13 \pm 1.2\%$, which was attributed to the homogeneous crystal particle size and distribution in the glassy matrix. The samples with 0.75 at% Sn plastically deformed in a similar way, but no work hardening was observed. The compressive stress increased up to 1838 ± 6 MPa at a strain of $5.3 \pm 0.4\%$ after yielding at 1612 ± 45 MPa, then decreased to the fracture strength of 1710 ± 41 MPa at $15.4 \pm 2.0\%$. However, samples with 0.5 at% Sn and 1 at% Sn addition exhibited lower yielding points and limited plasticity even though both of them contained B2-CuZr phase with $11.9 \pm 2.1\text{vol}\%$ and $29.9 \pm 5.6\text{vol}\%$, respectively. The trend in plasticity with Sn content was clearly shown in the inset of Figure 4.20a. Therefore, the size and distribution of the crystal particles in the amorphous matrix will determine the mechanical performance of the alloys to a great extent in comparison with the crystalline volume fraction. It agrees well with the findings in the literature [50, 51].

In addition, the elastic mismatch between crystalline phase and glassy matrix will influence the interactions between two phases, thus determining the materials response to the deformation. The hardness variations of the spherical crystals and amorphous matrix for the as-cast CuZr metallic glass composites with different Sn additions were measured with nanoindentation, as illustrated in Figure 4.20b. The hardness for the amorphous phase was around 7 GPa, while that for crystalline phase varied wildly as Sn content increased from 0.25 to 1 at%. As a result, the hardness difference between crystalline and glassy phases changes considerably with a change in the Sn content. The largest disparity with the value of 1.4 GPa is in the samples with 0.25 at% Sn, followed by 1.0 GPa in the samples with 0.75 at% Sn, then 0.5 GPa in those with 1 at% Sn, and the last is in the samples with 0.5 at% Sn. This agrees well with the corresponding mechanical performances.

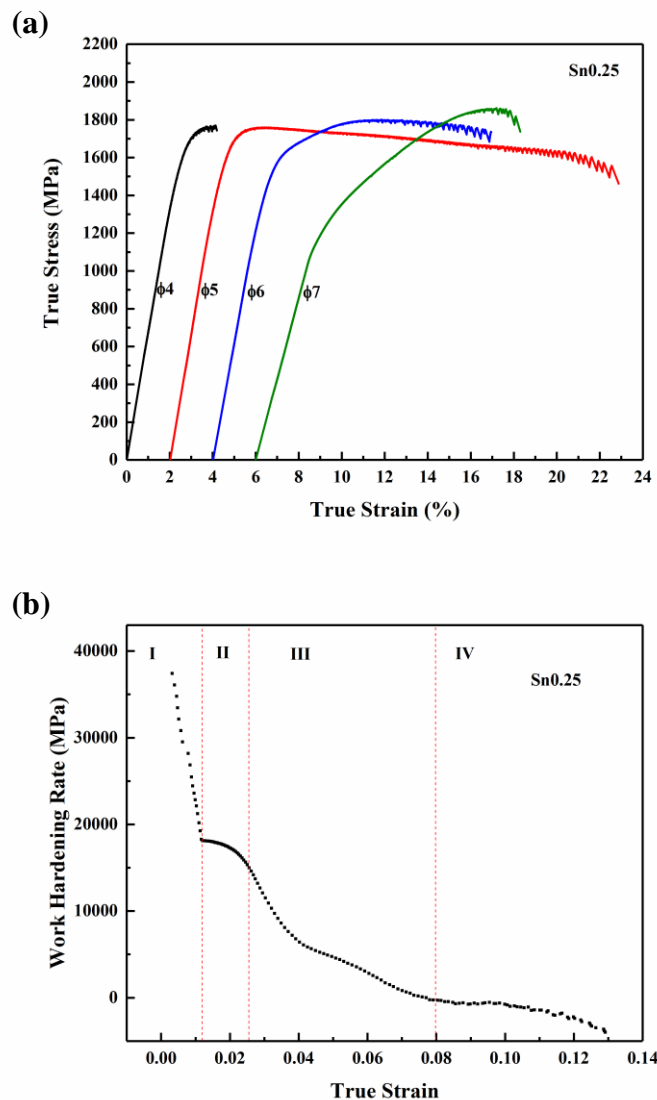


Figure 4.21. (a) True compressive stress strain curves of the as-cast $\text{Cu}_{47.75}\text{Zr}_{48}\text{Al}_4\text{Sn}_{0.25}$ BMGMCs with various casting diameters; (b) A representative work-hardening rate vs. true strain curve for the as-cast $\text{Cu}_{47.75}\text{Zr}_{48}\text{Al}_4\text{Sn}_{0.25}$ BMGMCs in the diameter of 6 mm.

CuZr-based BMG composite specimens with different Sn addition plastically deformed in a similar manner upon compression when the cast diameter was below 7 mm, among which samples with 0.25 at% Sn exhibited the largest plasticity, followed by those with 0.75at% Sn, then those with 1 at% Sn addition and the last was with 0.5 at% Sn addition. When the size was increased to 7 mm, specimens with 0.5 at% and 1 at% Sn addition yielded at lower strength due to the coalescence of the crystalline phase. The corresponding compressive properties are

summarized in the Appendix. The mechanical deformation behaviour for the as-cast $\text{Cu}_{47.75}\text{Zr}_{48}\text{Al}_4\text{Sn}_{0.25}$ BMG composites will be discussed in detail as follows.

Table 4.4. Plastic properties in compression of as-cast $\text{Cu}_{47.75}\text{Zr}_{48}\text{Al}_4\text{Sn}_{0.25}$ BMGMCs.

Diameter (mm)	σ_Y (MPa)	σ_m (MPa)	ε_m (%)	ε_f (%)
4	1361 ± 17	1763 ± 17	3.7 ± 0.8	4.5 ± 2.2
5	1419 ± 6	1753 ± 17	3.8 ± 0.2	20.8 ± 2.3
6	1413 ± 30	1800 ± 30	7.9 ± 0.8	13 ± 1.2
7	1100 ± 25	1855 ± 25	10.5 ± 0.8	12.3 ± 1.1

Note: σ_Y – yield strength; σ_m – maximum strength;

ε_m – the strain at maximum strength; ε_f – fracture strain.

The representative true compressive stress strain curves of the as-cast $\text{Cu}_{47.75}\text{Zr}_{48}\text{Al}_4\text{Sn}_{0.25}$ BMG composites for various diameters are displayed in Figure 4.21a. The characteristic deformation properties are summarized in Table 4.4. The measured values fluctuated in a range due to the imperfect flatness and parallelism of the surfaces. All samples exhibited distinct work hardening ability in spite of varying plasticity. It probably resulted from the discrepancy in the crystal particle size range and distribution in the glassy matrix. To quantify the work hardening behaviour and further understand the role of the crystalline phase during deformation, the work hardening rate – true strain curves for the specimens were calculated. Figure 4.21b shows a characteristic work hardening rate – true strain curve for the samples in 6 mm diameter as an example. It could be divided into four stages on the basic of the work hardening rate change. Firstly, in the stage I, the work hardening rate drops drastically, and the applied stress reaches ~ 720 MPa; then in the stage II, the decline in work hardening rate slows down and reaches a “plateau” right after the yield point ~ 1450 MPa; next in the stage III, the work hardening rate gradually reduces to zero, where the maximum stress is reached ~ 1800 MPa; and lastly, in stage IV, the work hardening rate becomes negative, where stress drops slowly till fracture.

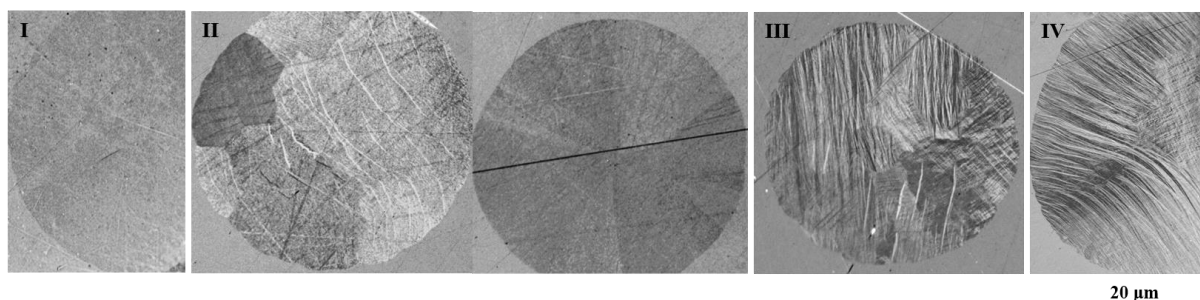


Figure 4.22. Polarized light optical microscope images showing microstructure evolution of the spherical crystalline phase corresponding to the different deformation stages – I, II, III, IV.

Figure 4.22 displays microstructure evolution of the embedded spherical crystalline phase during compressive deformation process. It should be pointed out that stage I and II are corresponding to the elastic deformation of the as-cast glassy composites. In the initial deformation process, *i.e.* stage I, both crystalline phase and glassy matrix elastically deformed without transferring load. No obvious structural changes were observed in the crystalline sphere (Figure 4.22 I).

As the applied stress increases to ~ 720 MPa, corresponding to stage II, strain-induced martensitic phase transformation, from B2 to B19', or slip in crystalline grains, may be actuated. As is well known, the yield strength and Young's modulus of CuZr-based BMGMCs is strongly affected by the volume fraction of the constituent crystalline and amorphous phases [42]. *In-situ* diffraction study of the plastic deformation proved that martensitic transformation can be triggered at an applied stress lower than macroscopic yielding [52, 53]. Some bright strips were observed in some crystalline grains (Figure 4.22 II), confirming the occurrence of phase transformation or slips in the macroscopic elastic stage. Furthermore, bright-dark contrast in spherical grains indicates different crystalline orientations. The applied stress resulted in the preferred selection of grain orientation in the parent B2 phase as well as favourable orientation for martensitic phase transformation [54, 55]. As a result, the surrounding amorphous phase suffered from higher stress than others. In addition, nanoindentation measurement (Figure 4.23) indicated that amorphous phase was more rigid compared to the crystalline phase before deformation. Thus, it is speculated that glassy matrix carried more load, finally approaching to its limit at ~ 1450 MPa, where shear bands initiated in the glassy matrix and the metallic glass composites entered into the macroscopic plastic region. During stage II, B2 phase plastically deformed, martensitic phase transformation initiated and shear bands were triggered in the

amorphous matrix as well. Therefore, work hardening rate in this stage decreased slowly and entered a plateau.

In stage III, the reduction in work hardening rate slightly speeds up at the beginning and then slows down as the applied stress reaches ~ 1695 MPa. In the early process, shear band initiation in the glassy matrix was dominant due to the heterogeneous stress concentration distribution, leading to rapid decline in work hardening rate. As the applied stress increased, more orientations were activated for phase transformation (Figure 4.22 III). Meanwhile, the propagation of the shear bands was hindered by the untransformed or transforming B2 crystals and the formed B19' crystals, resulting in the multiplication of shear bands in turn. Moreover, dislocations and twinning in the distributed crystalline phase may contribute to work hardening. The interactions between them may account for the stable and homogeneous plastic deformation in this stage [55].

In stage IV, the work hardening rate approached zero and eventually turns negative. As the applied stress increases, the ability of phase transformation for distributed crystalline phase tends to saturate. As evidenced in Figure 4.22 IV, crystalline phase deformed intensely. It is anticipated that the rigid untransformed B2 and formed B19' crystals will hinder the propagation of shear bands in the amorphous matrix in a significant degree until the specimen fractures, where the glassy matrix has lost its strain accommodation capability. Thus, the work hardening rate tends to zero. The TEM study in microstructural evolution for embedded crystalline phase and amorphous phase upon deformation is a subject of further work.

4.3.5.2 Phase transformation and deformation mechanism

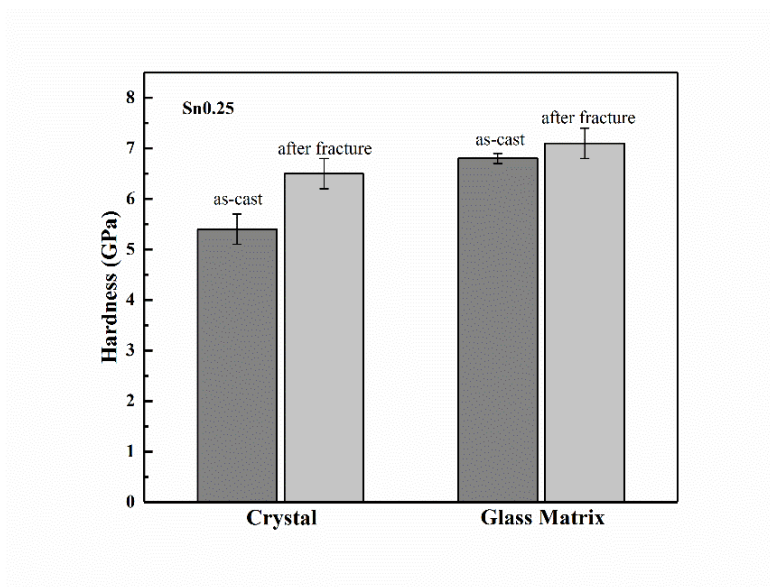


Figure 4.23. Microhardness of the crystalline phase and amorphous matrix in the as-cast and after fractured $\text{Cu}_{47.75}\text{Zr}_{48}\text{Al}_4\text{Sn}_{0.25}$ samples with diameter of 7 mm.

The prominent mechanical performance of shape memory BMGMCs has been attributed to the martensitic transformation of the in situ formed B2 CuZr phase during deformation. In the present study, the interactions between embedded crystalline phase and amorphous matrix, between transforming/transformed crystals and amorphous matrix during different deformation stages were described in the light of crystalline microstructure changes upon deformation process. Figure 4.23 compares the microhardness of the crystalline spheres and surrounding amorphous phase for the as-cast and fractured specimens. It is evident that spherical crystalline phase is softer than the amorphous matrix in the as-cast $\text{Cu}_{47.75}\text{Zr}_{48}\text{Al}_4\text{Sn}_{0.25}$ samples. Thus, in the initial deformation stage, the glassy matrix will bear additional stress and the embedded crystalline spheres will suffer from high hydrostatic compressive stress. As the deformation proceeds, spherical crystalline phase turns to deform plastically and stress concentration in vicinity of interface accumulates. As illustrated in Figure 4.23, microhardness for crystals increases from 5.4 ± 0.3 GPa in the as-cast state to 6.5 ± 0.3 GPa after fracture, and that for glassy matrix slightly increases from 6.8 ± 0.1 GPa to 7.1 ± 0.3 GPa after fracture. The discrepancy in hardness for two phases is 1.4 ± 0.2 GPa in the as-cast state, and changes to 0.6 ± 0.1 GPa after fracture. It is evident that phase transformation in crystalline phase may occur during deformation. It is well known that amorphous phase will be softened after deformation

due to the extensive shear band formation [9]. However, the amorphous phase becomes harder after deformation for the current $\text{Cu}_{47.75}\text{Zr}_{48}\text{Al}_4\text{Sn}_{0.25}$ BMGMCs.

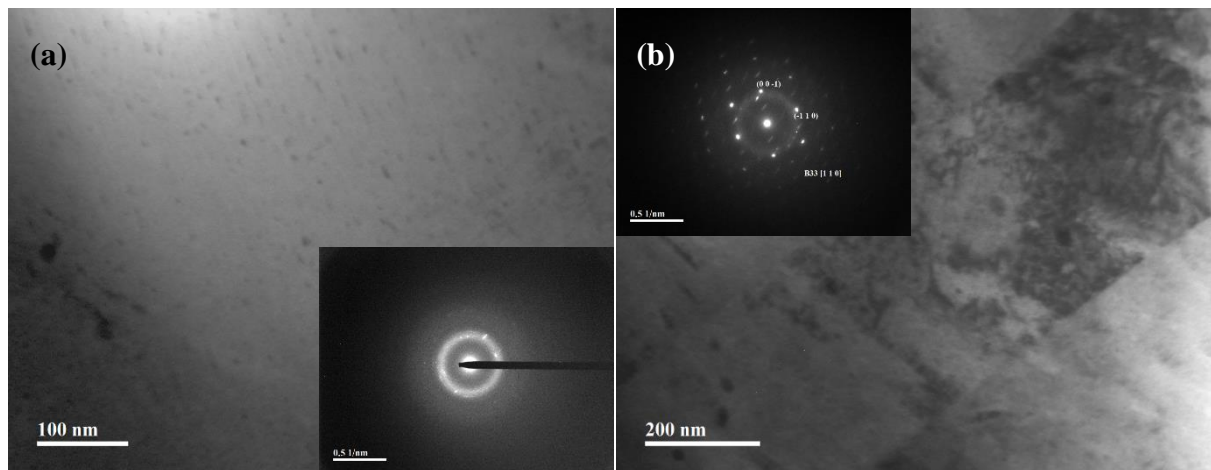


Figure 4.24. Bright field TEM images of the fractured $\text{Cu}_{47.75}\text{Zr}_{48}\text{Al}_4\text{Sn}_{0.25}$ samples with diameter of 7 mm: the insets are corresponding SAED patterns.

To further understand the materials responses to the applied loading from a microstructural perspective, bright field TEM was carried out for $\text{Cu}_{47.75}\text{Zr}_{48}\text{Al}_4\text{Sn}_{0.25}$ samples with the diameter of 7 mm in the as-cast (Figure 4.14) and after fractured states (Figure 4.24). Figure 4.24b shows the morphology of the crystalline phase after deformation, and it can be identified as the monoclinic martensitic phase, further verifying the occurrence of the martensitic transformation. In comparison with amorphous phase in as-cast samples, some nano-sized particles precipitated in the glassy matrix (Figure 4.24a). The inset in Figure 4.24a shows a selected area electron diffraction pattern of the whole area. It displays a diffuse halo ring with some spots inside, implying the formation of nanoscaled crystals in the amorphous phase. They are in the size of 10 – 30 nm. No high resolution TEM images and corresponding fast Fourier transformation (FFT) images were obtained yet, therefore, the precipitated crystalline phase could not be identified. Due to extremely constrained long-distance atomic diffusion in the strained region, it is unlikely to form equilibrium phases $\text{Cu}_{10}\text{Zr}_7$ and CuZr_2 [56, 57]. B2 CuZr crystals, with similar composition as the parent amorphous matrix, preferentially crystallizes. The nanoscaled crystals were believed to be B2-CuZr phase. Microstructural characterization and phase identification of the precipitated crystals are required, but this would have to be the subject of a future study.

As mentioned in the section 4.3.3.2, extensive local crystal-like ordering was formed in the supercooled liquid. They might act as nucleation sites for crystallization upon cooling. Some local ordering clusters may have remained in the solidified materials due to rapid cooling rate. This local ordering may be the nucleation sites for nanocrystallization during the deformation process. In the early deformation stage, embedded crystals and amorphous matrix are elastically deformed. As deformation proceeded, crystalline spheres yielded while the glassy phase deformed elastically, leading to the stress concentration accumulation in the vicinity of the interface, where the martensitic transformation was initiated. In addition, the preferential crystal orientation in phase transformation and the existing local crystalline orderings resulted in the heterogeneous stress distribution in the glassy matrix, further leading to structural rearrangement and the precipitation of B2-CuZr nanocrystals in the amorphous matrix. Meanwhile, some shear bands developed. The propagation of shear bands was hampered by the transformed, untransformed and newly formed crystals. The interactions among martensitic transformation, nanoscaled B2-CuZr precipitates and multiple shear bands formation contributed to the improved plasticity and work hardening capability. Once the strain accommodation capability of the glassy matrix was exhausted, the specimen fractured.

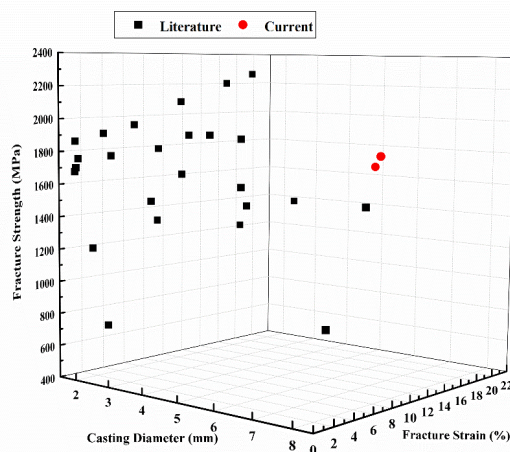


Figure 4.25. Fracture strength vs. fracture strain vs. casting diameter of the current $\text{Cu}_{47.75}\text{Zr}_{48}\text{Al}_4\text{Sn}_{0.25}$ ($d=7\text{mm}$) and $\text{Cu}_{47.25}\text{Zr}_{48}\text{Al}_4\text{Sn}_{0.75}$ BMGMCs ($d=8\text{mm}$) and other CuZr-based metallic glass composites reported in literature [9, 15, 38, 41, 50, 51, 58-67].

Figure 4.25 summarizes the fracture strength vs. fracture strain vs. casting diameters of the CuZr-based metallic glass composites in the literature [9, 15, 38, 41, 50, 51, 58-67] as well as current synthesized large-scaled $\text{Cu}_{47.75}\text{Zr}_{48}\text{Al}_4\text{Sn}_{0.25}$ and $\text{Cu}_{47.25}\text{Zr}_{48}\text{Al}_4\text{Sn}_{0.75}$ BMG composites.

It is clear that most of them are located in the small size region (≤ 4 mm) despite improved plasticity or fracture strength. However, the current synthesized $\text{Cu}_{47.75}\text{Zr}_{48}\text{Al}_4\text{Sn}_{0.25}$ and $\text{Cu}_{47.25}\text{Zr}_{48}\text{Al}_4\text{Sn}_{0.75}$ BMG composites stand out from the trend, suggesting a superior combination of strength, plasticity and casting size. However, microstructure evolution during deformation needs to be further investigated to reveal the underlying mechanism.

4.4 Conclusions

In this chapter, CuZr-based metallic glass composites with large dimension and improved mechanical properties were fabricated by adjusting minor alloying addition and manufacturing conditions.

(1) The purity of the raw materials significantly influences the precipitation and distribution of crystalline phase in the amorphous matrix, thereby affecting the mechanical properties.

(2) Manufacturing conditions, including melting time and melting temperature, and even the geometry of the casting mould will have significant effect on the precipitation, size and distribution of crystalline phase in the glassy matrix. Proper manufacturing parameters were obtained for the current $\text{Cu}_{48-x}\text{Zr}_{48}\text{Al}_4\text{Sn}_x$ ($x=0.25, 0.5, 0.75, 1\text{at}\%$) metallic glass system.

(3) By systematic investigation of $\text{Cu}_{48-x}\text{Zr}_{48}\text{Al}_4\text{Sn}_x$ ($x=0.25, 0.5, 0.75, 1\text{at}\%$) metallic glass alloy, the relationship between cooling rate, Sn addition content, microstructure and mechanical property was established. It was found that 0.25 at% and 0.75 at% Sn addition could improve GFA of the alloy.

(4) Dimension for $\text{Cu}_{47.75}\text{Zr}_{48}\text{Al}_4\text{Sn}_{0.25}$ BMG composites reinforced by homogeneously distributed single crystalline B2-CuZr phase could reach 7 mm in diameter. For the alloy in size of 5 mm to 7 mm, all exhibited improved plasticity and obvious work hardening capability. The block effect, phase transformation and nanocrystallization account for the improved properties.

(5) Dimension for $\text{Cu}_{47.25}\text{Zr}_{48}\text{Al}_4\text{Sn}_{0.75}$ BMG composites reinforced by homogeneously distributed spherical crystalline phase could reach 8 mm in diameter. TEM analysis indicates the formation of nanoscale martensitic structure in the vicinity of the interface, which may be

caused by thermal stress concentration during rapid solidification or the introduction of minor Sn addition.

(6) The mechanical properties for Sn-doped BMGMCs with different sizes are as summarized in Table 4.5.

Table 4.5. The summary of mechanical properties for Sn-doped BMGMCs with different sizes.

Sn addition (at%)	Diameter (mm)	σ_Y (MPa)	σ_m (MPa)	ϵ_m (%)	ϵ_f (%)	T_g (K)	T_x (K)	Crystal fraction (%)	Crystal size (μm)
0.25	4	1361 \pm 17	1763 \pm 17	3.7 \pm 0.8	4.5 \pm 2.2	694	761	8.2 \pm 0.6	20-35
	5	1419 \pm 6	1753 \pm 17	3.8 \pm 0.2	20.8 \pm 2.3	688	747	8.4 \pm 0.5	25-45
	6	1413 \pm 30	1800 \pm 30	7.9 \pm 0.8	13 \pm 1.2	687	746	8.5 \pm 0.5	8-12
	7	1100 \pm 25	1855 \pm 25	10.5 \pm 0.8	12.3 \pm 1.1	686	746	8.8 \pm 0.8	8-16
0.5	4	1464 \pm 25	1657 \pm 25	2.8 \pm 1.0	2.9 \pm 1.0	698	764	-	-
	5	1283 \pm 1.4	1782 \pm 37	-	3.6 \pm 0.2	689	748	4.5 \pm 1.0	200-500
	6	1333 \pm 68	1810 \pm 50	4.7 \pm 1.0	7.2 \pm 1.7	688	749	11.9 \pm 2.1	5-900
	7	855.2 \pm 50	1866.3 \pm 50	11.6 \pm 1.0	12.1 \pm 1.0	690	749	36.8 \pm 10	20-600
0.75	4	1368 \pm 17	1834 \pm 17	2.7 \pm 0.7	3.7 \pm 0.4	701	767	-	-
	5	1498 \pm 17	1784 \pm 17	5.0 \pm 0.7	13.8 \pm 0.3	692	752	9.1 \pm 1	10-25
	6	1612 \pm 30	1838 \pm 8	5.2 \pm 0.6	15.4 \pm 1.7	691	750	8.9 \pm 1.1	20-50
	7	1235 \pm 25	1928 \pm 25	9.6 \pm 1.3	12 \pm 2.5	691	752	14.3 \pm 0.8	80-100
	8	1236.8 \pm 20	1831.4 \pm 20	7.6 \pm 1.1	8.3 \pm 1.2	705	762	34.7 \pm 1.8	80-100
1.0	4	1560 \pm 50	1680 \pm 50	3.5 \pm 1.0	4.0 \pm 1.0	705	770	4.8 \pm 0.5	3-40
	5	1408 \pm 50	1719 \pm 50	4.0 \pm 1.0	7.2 \pm 1.0	694	753	10.2 \pm 2.1	50-500
	6	1211 \pm 50	1751 \pm 50	-	7.3 \pm 1.0	696	749	44.5 \pm 6.0	8-160
	7	817.5 \pm 50	1627 \pm 50	8.7 \pm 1.0	8.8 \pm 1.0	689	750	58.6 \pm 7.4	31-770

4.5 References

- [1] J. F. Löffler, "Bulk metallic glasses," *Intermetallics*, vol. 11, pp. 529-540, 2003/06/01/ 2003.
- [2] W. L. Johnson, "Bulk metallic glasses — a new engineering material," *Current Opinion in Solid State and Materials Science*, vol. 1, pp. 383-386, 1996/06/01/ 1996.
- [3] W. H. Wang, C. Dong, and C. H. Shek, "Bulk metallic glasses," *Materials Science and Engineering: R: Reports*, vol. 44, pp. 45-89, 6/1/ 2004.
- [4] C. A. Schuh, T. C. Hufnagel, and U. Ramamurty, "Mechanical behavior of amorphous alloys," *Acta Materialia*, vol. 55, pp. 4067-4109, 2007/07/01/ 2007.
- [5] M. Chen, "A brief overview of bulk metallic glasses," *Npg Asia Materials*, vol. 3, p. 82, 09/22/online 2011.
- [6] M. F. Ashby and A. L. Greer, "Metallic glasses as structural materials," *Scripta Materialia*, vol. 54, pp. 321-326, 2006/02/01/ 2006.
- [7] D. C. Hofmann, "Shape memory bulk metallic glass composites," *Science*, vol. 329, pp. 1294-1295, 2010.
- [8] S. Pauly, J. Das, J. Bednarcik, N. Mattern, K. B. Kim, D. H. Kim, *et al.*, "Deformation-induced martensitic transformation in Cu–Zr–(Al,Ti) bulk metallic glass composites," *Scripta Materialia*, vol. 60, pp. 431-434, 2009/03/01/ 2009.
- [9] Y. Wu, Y. Xiao, G. Chen, C. T. Liu, and Z. Lu, "Bulk Metallic Glass Composites with Transformation-Mediated Work-Hardening and Ductility," *Advanced Materials*, vol. 22, pp. 2770-2773, 2010.
- [10] W. S. Rasband. (1997-2016). *ImageJ*. Available: <https://imagej.nih.gov/ij/>
- [11] S. V. Madge, T. Wada, D. V. Louzguine-Luzgin, A. L. Greer, and A. Inoue, "Oxygen embrittlement in a Cu–Hf–Al bulk metallic glass," *Scripta Materialia*, vol. 61, pp. 540-543, 2009/09/01/ 2009.
- [12] Y. X. Wang, H. Yang, G. Lim, and Y. Li, "Glass formation enhanced by oxygen in binary Zr–Cu system," *Scripta Materialia*, vol. 62, pp. 682-685, 2010/05/01/ 2010.

- [13] F. Jiang, Z. J. Wang, Z. B. Zhang, and J. Sun, "Formation of Zr-based bulk metallic glasses from low purity materials by scandium addition," *Scripta Materialia*, vol. 53, pp. 487-491, 2005/09/01/ 2005.
- [14] Z. P. Lu, H. Bei, Y. Wu, G. L. Chen, E. P. George, and C. T. Liu, "Oxygen effects on plastic deformation of a Zr-based bulk metallic glass," *Applied Physics Letters*, vol. 92, p. 011915, 2008/01/07 2008.
- [15] Z. Liu, R. Li, G. Liu, K. Song, S. Pauly, T. Zhang, *et al.*, "Pronounced ductility in CuZrAl ternary bulk metallic glass composites with optimized microstructure through melt adjustment," *AIP Advances*, vol. 2, p. 032176, 2012.
- [16] S. Pauly, G. Liu, G. Wang, U. Kühn, N. Mattern, and J. Eckert, "Microstructural heterogeneities governing the deformation of Cu 47.5 Zr 47.5 Al 5 bulk metallic glass composites," *Acta Materialia*, vol. 57, pp. 5445-5453, 2009.
- [17] D. C. Hofmann, J.-Y. Suh, A. Wiest, G. Duan, M.-L. Lind, M. D. Demetriou, *et al.*, "Designing metallic glass matrix composites with high toughness and tensile ductility," *Nature*, vol. 451, pp. 1085-1089, 2008.
- [18] J. Mao, H. F. Zhang, H. M. Fu, A. M. Wang, H. Li, and Z. Q. Hu, "The Effects of Casting Temperature on the Glass Formation of Zr-Based Metallic Glasses," *Advanced Engineering Materials*, vol. 11, pp. 986-991, 2009/12/01 2009.
- [19] C. Fan, C. T. Liu, G. Chen, G. Chen, P. K. Liaw, and H. G. Yan, "Effect of molten quenching temperature on glass-forming ability of nanoquasi-crystal-forming Zr-based metallic glasses," *Scripta Materialia*, vol. 68, pp. 534-537, 2013/04/01/ 2013.
- [20] H. Hermann, V. Kokotin, and J. Eckert, "Locally fluctuating cooling rate as possible reason for non-crystalline plasticity in metallic glasses," *EPL (Europhysics Letters)*, vol. 98, p. 16003, 2012.
- [21] G. Kumar, T. Ohkubo, and K. Hono, "Effect of melt temperature on the mechanical properties of bulk metallic glasses," *Journal of Materials Research*, vol. 24, pp. 2353-2360, 2009.
- [22] P. S. Popel and V. E. Sidorov, "Microheterogeneity of liquid metallic solutions and its influence on the structure and properties of rapidly quenched alloys," *Materials Science and Engineering: A*, vol. 226-228, pp. 237-244, 1997/06/15/ 1997.

- [23] W. Hoyer and R. Jödicke, "Short-range and medium-range order in liquid Au□Ge alloys," *Journal of Non-Crystalline Solids*, vol. 192-193, pp. 102-105, 1995/12/02/ 1995.
- [24] J. Schroers, "Processing of Bulk Metallic Glass," *Advanced Materials*, vol. 22, pp. 1566-1597, 2010/04/12 2009.
- [25] C. N. Kuo, J. C. Huang, J. B. Li, J. S. C. Jang, C. H. Lin, and T. G. Nieh, "Effects of B2 precipitate size on transformation-induced plasticity of Cu–Zr–Al glassy alloys," *Journal of Alloys and Compounds*, vol. 590, pp. 453-458, 2014/03/25/ 2014.
- [26] S. Mukherjee, Z. Zhou, J. Schroers, W. Johnson, and W. Rhim, "Overheating threshold and its effect on time–temperature–transformation diagrams of zirconium based bulk metallic glasses," *Applied physics letters*, vol. 84, pp. 5010-5012, 2004.
- [27] J. J. Wall, C. T. Liu, W. K. Rhim, J. J. Z. Li, P. K. Liaw, H. Choo, *et al.*, "Heterogeneous nucleation in a glass-forming alloy," *Applied Physics Letters*, vol. 92, p. 244106, 2008/06/16 2008.
- [28] X. H. Lin, W. L. Johnson, and W. K. Rhim, "Effect of Oxygen Impurity on Crystallization of an Undercooled Bulk Glass Forming Zr-Ti-Cu-Ni-Al Alloy," *Materials Transactions, JIM*, vol. 38, pp. 473-477, 1997.
- [29] A. Gebert, J. Eckert, and L. Schultz, "Effect of oxygen on phase formation and thermal stability of slowly cooled Zr₆₅Al_{17.5}Cu_{17.5}Ni₁₀ metallic glass," *Acta Materialia*, vol. 46, pp. 5475-5482, 9/18/ 1998.
- [30] H. Zhai, H. Wang, and F. Liu, "Effects of Sn addition on mechanical properties of Ti-based bulk metallic glass composites," *Materials & Design*, vol. 110, pp. 782-789, 2016/11/15/ 2016.
- [31] Z. Y. Zhang, Y. Wu, J. Zhou, W. L. Song, D. Cao, H. Wang, *et al.*, "Effects of Sn addition on phase formation and mechanical properties of TiCu-based bulk metallic glass composites," *Intermetallics*, vol. 42, pp. 68-76, 11// 2013.
- [32] W. Song, Y. Wu, H. Wang, X. Liu, H. Chen, Z. Guo, *et al.*, "Microstructural Control via Copious Nucleation Manipulated by In Situ Formed Nucleants: Large-Sized and Ductile Metallic Glass Composites," *Advanced Materials*, vol. 28, pp. 8156-8161, 2016.

- [33] Y. Liu, C. T. Liu, E. P. George, and X. Z. Wang, "Thermal diffusion and compositional inhomogeneity in cast Zr₅₀Cu₅₀ bulk metallic glass," *Applied Physics Letters*, vol. 89, p. 051919, 2006/07/31 2006.
- [34] Y. Liu, C. T. Liu, E. P. George, and X. Z. Wang, "The Soret effect in bulk metallic glasses," *Intermetallics*, vol. 15, pp. 557-563, 2007/04/01/ 2007.
- [35] D. A. Porter, K. E. Easterling, and M. Sherif, *Phase Transformations in Metals and Alloys, (Revised Reprint)*: CRC press, 2009.
- [36] J. Schroers and W. L. Johnson, "History dependent crystallization of Zr₄₁Ti₁₄Cu₁₂Ni₁₀Be₂₃ melts," *Journal of Applied Physics*, vol. 88, pp. 44-48, 2000.
- [37] B. Yao, B. Z. Ding, G. L. Sui, A. M. Wang, and Z. Q. Hu, "Effect of high pressure on the preparation of Pd–Si–Cu bulk nanocrystalline material," *Journal of Materials Research*, vol. 11, pp. 912-916, 2011.
- [38] J. Schroers, A. Masuhr, W. L. Johnson, and R. Busch, "Pronounced asymmetry in the crystallization behavior during constant heating and cooling of a bulk metallic glass-forming liquid," *Physical Review B*, vol. 60, pp. 11855-11858, 11/01/ 1999.
- [39] A. Takeuchi and A. Inoue, "Classification of bulk metallic glasses by atomic size difference, heat of mixing and period of constituent elements and its application to characterization of the main alloying element," *Materials Transactions*, vol. 46, pp. 2817-2829, 2005.
- [40] Z. W. Zhu, S. J. Zheng, H. F. Zhang, B. Z. Ding, Z. Q. Hu, P. K. Liaw, *et al.*, "Plasticity of bulk metallic glasses improved by controlling the solidification condition," *Journal of Materials Research*, vol. 23, pp. 941-948, 2008.
- [41] Y. F. Sun, B. C. Wei, Y. R. Wang, W. H. Li, T. L. Cheung, and C. H. Shek, "Plasticity-improved Zr–Cu–Al bulk metallic glass matrix composites containing martensite phase," *Applied Physics Letters*, vol. 87, p. 051905, 2005/08/01 2005.
- [42] K. Song, S. Pauly, Y. Zhang, R. Li, S. Gorantla, N. Narayanan, *et al.*, "Triple yielding and deformation mechanisms in metastable Cu_{47.5}Zr_{47.5}Al₅ composites," *Acta Materialia*, vol. 60, pp. 6000-6012, 2012.
- [43] Y. Wu, D. Zhou, W. Song, H. Wang, Z. Zhang, D. Ma, *et al.*, "Ductilizing bulk metallic glass composite by tailoring stacking fault energy," *Physical review letters*, vol. 109, p. 245506, 2012.

- [44] D. Q. Zhou, Y. Wu, H. Wang, X. D. Hui, X. J. Liu, and Z. P. Lu, "Alloying effects on mechanical properties of the Cu–Zr–Al bulk metallic glass composites," *Computational Materials Science*, vol. 79, pp. 187-192, 11// 2013.
- [45] K. Matsushita and S. Sakka, "Kinetic Study on Non-Isothermal Crystallization of Glass by Thermal Analysis (Commemoration Issue Dedicated to Professor Megumi Tashiro on the Occation of his Retirement)," 1981.
- [46] H. E. Kissinger, "Reaction kinetics in differential thermal analysis," *Analytical chemistry*, vol. 29, pp. 1702-1706, 1957.
- [47] P. Gong, K. F. Yao, and H. Y. Ding, "Crystallization kinetics of TiZrHfCuNiBe high entropy bulk metallic glass," *Materials Letters*, vol. 156, pp. 146-149, 2015/10/01/ 2015.
- [48] F. X. Qin, H. F. Zhang, B. Z. Ding, and Z. Q. Hu, "Nanocrystallization kinetics of Ni-based bulk amorphous alloy," *Intermetallics*, vol. 12, pp. 1197-1203, 2004/10/01/ 2004.
- [49] H.-R. Wang, Y.-L. Gao, G.-H. Min, X.-D. Hui, and Y.-F. Ye, "Primary crystallization in rapidly solidified Zr₇₀Cu₂₀Ni₁₀ alloy from a supercooled liquid region," *Physics Letters A*, vol. 314, pp. 81-87, 2003/07/21/ 2003.
- [50] Z. Liu, R. Li, G. Liu, W. Su, H. Wang, Y. Li, *et al.*, "Microstructural tailoring and improvement of mechanical properties in CuZr-based bulk metallic glass composites," *Acta Materialia*, vol. 60, pp. 3128-3139, 4// 2012.
- [51] Y. Wu, H. Wang, H. H. Wu, Z. Y. Zhang, X. D. Hui, G. L. Chen, *et al.*, "Formation of Cu–Zr–Al bulk metallic glass composites with improved tensile properties," *Acta Materialia*, vol. 59, pp. 2928-2936, 5// 2011.
- [52] D. Wang, J. Mu, Y. Chen, Y. Qi, W. Wu, Y. Wang, *et al.*, "A study of stress-induced phase transformation and micromechanical behavior of CuZr-based alloy by in-situ neutron diffraction," *Journal of Alloys and Compounds*, vol. 696, pp. 1096-1104, 2017/03/05/ 2017.
- [53] D. M. Wang, Y. Chen, J. Mu, Z. W. Zhu, H. F. Zhang, Y. D. Wang, *et al.*, "An in situ neutron diffraction study of plastic deformation in a Cu_{46.5}Zr_{46.5}Al₇ bulk metallic glass composite," *Scripta Materialia*, vol. 153, pp. 118-121, 8// 2018.

- [54] Y. Wu, D. Ma, Q. K. Li, A. D. Stoica, W. L. Song, H. Wang, *et al.*, "Transformation-induced plasticity in bulk metallic glass composites evidenced by in-situ neutron diffraction," *Acta Materialia*, vol. 124, pp. 478-488, Feb 1 2017.
- [55] J. Mu, Z. Zhu, R. Su, Y. Wang, H. Zhang, and Y. Ren, "In situ high-energy X-ray diffraction studies of deformation-induced phase transformation in Ti-based amorphous alloy composites containing ductile dendrites," *Acta Materialia*, vol. 61, pp. 5008-5017, 2013/08/01/ 2013.
- [56] M. Chen, A. Inoue, W. Zhang, and T. Sakurai, "Extraordinary Plasticity of Ductile Bulk Metallic Glasses," *Physical Review Letters*, vol. 96, p. 245502, 06/21/ 2006.
- [57] S. Pauly, S. Gorantla, G. Wang, U. Kuhn, and J. Eckert, "Transformation-mediated ductility in CuZr-based bulk metallic glasses," *Nat Mater*, vol. 9, pp. 473-7, Jun 2010.
- [58] F. F. Wu, K. C. Chan, S. H. Chen, S. S. Jiang, and G. Wang, "ZrCu-based bulk metallic glass composites with large strain-hardening capability," *Materials Science and Engineering: A*, vol. 636, pp. 502-506, 6/11/ 2015.
- [59] F. F. Wu, S. T. Li, G. A. Zhang, X. F. Wu, and P. Lin, "Plastic stability of metallic glass composites under tension," *Applied Physics Letters*, vol. 103, p. 151910, Oct 7 2013.
- [60] F. F. Wu, K. C. Chan, S. T. Li, and G. Wang, "Stabilized shear banding of ZrCu-based metallic glass composites under tensile loading," *Journal of Materials Science*, vol. 49, pp. 2164-2170, Mar 2014.
- [61] F.-F. Wu, K. Chan, S.-S. Jiang, S.-H. Chen, and G. Wang, "Bulk metallic glass composite with good tensile ductility, high strength and large elastic strain limit," *Scientific reports*, vol. 4, p. 5302, 2014.
- [62] H. C. Sun, Z. L. Ning, G. Wang, W. Z. Liang, S. Pauly, Y. J. Huang, *et al.*, "In-situ tensile testing of ZrCu-based metallic glass composites," *Scientific Reports*, vol. 8, p. 4651, 2018/03/15 2018.
- [63] J. Das, M. B. Tang, K. B. Kim, R. Theissmann, F. Baier, W. H. Wang, *et al.*, "'Work-Hardenable' Ductile Bulk Metallic Glass," *Physical Review Letters*, vol. 94, p. 205501, 05/23/ 2005.
- [64] S. S. Jiang, Y. J. Huang, F. F. Wu, P. Xue, and J. F. Sun, "A CuZr-based bulk metallic glass composite with excellent mechanical properties by optimizing microstructure," *Journal of Non-Crystalline Solids*, vol. 483, pp. 94-98, Mar 1 2018.

- [65] W. Zhou, J. Hou, and W. Weng, "Microstructure, thermal stability and mechanical properties of Zr–Cu–Al–Sn bulk metallic glass," *Journal of Non-Crystalline Solids*, vol. 429, pp. 208-212, 12/1/ 2015.
- [66] J. Xu, L. Ma, Y. Xue, Z. Nie, Y. Long, L. Wang, *et al.*, "Work-hardening behavior, strain rate sensitivity, and failure behavior of in situ CuZr-based metallic glass matrix composite," *Journal of Materials Science*, pp. 1-10, 2016.
- [67] J. Wu, Y. Pan, X. Li, and X. Wang, "Microstructure evolution and mechanical properties of Nb-alloyed Cu-based bulk metallic glasses and composites," *Materials & Design*, vol. 75, pp. 32-39, 6/15/ 2015.

Chapter 5 Formation of CuZr-based Bulk Metallic Glass Composites with improved mechanical properties by optimizing microstructure

5.1 Introduction

Bulk metallic glasses (BMGs) have attracted lots of attention because of their excellent properties, such as high strength, large elastic limit (up to 2%), high strength and hardness and excellent corrosion resistance [1-3]. Nevertheless, strain softening behaviour and room-temperature brittleness have limited their real structural application [4-6]. To overcome this shortcoming many strategies have been proposed and shape memory phase reinforced bulk metallic glass composites (BMGMCs) have proved to be an effective solution [7-11]. The extensively studied shape memory phase reinforced BMGMCs are CuZr-based composites with ductile CuZr phase as reinforcement. The intermetallic CuZr compound is stable above 988 K with a B2 crystalline structure and tends to decompose into $\text{Cu}_{10}\text{Zr}_7$ and Zr_2Cu at low temperatures [12]. However, metastable B2 phase can be retained at high cooling rates. Upon deformation metastable ductile B2 phase will undergo a martensitic transformation from a cubic primitive B2 phase to monoclinic martensitic phase [13], thus resulting in work-hardening and plasticity in the BMGMCs. It has been reported that glass forming ability (GFA) and microstructures of the BMGMCs are sensitive to minor alloying addition [14-16], thereby affecting mechanical performance.

In this study, Ni was chosen as a minor addition (0.25 at% - 1 at%) to replace Cu in the alloy $\text{Cu}_{48}\text{Zr}_{48}\text{Al}_4$ to optimize the microstructure and corresponding mechanical behaviour. The microstructure evolution and compressive deformation responses will be systematically investigated to shed light on related deformation mechanisms.

5.2 Experimental

Master alloys with nominal composition of $\text{Cu}_{48-x}\text{Zr}_{48}\text{Al}_4\text{Ni}_x$ ($x=0, 0.25, 0.5, 0.75, 1$ at%) were fabricated by arc melting constituting elements with high purity ($\geq 99.8\%$) in a Ti-gettered argon atmosphere. The specimen fabrication process was given in Chapter 3. Cylinder

samples with diameter of 2 mm, 3 mm and length of 30 mm were prepared by water-cooled copper mould suction casting.

Nanoindentation testing was carried out on a well-polished transverse section surface of the as-cast and as-fractured specimen $\text{Cu}_{47.5}\text{Zr}_{48}\text{Al}_4\text{Ni}_{0.75}$ for the 3 mm diameter bar at room temperature using a Hysitron TI Premier Nano-mechanical testing instrument. Uniaxial compression testing was performed on 3 mm diameter samples at a strain rate of $1 \times 10^{-4} \text{ s}^{-1}$ at room temperature. The testing samples with aspect of 2:1 were cut from the rods.

5.3 Results

5.3.1 Microstructure evolution with Ni addition

Figure 5.1 shows XRD patterns of as-cast alloys with diameter of 2 mm and 3 mm with different Ni additions. The as-cast 2 mm diameter alloy rods exhibited a broad halo diffraction pattern typical of the BMG alloy. As the size increased to 3 mm, the ternary $\text{Cu}_{48}\text{Zr}_{48}\text{Al}_4$ BMG alloy without Ni doping displays typical BMGMCs diffraction pattern, namely a sharp diffraction peak, which is identified as B2 CuZr phase [9, 13, 17, 18], superimposed on a broad hump. The sharp diffraction peak became indistinctive for the BMG alloy with 0.25 at% Ni doping, indicating an improved glass forming ability (GFA). With further increase of Ni addition, the B2 CuZr phase crystalline peaks emerged, again overlapped with the glassy hump. Therefore, B2 CuZr phase reinforced BMGMCs can be obtained by properly adjusting Ni doping contents and corresponding cooling rates. Figure 5.2 displays the DSC results of the as-cast BMG alloys with Ni additions. They present a similar thermal behaviour with one exothermic event preceded by a glass transition. The glass transition temperature (T_g), crystallization temperature (T_x) and supercooled liquid region (ΔT_x) are summarized in Table 5.1. As listed in Table 5.1, the values of ΔT_x increase slightly from 65 K to 67 K as the Ni addition increases from 0.25 at% to 1 at%. It indicates that the thermal behaviour remains almost the same with the minor addition of Ni.

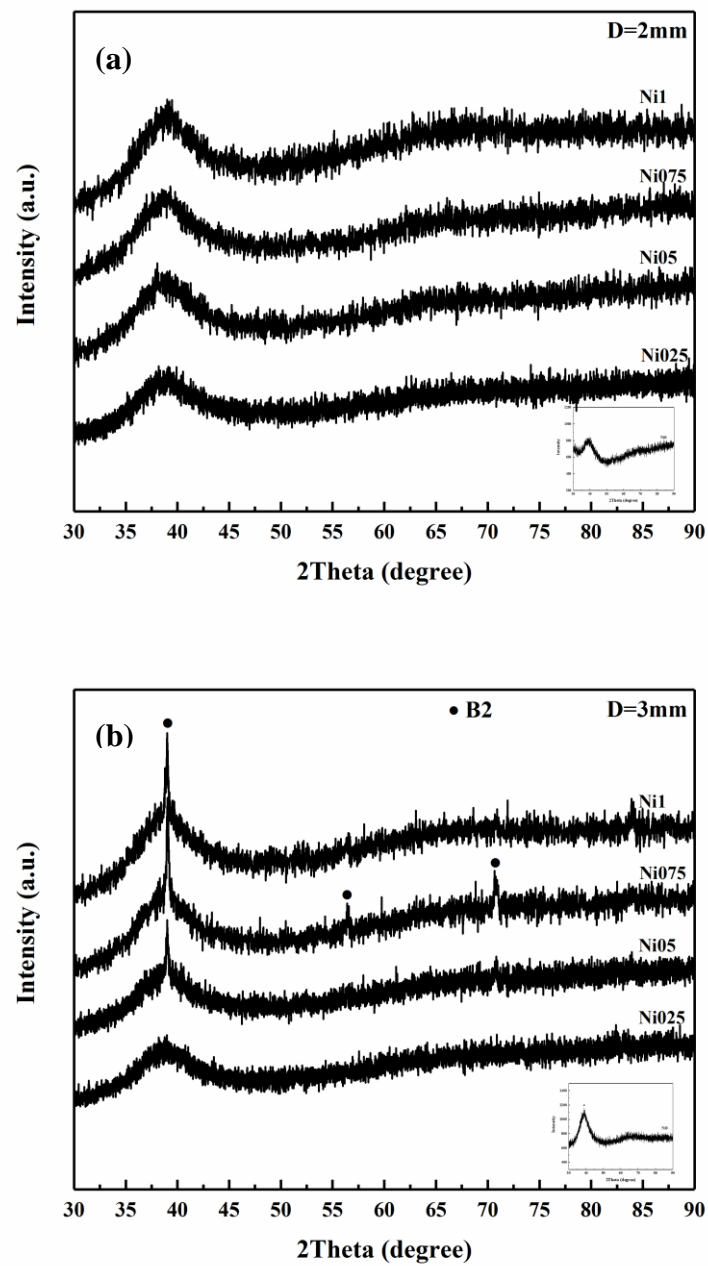


Figure 5.1. XRD patterns of as-cast rods with diameter of (a) 2 mm and (b) 3 mm for $\text{Cu}_{48-x}\text{Zr}_{48}\text{Al}_4\text{Ni}_x$ ($x=0, 0.25, 0.5, 0.75, 1\text{at}\%$) BMG alloys.

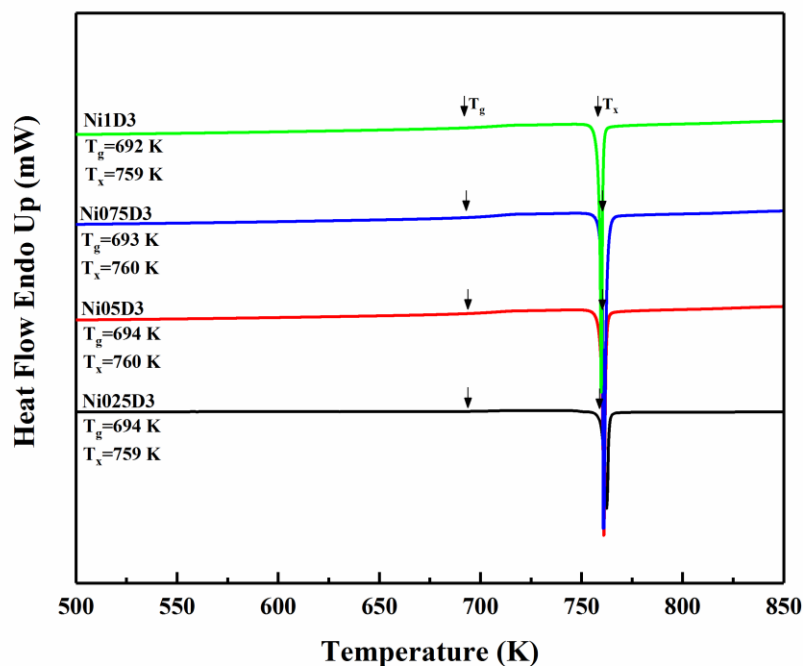


Figure 5.2. DSC results of the as-cast $\text{Cu}_{48-x}\text{Zr}_{48}\text{Al}_4\text{Ni}_x$ ($x=0.25, 0.5, 0.75, 1$ at%) BMG alloys, which shows glass transition temperature T_g , crystallization transformation temperature T_x .

Table 5.1. The thermal stability of the as-cast rods with different Ni additions for CuZr-based BMG alloys for the diameter of 3 mm.

	Ni0.25	Ni0.5	Ni0.75	Ni1
T_g / K	694	694	693	692
T_x / K	759	760	760	759
ΔT_x / K	65	66	67	67

Figure 5.3 shows backscattered SEM images of the cross-sections of the as-cast Ni doped CuZr-based BMGMCs with a diameter of 3 mm. Limited number of B2 CuZr phase particles (~ 3% volume fraction) with heterogeneous distribution and size range from 7 μm to 36 μm is sparsely embedded in the amorphous matrix for the Ni-free samples (Figure 5.3a). The distribution and the particle size range of the B2 CuZr phase changed as the Ni addition content changed. The 0.25 at% Ni-doped BMG alloys exhibited a featureless morphology characteristic, which agrees well with the XRD results, further confirming its amorphous nature (not shown

here). With 0.5 at% Ni addition, a number of B2 CuZr particles with size of 9 μm precipitated in the glassy matrix in addition to a few large ($\sim 40 \mu\text{m}$) B2 spheres, as shown in Figure 5.3b and Figure 5.4b. For alloys with 0.75 at% Ni addition, the size distribution of the precipitated B2 CuZr spheres tended to be uniform (Figure 5.3c and Figure 5.4c), mainly in the range from 10 μm to 20 μm . As the Ni addition increased to 1 at%, the size of B2 phase particles further increased to the range from 15 μm to 35 μm (Figure 5.3d and Figure 5.4d). The volume fraction of B2 phase particles in the Ni-doped alloys increased in comparison with Ni-free BMG alloys, however, it decreased with further increase of Ni addition, from $\sim 20\%$ for the 0.5 at% Ni-doped sample to $\sim 9\%$ for the 1 at% Ni-doped sample, as present in Figure 5.4a.

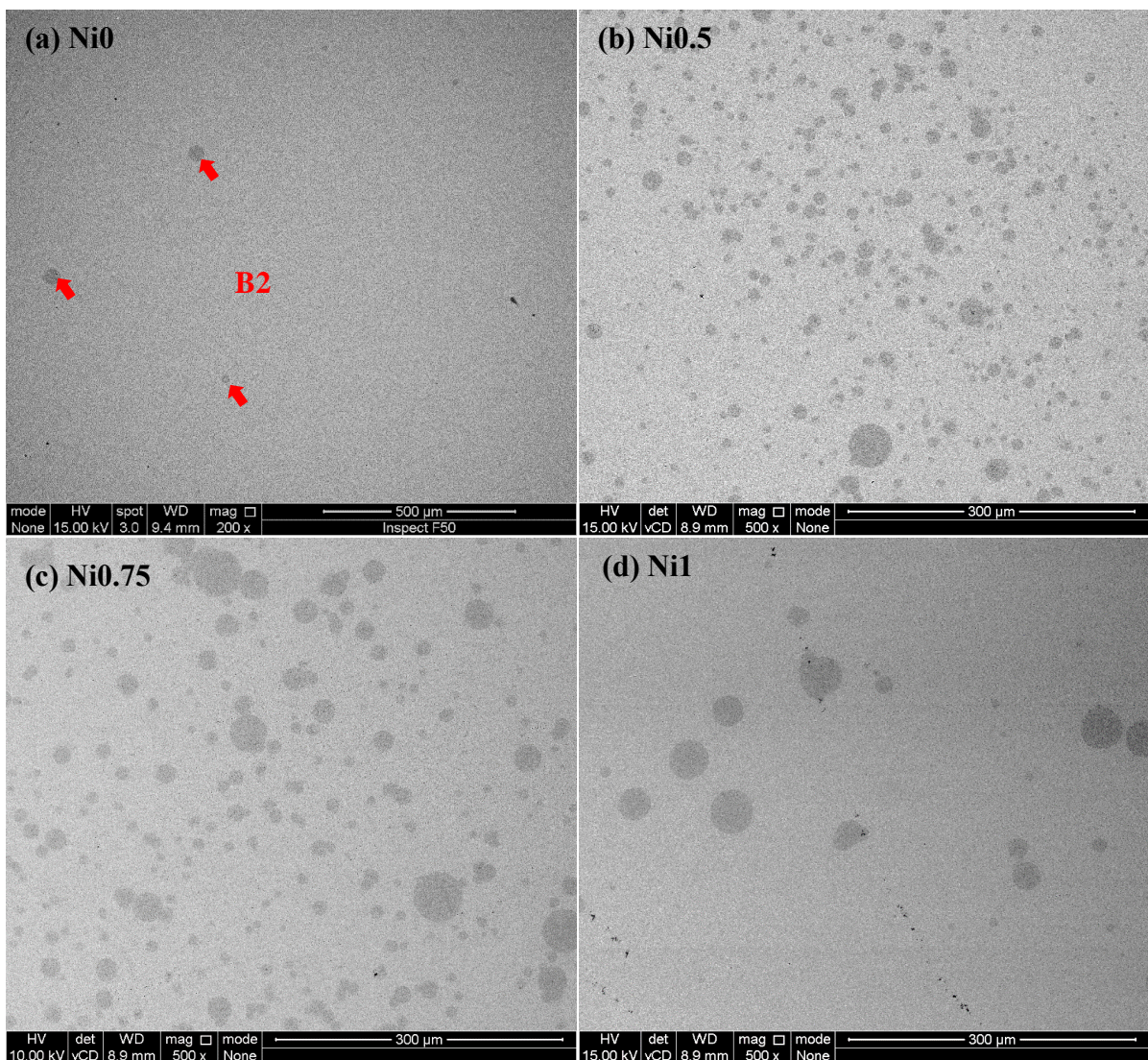


Figure 5.3. Cross-section backscattered SEM images of the as-cast $\text{Cu}_{48-x}\text{Zr}_{48}\text{Al}_4\text{Ni}_x$ ($x=0, 0.5, 0.75, 1$ at%) BMG alloys with diameter of 3 mm.

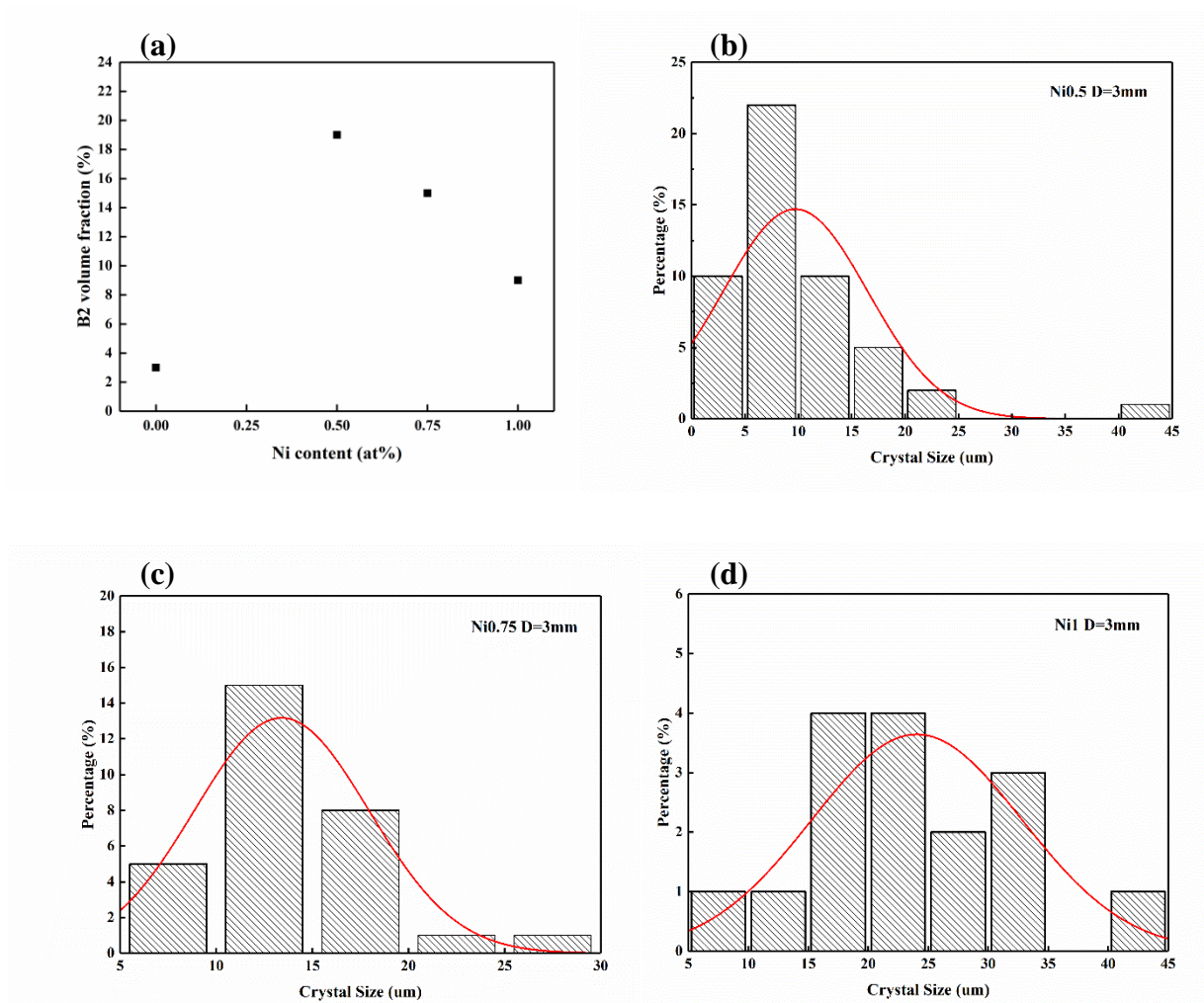


Figure 5.4. (a) Crystal volume fraction changes with different Ni additions; crystal size distribution of the microscale B2 CuZr phase for the as-cast 3 mm diameter Ni alloyed BMGMCs (b) Ni0.5 addition; (c) Ni0.75 addition; (d) Ni1 addition.

5.3.2 Mechanical properties

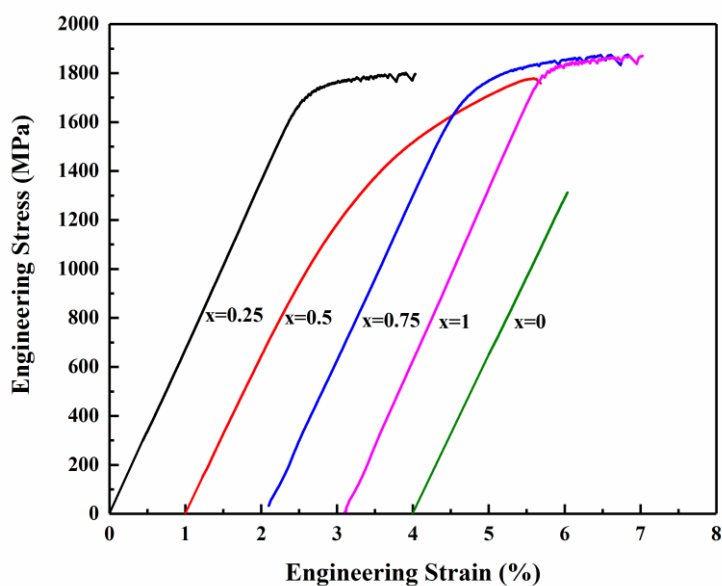


Figure 5.5. Compressive engineering stress strain curves of the as-cast $\text{Cu}_{48-x}\text{Zr}_{48}\text{Al}_4\text{Ni}_x$ ($x=0, 0.25, 0.5, 0.75, 1$ at%) BMG alloys with diameter of 3 mm.

Table 5.2. Compressive yield strength (σ_y), elastic strain (ε_y), fracture strength (σ_f) and fracture strain (ε_f) of as-cast $\text{Cu}_{48-x}\text{Zr}_{48}\text{Al}_4\text{Ni}_x$ ($x=0, 0.25, 0.5, 0.75, 1$ at%) BMG alloys in the diameter of 3 mm.

	σ_y / MPa	ε_y / %	σ_f / MPa	ε_f / %
Ni0	1313	2.0	-	-
Ni0.25	1610	2.3	1796	4.0
Ni0.5	1147	1.9	1758	4.6
Ni0.75	1493	2.0	1748	5.1
Ni1	1657	2.4	1796	4.0

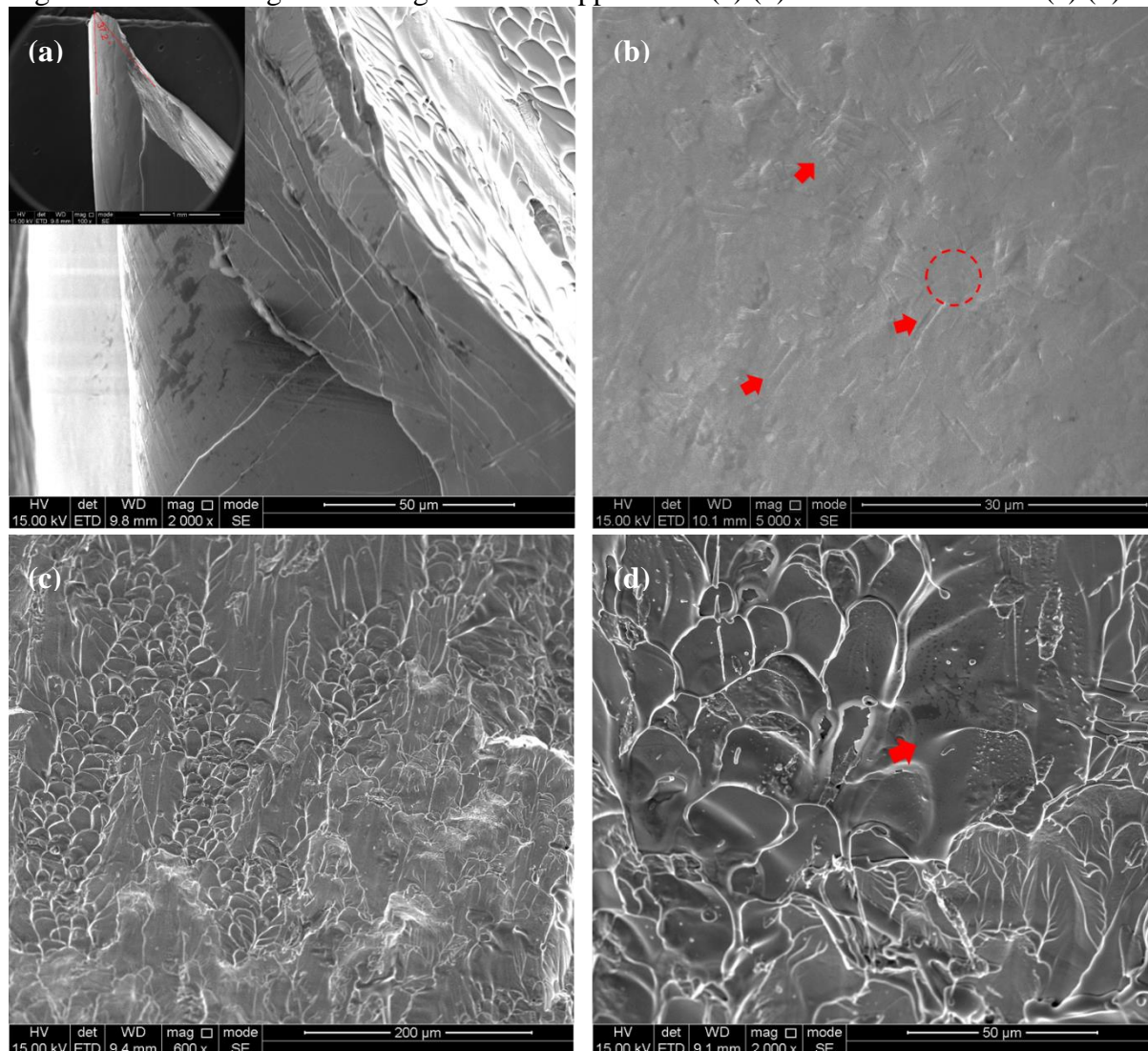
To examine the mechanical properties of the BMG alloys with different Ni additions, compression testing was carried out on the 3 mm diameter samples with aspect ratio of 2:1. As displayed in Figure 5.5, the samples exhibited different compressive mechanical behaviour

dependent on their microstructure. The ternary Ni-free sample fractured at ~ 1313 MPa catastrophically with negligible plasticity in accordance with low crystalline volume fraction. The compressive plasticity of the BMG alloys was improved for the Ni-doped BMG alloys. The alloys with minor addition of 0.25 at% Ni exhibited an improved plasticity of $\sim 4\%$ with the yielding at ~ 1610 MPa. The BMGMC with 1 at% Ni addition behaves in a similar manner with 0.25 at% Ni-doped BMG with a fracture strength of ~ 1796 MPa, a plasticity of $\sim 4\%$ and a yield strength of ~ 1657 MPa. With the increase in crystalline volume fraction (20%) in 0.5 at% Ni-doped BMGMCs shows prominent work hardening ability and improved plasticity of $\sim 4.6\%$. The compressive yield point, however, decreases to ~ 1147 MPa, probably a result of the high volume fraction of B2 CuZr phase. For the 0.75 at% Ni-doped BMGMCs, which had a slightly lower (15%) precipitated crystalline phase, the yield point increased to ~ 1493 MPa with an improved plasticity of $\sim 5.1\%$. With the decrease in crystalline volume fraction in Ni-doped BMG/BMGMCs the strength increased, however, the plasticity increased first and then decreases. The trend agrees well with the previous report by Pauly *et al.* [13, 19]. Therefore, the content of crystalline B2 CuZr phase and its size distribution will determine the compressive mechanical properties of the BMGMCs and the doping element addition will play an effective role in tailoring microstructure and the resultant mechanical properties.

To further reveal and understand the deformation and fracture mechanism on compression, lateral and fractural surfaces of the fractured $\text{Cu}_{47.25}\text{Zr}_{48}\text{Al}_4\text{Ni}_{0.75}$ BMGMCs were observed, as presented in Figure 5.6. Typical compressive fracture characteristics for bulk metallic glass alloys were observed, with a shear fracture with a shear angle of 37° (less than 45°) with respect to the compression loading direction [20, 21], as shown in the inset of Figure 5.6a. A high density of detoured shear bands and a few cracks were observed on the side-view surfaces, indicating the occurrence of severe compressive deformation (Figure 5.6a). Profuse short shear bands and martensite slats with size of $5\text{-}6\ \mu\text{m}$, as denoted by the red arrows, were found in the high-magnification SEM image in Figure 5.6b. A particular B2 CuZr crystalline sphere has been highlighted in a red circular frame in Figure 5.6b to reveal the compressive deformation process. The propagation of shear bands will have been hindered by the reinforcing B2 particles as they meet and interact with each other, which is known as the “blocking effect” [9, 22, 23]. Then more shear bands will have been formed in the interfaces between the glass matrix and the embedded B2 particles as a result of the stress concentration. Both processes will have resulted in the enhanced plasticity. The fracture surface morphologies of the $\text{Cu}_{47.25}\text{Zr}_{48}\text{Al}_4\text{Ni}_{0.75}$ BMGMCs are displayed in Figure 5.6c and d. Dense vein patterns

dominated the fracture surface. As highlighted by the red arrow in the Figure 5.6d, vein patterns were interrupted by the distorted crystalline particles, which further confirms the “blocking effect” of the crystalline phase during the deformation process.

Figure 5.6. SEM images revealing the lateral appearance (a) (b) and fracture surface (c) (d) of



the fractured $\text{Cu}_{47.25}\text{Zr}_{48}\text{Al}_4\text{Ni}_{0.75}$ BMGMCs with 3 mm diameter after room-temperature compression.

5.3.3 Microstructure of the as-cast 0.75 at% Ni-doped CuZr BMGMCs

To further identify the shape memory phase reinforced microstructure and reveal the corresponding influence on the mechanical performance, a TEM study was performed on the as-cast 0.75 at% Ni-doped CuZr composites. Bright field (BF) TEM images of the crystalline phase and the interface between CuZr crystalline phase and the amorphous matrix in the low

magnification are displayed in Figure 5.7. The light and dark areas in Figure 5.7a and b indicated the CuZr crystalline phase and the amorphous matrix, respectively. In the area of 300 nm close to the interface, some strip-like features were observed in the sub-boundaries (as denoted by a red circle in Figure 5.7b). It was suggested to be the preferential martensitic nucleation sites under loading [24]. From the interface further inside to the crystalline region of 1 μm , some needle-like phase was randomly present, as denoted by red arrows in Figure 5.7a. The needle-like phase is indexed as martensitic B19' phase with a zone axis of $[1\ 0\ 0]$ and the surrounding phase corresponds to austenitic B2 phase with a zone axis of $[0\ 1\ 0]$, as selected area electron diffraction (SAED) patterns shown in the insets in Figure 5.7d. However, there was no martensitic phase detected in XRD measurement. This was attributed to the small volume fraction and small size of the martensitic phase, and also any signal present would have overlapped that of amorphous phase and CuZr B2 phase. Moving further inwards from the interface towards the centre of the crystalline region, the typical feature is as presented in Figure 5.7c. It seems that profuse dislocations are present, indicating stress concentration within the spherical crystalline phase, which may have resulted from the rapid solidification during casting. The SAED pattern, shown in the inset in Figure 5.7c, with a zone axis of $[1\ 1\ 3]$ indicates austenitic B2 phase in a primary cubic structure. In this regard, the reinforced spherical crystalline phase in the current Ni-doped composites can be treated as a “composite” structure with needle-like B19' phase distributed in the B2 phase matrix.

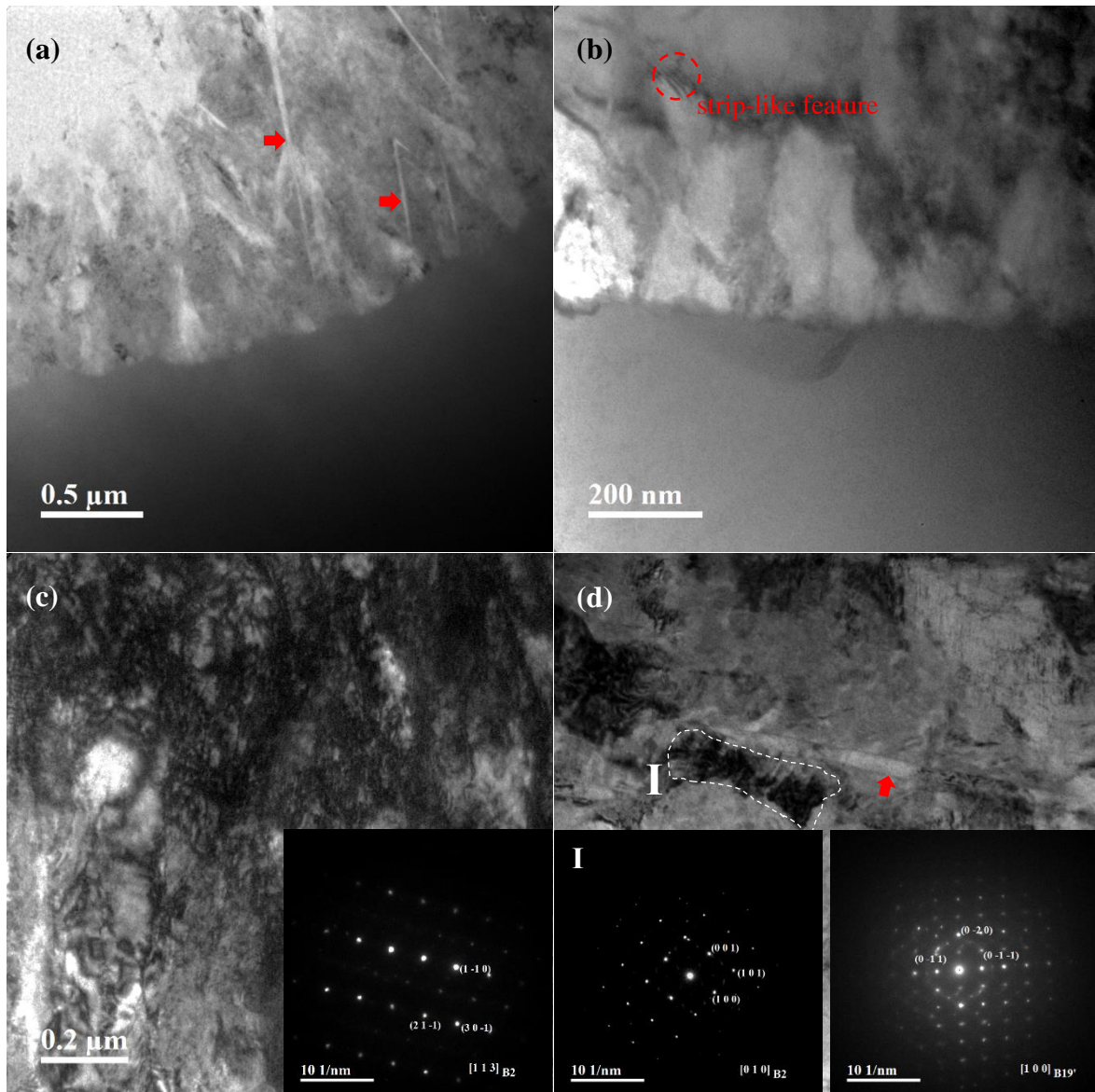


Figure 5.7. TEM bright field (BF) images of (a) (b) the interface between crystals and amorphous matrix and (c)-(d) crystalline phases in the as-cast 0.75 at% Ni-doped BMGMCs.

5.4 Discussion

5.4.1 Effect of Ni on the GFA

The influence of Ni addition on the GFA of the Ni-doped BMGMCs alloy was investigated. It has been reported that large atomic radius difference will contribute to GFA in the metallic glass [25, 26]. Ni has the smallest atomic size compared with other constituent elements [27, 28]. Therefore, the addition of Ni alloying will increase the atomic size mismatch, retard the

long-range rearrangement for crystallization and decrease the volume fraction of the crystalline phase. This is in accordance with the results in the current CuZr-based BMG system. As minor Ni addition slightly increases from 0.5 at% to 1 at%, supercooled liquid region (ΔT_x) increases and the crystalline phase content decreases correspondingly. Furthermore, the mixing enthalpy of Ni-Cu is positive, with the value of +4 kJ/mol [25] and the mixing enthalpy between other constituent elements is negative. In this perspective, the GFA of the current CuZr-based BMG alloys will be decreased when Ni is added to replace Cu. The structural nature of the alloy system is amorphous with 0.25 at% Ni doping and then changes to crystalline phase reinforced glass matrix composites with increase in Ni addition, which is in accordance with the results presented in section 5.3.1.

5.4.2 Deformation mechanisms

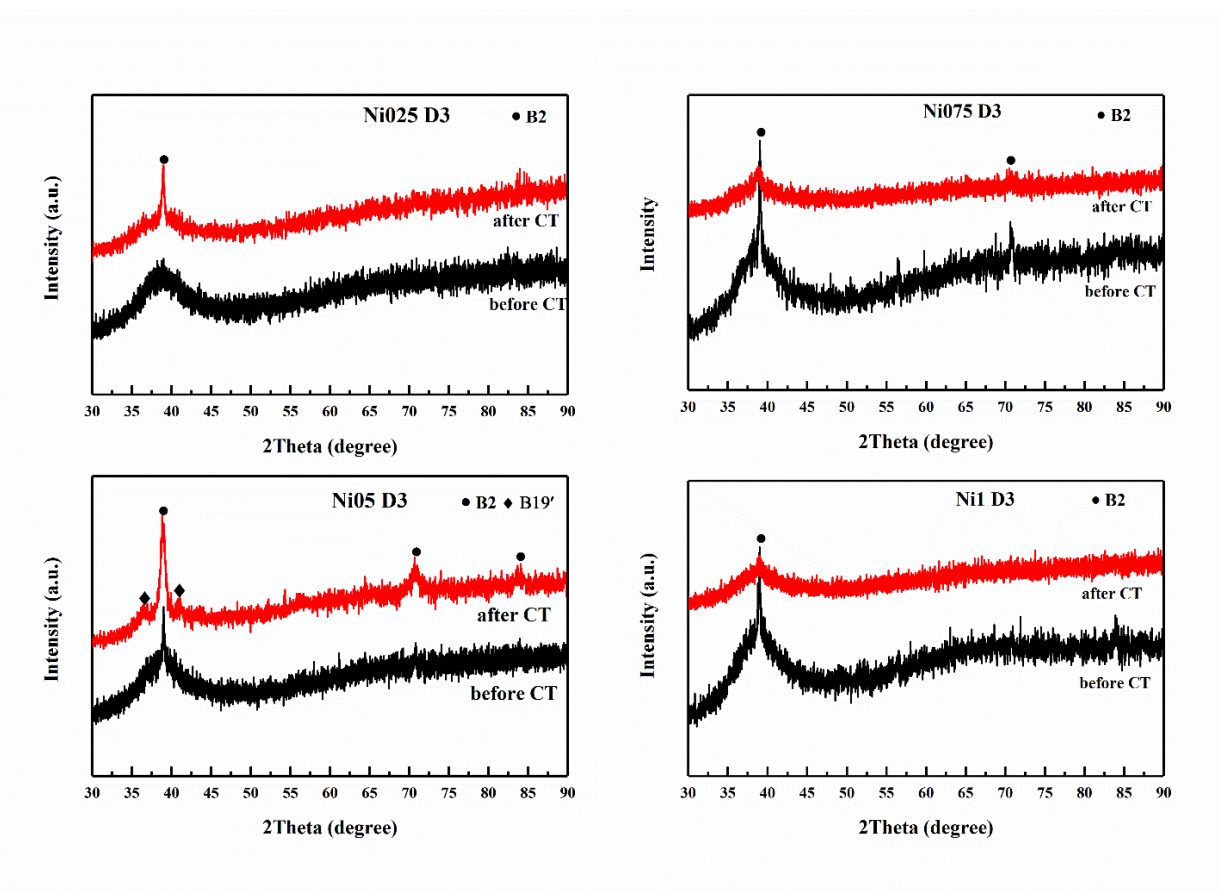


Figure 5.8. XRD patterns comparison of the as-cast and fractured Ni-doped CuZr-based BMG alloys.

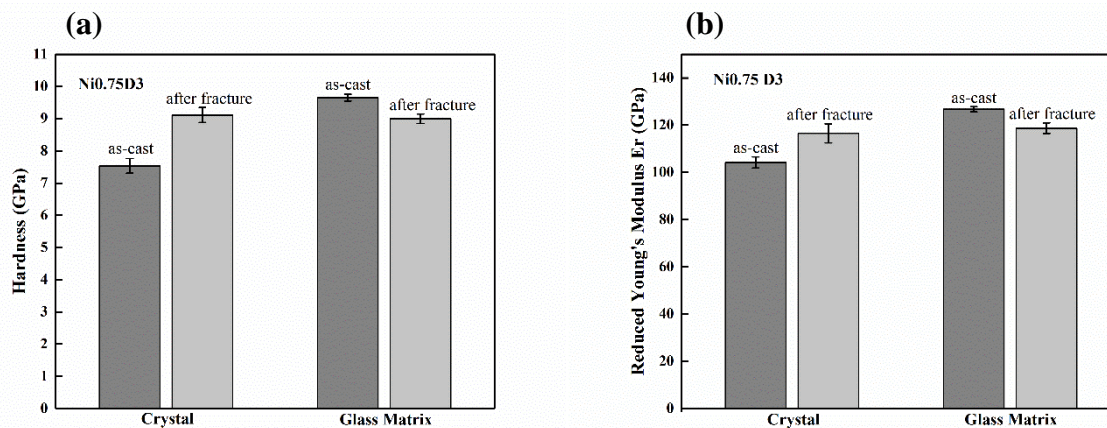


Figure 5.9. (a) Micro-hardness (H) and (b) Reduced Young's Modulus (E_r) of the crystalline phase and amorphous matrix in the as-cast and fractured 0.75 at% Ni doped CuZr BMGMCs.

Table 5.3. Hardness (H) of the crystalline phase and amorphous matrix of as-cast and fractured 0.75 at% Ni doped CuZr BMGMCs obtained from nanoindentation.

$\text{Cu}_{47.25}\text{Zr}_{48}\text{Al}_4\text{Ni}_{0.75}$	As-cast (GPa)	After fractured (GPa)
Crystalline phase	7.54 ± 0.23	9.12 ± 0.23
Amorphous matrix	9.65 ± 0.11	9.00 ± 0.15

In order to further investigate the effect of microstructure and related deformation mechanism, XRD patterns of the as-cast and deformed CuZr-based BMGMCs with different Ni addition are compared in Figure 5.8. As shown in the XRD traces, these CuZr-based BMGMCs with different Ni doping experienced different deformation processes. After compression, CuZr B2 phase was detected in 0.25 at% Ni-doped alloys, indicating that metastable CuZr B2 phase was polymorphically precipitated in the amorphous matrix during deformation. As the Ni addition increased to 0.5 at%, the XRD pattern of fractured samples presents different sharp crystal peaks, which is identified as the martensitic CuZr B19' phase, suggesting martensitic transformation from CuZr B2 phase to B19' has occurred during the compressive deformation. This is in accordance with previous reports [9, 17, 29-31]. However, no CuZr martensitic phase B19' was detected as the Ni addition was further increased to 0.75

at% and 1 at%, with only the CuZr B2 phase peak detected, but with significantly decreased intensity. The broadening of the XRD peaks is usually caused by either the limitation in the spatial extent of the coherent scattering volumes (like grain size) or the presence of inhomogeneous residual stress [32, 33]. As exhibited in Figure 5.6b, a large number of martensite laths with size of 5-6 μm were present in the lateral surface of the fractured 0.75 at% Ni-doped samples. Therefore, it may be attributed to the low crystalline phase volume fraction and severe deformation in the present case. Therefore, further investigation is required to reveal the deformation mechanism underneath.

In addition, nanoindentation tests on the reinforced crystalline phase and amorphous matrix were carried out in the as-cast and fractured 0.75 at% Ni-doped CuZr BMGMCs to evaluate the relationship between microstructure evolution and mechanical properties. The corresponding measurements are given in Figure 5.9 and Table 5.3. The reduced Young's modulus and hardness variations of the crystalline phase and amorphous matrix for the as-cast and deformed specimens are illustrated in Figure 5.9. It is clear that the crystalline B2 phase is softer than the amorphous phase in the as-cast CuZr BMGMCs. As compressive deformation proceeds, the crystalline B2 phase starts to transform into martensitic B19' phase and become progressively harder, while the amorphous matrix is softened as a result of the extensive shear bands formation. Therefore, it is reasonable to deduce that the observed work-hardening phenomenon is a result of the hardening of the CuZr B2 phases. Nevertheless, the role of CuZr B2 phase and amorphous matrix and their interaction in the deformation cannot be ruled out.

In order to obtain a greater insight into the microstructural evolution during compressive deformation and its influence on the mechanical performance, detailed TEM analysis, including glassy matrix and precipitated crystalline phase, was carried out on the plastically deformed 0.75 at% Ni-doped composites. BF TEM images of the severely deformed amorphous phase region in the vicinity of the fracture surface are shown in Figure 5.10. In comparison with the undeformed specimen (Figure 5.7), a bundle of shear bands with a width of 60 – 70 nm with slight dark-grey contrast as highlighted by the white dotted lines was observed, suggesting that the deformation strain in the amorphous matrix is achieved by multiple shearing behaviour. SAED patterns corresponding to dark and grey contrast sheared regions shown in the inset to Figure 5.10a which only contain diffuse halos typical of an amorphous structure. HRTEM images for the dark and grey sheared regions are shown in Figure 5.10b and c. Only a typical amorphous structure was seen without any detectable nanocrystalline phase within each shear band, in agreement with the SAED results in the inset

to Figure 5.10a. A similar phenomenon in a Zr-based BMG has been reported before [34]. The amorphous matrix was softened after deformation according to the hardness changes measured by nanoindentation. Deformation strain accommodation in the amorphous matrix was achieved by the multiple shear bands formation, and thereby contributing to the improved plasticity. It is reasonable to deduce that strength enhancement and work-hardening ability should be the contribution from the reinforced spherical crystalline phases. Therefore, the microstructure of the reinforced crystalline phases and interfaces of the fractured composites will be explored to rationalize the deformation micromechanism.

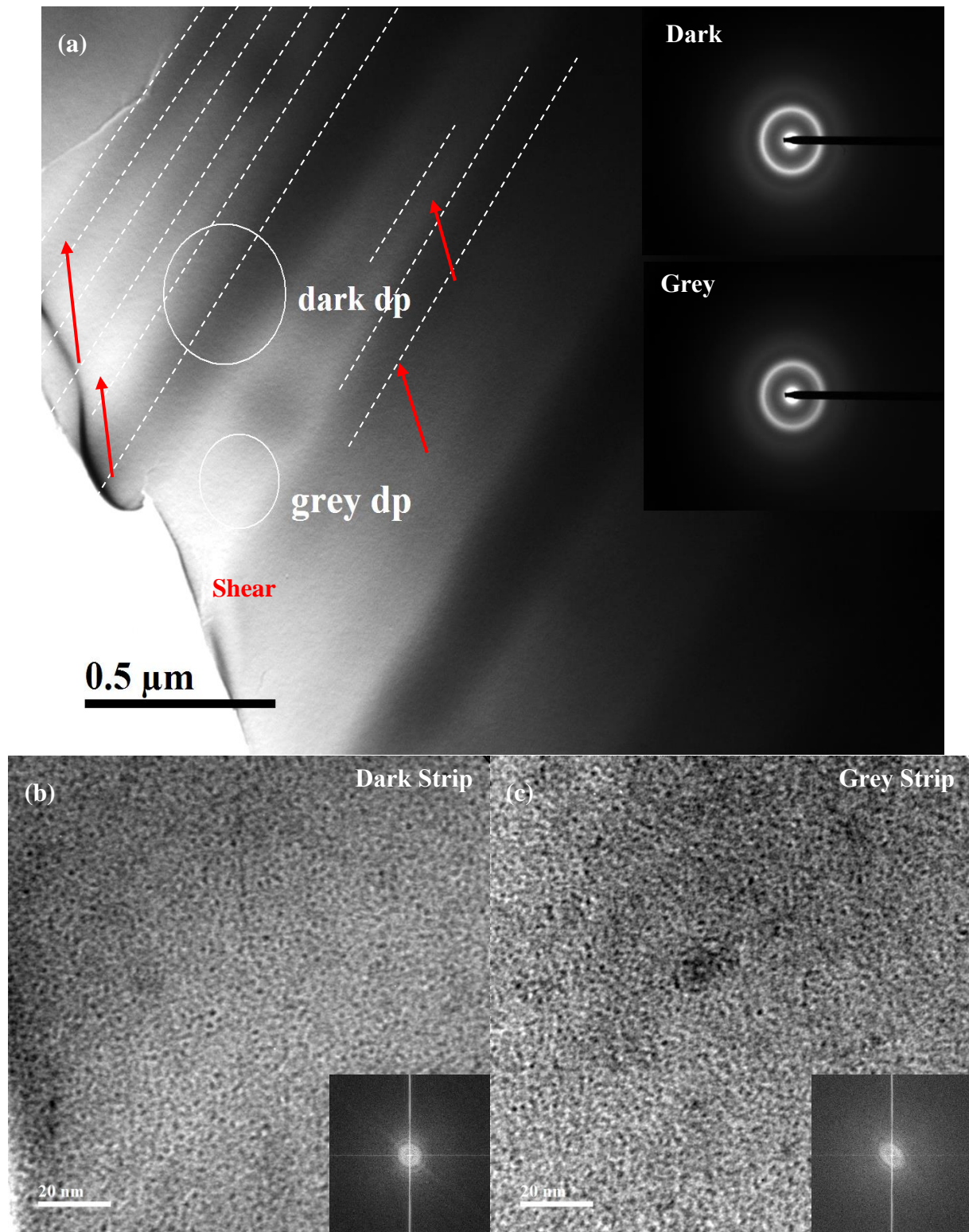


Figure 5.10. TEM bright field (BF) images of the as-deformed 0.75 at% Ni-doped CuZr BMGMCs: (a) low-magnification BF images; (c) (d) HRTEM images for dark strip and grey strip.

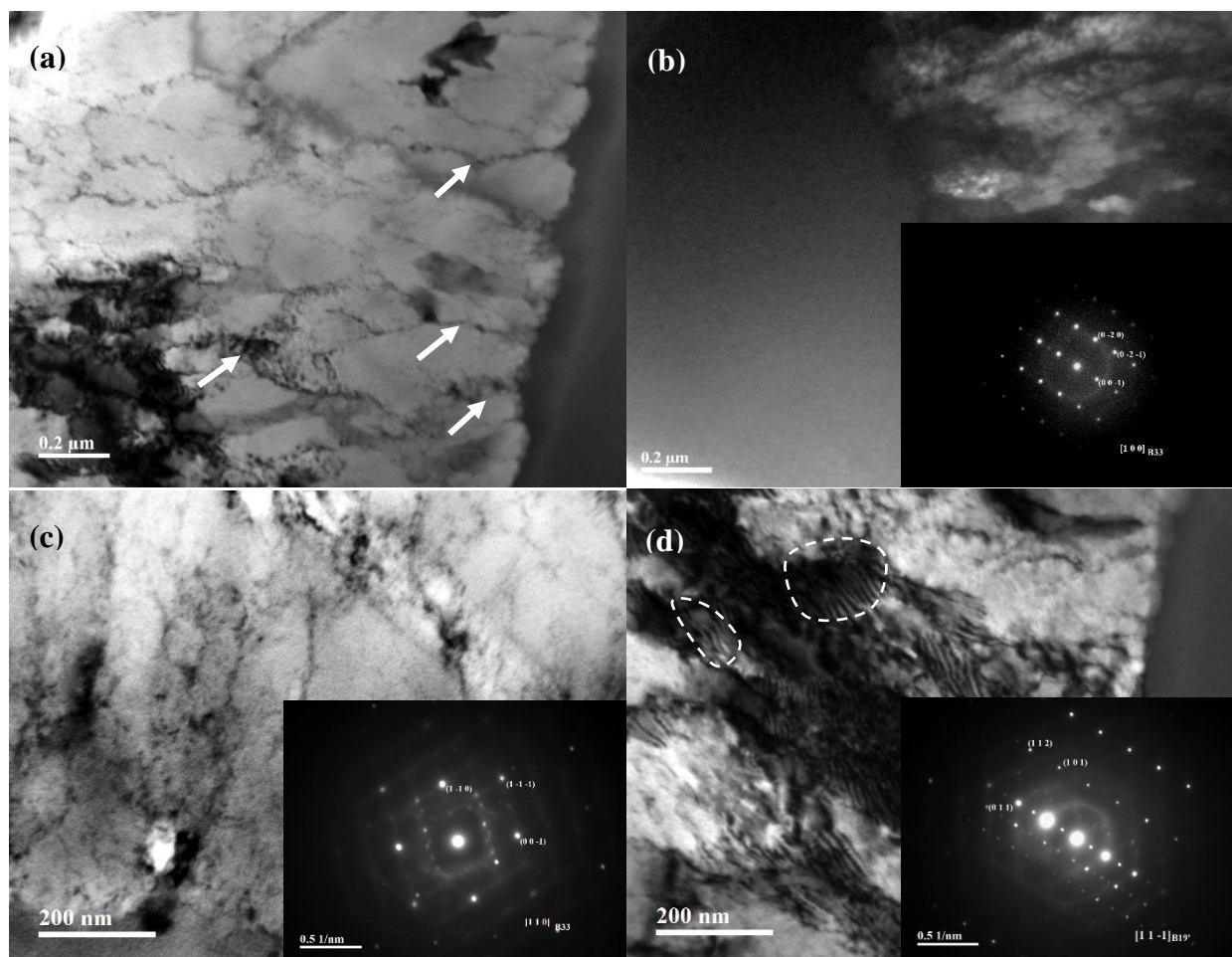


Figure 5.11. TEM bright field (BF) images of interface between crystalline phase and amorphous matrix in the fractured 0.75 at% Ni-doped CuZr BMGMCs.

Figure 5.11 shows BF TEM images of the spherical crystal phases and the interfaces between crystals and amorphous phase of the heavily deformed composite specimen. In comparison with the morphology of crystals of the as-cast samples in Figure 5.7, subdivisions separated by dense dislocation walls, as denoted by white arrows in Figure 5.11a, are present in the fractured samples. They may have formed either along with martensitic transformation [35] or as a result of severe and harmonized deformation [36]. In addition, tortuous martensitic slats, as marked in dashed circles (Figure 5.11d), appeared in the vicinity of the interface, indicating the existence of large residual stress and thereby heavy deformation in the crystalline phase. Two martensite variants are identified in the deformed specimens. The SAED in the inset (Figure 5.11d) confirms the existence of the monoclinic martensite B19'. Another martensite variant close to the interface is identified as B33 on the zone axis $[1\ 0\ 0]$ and $[1\ 1\ 0]$ (Figure 5.11b and c), respectively, indicating different orientations. As reported previously,

CuZr shape memory phase will undergo a martensitic transformation from a B2 structure to two monoclinic martensitic structures upon heating: one is a base structure (B19') with P21/m symmetry and the other is a superstructure (Cm) with Cmcm symmetry [37, 38]. The structural characteristics of martensite B19' and B33 are dense dislocation and twins, respectively [38]. It is believed that they will be responsible for further improvement in plasticity and work-hardening after phase transformation.

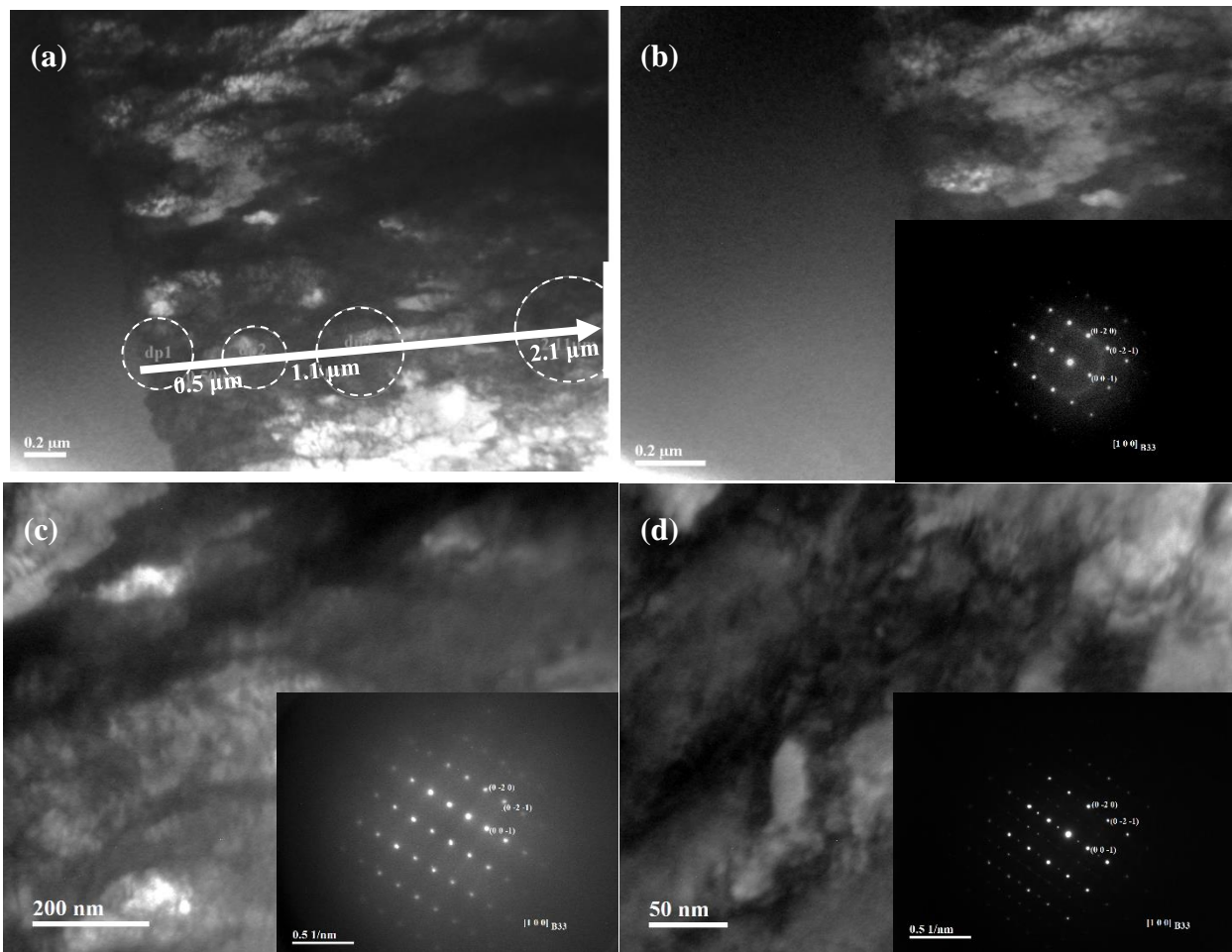


Figure 5.12. TEM bright field (BF) images of microstructure evolution from interface into the crystalline phase in the fractured 0.75 at% Ni-doped CuZr BMGMCs: (a) overall illustration; (b) near interface; (c) further inside 1 μm ; (d) further inside 2 μm .

Figure 5.12 gives the BF TEM images showing the martensitic transformation dimensional range. The corresponding SAED patterns, from the area close to the interface to the region 2 μm inwards, were identified as martensite B33 phase on zone axis [1 0 0], demonstrating the stress-induced martensitic transformation from B2 to B33. Compared to the microstructure in the undeformed samples, this is clear evidence that the stress-induced martensitic

transformation occurred from the interface and the distance over which the martensitic transformation occurred was more than 2 μm . For more detailed structural changes, HRTEM analysis is required.

On the basis of the TEM investigation for the microstructural evolution from the as-cast state to the fractured state, it is confirmed that the martensitic transformation initiated upon deformation in the vicinity of the interface between crystalline reinforcement and amorphous matrix and gradually moved to the inside of crystalline phase as the deformation proceeded. The deformation process involved three interactions: amorphous matrix to spherical crystalline phase (mainly B2 phase) in the initial deformation stage, transformed B19' and B33 to the amorphous phase, different transformed martensitic variants [39, 40]. At the early deformation stage, the stress concentration at the interface results from both lattice mismatch and elastic modulus mismatch between crystalline phases (mainly B2) and the amorphous matrix. The stress concentration would have been released by the initiation of the martensitic transformation in the vicinity of the interface [41]. The interface and sparsely distributed martensites will act as the nucleation sites for further the martensitic transformation. As the stress continued to increase, the martensitic transformation zone would have gradually moved to the inside of the crystalline phase. As the deformation continued, the stress concentration close to the interface between transformed martensites and amorphous phase increased, promoting the initiation of the shear bands in the amorphous matrix [42]. The formation of multiple shear bands will lead to the softening of the matrix phase, and the propagation of shear bands will be hindered due to the martensitic phase transformation. At the same time, orientation accommodation of transformed martensitic variants and dislocation formation between crystals will further enhance plasticity and work-hardening ability in the current composites.

5.5 Conclusion

In summary, the microstructures and the mechanical properties of CuZr-based BMGMCs with different Ni additions (0, 0.25, 0.5, 0.75, 1 at%) were systematically investigated. The size and distribution of crystalline CuZr precipitates in an amorphous matrix can be adjusted by appropriate Ni additions, thereby affecting mechanical properties. TEM was used to analyse the microstructure changes in the spherical crystals, amorphous matrix and interface between them in the 0.75 at% Ni-doped CuZr-based composites from as-cast state to severely fractured

state. Upon loading, martensitic transformation from austenitic B2 phase to martensitic phases was initiated in the vicinity of the interface. Pre-existed needle-like martensites and interface acted as the nucleation sites for further martensitic transformation. With the deformation proceeding, martensitic transformation zone gradually extended from the interface to the inside of crystalline phase (mainly B2). Interaction between untransformed crystalline phase and amorphous matrix, and between transformed crystalline phase and amorphous matrix contributed to the improved plasticity and work-hardening ability in the current composites. The mechanical properties for Ni-doped BMGMCs in the size of 3 mm are as summarized in Table 5.4.

Table 5.4. The summary of mechanical properties for Ni-doped BMGMCs in the size of 3mm.

Ni addition (at%)	σ_Y (MPa)	σ_f (MPa)	ε_y (%)	ε_f (%)	T_g (K)	T_x (K)	ΔT_x (K)	Crystal fraction (%)	Crystal size (μm)
0.25	1610	1796	2.3	4.0	694	759	65	-	-
0.50	1147	1758	1.9	4.6	694	760	66	~ 20	~ 9
0.75	1493	1748	2.0	5.1	693	760	67	~ 15	~ 14
1.00	1657	1796	2.4	4.0	692	759	67	~ 9	~ 24

5.6 References

- [1] W. H. Wang, C. Dong, and C. H. Shek, "Bulk metallic glasses," *Materials Science and Engineering: R: Reports*, vol. 44, no. 2, pp. 45-89, 2004/06/01/ 2004.
- [2] J. F. Löffler, "Bulk metallic glasses," *Intermetallics*, vol. 11, no. 6, pp. 529-540, 2003.
- [3] J. Schroers, "Processing of Bulk Metallic Glass," *Advanced Materials*, vol. 22, no. 14, pp. 1566-1597, 2010/04/12 2009.
- [4] C. A. Schuh, T. C. Hufnagel, and U. Ramamurty, "Mechanical behavior of amorphous alloys," *Acta Materialia*, vol. 55, no. 12, pp. 4067-4109, 2007/07/01/ 2007.
- [5] M. Chen, "A brief overview of bulk metallic glasses," *Npg Asia Materials*, Review vol. 3, p. 82, 09/22/online 2011.
- [6] M. F. Ashby and A. L. Greer, "Metallic glasses as structural materials," *Scripta Materialia*, vol. 54, no. 3, pp. 321-326, 2006/02/01/ 2006.
- [7] D. C. Hofmann, "Shape memory bulk metallic glass composites," *Science*, vol. 329, no. 5997, pp. 1294-1295, 2010.
- [8] F. F. Wu, Z. F. Zhang, S. X. Mao, A. Peker, and J. Eckert, "Effect of annealing on the mechanical properties and fracture mechanisms of a Zr_{56.2}Ti_{13.8}Nb_{5.0}Cu_{6.9}Ni_{5.6}Be_{12.5} bulk metallic glass composite," *Physical Review B*, vol. 75, no. 13, p. 134201, 04/09/ 2007.
- [9] Y. Wu *et al.*, "Formation of Cu–Zr–Al bulk metallic glass composites with improved tensile properties," *Acta Materialia*, vol. 59, no. 8, pp. 2928-2936, 2011/05/01/ 2011.

- [10] S. Pauly *et al.*, "Deformation-induced martensitic transformation in Cu–Zr–(Al, Ti) bulk metallic glass composites," *Scripta Materialia*, vol. 60, no. 6, pp. 431-434, 2009.
- [11] J. Das *et al.*, "Work-Hardenable" Ductile Bulk Metallic Glass," *Physical Review Letters*, vol. 94, no. 20, p. 205501, 05/23/ 2005.
- [12] T. Abe, M. Shimono, M. Ode, and H. Onodera, "Thermodynamic modeling of the undercooled liquid in the Cu–Zr system," *Acta Materialia*, vol. 54, no. 4, pp. 909-915, 2006/02/01/ 2006.
- [13] S. Pauly, G. Liu, G. Wang, U. Kühn, N. Mattern, and J. Eckert, "Microstructural heterogeneities governing the deformation of Cu_{47.5}Zr_{47.5}Al₅ bulk metallic glass composites," *Acta Materialia*, vol. 57, no. 18, pp. 5445-5453, 2009.
- [14] Z. P. Lu and C. T. Liu, "Role of minor alloying additions in formation of bulk metallic glasses: A Review," *Journal of Materials Science*, vol. 39, no. 12, pp. 3965-3974, 2004/06/01 2004.
- [15] W. H. Wang, "Roles of minor additions in formation and properties of bulk metallic glasses," *Progress in Materials Science*, vol. 52, no. 4, pp. 540-596, 2007/05/01/ 2007.
- [16] Y. Wu *et al.*, "Ductilizing bulk metallic glass composite by tailoring stacking fault energy," *Physical review letters*, vol. 109, no. 24, p. 245506, 2012.
- [17] Y. Wu, Y. Xiao, G. Chen, C. T. Liu, and Z. Lu, "Bulk Metallic Glass Composites with Transformation-Mediated Work-Hardening and Ductility," *Advanced Materials*, vol. 22, no. 25, pp. 2770-2773, 2010.
- [18] S. Pauly, J. Das, C. Duhamel, and J. Eckert, "Martensite Formation in a Ductile Cu_{47.5}Zr_{47.5}Al₅ Bulk Metallic Glass Composite," *Advanced Engineering Materials*, vol. 9, no. 6, pp. 487-491, 2007.

- [19] S. Pauly *et al.*, "Modeling deformation behavior of Cu–Zr–Al bulk metallic glass matrix composites," *Applied Physics Letters*, vol. 95, no. 10, pp. 101906-101906-3, 2009.
- [20] Z. F. Zhang, J. Eckert, and L. Schultz, "Difference in compressive and tensile fracture mechanisms of Zr₅₉Cu₂₀Al₁₀Ni₈Ti₃ bulk metallic glass," *Acta Materialia*, vol. 51, no. 4, pp. 1167-1179, 2/25/ 2003.
- [21] A. Inoue and B. L. Shen, "A New Fe-based Bulk Glassy Alloy with Outstanding Mechanical Properties," *Advanced Materials*, vol. 16, no. 23-24, pp. 2189-2192, 2004/12/17 2004.
- [22] Y. Wei, J. Du, and R. Chen, "Martensitic transformation induced plasticity in ZrCuAl metallic glass composites: Precipitate size and volume effects," *Intermetallics*, vol. 68, pp. 1-4, 1// 2016.
- [23] S. H. Hong *et al.*, "Work-hardening and plastic deformation behavior of Ti-based bulk metallic glass composites with bimodal sized B₂ particles," *Intermetallics*, vol. 62, no. 0, pp. 36-42, 7// 2015.
- [24] J. Ding, Z. Liu, H. Wang, and T. Zhang, "Large-sized CuZr-based Bulk Metallic Glass Composite with Enhanced Mechanical Properties," *Journal of Materials Science & Technology*, vol. 30, no. 6, pp. 590-594, 6// 2014.
- [25] A. Takeuchi and A. Inoue, "Classification of bulk metallic glasses by atomic size difference, heat of mixing and period of constituent elements and its application to characterization of the main alloying element," *Materials Transactions*, vol. 46, no. 12, pp. 2817-2829, 2005.
- [26] T. Egami and Y. Waseda, "Atomic size effect on the formability of metallic glasses," *Journal of Non-Crystalline Solids*, vol. 64, no. 1, pp. 113-134, 1984/04/01/ 1984.
- [27] *Periodic Table*. Available: <http://www.rsc.org/periodic-table>

- [28] W. Martienssen and H. Warlimont, *Springer handbook of condensed matter and materials data*. Springer Science & Business Media, 2006.
- [29] K. Song *et al.*, "Formation of Cu–Zr–Al–Er bulk metallic glass composites with enhanced deformability," *Intermetallics*, vol. 30, pp. 132-138, 2012.
- [30] S. Pauly *et al.*, "Criteria for tensile plasticity in Cu–Zr–Al bulk metallic glasses," *Acta Materialia*, vol. 58, no. 14, pp. 4883-4890, 8// 2010.
- [31] Y. J. Liu *et al.*, "Designing ductile CuZr-based metallic glass matrix composites," *Materials Science and Engineering: A*, vol. 682, pp. 542-549, 1/13/ 2017.
- [32] Z. Budrovic, H. Van Swygenhoven, P. M. Derlet, S. Van Petegem, and B. Schmitt, "Plastic Deformation with Reversible Peak Broadening in Nanocrystalline Nickel," *Science*, 10.1126/science.1095071 vol. 304, no. 5668, p. 273, 2004.
- [33] H. P. Klug and L. E. Alexander, "X-ray diffraction procedures: for polycrystalline and amorphous materials," *X-Ray Diffraction Procedures: For Polycrystalline and Amorphous Materials, 2nd Edition*, by Harold P. Klug, Leroy E. Alexander, pp. 992. ISBN 0-471-49369-4. Wiley-VCH, May 1974., p. 992, 1974.
- [34] X. H. Du *et al.*, "Phase-separated microstructures and shear-banding behavior in a designed Zr-based glass-forming alloy," *Intermetallics*, vol. 17, no. 8, pp. 607-613, 8// 2009.
- [35] T. Simon, A. Kröger, C. Somsen, A. Dlouhy, and G. Eggeler, "On the multiplication of dislocations during martensitic transformations in NiTi shape memory alloys," *Acta Materialia*, vol. 58, no. 5, pp. 1850-1860, 2010/03/01/ 2010.
- [36] J. Qiao, A. Sun, E. Huang, Y. Zhang, P. Liaw, and C. Chuang, "Tensile deformation micromechanisms for bulk metallic glass matrix composites: From

- work-hardening to softening," *Acta Materialia*, vol. 59, no. 10, pp. 4126-4137, 2011.
- [37] J. W. Seo and D. Schryvers, "TEM investigation of the microstructure and defects of CuZr martensite. Part I: Morphology and twin systems," *Acta Materialia*, vol. 46, no. 4, pp. 1165-1175, 2/13/ 1998.
- [38] J. W. Seo and D. Schryvers, "TEM investigation of the microstructure and defects of CuZr martensite. Part II: Planar defects," *Acta Materialia*, vol. 46, no. 4, pp. 1177-1183, 1998/02/13/ 1998.
- [39] Y. Wu *et al.*, "Transformation-induced plasticity in bulk metallic glass composites evidenced by in-situ neutron diffraction," (in English), *Acta Materialia*, vol. 124, pp. 478-488, Feb 1 2017.
- [40] D. M. Wang *et al.*, "An in situ neutron diffraction study of plastic deformation in a Cu_{46.5}Zr_{46.5}Al₇ bulk metallic glass composite," *Scripta Materialia*, vol. 153, pp. 118-121, 8// 2018.
- [41] S. H. Hong *et al.*, "Gradual martensitic transformation of B2 phase on TiCu-based bulk metallic glass composite during deformation," *Intermetallics*, vol. 75, pp. 1-7, 2016/08/01/ 2016.
- [42] Z. Liu, G. Liu, R. Qu, Z. Zhang, S. Wu, and T. Zhang, "Microstructural percolation assisted breakthrough of trade-off between strength and ductility in CuZr-based metallic glass composites," *Scientific reports*, vol. 4, 2014.

Chapter 6 Phase Separation in $\text{Cu}_{47.5}\text{Zr}_{48}\text{Al}_4\text{Co}_{0.5}$ Bulk Metallic Glass

6.1 Introduction

Bulk metallic glasses (BMGs), as a potential structural material, have been studied extensively [1-4]. BMGs possess of many desired properties, such as large elastic strain limits (up to 2%), high strength and hardness and excellent corrosion resistance. However, BMGs are still far from practical application because of its catastrophic failure under tensile loading. Thus, there have been substantial effort to improve their plasticity. At present, three strategies have been proposed [5-10]: in-situ induced dendrite reinforced BMG composite structure; ex-situ induced crystalline reinforced BMG composite structure and liquid phase separation BMG structure.

Recently, bulk metallic glass with composition of $\text{Cu}_{47.5}\text{Zr}_{48}\text{Al}_4\text{Co}_{0.5}$ has attracted extensive research interests due to its excellent tensile plasticity and distinctive work hardening [11-14]. Martensitic phase transformation of shape memory phase, from cubic austenite B2 phase to monoclinic martensite B19' phase, results in appreciable improvement in mechanical properties. The observation of phase separation in an amorphous matrix makes it more interesting, which may contribute to its enhanced plasticity to some extent, but the precise effect is unknown.

Liquid phase separation, as a strategy to develop bulk metallic glass with large plasticity, has been studied in several systems, including CuZr-based BMG system [15-18]. It was stated that structural heterogeneity could not only lead to multiplication of shear bands, but also could block the propagation of shear bands during deformation. In most circumstances, phase separation can be introduced into the system by adding alloying element that have a positive enthalpy of mixing with other constituents. According to Inoue's empirical rules [19, 20], however, addition of elements with positive enthalpy of mixing will degrade glass forming ability (GFA) of the system.

Thus, in most cases only minor alloying addition was induced into the system. For example, minor Ag was added into Cu-Zr-Al system to introduce liquid phase separation[16]. In this situation, mixing enthalpy of Ag-Cu is +5kJ/mol, which leads to the formation of Cu-rich and Ag-rich amorphous phases in the specimen. Similarly, for the current BMG, Co has a small positive enthalpy of mixing with Cu ($\Delta H_{\text{Co-Cu}}=+6\text{kJ/mol}$) and has a large negative enthalpy of mixing with Zr ($\Delta H_{\text{Co-Zr}}=-41\text{kJ/mol}$), as shown in Figure 6.1. Thus, it is probable that phase separation will occur in the Cu-Zr-Al-Co quaternary system.

The aim of this study is to investigate whether or not there any inhomogeneity (phase separation) occurs in the as-cast $\text{Cu}_{47.5}\text{Zr}_{48}\text{Al}_4\text{Co}_{0.5}$ alloy by SEM, TEM, atomic force microscopy (AFM) and nanoindentation, and to explain whether or not phase separation contributes to enhanced plasticity under compression.

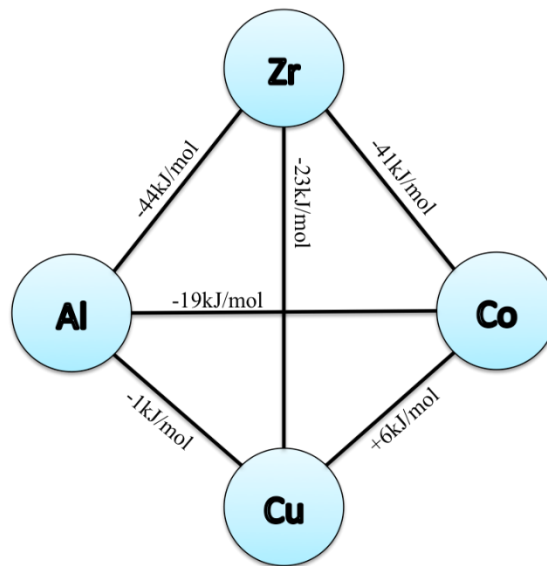


Figure 6.1. Mix enthalpy (ΔH_{mix}) calculated by Miedema's model between atomic element pairs in the studied $\text{Cu}_{47.5}\text{Zr}_{48}\text{Al}_4\text{Co}_{0.5}$ BMGs [19].

6.2 Experimental

Master alloys with a nominal composition of $\text{Cu}_{47.5}\text{Zr}_{48}\text{Al}_4\text{Co}_{0.5}$ (at%) were prepared by arc melting constituting elements with high purity ($\geq 99.8\%$) in a Ti-gettered argon atmosphere. Each sample was remelted at least 4 times to obtain chemical homogeneity. Mass loss for each alloy during preparation was negligible (≤ 0.1 wt%). Cylinder ingots with diameter of 2 mm, 3 mm, 4 mm and length of 30mm were obtained by copper mould suction casting. Rapidly quenched ribbons with the same composition were produced by remelting the alloys in quartz crucibles, and ejecting with an overpressure of 40 kPa through a nozzle onto a copper wheel rotating with a surface velocity of 45 m/s.

Nanoindentation testing was conducted on a well-polished transverse section surface of the as-cast specimen $\text{Cu}_{47.5}\text{Zr}_{48}\text{Al}_4\text{Co}_{0.5}$ with 3 mm diameter at room temperature using a TriboScope system mounted on a DI AFM with a Nanoscope III controller. Separate individual indents on dark and light phase areas were performed carefully to avoid interactions. The number of indents performed allows statistical calculations from the raw data. Load-displacement curves were stored for each single indent and hardness and elastic modulus were calculated using the Oliver and Pharr method [22]. Compression testing was performed at a strain rate of $1 \times 10^{-4} \text{ s}^{-1}$ at room temperature. The testing samples with aspect of 2:1 were cut from the rods.

6.3 Results

6.3.1 Structural characterization of the as-spun and as-cast samples

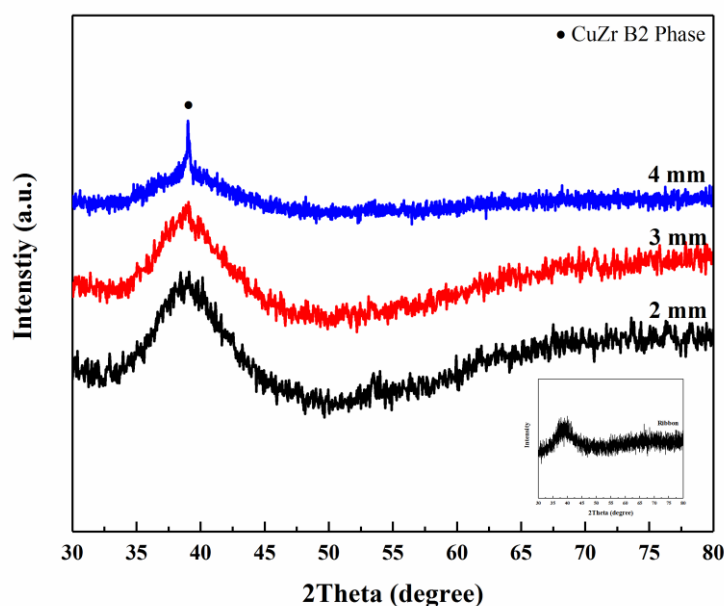


Figure 6.2. XRD patterns of as-cast rods with diameters of 2 mm, 3 mm and 4 mm for $\text{Cu}_{47.5}\text{Zr}_{48}\text{Al}_4\text{Co}_{0.5}$ BMG alloys. The inset is the XRD pattern for the as-spun ribbon.

Figure 6.2 shows the XRD patterns of as-cast rods with diameters of 2 mm, 3 mm and 4 mm and as-spun ribbon (as inset) for the $\text{Cu}_{47.5}\text{Zr}_{48}\text{Al}_4\text{Co}_{0.5}$ BMG alloys. For rapidly quenched ribbon alloy and as-cast rod alloys with the diameters of 2 mm and 3 mm, there are no appreciable diffraction peaks on the main broad maxima, indicating a fully amorphous structure. For the as-cast rod with a diameter of 4 mm, a small crystalline peak superimposed with a typical amorphous diffuse hump was observed, which demonstrates the formation of crystalline CuZr B2 phase in the amorphous matrix with the decreasing cooling rates.

Figure 6.3 displays DSC results of as-spun ribbon and as-cast rods with diameters

of 2 mm, 3 mm and 4 mm for the $\text{Cu}_{47.5}\text{Zr}_{48}\text{Al}_4\text{Co}_{0.5}$ BMG alloys, all exhibiting an endothermic event characteristic of the glass transition, a distinct supercooled liquid region and an exothermic peak due to crystallization. Glass transition temperature (T_g), crystallization temperature (T_x) and supercooled liquid region (ΔT_x) is summarized in Table 6.1. It can be seen that all the as-cast alloys display a large ΔT_x of 67 K, 66 K and 63 K with the increasing sample size from 2 mm to 4 mm. As the cooling rate decreases, both T_g and T_x move to high temperatures for the as-cast alloys. To further determine the crystallinity of the as-spun ribbon and the as-cast rod alloys, the crystallization enthalpy (ΔH_c) for each sample was measured by DSC (as summarized in Table 6.1). On the basis of a simplified assumption that the as-spun ribbon was fully amorphous, the volume fraction of amorphous phase in each sample could be determined by the ratio of the crystallization enthalpy for each sample in comparison with that of the as-spun ribbon. As calculated, the volume fraction of CuZr B2 phase is estimated to be 0%, 0% and 27% for the rods with diameters from 2 mm to 4 mm, respectively (Table 6.1). As reported by Wu *et al.* [13] and Kozachkov *et al.* [14], the volume fraction of crystalline B2 phase in the rod with the diameter of 3 mm is about 25%, which exhibits distinct tensile ductility of 10%. In this study, the specimens in the size of 4 mm possess the similar crystalline volume fraction, while the samples with smaller size (≤ 3 mm) are supposed to be fully amorphous.

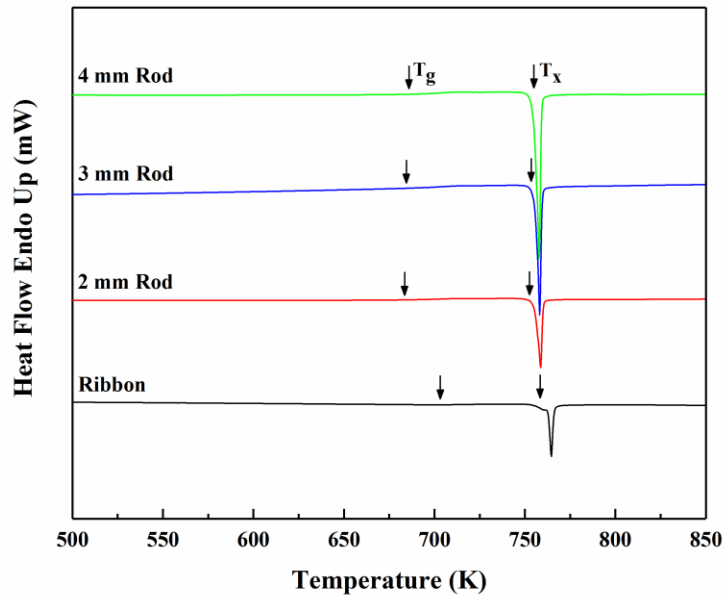


Figure 6.3. DSC curve from as-spun ribbon and as-cast rods with diameters of 2 mm, 3 mm and 4 mm for the $\text{Cu}_{47.5}\text{Zr}_{48}\text{Al}_4\text{Co}_{0.5}$ BMG alloys, which shows glass transition temperature T_g , crystallization transformation temperature T_x .

Table 6.1. The thermal stability and the crystalline volume fraction of the as-spun ribbon and as-cast rods with different diameters for $\text{Cu}_{47.5}\text{Zr}_{48}\text{Al}_4\text{Co}_{0.5}$ BMG alloys.

$\text{Cu}_{47.5}\text{Zr}_{48}\text{Al}_4\text{Co}_{0.5}$ BMG alloys (at %)	T_g (K)	T_x (K)	ΔT_x (K)	ΔH_c (J/g)	B2 phase volume fraction (%)
As-spun ribbon	703	753	50	-53.5	-
D=2 mm rod	685	752	67	-53.8	Nil
D=3 mm rod	687	753	66	-53.7	Nil
D=4 mm rod	691	754	63	-38.8	27

To reveal their microstructures, as-cast $\text{Cu}_{47.5}\text{Zr}_{48}\text{Al}_4\text{Co}_{0.5}$ BMG alloys with the diameter of 2 mm, 3 mm and 4 mm were characterized through SEM. The microstructure is consistent with the XRD and DSC measurements. The 2 mm diameter alloy displayed a uniform structure without any crystal formation; the alloy with the

size of 3 mm exhibits an interconnected ‘two phase’ structure – one slightly brighter in contrast and the other slightly darker. The 4mm diameter alloy exhibited a composite structure with spherical CuZr B2 phase distributed in the glassy phase matrix. Phase separation occurred in the $\text{Cu}_{47.5}\text{Zr}_{48}\text{Al}_4\text{Co}_{0.5}$ BMGs with the size of 3 mm in diameter.

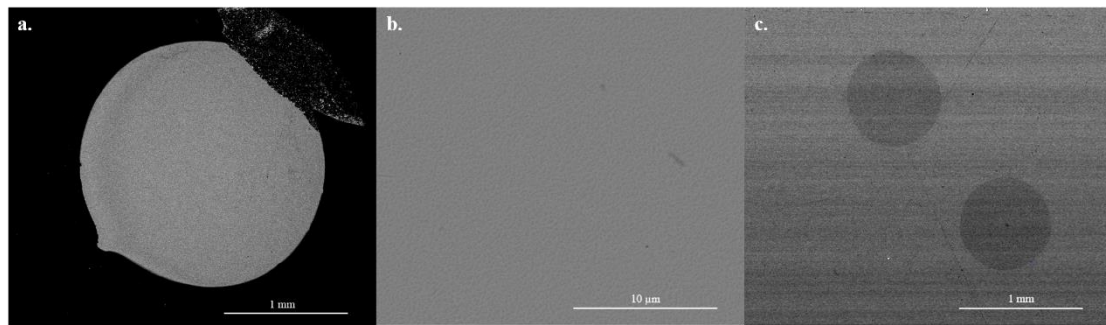


Figure 6.4. SEM images (in Backscattered electron mode) of as-cast rods for $\text{Cu}_{47.5}\text{Zr}_{48}\text{Al}_4\text{Co}_{0.5}$ BMGs: (a) 2 mm rod; (b) 3 mm rod; (c) 4 mm rod.

The interconnected structure, *i.e.* phase separation structure, in $\text{Cu}_{47.5}\text{Zr}_{48}\text{Al}_4\text{Co}_{0.5}$ alloys was further confirmed through atomic force microscopy (AFM) as shown in Figure 6.5. The surface topography and 3D image (Figure 6.5a and b) shows a rough surface texture, which provided a clear and compelling evidence for the occurrence of phase separation in the current CuZr-based BMG alloy. An arbitrary sectional roughness image (Figure 6.5c) shows that the distance between the top point and the bottom point is around 4 nm.

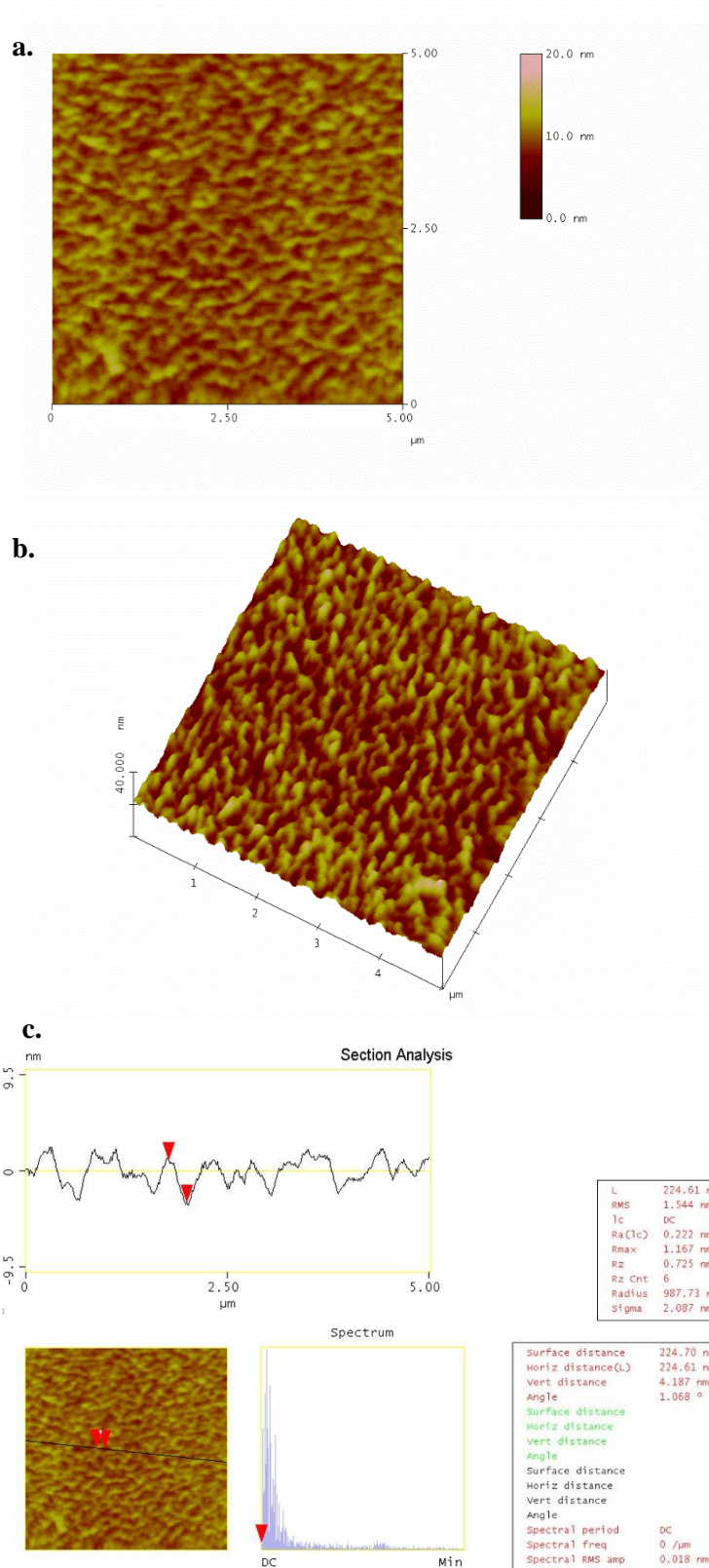


Figure 6.5. AFM images of the as-cast rods with diameter of 3 mm for $\text{Cu}_{47.5}\text{Zr}_{48}\text{Al}_4\text{Co}_{0.5}$ BMG: (a) surface topology image; (b) 3D image; (c) surface roughness image.

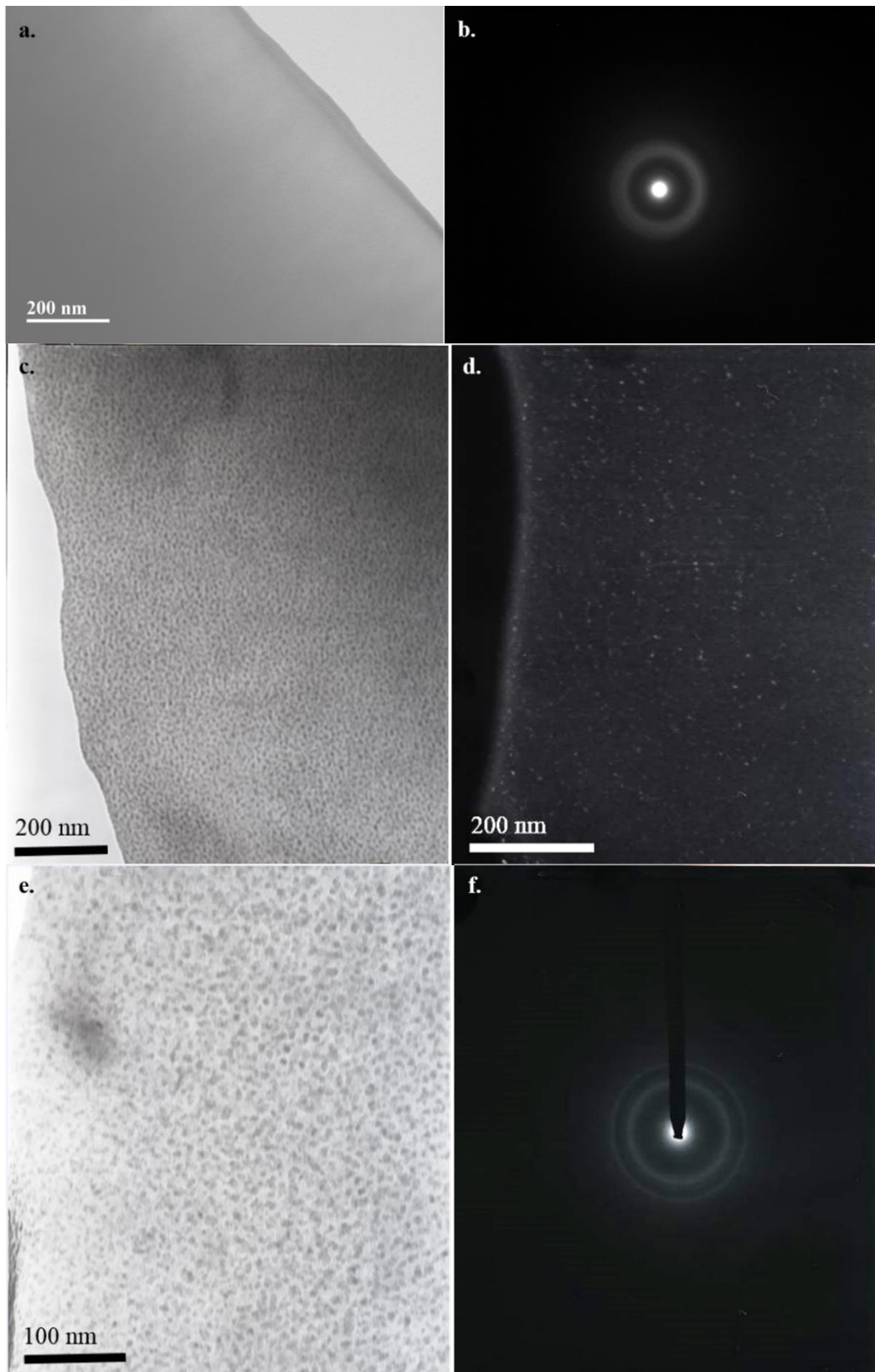


Figure 6.6. TEM images of $\text{Cu}_{47.5}\text{Zr}_{48}\text{Al}_4\text{Co}_{0.5}$ BMG: (a) (b) bright field image and diffraction pattern for as-spun BMG; (c) (e) bright field image, (d) dark field image, (f) diffraction pattern for as-cast BMG with diameter of 3 mm.

TEM images taken from as-spun ribbon and cross-sectioned as-cast Co_{0.5}D₃ rods were presented in Figure 6.6. There is no phase separation for the as-spun samples, exhibiting a simple grey contrast and a single halo diffuse ring, as shown in Figure 6.6a and b. It indicates that the structure for as-spun ribbon is homogeneous. In contrast, the bright field and the dark field TEM images of as-cast Co_{0.5}D₃ BMG (Figure 6.6c, d and e) clearly shows the presence of two different phases with darker and brighter contrast. The dark areas with the size of around 20 nm are surrounded by the bright areas. The selective area electron diffraction pattern (SADP) (Figure 6.6f) displays two diffuse halo rings without any diffraction spots formation, confirming their amorphous nature for both dark and bright phases, in good agreement with the XRD results.

6.3.2 Mechanical properties

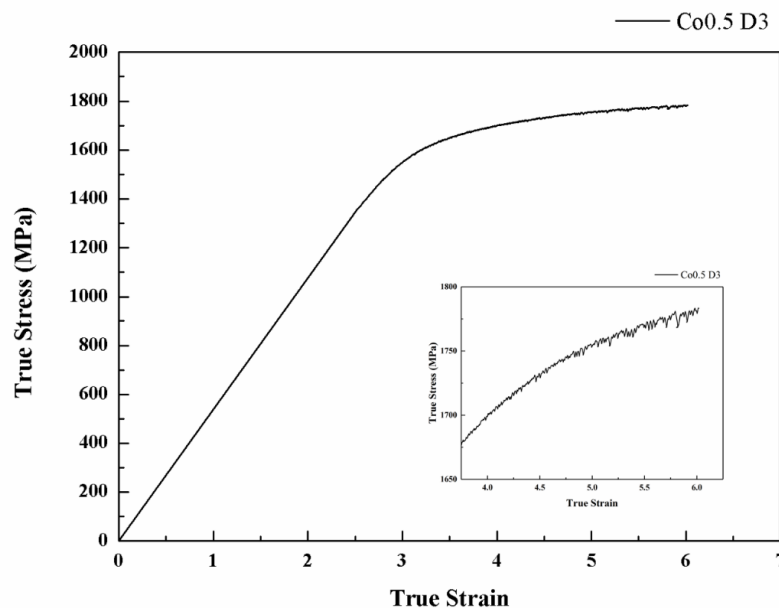


Figure 6.7. Compressive stress-strain curves for the as-cast Cu_{47.5}Zr₄₈Al₄Co_{0.5} BMG rods with 3 mm diameter at room temperature, Inset: enlarged work hardening part to clearly illustrate serrated flow pattern.

The compressive true stress-strain curve of as-cast Cu_{47.5}Zr₄₈Al₄Co_{0.5} BMG rods

with 3mm diameter at room temperature is given in Figure 6.7. A large elastic strain limit of nearly 2.5% was observed before yielding at 1382 MPa under quasi-static loading. After yield, the alloy exhibits distinctive work hardening to its maximum true stress of 1784 MPa, and then fractures catastrophically the same as other BMGs. The total true compressive plasticity of the current $\text{Cu}_{47.5}\text{Zr}_{48}\text{Al}_4\text{Co}_{0.5}$ BMG reaches 6%, which is slightly lower than the reported tensile ductility value of around 7% in total [13]. The work-hardening behaviour may result from the continuous initiation of multiple shear bands with different critical shear stress at different regions and their interactions in the BMG alloys.

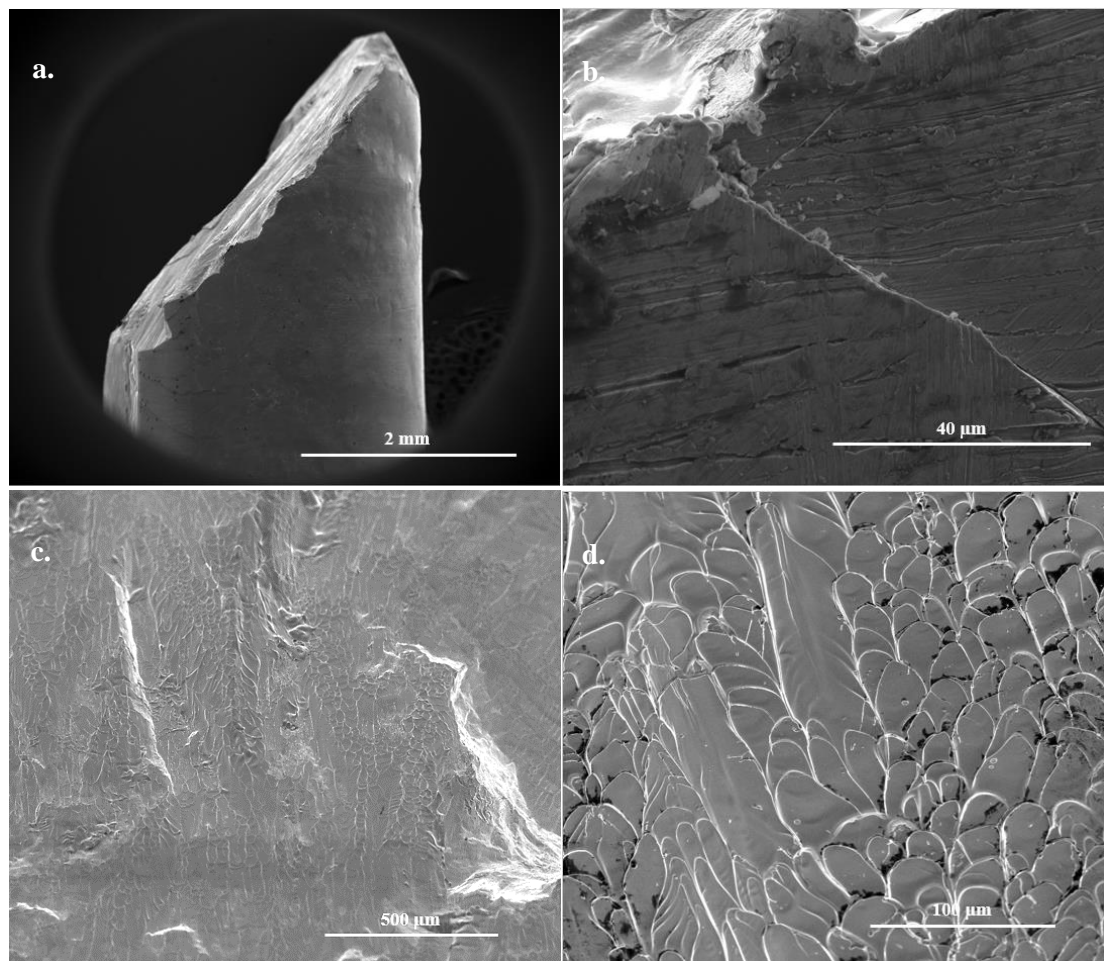


Figure 6.8. SEM images revealing the lateral appearance (a) (b) and fracture surface (c) (d) of as-fractured $\text{Cu}_{47.5}\text{Zr}_{48}\text{Al}_4\text{Co}_{0.5}$ BMG rods with 3 mm diameter after compression at room temperature.

The morphologies of the side surface of the amorphous alloy after compression

failure is presented in Figure 6.8 (a) and (b). The glassy alloy deformed and fractured in a shear mode with a shear off angle of around 46° (Figure 6.8a), indicating a typical fracture behaviour of BMG alloys under compressive loading. In addition, it can be seen that extensive shear bands were formed along the fracture surface (Figure 6.8b), which should account for the enhanced plasticity of the BMG alloy. The fracture surface morphologies of the glassy alloy are displayed in Figure 6.8 (c) and (d). It mainly exhibits two kinds of fracture characteristic zones: one is ordered arrangement of vein-like pattern, the other is a near smooth pattern. Besides, some molten drops could be observed in both areas. It is considered that local deformation will result in local heating in shear bands. As reported by Chen [23], the temperature rise in the shear band could be as high as 400 K, and the continuous work hardening may cause further temperature increase around shear bands, and thereby leading to local melting. Similar fracture morphology features were also found in some other BMGs with good room temperature plasticity [24, 25].

6.4 Discussion

6.4.1 Structural phase separation

From Figure 6.5 and Figure 6.6, it is shown that the microstructure is heterogeneous for the as-cast amorphous alloy with alloying $\text{Co}_{0.5}$ for the cast size of 3 mm. The formation of the phase separation can be interpreted from the viewpoint of mixing enthalpy among the components in the amorphous system. The heat of mixing between Cu and Co is positive, with the value of +6 kJ/mol. Therefore, there exists repelling force between Cu atoms and Co atoms. They may separate from each other during solidification, resulting in the formation of Cu-rich or Co-rich clusters. Furthermore, Co tends to be more easily attracted by Zr due to the large heat of mixing between them ($\Delta H_{\text{Zr-Co}} = -41$ kJ/mol), leading to the formation of ZrCo-rich clusters. It has been suggested that the diffusivity of Cu in Cu-Zr alloy is up to 10^5 times faster

than that of Zr [26], facilitating the dispersion of Cu-rich cluster in the supercooled liquid. The mobility and further growth of these clusters may be inhibited by Zr and Al atoms because of their larger atomic size and slower mobility. Therefore, phase separation with formation of two atomic clusters may occur during the solidification in the BMG system. There may exist two different regions, dense (or hard) region and loose (or soft) region due to the different chemical affinity and atomic packing density of the clusters [27]. Accordingly, in the current BMG system, the Cu-rich phase should be the soft phase, rich in free volume, and the ZrCo-rich phase should be the hard one, rich in icosahedra.

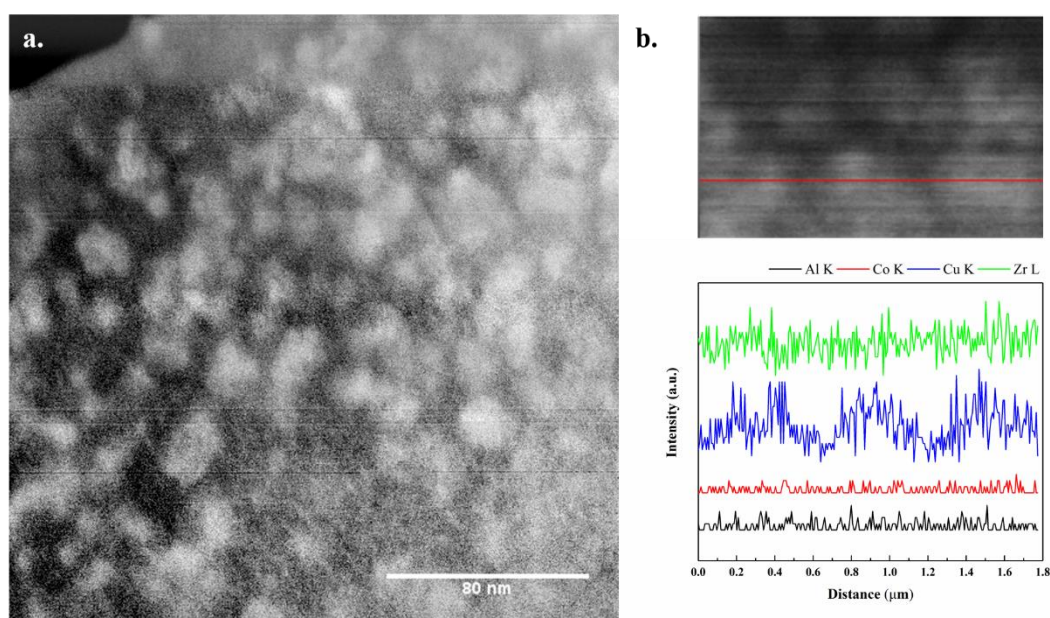


Figure 6.9. TEM images of as-cast rod with diameter of 3 mm for $\text{Cu}_{47.5}\text{Zr}_{48}\text{Al}_4\text{Co}_{0.5}$ BMG: (a) High-angle annular dark-field scanning transmission electron microscopy (HAADF STEM); (b) Line-EDS with EDS spectrum.

The small positive mixing enthalpy of Zr-Co and the minor content of Co alloying will move the solution to the metastable liquid region (outside of spinodal region) and lead to the formation of small chemical fluctuations in the supercooled melt during cooling. The compositional fluctuations will increase the Gibbs energy of the liquid,

which may initiate phase separation in the solution to lower its free energy. The separated liquids may transform into different amorphous phases with further cooling. It has been found that the cooling rate will affect the formation of phase separation in the metallic glass system [28]. In the current metallic glass system, there is sufficient time for the nucleation and growth of the Zr-Co-rich and Cu-rich liquid clusters by diffusion because of the lower cooling rate (3 mm in diameter). The two liquids will solidify into two different amorphous phases with further cooling.

A clear bright-dark phase separated structure of $\text{Cu}_{47.5}\text{Zr}_{48}\text{Al}_4\text{Co}_{0.5}$ BMG in 3 mm rod in HAADF STEM mode has been displayed in Figure 6.9 (a). The darker contrast phase is surrounded by the bright phase, with the size 15 – 25 nm, which is in accordance with the results in section 6.3.1. As reported, the characteristic size of the amorphous phases in phase-separated system is determined by both the metallic system and the local cooling rate. For example, the dark phase is in the scale of 15 – 35 nm in the as-cast $\text{Cu}_{47.2}\text{Zr}_{46.5}\text{Al}_{5.5}\text{Nb}_{0.8}$ rod [28], is around 50 nm in the as-spun $\text{Cu}_{46}\text{Zr}_{22}\text{Gd}_{25}\text{Al}_7$ ribbon [29], is around 20 nm in the as-cast $\text{Cu}_{45}\text{Zr}_{47}\text{Al}_7\text{Fe}_1$ rod [25], and is in the range of 0.5 – 1 μm in as cast $\text{Zr}_{63.8}\text{Ni}_{16.2}\text{Cu}_{15}\text{Al}_5$ rod [30] and so on. Line chemical distribution mapping crossing both bright and dark phases was obtained in a STEM mode with a nominally 1.0 nm electron probe. It revealed that the brighter contrast phase contains more Zr than the darker contrast phase, however, it is difficult to detect the difference for Al and Co in both phases. Therefore, electron energy loss spectroscopy (EELS) was carried out to clarify Co element distribution in bright and dark phases, as shown in Figure 6.10. Due to the minor addition of Co, however, only a weak signal could be collected. Based on line-EDS results and the mixing enthalpy theory, the bright phase is rich in Zr-Co, while the dark phase is rich in Cu, indicating the occurrence of phase separation in the as-cast $\text{Cu}_{47.5}\text{Zr}_{48}\text{Al}_4\text{Co}_{0.5}$ BMG during rapid solidification. However, the uncertainty of the structure arising from imaging and sample preparation artefacts could not be ruled out.

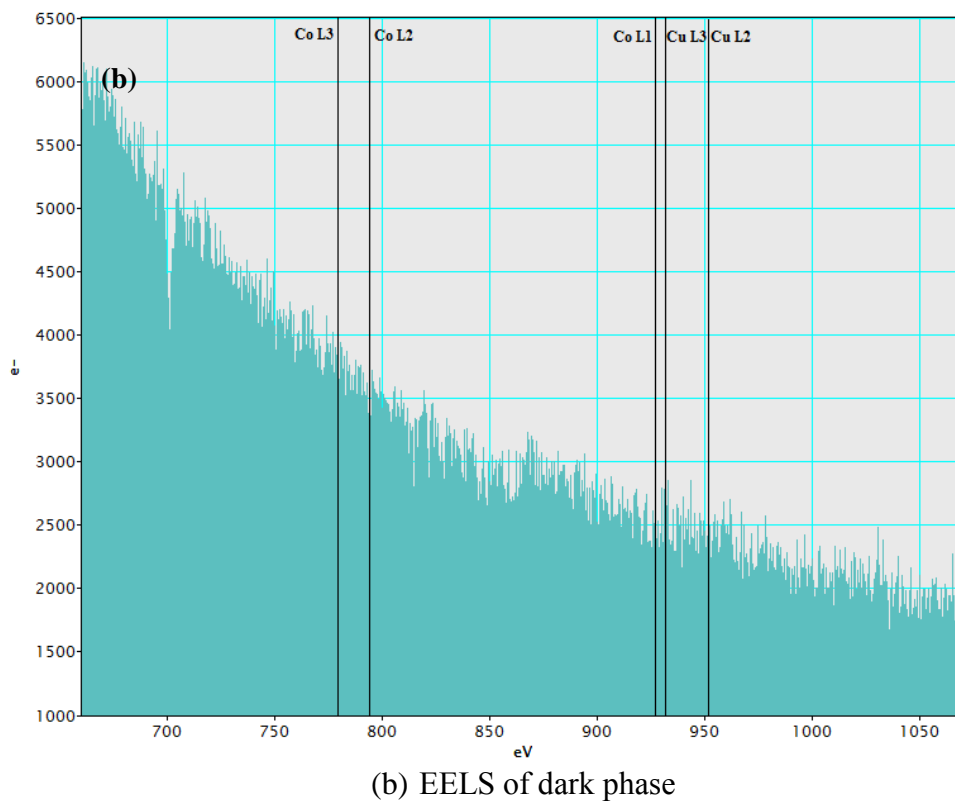
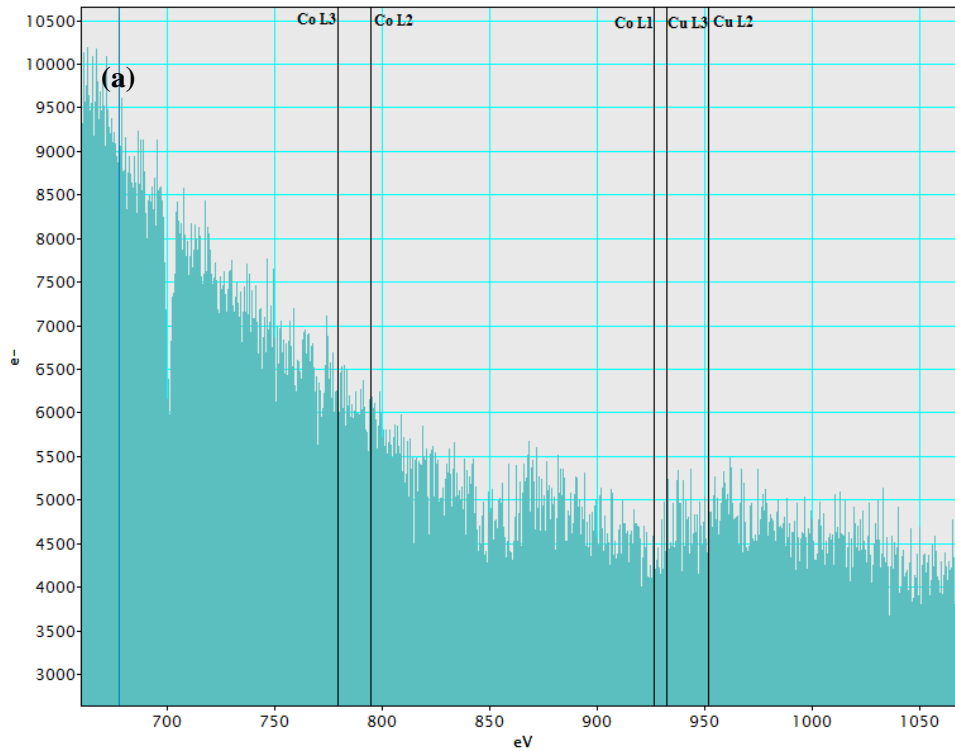


Figure 6.10. EELS of (a) bright phase and (b) dark phase in the as-cast $\text{Cu}_{47.5}\text{Zr}_{48}\text{Al}_4\text{Co}_{0.5}$ BMG with diameter of 3 mm.

6.4.2 Relationship between phase separation and mechanical property

As mentioned in section 6.3.2, the phase separated $\text{Cu}_{47.5}\text{Zr}_{48}\text{Al}_4\text{Co}_{0.5}$ BMG alloy not only exhibits modest plasticity but also remarkable work hardening. In order to shed light upon the underlying mechanism, the microstructure after fracture has been obtained, as shown in Figure 6.11. It is still amorphous in nature after deformation. There is no nanocrystalline precipitation during deformation, suggesting the structural heterogeneity may account for the mechanical properties.

It is expected that they should have different hardness, modulus and critical shear stress for these two distinct phases because of different chemical compositions, different packing density and different coordination numbers [30, 31]. Therefore, the reduced Young's modulus (E_r) and hardness (H) for each phase were measured with nanoindentation, as summarized in Table 6.2. According to the measurement, one phase is comparatively hard, with E_r of 202.7 ± 18.9 GPa and H of 11.9 ± 1.5 GPa, the other phase is comparatively soft, with E_r of 159.8 ± 7.2 GPa and H of 10.4 ± 1.1 GPa. The differences between the reduced Young's modulus and the hardness for these two distinct phases are 42.9 GPa and 1.5 GPa, respectively. Thus, in the current metallic system, phase separation may play an important role in its mechanical property. The measured Poisson ratio with the ultrasonic measurement is 0.333 for the $\text{Cu}_{47.5}\text{Zr}_{48}\text{Al}_4\text{Co}_{0.5}$ BMG. Assuming the difference of Poisson ration of the two phases is small enough to neglect, according to the relationship between the elastic moduli [32], the shear modulus and bulk modulus for two amorphous phases are 59.9 ± 2.7 GPa, 159.5 ± 7.2 GPa and 76 ± 7.1 GPa, 202.3 ± 18.9 GPa, respectively, as summarized in Table 6.2.

On the basis of the shear transformation zone (STZ) theory, the plasticity of the BMGs results from the formation and cooperative shearing of STZs. Upon loading, STZs prefer to nucleate in the regions where the energy barrier is lower when the critical shear stress is reached. These sites in the heterogeneous BMGs are supposed to be the

interface or the phase with lower modulus. When one STZ in a preferential site is activated, the second one will be generated subsequently around it. Once a critical number of STZs have been activated, they will transform into a shear band. The shear band will propagate along the plane with maximum applied shear stress, meet in the site with higher critical shear stress, and then its propagation will be hindered. The shear bands are generated continuously, resulting in the work hardening like behaviour. For the current $\text{Cu}_{47.5}\text{Zr}_{48}\text{Al}_4\text{Co}_{0.5}$ BMG alloy, the difference in shear modulus for two phases is around 16 GPa, which is pronounced. When the shear band is activated in the interface or in the soft phase domain (with lower shear modulus), it prefers to propagate along the soft phase domain. It takes more energy to move into the hard phase domain, therefore, the propagation of the shear band may be blocked. As a result, the shear bands coalesce, the free volumes agglomerate, and the crack generates, then finally fractured catastrophically.

Table 6.2. The reduced Young's modulus (E_r) and hardness (H) for the bright and the dark phase in the $\text{Cu}_{47.5}\text{Zr}_{48}\text{Al}_4\text{Co}_{0.5}$ BMG alloy with the diameter of 3 mm.

$\text{Cu}_{47.5}\text{Zr}_{48}\text{Al}_4\text{Co}_{0.5}$ Alloy (Co05D3, at.%)	Reduced Young's Modulus E_r (GPa)	Hardness H (GPa)	Shear Modulus G (GPa)	Bulk Modulus B (GPa)
Bright Phase (in AFM)	159.8±7.2	10.4±1.1	59.9±2.7	159.5±7.2
Dark Phase (in AFM)	202.7±18.9	11.9±1.5	76±7.1	202.3±18.9

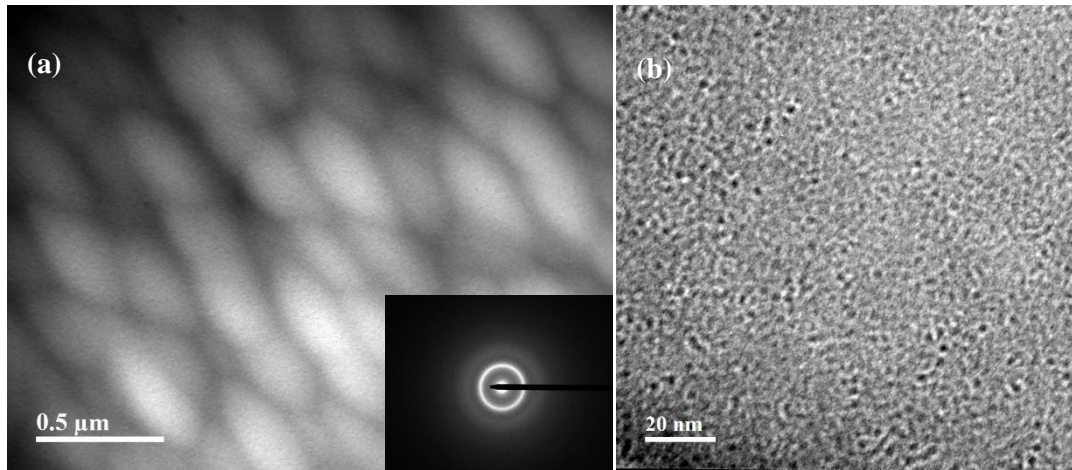


Figure 6.11. TEM images of the as-fractured $\text{Cu}_{47.5}\text{Zr}_{48}\text{Al}_4\text{Co}_{0.5}$ BMG: (a) The low magnification bright-field TEM image, inset shows the corresponding diffraction pattern; (b) HRTEM image of the interface.

6.5 Conclusions

In this chapter, phase separation in $\text{Cu}_{47.5}\text{Zr}_{48}\text{Al}_4\text{Co}_{0.5}$ BMG alloy has been reported. The AFM and TEM results give the direct evidence of the microstructural heterogeneity. Line EDS measurement further confirm that the bright phase is Zr-Co rich domain while the dark phase is Cu-rich domain. The $\text{Cu}_{47.5}\text{Zr}_{48}\text{Al}_4\text{Co}_{0.5}$ BMG alloy with phase separated structure exhibits a modest plasticity of $\sim 6\%$ in compression with remarkable work hardening ability at the room temperature. The measurement of hardness and Young's modulus for two phases with nanoindentation and corresponding calculation of shear modulus reveals the underlying mechanism. Liquid phase separation, as a structural heterogeneity, can contribute to multiplication of shear bands; on the other hand, it can retard the propagation of shear bands during deformation, resulting the work hardening-like behaviour. The difference in shear modulus is ~ 16 GPa, therefore, it will take more energy for shear band to propagate from soft region to hard region, accounting for the modest plasticity.

6.6 References

- [1] D. C. Hofmann, "Bulk metallic glasses and their composites: a brief history of diverging fields," *Journal of Materials*, vol. 2013, 2013.
- [2] D. C. Hofmann and W. L. Johnson, "Improving Ductility in Nanostructured Materials and Metallic Glasses: "Three Laws", in *Materials Science Forum*, 2010, pp. 657-663.
- [3] D. C. Hofmann, J.-Y. Suh, A. Wiest, G. Duan, M.-L. Lind, M. D. Demetriou, *et al.*, "Designing metallic glass matrix composites with high toughness and tensile ductility," *Nature*, vol. 451, pp. 1085-1089, 2008.
- [4] D. C. Hofmann, J.-Y. Suh, A. Wiest, M.-L. Lind, M. D. Demetriou, and W. L. Johnson, "Development of tough, low-density titanium-based bulk metallic glass matrix composites with tensile ductility," *Proceedings of the National Academy of Sciences*, vol. 105, pp. 20136-20140, 2008.
- [5] J. Schroers and W. L. Johnson, "Ductile bulk metallic glass," *Physical Review Letters*, vol. 93, p. 255506, 2004.
- [6] W. H. Wang, C. Dong, and C. H. Shek, "Bulk metallic glasses," *Materials Science and Engineering: R: Reports*, vol. 44, pp. 45-89, 6/1/ 2004.
- [7] J. Eckert, J. Das, S. Pauly, and C. Duhamel, "Processing Routes, Microstructure and Mechanical Properties of Metallic Glasses and their Composites," *Advanced Engineering Materials*, vol. 9, pp. 443-453, 2007.
- [8] J. Eckert, J. Das, K. B. Kim, F. Baier, M. B. Tang, W. H. Wang, *et al.*, "High strength ductile Cu-base metallic glass," *Intermetallics*, vol. 14, pp. 876-881, 8// 2006.
- [9] S. Pauly, S. Gorantla, G. Wang, U. Kuhn, and J. Eckert, "Transformation-mediated ductility in CuZr-based bulk metallic glasses," *Nat Mater*, vol. 9, pp. 473-7, Jun 2010.
- [10] J. Qiao, "In-situ dendrite/metallic glass matrix composites: a review," *Journal of Materials Science & Technology*, vol. 29, pp. 685-701, 2013.
- [11] D. C. Hofmann, "Shape memory bulk metallic glass composites," *Science*, vol. 329, pp. 1294-1295, 2010.
- [12] P. Gargarella, S. Pauly, K. Song, J. Hu, N. Barekar, M. Samadi Khoshkhoo, *et al.*, "Ti-Cu-Ni shape memory bulk metallic glass composites," *Acta Materialia*, vol. 61, pp.

- 151-162, 2013.
- [13] Y. Wu, Y. Xiao, G. Chen, C. T. Liu, and Z. Lu, "Bulk Metallic Glass Composites with Transformation-Mediated Work-Hardening and Ductility," *Advanced Materials*, vol. 22, pp. 2770-2773, 2010.
- [14] H. Kozachkov, J. Kolodziejska, W. L. Johnson, and D. C. Hofmann, "Effect of cooling rate on the volume fraction of B2 phases in a CuZrAlCo metallic glass matrix composite," *Intermetallics*, vol. 39, pp. 89-93, 2013.
- [15] E. S. Park and D. H. Kim, "Phase separation and enhancement of plasticity in Cu–Zr–Al–Y bulk metallic glasses," *Acta Materialia*, vol. 54, pp. 2597-2604, 6// 2006.
- [16] J. C. Oh, T. Ohkubo, Y. C. Kim, E. Fleury, and K. Hono, "Phase separation in Cu₄₃Zr₄₃Al₇Ag₇ bulk metallic glass," *Scripta Materialia*, vol. 53, pp. 165-169, 7// 2005.
- [17] S. S. Chen and I. Todd, "Enhanced plasticity in the Zr–Cu–Ni–Al–Nb alloy system by in-situ formation of two glassy phases," *Journal of Alloys and Compounds*, vol. 646, pp. 973-977, 10/15/ 2015.
- [18] D. H. Kim, W. T. Kim, E. S. Park, N. Mattern, and J. Eckert, "Phase separation in metallic glasses," *Progress in Materials Science*, vol. 58, pp. 1103-1172, 10// 2013.
- [19] A. Inoue, "Stabilization of metallic supercooled liquid and bulk amorphous alloys," *Acta materialia*, vol. 48, pp. 279-306, 2000.
- [20] A. Inoue and W. Zhang, "Formation, thermal stability and mechanical properties of Cu–Zr–Al bulk glassy alloys," *Materials Transactions*, vol. 43, pp. 2921-2925, 2002.
- [21] B. B. Sun, Y. B. Wang, J. Wen, H. Yang, M. L. Sui, J. Q. Wang, *et al.*, "Artifacts induced in metallic glasses during TEM sample preparation," *Scripta Materialia*, vol. 53, pp. 805-809, Oct 2005.
- [22] W. C. Oliver and G. M. Pharr, "An improved technique for determining hardness and elastic modulus using load and displacement sensing indentation experiments," *Journal of Materials Research*, vol. 7, pp. 1564-1583, 1992.
- [23] H. S. Chen, "Stored energy in a cold-rolled metallic glass," *Applied Physics Letters*, vol. 29, pp. 328-330, 1976/09/15 1976.
- [24] E. S. Park, H. J. Chang, and D. H. Kim, "Effect of addition of Be on glass-forming

- ability, plasticity and structural change in Cu–Zr bulk metallic glasses," *Acta Materialia*, vol. 56, pp. 3120-3131, 2008/08/01/ 2008.
- [25] J. Pan, L. Liu, and K. C. Chan, "Enhanced plasticity by phase separation in CuZrAl bulk metallic glass with micro-addition of Fe," *Scripta Materialia*, vol. 60, pp. 822-825, 5// 2009.
- [26] A. L. Greer, "Stress effects on interdiffusion in amorphous multilayers," in *Defect and Diffusion Forum*, 1996, pp. 163-180.
- [27] T. Wang, Y. Wu, J. Si, Y. Liu, and X. Hui, "Plasticizing and work hardening in phase separated Cu-Zr-Al-Nb bulk metallic glasses by deformation induced nanocrystallization," *Materials & Design*, 2018/01/03/ 2018.
- [28] S. S. Chen, H. R. Zhang, and I. Todd, "Phase-separation-enhanced plasticity in a Cu_{47.2}Zr_{46.5}Al_{5.5}Nb_{0.8} bulk metallic glass," *Scripta Materialia*, vol. 72–73, pp. 47-50, 2// 2014.
- [29] E. S. Park, J. S. Kyeong, and D. H. Kim, "Phase separation and improved plasticity by modulated heterogeneity in Cu–(Zr,Hf)–(Gd,Y)–Al metallic glasses," *Scripta Materialia*, vol. 57, pp. 49-52, 2007/07/01/ 2007.
- [30] X. H. Du, J. C. Huang, K. C. Hsieh, Y. H. Lai, H. M. Chen, J. S. C. Jang, *et al.*, "Two-glassy-phase bulk metallic glass with remarkable plasticity," *Applied Physics Letters*, vol. 91, p. 131901, 2007.
- [31] K. F. Yao and C. Q. Zhang, "Fe-based bulk metallic glass with high plasticity," *Applied Physics Letters*, vol. 90, p. 061901, 2007/02/05 2007.
- [32] G. E. Dieter and D. J. Bacon, *Mechanical metallurgy* vol. 3: McGraw-hill New York, 1986.

Chapter 7 Alloying Addition Effects

7.1 Discussion

In this project, $\text{Cu}_{48}\text{Zr}_{48}\text{Al}_4$ was chosen as the base alloy. It was reported that a fully amorphous structure in a critical diameter of 2 mm could be fabricated by copper mould suction casting [1]. As reported in the literature [2], the introduction of minor Co (~0.5 at%) to the CuZr-based alloy could induce significant tensile ductility, which was due to the increase in the size of B2-CuZr spheres (~100 μm). Further study [3] indicated that the addition of Co can promote deformation twinning and martensitic transformation by reducing stacking fault energy. Sn and Ni were selected as minor doping additions to replace Cu to optimize the microstructure and thereby improving mechanical properties on the account of similar features as Co with respect to the CuZr-based system, *i.e.*, the mixing enthalpy between Sn and Zr and that between Ni and Zr are in large negative values and the mixing enthalpy between Sn and Cu and that between Ni and Cu are in small positive values. It was expected to cause structural perturbations in the undercooled liquid melt and thereby modifying microstructures of the resultant alloys. The mixing enthalpy between the doping additions and Cu/Zr/Al are listed in the Table 7.1. Large negative heat of mixing with Zr may lead to the formation of numerous short-range crystalline orders in the supercooled metallic melt, which may serve as potent nucleus during solidification, thereby leading to the heterogeneous nucleation and microstructure optimization.

Table 7.1. The mixing enthalpy between doping additions (*e.g.*, Sn, Ni and Co) and Cu/Zr/Al [4].

ΔH_{mixing} (kJ/mol)	Cu	Zr	Al
Sn	+7	-43	+4
Ni	+4	-49	-22
Co	+6	-41	-19

As reported in the previous chapters, the minor alloying additions of Sn, Ni, and Co to the base alloy result in the different changes in the microstructures and corresponding mechanical properties. The CuZr-based BMG alloy with the composition of $\text{Cu}_{47.5}\text{Zr}_{48}\text{Al}_4\text{Co}_{0.5}$ was reproduced in the form of ribbon and rod with different sizes. Liquid phase separation phenomenon was observed in the Co-doped amorphous alloy in the diameter of 3 mm, which was different from the literature [2]. In the amorphous alloy, the heat of mixing between Co and Zr is largely negative, with the value of - 41 kJ/mol, and that between Co and Cu is slightly positive, with the value of +6 kJ/mol [4]. Therefore, it is possible to form liquid separated structure under suitable fabrication conditions.

As reported in the previous chapters, the minor Sn addition leads to the formation of large-sized BMGMCs with the size up to 8 mm without sacrificing mechanical properties (as summarized in the Table 4.5), while the minor addition of Ni results in the modification of microstructure and improvement in mechanical properties without increasing the rod size ($d=3$ mm, as summarized in the Table 5.4). Gradual increase of Sn alloying in the base alloy from 0.25 at% to 1 at% leads to the formation of different microstructures (including size and distribution of B2-CuZr spheres in the amorphous matrix), critical rod sizes and mechanical performances. The composites doped with 0.25 at% Sn and 0.75 at% Sn exhibit large critical rod sizes up to 8 mm with excellent compressive strength and plasticity even though the size, distribution and volume fraction of in-situ formed crystalline phases are different. It was speculated that the resultant structures of BMG composites benefit from the pre-formed short-range atomic clusters in the undercooled metallic melt. They served as potent nucleation sites, promoting homogeneous distribution of crystals and further improving mechanical properties, which is similar as incubation techniques to refine grain size in the industry. However, how Sn atoms interact with other atoms in the liquid melts, crystal growth dynamics and why slight difference in Sn content causes changes in structure and mechanical behaviour need further study in the future.

With respect to minor Ni alloying additions to the base alloy system, compressive properties of the corresponding composites have been improved moderately compared to the Cu-Zr-Al ternary BMGMCs by optimizing composite microstructure, i.e., the size, distribution and volume fraction of crystalline spheres in the glassy matrix. The attainable size was still in the diameter of 3 mm. Introduction of Ni results in the formation of nano-scaled strip-like features and needle-like martensites in the vicinity of interface, which may act as preferred

phase transformation nucleation sites upon deformation and thereby facilitating mechanical properties.

Even though Sn, Ni and Co all exhibit similar thermodynamic properties (*i.e.*, large negative heat of mixing with Zr and small positive heat of mixing with Cu) in the Cu-Zr-Al system, the resultant microstructures and mechanical behaviours varies from each other. Sn and Ni leads to the formation of spherical crystal reinforced BMGMCs structure and Co causes liquid phase separation structure. According to the TEM analysis on both glassy matrix and precipitated crystalline phase of Sn-doped and Ni-doped BMGMCs after fracture, the role of glassy phases played in the deformation behaviour were different. In 0.25 at% Sn-doped CuZr-based BMGMCs, nanocrystallization occurred and contributed to the improved compressive strength and plasticity; while only shear bands were observed in the amorphous matrix in fractured 0.75 at% Ni-alloyed BMGMCs. The different changes of amorphous phases may results from different minor alloying additions. Furthermore, the sub-microstructure in spherical crystals, the preferred crystalline orientations of in-situ formed crystals and martensitic transformation will be affected by minor alloying additions. The mechanism underneath needs further work to be done.

7.2 References

- [1] Y. Wu, H. Wang, H.H. Wu, Z.Y. Zhang, X.D. Hui, G.L. Chen, D. Ma, X.L. Wang, Z.P. Lu, Formation of Cu–Zr–Al bulk metallic glass composites with improved tensile properties, *Acta Materialia* 59(8) (2011) 2928-2936.
- [2] Y. Wu, Y. Xiao, G. Chen, C.T. Liu, Z. Lu, Bulk Metallic Glass Composites with Transformation-Mediated Work-Hardening and Ductility, *Advanced Materials* 22(25) (2010) 2770-2773.
- [3] D.Q. Zhou, Y. Wu, H. Wang, X.D. Hui, X.J. Liu, Z.P. Lu, Alloying effects on mechanical properties of the Cu–Zr–Al bulk metallic glass composites, *Computational Materials Science* 79 (2013) 187-192.
- [4] A. Takeuchi, A. Inoue, Classification of bulk metallic glasses by atomic size difference, heat of mixing and period of constituent elements and its application to characterization of the main alloying element, *Materials Transactions* 46(12) (2005) 2817-2829.

Chapter 8 Summary and Conclusions

In this project, different CuZr-based bulk metallic glass composites with improved mechanical performance were produced by introducing different alloying additions. The important conclusions are summarized as follows:

1. Minor alloying additions, such like Ni and Sn, which have large negative heat of mixing with Zr and small heat of mixing with Cu, could optimize the size and distribution of crystals in the glassy matrix. Large negative heat of mixing with Zr may result in the formation of numerous crystal-like clusters in the supercooled melt, which may serve as potent nucleus during solidification, thereby leading to the heterogeneous nucleation and microstructure optimization.

2. The purity of raw materials will influence the microstructure, in situ formed phases and deformation behaviours of the resultant bulk metallic glass composites. High oxygen content in the raw materials may result in the formation of brittle crystalline phase in the glassy matrix, leading to the instability in the flow stress and catastrophic failure.

3. The microstructure of the shape memory metallic glass composites, *i.e.* size, distribution of spherical crystals in the amorphous matrix and its volume fraction, is sensitive to the manufacturing conditions. These manufacturing factors, including melting times, melting current and pressure difference for the suction casting, should be controlled at the same level as far as possible for each fabrication (melting and casting) batch. Long melting time or high melting current suggests high initial temperature of the liquid melt in the casting mould, thereby affecting the microstructure of the as-cast CuZr-based BMG/BMGMCs. Lower melt temperature leads to higher undercooling, promoting crystallization. Hence, the precipitated crystals have potential to coalesce with each other and form large crystalline aggregates. Nevertheless, higher melt temperature indicates lower undercooling, thereby hindering crystalline nucleation to some extent. In addition, long melting times may increase the opportunity for the liquid melt to absorb the residual oxygen in the atmosphere, which may lead to the formation of unfavourable brittle phase and deteriorate the mechanical performance. Therefore, the manufacturing conditions, such as melting time and melting current, should be properly adjusted to optimize the microstructure of the CuZr-based bulk metallic glass composites.

4. For the fabrication of CuZr-based bulk metallic glass composites with large diameters ($d \geq 5$ mm), the casting mould shape configuration will affect the resultant microstructures and mechanical properties. In order to control the melt status before casting, the casting mould was modified into the one with a narrow short inlet. This allowed melting temperature adjustment. The detrimental effect of oxides and other contaminants can also be mitigated and eliminated by properly increasing the melting temperature. As a result, the heterogeneous nucleation of CuZr B2 crystals was suppressed, leading to the homogenization of the size and distribution of the crystalline particles in the amorphous matrix.

5. Glass forming ability of the CuZr-based bulk metallic glass composites can be effectively improved with minor Sn additions. The casting size for the CuZr-based bulk metallic glass composites with the composition of $\text{Cu}_{47.75}\text{Zr}_{48}\text{Al}_4\text{Sn}_{0.25}$ was up to 7 mm. The corresponding microstructural evolution is from fully amorphous (≤ 3 mm) to B2 CuZr phase + amorphous matrix (≥ 4 mm) as the cooling rate decreases. The crystal size was in the range of 20 – 40 μm for 4 mm and 5 mm rods, and in the range of 10 – 20 μm for 6 mm and 7 mm rods. The crystal growth was suppressed to some extent. Furthermore, the crystalline volume fractions were maintained around 9 vol% despite the difference in casting sizes. Therefore, it is speculated that the addition of minor Sn (0.25 at%) causes local compositional fluctuation in the melt, leading to the formation of atomic clusters. It is supposed to account for the homogenization of crystal size and its distribution in the amorphous matrix in $\text{Cu}_{47.75}\text{Zr}_{48}\text{Al}_4\text{Sn}_{0.25}$ BMGMCs.

The casting size for the CuZr-based bulk metallic glass composites with the composition of $\text{Cu}_{47.25}\text{Zr}_{48}\text{Al}_4\text{Sn}_{0.75}$ was up to 8 mm. The B2 crystal size and volume fraction grows as the casting size increases for the alloys with 0.75 at% Sn addition in spite of uniform spherical crystals distribution in the amorphous matrix. The reinforced spherical crystalline particles exhibited a substructure with a core surrounded by columnar grains, similar to a characteristic casting ingot structure. BF TEM results confirmed the formation of needle-like martensitic features close to the interface between the crystalline phase and amorphous matrix.

The calculated activation energy corresponding to the glass transition (E_g) and crystallization (E_x) process under continuous heating on the basis of Kissinger equation indicates that grain growth process is more difficult than the nucleation process for both alloys. Hence, it is rationalized that the formation of large-sized cylindrical rods with well separated and uniformly distributed crystals in glassy matrix can be achieved for these two compositions. Furthermore, the lower energy barrier must be overcome to initiate nucleation and more energy

is required for further growth for $\text{Cu}_{47.75}\text{Zr}_{48}\text{Al}_4\text{Sn}_{0.25}$ alloys in comparison to that for $\text{Cu}_{47.25}\text{Zr}_{48}\text{Al}_4\text{Sn}_{0.75}$ alloys. As a result, the size of in situ formed crystals in 0.25 at% Sn doped alloys was smaller than that in 0.75 at% Sn doped alloys with the same casting diameter.

The compression properties of the current Sn-doped CuZr-based BMGMCs with different casting diameters were systematically investigated. The 0.25 at% Sn samples in the size of 6 mm and 7 mm exhibited excellent work-hardening ability and plasticity. The 0.75 at% Sn samples of 6 mm diameter possessed excellent plasticity, up to ~ 15.4%, yet with no work hardening. With the increase in casting size for 0.75 at% Sn alloys, the extent of work hardening became significant. However, samples with 0.5 at% Sn and 1 at% Sn addition exhibited lower yield points and limited plasticity even though they contained more CuZr-B2 phase. Therefore, the size and distribution of the crystal particles in the amorphous matrix will determine the mechanical performance of the alloys to a great extent in comparison with the crystalline volume fraction. The elastic mismatch, *i.e.* hardness and reduced Young's modulus, between crystalline phase and glassy matrix in the Sn-doped CuZr-based metallic glass composites indicates that the larger the disparity, the better the mechanical performance.

In comparison with the CuZr-based bulk metallic glass composites in the literature, the current synthesized $\text{Cu}_{47.75}\text{Zr}_{48}\text{Al}_4\text{Sn}_{0.25}$ and $\text{Cu}_{47.25}\text{Zr}_{48}\text{Al}_4\text{Sn}_{0.75}$ BMG composites are outstanding with a superior combination of strength, plasticity and casting size. However, microstructure evolution during deformation needs to be further investigated to reveal the underlying mechanism.

6. Minor Ni additions (0.25, 0.5, 0.75, 1 at%) were made to the ternary metallic glass alloy $\text{Cu}_{47}\text{Zr}_{47}\text{Al}_4$, the size and distribution of in situ formed crystalline phase in the amorphous matrix was effectively adjusted, thereby improving the mechanical properties. TEM analysis in the microstructural changes of the spherical crystals, amorphous matrix and interface between them in the 0.75 at% Ni-doped metallic glass composites from the as-cast state to the fractured state indicates that pre-existing needle-like martensite and the interface acted as the nucleation sites for the phase transformation. As the deformation proceeded, the martensitic transformation zone gradually extended from the interface to the inside area of the crystalline phase. Interaction between untransformed crystalline phase and amorphous matrix, between transformed crystalline phase and amorphous matrix, between untransformed and transformed crystalline phase contributed to the improved plasticity and work-hardening ability in the current composites.

7. Phase separation was observed in the $\text{Cu}_{47.5}\text{Zr}_{48}\text{Al}_4\text{Co}_{0.5}$ BMG alloy, which has not been reported before. Both AFM and TEM results provided straightforward evidence of the occurrence of the microstructural separation. Line EDS measurement indicated that the phase with bright contrast was Zr-Co rich and the phase with dark contrast was Cu-rich. Unfortunately, the corresponding composition could not be obtained using the available techniques. The phase separated $\text{Cu}_{47.5}\text{Zr}_{48}\text{Al}_4\text{Co}_{0.5}$ BMG alloy shows a modest compressive plasticity of ~ 6% with reasonable work hardening capability at room temperature. Liquid phase separation can contribute to multiplication of shear bands, on the other hand, it can retard the propagation of shear bands during deformation, resulting in the work hardening-like behaviour.

Chapter 9 Suggestions and Future work

1. It is known that microstructural features, including the in situ formed crystalline particle size and distribution in the amorphous matrix, are sensitive to the manufacturing conditions. Even though melting times, melting current, pressure difference required in suction casting were controlled as far as possible during the specimen preparation, the specimen repeatability is still an issue for the fabrication. In order to monitor the melting temperature, it is suggested an infrared pyrometer is used to measure the casting temperature, and therefore, effectively monitor and control it.

2. The dimension of CuZr-based bulk metallic glass composites with Sn addition (0.25at% and 0.75 at%) has reached up to 8 mm in the current study. However, on the limit of the manufacturing capability of the compact Arc melter MAM1 (Edmund Bühler, Germany), samples with larger diameters ($d \geq 9$ mm) cannot be manufactured. In future, specimens with diameters larger than 8 mm with Arc metler AM 500 (Edmund Bühler, Germany) should be prepared to further confirm the largest dimension it could reach.

3. In the CuZr-based bulk metallic glass composites with Sn addition, both 0.25 at% and 0.75 at% Sn alloyed composites exhibited excellent compressive mechanical properties. In this study, only the deformation mechanism for 0.25 at% Sn-doped alloys was studied due to the time limit and the equipment availability. The deformation mechanism, *i.e.* investigation of the the microstructure of the fractured 0.75 at% Sn-doped alloys in the 7 mm diameter specimen needs to be investigated. According to the work hardening rate – true strain curves, the deformation process could be divided into four stages. Microstructural evolution during these four stages is required to further understand the deformation mechanism.

4. The microstructural evolution of both in situ formed crystalline phase and amorphous phase during deformation process needs to be further revealed by TEM. It is known that the initiation of martensitic transformation is preferred by specific crystalline orientations. In the as-cast B2-CuZr phase reinforced metallic glass composites, the orientations for B2-CuZr particles are random. Therefore, the crystalline orientations will determine martensitic transformation actuation. Once the phase transformation is initiated, how the crystalline phases cooperate, and how the transformed phases and untransformed phases behave will determine the related plasticity and work hardening ability. Therefore, it is important to understand the

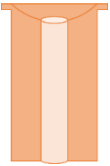
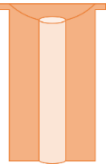
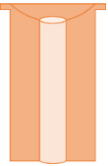
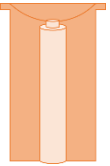
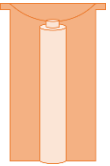
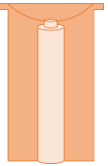
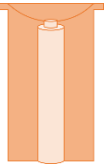
microstructural features of martensitic transformation for the crystalline phase constrained in the rigid amorphous matrix.

5. In this study, minor addition (≤ 1 at%) of Co, Ni and Sn was chosen to replace Cu in the base alloy $\text{Cu}_{47}\text{Zr}_{47}\text{Al}_4$, leading to different microstructure and mechanical properties. The underlying mechanism needs to be found out.

6. In this study, the in situ formed spherical crystalline phase ranges from 10 μm to more than 80 μm . Microstructures shown in TEM images only represent part of it, therefore, EBSD technique is considered to give an overall impression including orientation preference and phase identification in the larger scale. Even though EBSD has been tried several times, no signal has been detected yet. It may be caused by the internal thermal stress in the as-cast specimen or other unknown factors. Therefore, it is important to find out what causes the failure in EBSD in the first place. If the problem could be solved in some way, the understanding of the microstructure for the shape memory bulk metallic glass composites will be extended to larger scale. The orientation preference for martensitic transformation, crystalline phase growth and crystalline phase coalesce could be studied, leading to a deep understanding of solidification mechanism and deformation mechanism. Thus, it will help for the design and development of bulk metallic glass composites with optimized microstructure and improved mechanical properties.

Appendix

Table A.1. Manufacturing conditions for Sn-alloyed CuZr-based BMG/BMGMCs with different diameters.

Diameter (mm)	2	3	4	5	6	7	8
Ingot weight (g)	2	3	4	5	7.5	10.5	13.5
Mould configuration							
Melting current (% of full power)	40 ± 5	40 ± 5	50 ± 5	60 ± 5	60 ± 5	70 ± 5	80 ± 5
Melting time (s)	10 ± 1	10 ± 1	20 ± 1	20 ± 1	20 ± 1	20 ± 1	20 ± 1
Remelting times	5	5	5	5	5	5	5
Casting vacuum (Torr)	6.5×10^0	6.5×10^0	5.5×10^0	5.5×10^{-1}	4.0×10^{-1}	3.0×10^{-1}	2.5×10^{-1}
Casting pressure (bar)	0.65	0.65	0.65	0.65	0.65	0.65	0.65
Casting current (% of full power)	40 ± 5	40 ± 5	40 ± 5	50 ± 5	50 ± 5	70 ± 5	80 ± 5
Casting time (s)	15 ± 1	15 ± 1	15 ± 1	5 ± 1	5 ± 1	5 ± 1	5 ± 1

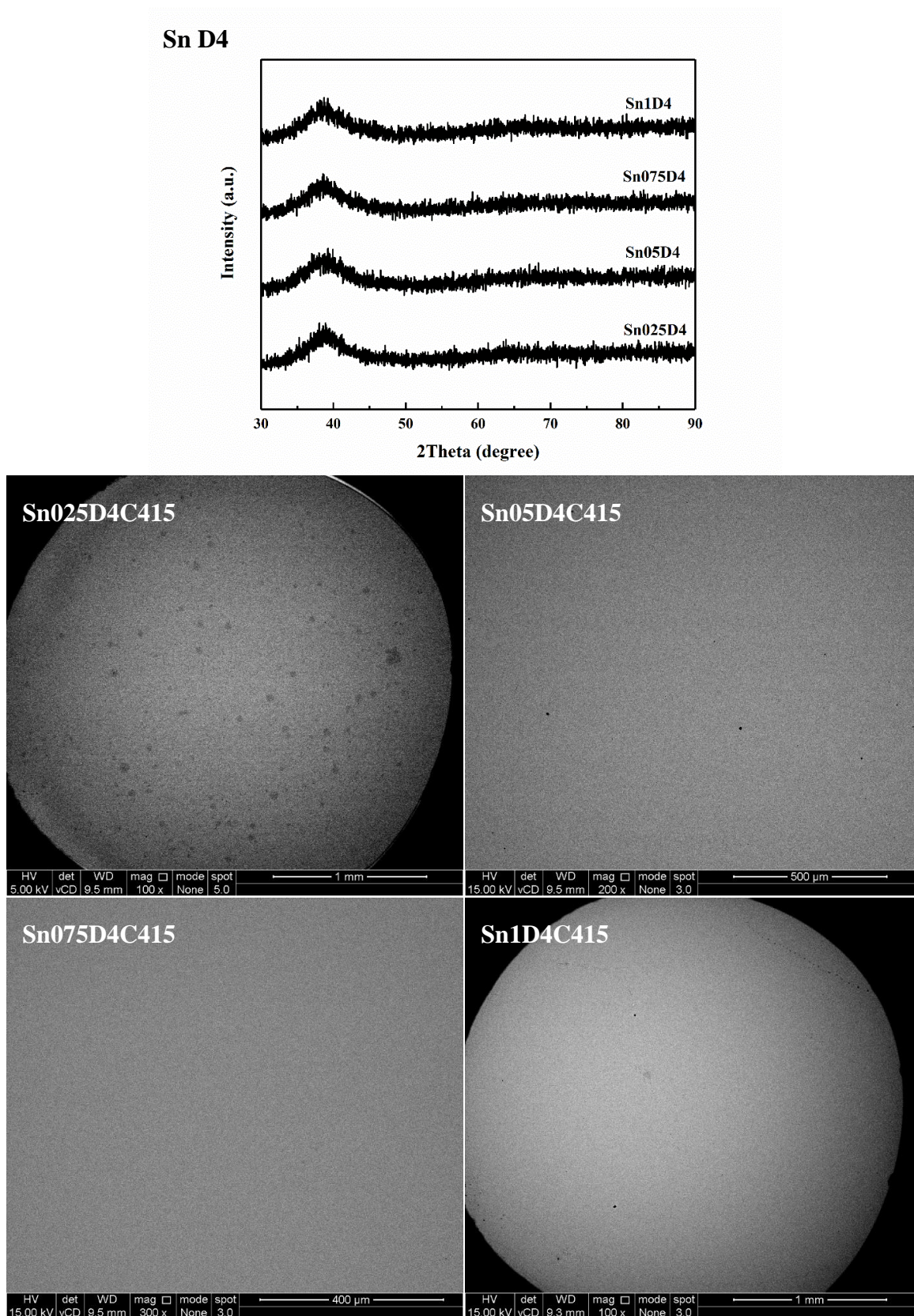


Figure A.1. XRD pattern and cross-section backscattered SEM images of the as-cast $\text{Cu}_{48-x}\text{Zr}_{48}\text{Al}_4\text{Sn}_x$ ($x=0, 0.5, 0.75, 1$ at%) BMG alloys with diameter of 4 mm.

Sn D5

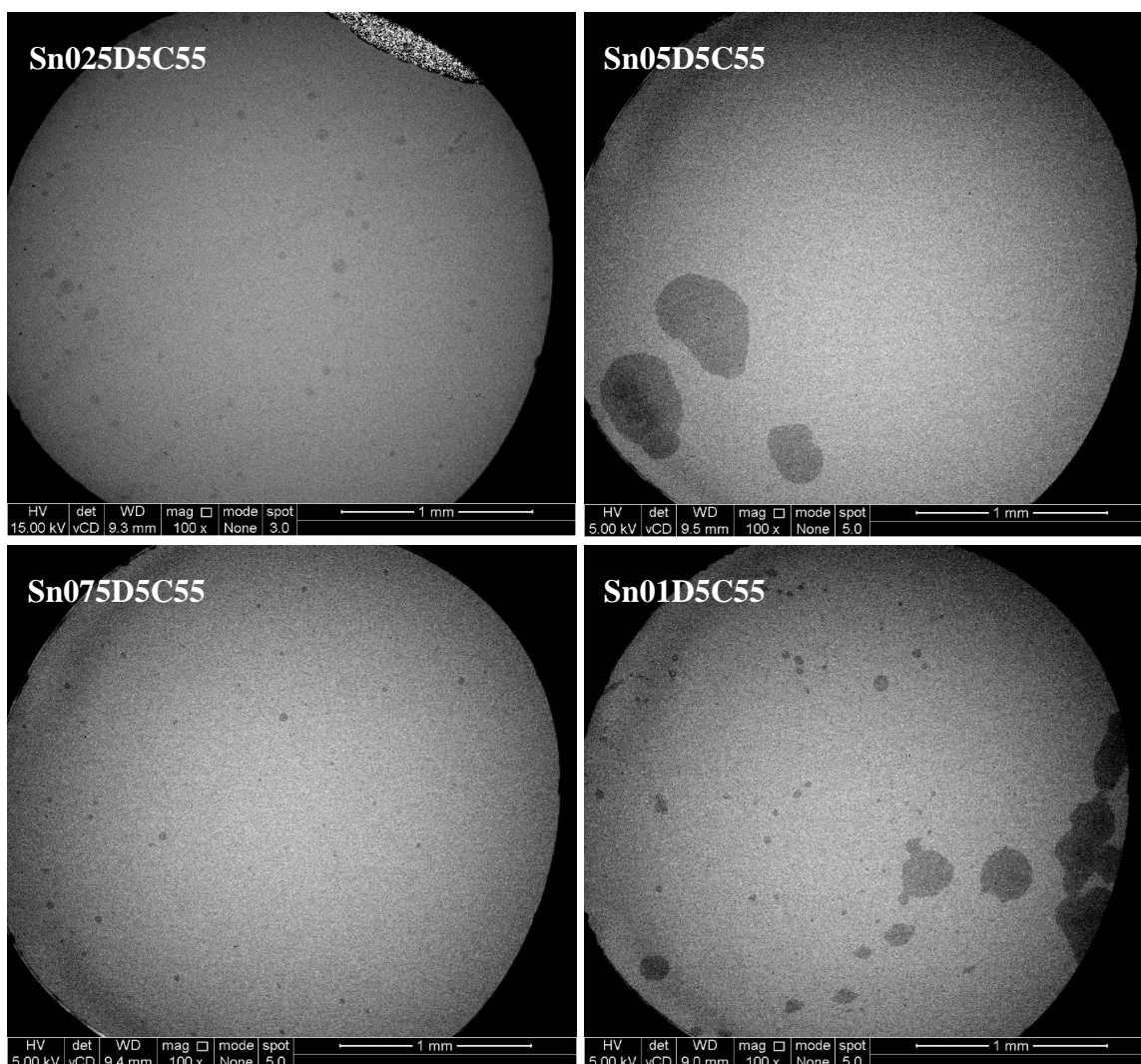
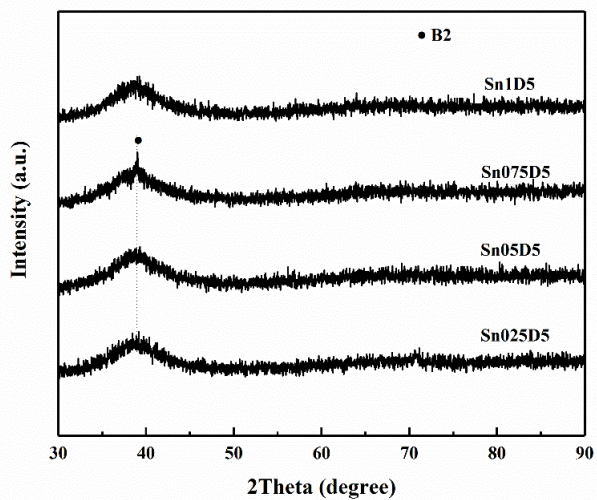


Figure A.2. XRD pattern and cross-section backscattered SEM images of the as-cast $\text{Cu}_{48-x}\text{Zr}_{48}\text{Al}_4\text{Sn}_x$ ($x=0, 0.5, 0.75, 1$ at%) BMG alloys with diameter of 5 mm.

Sn D6

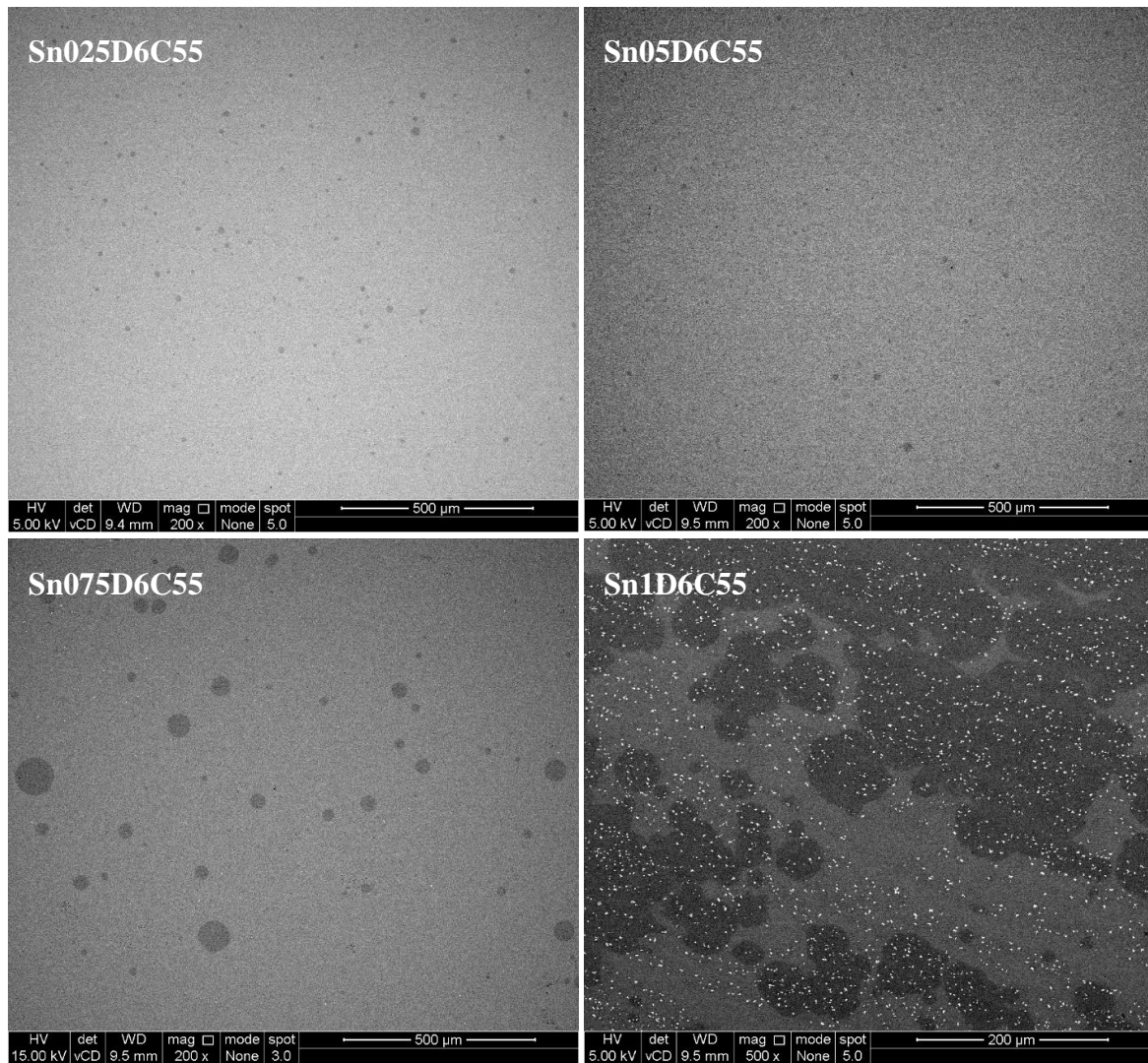
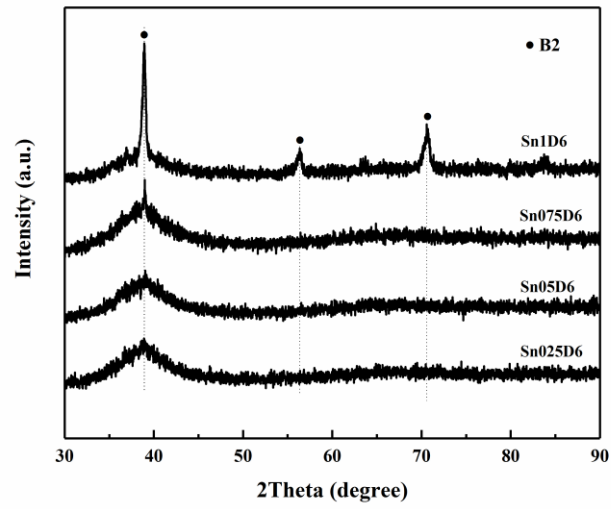


Figure A.3. XRD pattern and cross-section backscattered SEM images of the as-cast $\text{Cu}_{48-x}\text{Zr}_{48}\text{Al}_4\text{Sn}_x$ ($x=0, 0.5, 0.75, 1$ at%) BMG alloys with diameter of 6 mm.

Sn D7

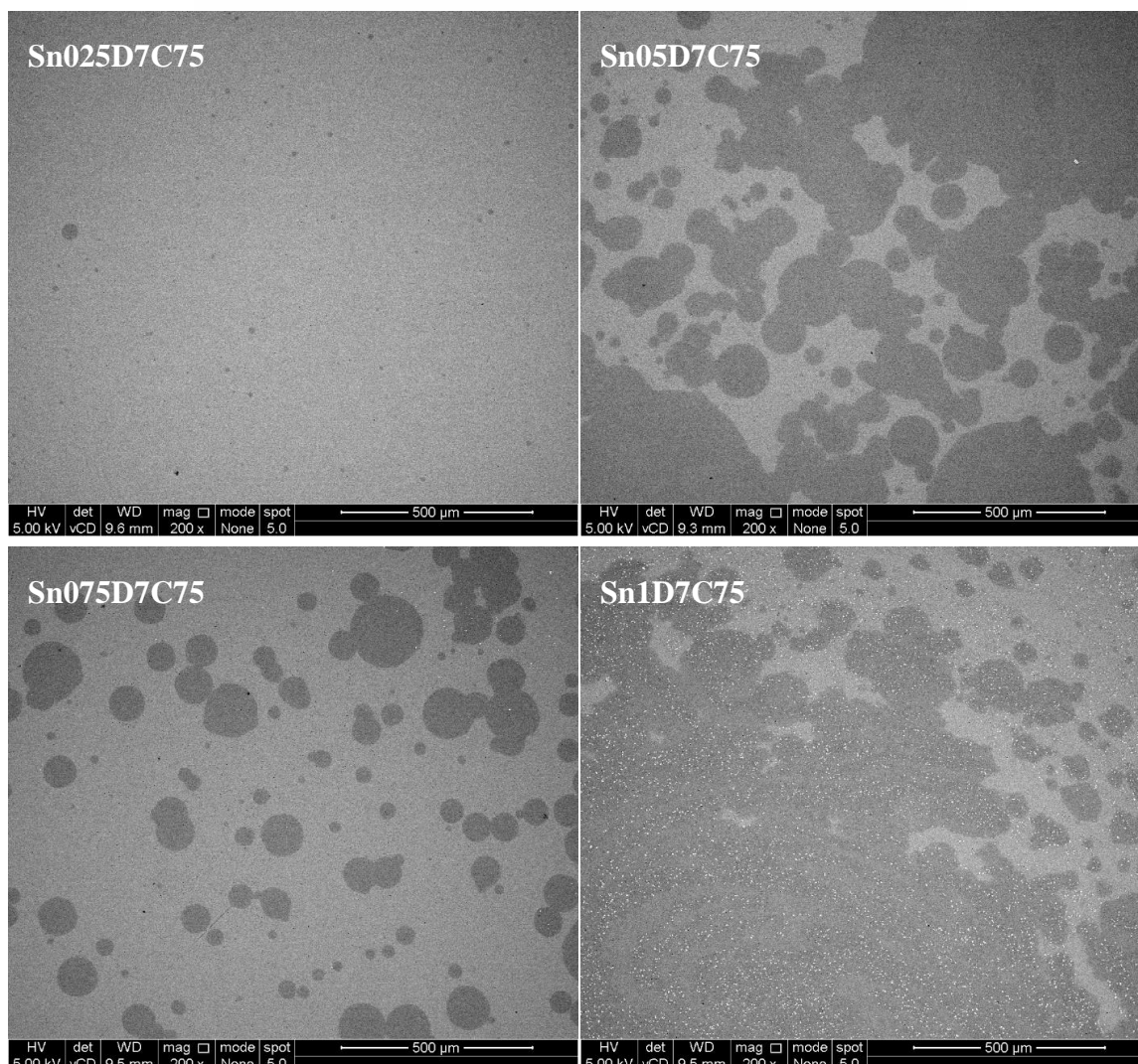
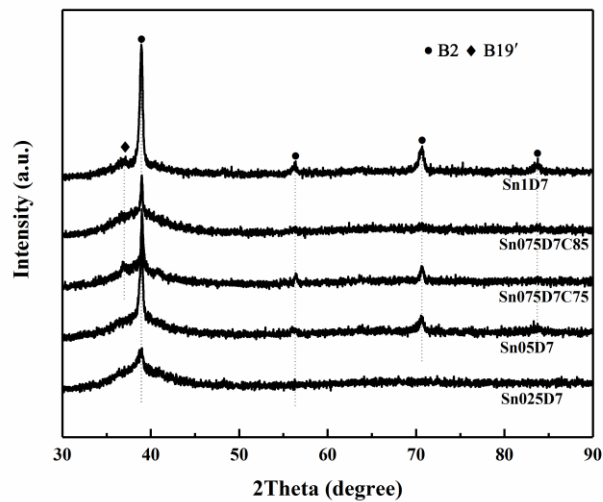


Figure A.4. XRD pattern and cross-section backscattered SEM images of the as-cast $\text{Cu}_{48-x}\text{Zr}_{48}\text{Al}_4\text{Sn}_x$ ($x=0, 0.5, 0.75, 1$ at%) BMG alloys with diameter of 7 mm.

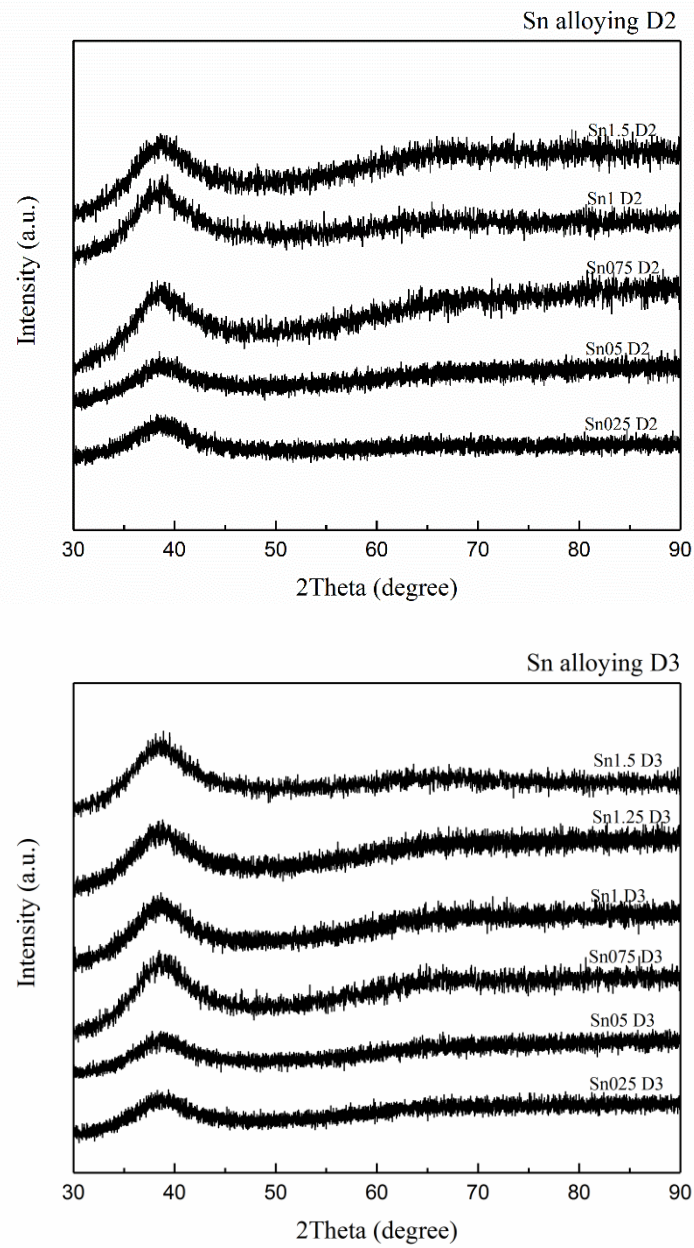


Figure A.5. XRD pattern the as-cast $\text{Cu}_{48-x}\text{Zr}_{48}\text{Al}_4\text{Sn}_x$ ($x=0, 0.5, 0.75, 1$ at%) BMG alloys with diameter of 2 mm and 3 mm.

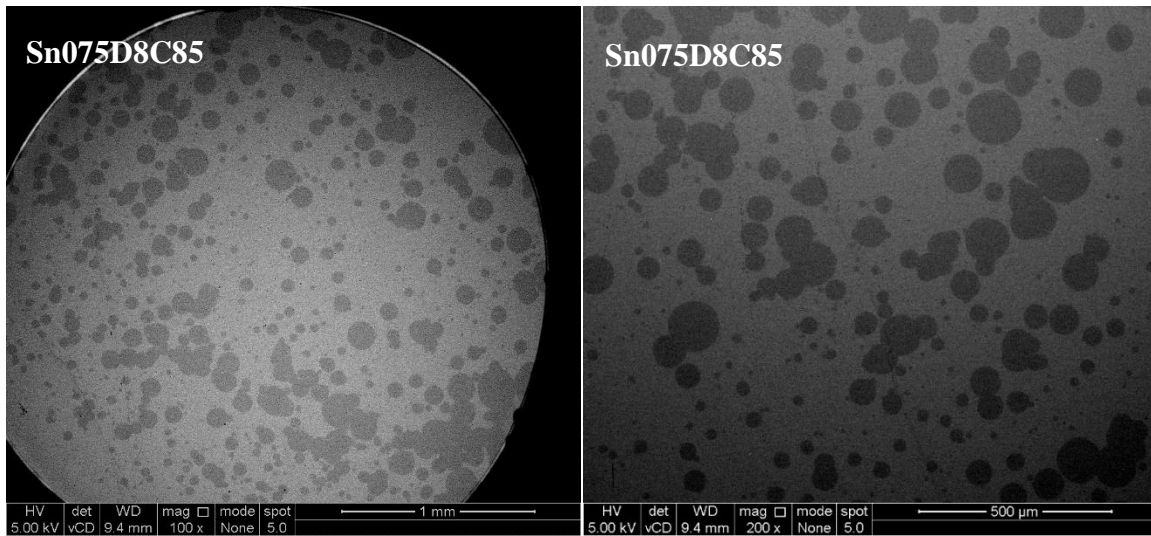


Figure A.6. Cross-section backscattered SEM images of the as-cast $\text{Cu}_{47.25}\text{Zr}_{48}\text{Al}_4\text{Sn}_{0.75}$ BMG alloys with diameter of 8 mm.

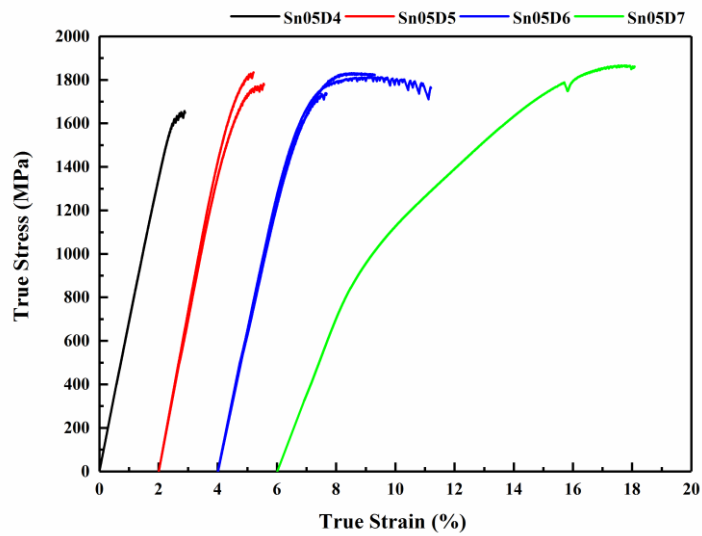


Figure A.7. True stress-strain curves for 0.5at% Sn-doped CuZr-based BMGMCs in different diameters.

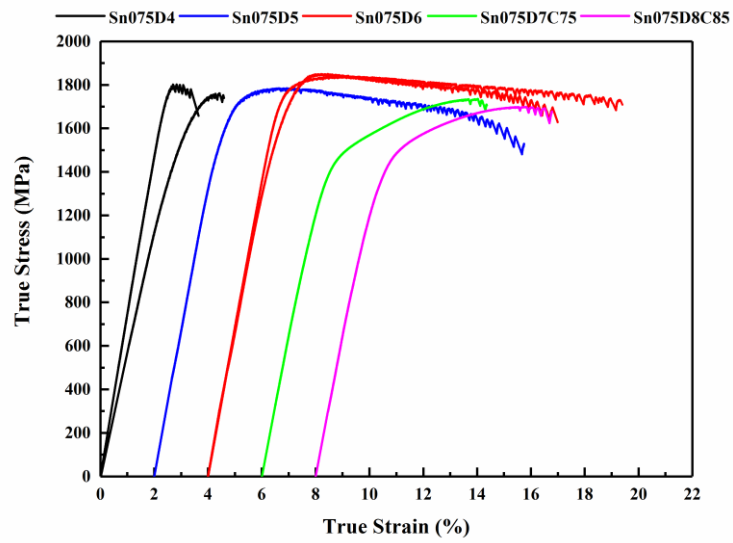


Figure A.8. True stress-strain curves for 0.75at% Sn-doped CuZr-based BMGMCs in different diameters.

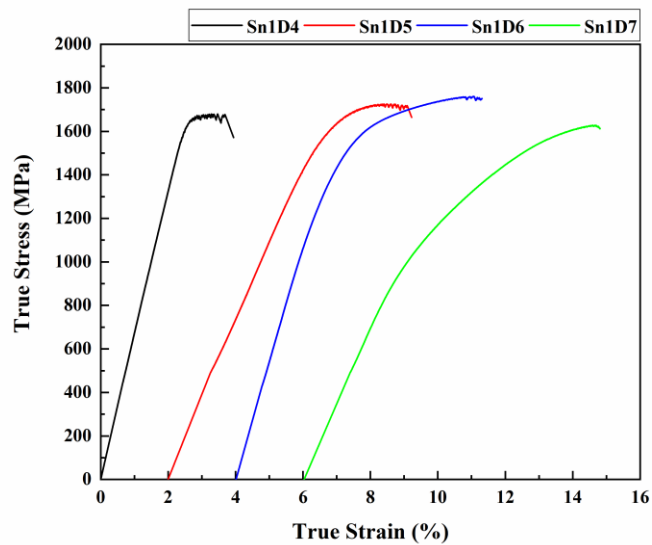


Figure A.9. True stress-strain curves for 1at% Sn-doped CuZr-based BMGMCs in different diameters.